Dust particle growth in protoplanetary disks

Frithjof Brauer

Dissertation

submitted to the
Combined Faculties for the Natural Sciences and for Mathematics
of the Ruperto-Carola University of Heidelberg (Germany)
for the degree of

Doctor of Natural Sciences

presented by

Diplom-Physicist

Frithjof Brauer

born in Eisenach (Germany)

Oral examination: January, 28th 2008

Dust particle growth in protoplanetary disks

Referees: Prof. Dr. Thomas Henning

Prof. Dr. Ralf S. Klessen

Abstract

This thesis deals with the initial stages of planet formation in protoplanetary disks. Particular interest lies on the growth process from sub-μm-sized dust grains towards planetesimals of km-size. To form such large objects in protoplanetary disks, the primary coagulation mechanism has to circumvent at least two severe obstacles, namely the rapid loss of solid material due to radial inward drift and particle fragmentation due to destructive collisions with high velocities. These two hurdles together are called the "Meter size barrier" for particle growth, whose investigation is the main subject of this thesis. We find that the initial dust-to-gas ratio is essential for the particles to overcome the radial drift barrier, i.e. the first part of the meter size barrier. If this ratio is increased by a factor of two compared with the canonical value for the interstellar medium, planetesimals can form within short time scales in the disk. Our simulation results also suggest that the fragmentation barrier, the second part of the meter size barrier, is only overcome if implausible high critical threshold velocities for particle fragmentation are assumed. For this reason, we investigate disk environments which could favour planetesimal formation. We focus on non-turbulent regions, so-called dead zones, around the disk midplane in the presence of the ice evaporation front. We find that in this specific disk environment, particle fragmentation is no longer an obstacle and boulders of km-size can form within only a few thousand years. One major conclusion of this thesis is, therefore, that solid material can overcome the meter size barrier of particle growth and that planetesimal formation due to hit-and-stick mechanisms is in fact possible.

Zusammenfassung

Diese Doktorarbeit beschäftigt sich mit den ersten Phasen der Planetenentstehung in protoplanetaren Scheiben. Besonderes Interesse kommt dabei dem Wachstumsprozeß von sub-μm großen Staubteilchen hin zu Planetesimalen von Kilometer größe zu. Um solch große Objekte in protoplanetaren Scheiben bilden zu können, muß der anfängliche Koagulationsprozeß zwei erhebliche Hürden umgehen; zum einen den schnellen Massenverlust der Staubscheibe auf Grund radialer Driftbewegungen von Staubteilchen zum Stern hin, zum anderen die Zerstörung bereits größerer Teilchen auf Grund von Kollisionen mit hoher Geschwindigkeit. Diese beiden Hürden zusammengenommen werden als die "Meter-Barriere" des Wachstumsprozesses bezeichnet, dessen Untersuchung den Hauptbestandteil dieser Arbeit darstellt. In der Arbeit wird gezeigt, daß das anfängliche Staub-Gas-Verhältnis von entscheidender Bedeutung ist, um das Problem der radialen Teilchenbewegung, also den ersten Teil des Problems der Meter-Barriere, zu umgehen. Wenn dieses Verhältnis, verglichen mit jenem des interstellaren Mediums, um einen Faktor zwei erhöht wird, so führt dies in astronomisch gesehen kurzer Zeit zur Bildung von Planetesimalen. Die Simulationsergebnisse weisen auch darauf hin, daß die Fragmentations-Barriere, der zweite Teil des Problems der Meter-Barriere, nur unter der Annahme unrealistisch hoher kritischer Fragmentationsgeschwindigkeiten umgangen werden kann. Aus diesem Grunde wird außerdem untersucht, ob bestimmte Umgebungen in der protoplanetaren Scheibe die Koagulation günstig beeinflussen können. Wir untersuchen den Einfluß von Regionen mit sehr geringer Turbulenz, sogenannte "Tote Zonen", in Gegenwart der Verdampfungsfront von Wassereis. Es zeigt sich, daß Teilchenfragmentation in dieser spezifischen Umgebung nicht länger ein Hindernis darstellt, da es in dieses Modell in nur wenigen tausend Jahren zur Bildung von Planetesimalen kommt. Eine grundlegende Schlußfolgerung dieser Arbeit ist somit, daß es protoplanetarem Staub möglich ist, die Meter-Barriere zu durchbrechen, und daß die Bildung von Planetesimalen durch Stoßinduzierte Wachstumsvorgänge tatsächlich möglich ist.

Acknowledgements

This thesis would not have been possible without the help of various persons to whom I owe thanks.

First of all, my direct supervisor, Kees Dullemond, who did not only guide me very thoroughly through these last years accompanied with dozens of handwritten lists of good ideas, but also taught me how to stand on my own feet and how to do my own science. In the same breath, I would like to thank my official supervisor, Thomas Henning, who's door was always open, and who helped me to recognize the important things in the big picture. Far beyond science, I owe both of them a great deal for supporting me especially during the last six month.

During these years, I learned a lot about turbulence from very fruitful discussions with Anders Johansen, Natalia Dzyurkevich, Andrej Bicanski and Hubert Klahr. The proximity of our two groups was very inspiring and led to great insight of each others topic. I also have to thank Andras Zsom and Andrej Bicanski for proof-reading my script and, hence, improving it substantially. I also thank Andras for providing my the plot about stochastic velocity fluctuations in this thesis. Thanks also to Martin Hennemann who helped me finding my way through the coppice of the formal PhD requirements and defense dates. Though millions of years away from my own PhD topic, I owe Martina Queck for making me reconsider many aspects of my work which helped me to understand it in a better way. I would also like to thank Juliet, Jelte and Holger for not talking about science with me.

I would not be here and writing my thesis without the comittment of Katrin Regenspurger and Steffen Rosahl. I thank Katrin for standing up for me, for her open door at day and night, and for her everlasting optimism which always brightens me up. Moreover, I have to thank Steffen Rosahl for lots of hours of intense concentration, and for his dedication and genuine honesty which I have learned to appreciate a lot.

Last but not least, I want to thank my family for supporting me through these years, for helping me to move two times within Heidelberg, for waiting for me for hours in long corridors, and for being there.

"Blödem Volke unverständlich
treiben wir des Lebens Spiel.
Gerade das, was unabwendlich,
fruchtet unserm Spott als Ziel.

Magst es Kinder-Rache nennen
an des Daseins tiefen Ernst;
Wirst das Leben besser kennen,
wenn du uns verstehen lernst."

Christian Morgenstern
– Galgenlieder –

Contents

Chapter 1

Preface and introduction

Man is fascinated, astonished and sometimes even a bit scared by what happens in the heavens above probably for as long as he can lift his head and watch the skies. To give a charming example, ancient Egyptian records tell us that every two weeks, the moon god suffers a terrible and bloody struggle with a wild pig which crosses the skies (Koestler 1980). From experience, this combat ends in the defeat of the moon god. The sudden death of the moon is shortly followed by its rebirth which, interestingly, also takes two weeks. Why the moon god – despite of his powers – is not able to win this struggle, the first astronomers of the Egyptian empire roughly 3000 yrs ago do not tell. The strength and intention of the gods was beyond human comprehension. But questionlessly, they controlled the destiny of the sublunar world and determined the fate of man. Associated with this broad variety of religious beliefs, the Egyptians had a quite remarkable understanding of astronomical time scales. It was known precisely how long the fight of the moon took place, how long the moon god traveled through the underworld and how long the process of rebirth was. It was also recognized that twelve struggles correspond roughly to one year. However, the Egyptians already realised that this finding was merely a coincidence. Even the discrepancy between a year and twelve moon phases was known which can surely lead to some admiration for these early scientists.

The impulse to categorise the world has not dropped during the last couple of thousand years. However, the fundamental question *"On what there is"* (Quine 1953) was accompanied by important changes. While the Egyptians were rather interested in measurement and prediction of repetetive events like moon phases and the changes from winter to summer, the ancient Greeks were one of the first cultures who invented theoretical models to explain the world. In the 6^{th} century BC, Pythagoras of Samos stated that *"Everything is number"*. He believed that the whole world can be described by laws of nature which represent fundamental principles. The universe and everything in it is bound to these laws and it has no choice but to follow the path they dictate. With time, religious perspectives were more and more replaced by models which tried to describe the world based on direct observations. And not surprisingly, scientific findings were all too often in contradiction with the current dogma of the authorities. The nine year lasting house arrest of Galileo Galilei in Arcetri after publishing his "*Dialogo*" (Galilei 1632), an essay in favour of the heliocentric solar system, is only one example for centuries of dissent between natural science and religion. Ironically,

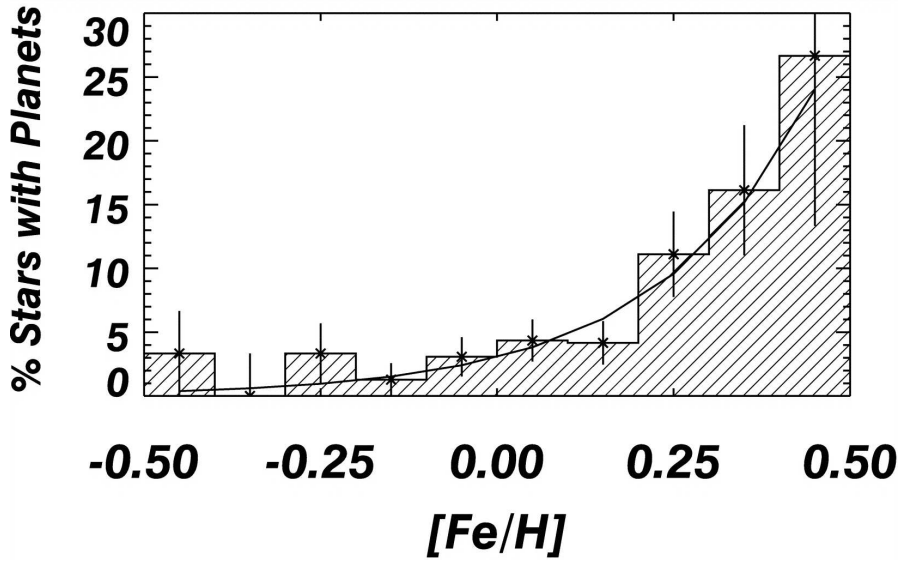

Figure 1.1: Probability of finding an exoplanet as a function of the host star metallicity. This figure is extracted from Fischer & Valenti (2005).

the town where Galileo was grounded domiciles a well know scientific institution today, the *Astrophysical Observatory of Arcetri.*

One of the most fundamental questions of mankind probably ever asked is mirrored by the very first sentence in a well-known book which reads "*In the beginning God created the heavens and the Earth.*" While cosmologists focus on the genesis and the evolution of the former creation, this thesis will mainly deal with the latter subject, i.e. with planet formation in the early solar system. This work will not only focus on the Earth in particular, but on the general formation of larger bodies. Regarding the diversity of what can be found in our solar neighbourhood, this topic is surely attractive, but also challenging at the same time. How did the gas giant planets form? Did they form at the location we find them today? Can planets form around any star or is the formation of the planets in our solar system merely a lucky coincidence which happens once in a billion? Unfortunately, the book Genesis does not provide any information about how all this formed a long time ago. But a lot of progress was made to answer this question during the last couple of decades. For example, more than 300 exoplanets were discovered within 150 pc distance from our own sun. To illustrate the value of this scientific progress, Fig. 1.1 shows the probability of finding an exoplanet around a host star of a certain metallicity (Fig. from Fischer & Valenti 2005). These results hint towards the fact that planet formation is not a rare event which happens only around one in a million stars, but that planets formation must occur quite frequently around host stars with at least solar metallicity.

In this first chapter, I will shortly present the ideas of how – we think today – precursors of planets such as our own Earth have formed billions of years ago. I will briefly review the theoretical models and observations of particular planet forming regions which will set the stage for the further play of this thesis.

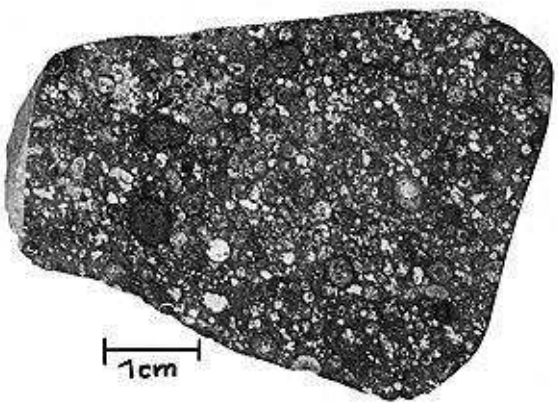

Figure 1.2: A cross-section through the Allende meterorite.

1.1 Protoplanetary disks

A good starting point is to ask the question of how old the Earth and our solar system is. Old rock units of the continental crust on Earth have ages of up to 3.8 Gyrs (Trieloff & Palme 2006). The olderst materials which can be found on Earth, i.e. zircons from Jack Hills in Western Australia, have ages of 4.404 ± 0.008 Gyrs (Wilde et al. 2001). However, since no terrestrial rock survived the early processing during planetary formation, these ages underestimate the true age of the solar system.

It is possible to obtain a more precise age determination by studying the most primitive building blocks of our solar system, namely meterorites. An example of such a primordial remnant, the Allende meteorite, is shown in Fig. 1.2. There are three major constituents which can be distinguished in carbonaceous meteorites, such as the Allende meteorite. First, calcium-aluminium-rich inclusions (CAIs) are up to cm-sized pebbles which are rich in calcium, aluminium and titanium. A closer analysis of these embedded particles unveils that they underwent several evaporation and condensation episodes before being integrated in the meteorite. Second, chondrules are sphericals silicate particles with sizes of several millimeters. These grains mainly consist of SiO_2, MgO, and FeO. Third, CAIs and chondrules are embedded in the so-called matrix of silicate material.

Now, isotope ratios in CAIs suggest an age of the early solar system of 4.5672 ± 0.0001 Gyrs. This is indeed roughly 160 Myrs older than the oldest rocks found on Earth (Amelin et al. 2002). Interestingly, the lead-lead isochrone ages of CAIs and chondrules suggest an age interval of 2.5 ± 1.2 Myrs between the formation of these two species (Amelin et al. 2002) indicating that CAI- and chondrule-forming events lasted for at least 1.3 Myrs. The formation of planetary precursors, hence, did not happen within the blink of an eye, but rather happened over time scales of several millions of years.

All the planets orbit the sun in the same sense. This observation already led Descartes (1644) to the idea that planets must have formed from a cloud of vortices surrounding the young sun. In a quite influential paper exactly 300 yrs later, Weizsäcker (1944) envisioned a disk of gas and dust, the solar nebula, in which planets form by agglomeration of smaller dust particles. The widely accepted paradigm of star and planet formation today begins in a dense molecular cloud. These clouds consist mainly of molecular hydrogen and helium, and

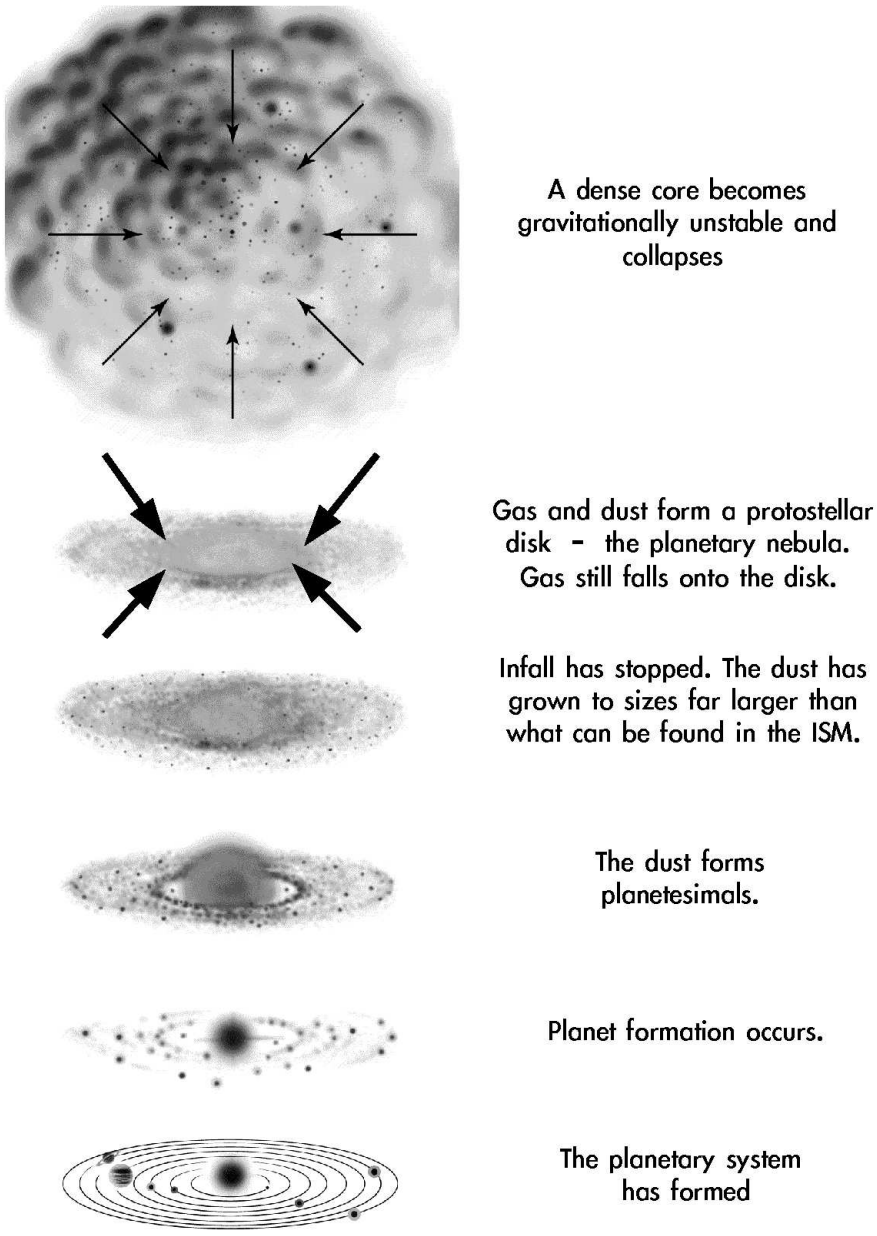

Figure 1.3: The paradigm of star and planet formation. A dense molecular cloud collapses under its own gravity. Due to the initial (possibly tiny) rotation of the cloud and the conservation of angular momentum, the cloud can not collapse and form a star alone. Thus, the collapsing cloud must also form a disk – the so-called planetary nebula – which carries most of the angular momentum. In the protoplanetary disk, tiny dust grains may form larger aggregates due to hit-and-stick mechanisms. These growing grains may evolve into planets over a time scale of several millions of years.

they can have masses up to 10^5 to 10^6 $M_\odot$ (Rosolowsky 2007; Bolatto et al. 2008). These very massive molecular clouds are also called giant molecular clouds. Prominent examples are, for example, the Orion Nebula and the Taurus molecular cloud. If certain regions of the cloud become sufficiently dense and the temperature is sufficiently low, then these cloud regions can collapse under its own gravity (c.f. Fig. 1.3). The precise criterion for gravitational collapse of an isothermal pressure supported gas cloud was investigated by Jeans (1902). He found that if the radius of a cloud with a given density ρ exceeds the Jeans radius

$$R_\mathrm{J} = \frac{c_\mathrm{s}}{\sqrt{G\rho}}\,, \tag{1.1}$$

then the molecular cloud will collapse. In this expression c_s and G denote the isothermal sound speed and the gravitational constant, respectively.

Due to the initial rotation of the cloud and the conservation of angular momentum, the cloud cannot collapse and form just a protostar, but must also form a disk – the so-called planetary disk – which carries most of the angular momentum. Hydrogen and Helium make up approximately 99% of the protoplanetary disk. The remaining mass fraction of $\sim 1\%$ is present in tiny dust grains (see e.g. Panić et al. 2008 and the references therein). These dust particles randomly collide in the disk which can lead to particle sticking due to van der Waals forces and, hence, to dust particle growth. It is believed that this successive growth leads to the formation of cm-sized pebbles, planetesimals of kilometer size and, eventually, planets after a few million years.

With the evolution of better observational techiques, in the nineties it became possible to obtain direct images of such protoplanetary disks in a nearby massive star forming region, the Orion Nebula. An example of these images is shown in Fig. 1.4 (McCaughrean & O'Dell 1996). The protoplanetary disk is seen edge-on against the bright background hydrogen recombination lines from the HII region and it surrounds a low-mass star with an age of roughly 1 Myr. More than a few hundred disks were observed, for example, with the Hubble Space Telescope (e.g. O'Dell et al. 1993; O'Dell & Wen 1994), with the Infrared Space Observatory (ISO) (e.g. Bouwman et al. 2000; Acke & van den Ancker 2004), Spitzer Space Telescope (e.g. Kessler-Silacci et al. 2007; Lahuis et al. 2007), and also via millimeter interferometry (e.g. Dutrey et al. 1996; Wilner et al. 2005; Rodmann et al. 2006; Andrews & Williams 2007). These observations give valuable input for planet formation models, e.g. the mass of the disk or the radial mass and temperature distribution (Beckwith et al. 1990; Andrews & Williams 2007; Eisner et al. 2008), and make disk evolution predictions possible in the first place.

By looking at the state of our own solar system today, it is possible to make an estimate of how massive the disk in our own solar nebula was and also how the mass of gas and dust was distributed within the cloud. This model is usually referred to as the Minimum Mass Solar Nebula (MMSN) (Weidenschilling 1977a; Hayashi 1981). We consider the known mass of heavy elements in each planet. We then augment this mass with enough hydrogen and helium until we reach a mixture of Solar composition. The Solar system is then divided into annuli, with one planet per annulus, and the augmented mass for each planet is distributed across these unnuli. By this procedure, we obtain a rough gas surface density at each location of the planets. This discrete mass distribution can be fitted by an analytical function given by

$$\Sigma_\mathrm{g}(r) = 1700\,\frac{\mathrm{g}}{\mathrm{cm}^2}\,\left(\frac{r}{\mathrm{AU}}\right)^{-1.5}\,. \tag{1.2}$$

Integrating this expression over the solar nebula which we assume extents out towards 30 AU corresponding to the orbit of Neptune, we obtain a disk mass of roughly 10^{-2} $M_\odot$.

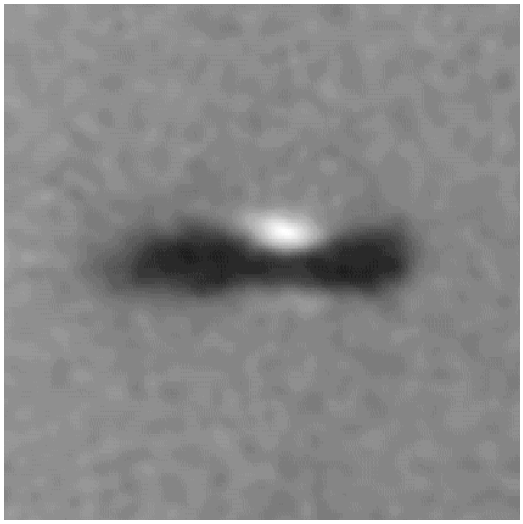

Figure 1.4: Picture of a protoplanetary disk taken by the *Hubble Space Telescope* as discussed in Sec. 1.1. The disk which is located in the Orion Nebula is seen edge-on against the bright background of hydrogen recombination lines (McCaughrean & O'Dell 1996). Optical and near-infrared stellar photometry is consistent with a young star of ~ 1 Myr.

We have to keep in mind that the MMSN disk mass estimate only poses a lower limit to the mass of the solar nebula since it only takes into account the heavy elements that are present in todays solar system bodies. There could have been significant loss of solid material in the disk due to various processes, i.e. outflows and jets from young stars (Königl & Pudritz 2000; Bally et al. 2007), disk photoevaporation which carries away the dust in the disk (Alexander et al. 2006), disk winds (Pudritz et al. 2007) and, as we shall see in this thesis, due to radial drift of cm and m-size dust aggregates. For this reason, it is somewhat risky to take the planets as we see them today and to derive a mass distribution for our early solar systen 4.5 Gyrs ago. To circumvent this risk, observational constraints for protoplanetary disk masses around other young stars are of high importance in order to set up reliable disk evolution models. Such observations were performed by, for example, Beckwith et al. (1990), Kitamura et al. (2002) or Andrews & Williams (2007). For a good review of multiwavelength imaging of young stellar disks see also Watson et al. (2007). The high spatial resolution submillimeter continuum surveys of circumstellar disks in the Taurus-Auriga and Ophiuchus-Scorpius star formation regions of Andrews & Williams (2007) suggest that protoplanetary disks around T Tauri stars have disk masses ranging from 10^{-3} up to 10^{-1} $M_{\odot}$. The mass of the MMSN, hence, seems to be a typical intermediate mass disk around a T Tauri star.

The MMSN model is based on another assumption which can be put in question. It assumes that the radial distribution of solid material did not change during the last billions of years. As far as we know today, this is not true. Due to drag forces between the gas and the dust, solid rocks of meter size are subject to fast radial inward motion in the disk (Whipple 1972; Weidenschilling 1977a). Radial drift time scales can be very short, i.e. of the order of 10^2 yrs on spatial scales of only 1 AU. Moreover, planets undergo radial migration due to planet disk interaction (Lin & Papaloizou 1993; Lin et al. 2000) which occurs over time scales of the order of 10^5 yrs (Papaloizou et al. 2007). Although planet migration time scales are significantly longer than radial drift time scales of meter sized bodies, planet

migration inheres the capacity to drastically change the distribution of solid material in the disk. Planets can undergo radial migration as long as the disk is still gas rich. Observations by Haisch et al. (2001) suggest gas disk life times of $\sim$ 6 Myrs. Numerical simulations of photoevaporation (Alexander et al. 2006) also suggest disk life times of several Myrs, which is much larger than typical planet migration time scales. Hence, the planet could have drifted far across the early solar system before the gas in the disk is dispersed and radial migration stops.

Observations indicate that the mass distribution in disks around T Tauri stars is different from the MMSN model which involves a surface density power law slope of -1.5. Andrews & Williams (2007) find a flatter median slope of -0.5 which means that more disk mass is located in the outer regions of the disk. Some disks in their sample, for example DN Tau or GO Tau, even involve radial surface density profiles which are hardly dependent on the location in the disk, i.e. power law indices of -0.2 or less. However, these very low values may be due to dust particle growth in the disk which systematically shifts the surface density power law index to lower values (c.f. Chapter 4 in this thesis). Recently, Desch (2007) modified the MMSN model by taking into account planetary dynamics after the gas disk has dissipated and only the sun, the planets, planetesimals and smaller debris remains. Due to gravitational interactions, the planets can exchange angular momentum with the disk and, hence, migrate and change their radial locations in the early solar system (Fernandez & Ip 1984; Tsiganis et al. 2005). Assuming that our own early solar system is not very different from typical protoplanetary disks, one would expect that in the revised MMSN model, the new mass distribution should resemble more closely the mass distributions derived from observations of disks around T Tauri stars. However, the revised model leads to an even steeper Σ-power law index of -2.17. This finding hints towards the possibility, that either our derivations of disk masses through observations suffer from a systematic error – or our own solar system is indeed different. On the other hand, the variety of different disk parameters indicates that protoplanetary disks have a remarkable diversity and general statements about disk properties must be considered with caution.

Except for the mass distribution in the disk, it is also important to know the temperature distribution in the disk. This is because radial inward drift velocities of dust particles which change the spatial particle distribution significantly are directly proportional to the temperature in the disk (c.f. Chapter 3). Throughout this thesis, we will assume that the temperature distribution in the disk is only determined by the irradiation of the central protostar. The disk is irradiated under a flaring angle $\alpha_{\rm irr}$ which leads to a temperature profile given by (Hayashi 1981; Kenyon & Hartmann 1987)

$$T(r) = \alpha_{\rm irr}^{1/4} \left(\frac{r}{R_\star}\right)^{-1/2} T_\star = 204\,{\rm K} \left(\frac{r}{\rm AU}\right)^{-1/2} \quad . \tag{1.3}$$

In the last step, we assumed that the disk is irradiated under an angle of 0.05 rad by a T Tauri star with a surface temperature of $T_\star = 4000$ K and a stellar radius of $R_\star = 2.5\ R_\odot$. Except for the stellar radiation, the disk can also be heated by viscous dissipation of turbulence (Lynden-Bell & Pringle 1974). However, for simplicity, we will ignore this effect here. We will also assume that the disk is isothermal in the vertical direction, which is reasonable for irradiation-dominated disks.

Finally, it is important to ask how long planetary disks actually survive? The typical inferred life time of a disk is very short compared to the age of our solar system. Surveys for circumstellar disks in a sample of young clusters that span a significant range in age (0.3-30 Myr) imply gas disk lifetimes of $\sim$ 6 Myrs (Haisch et al. 2001). For illustration, Fig. 1.5 shows

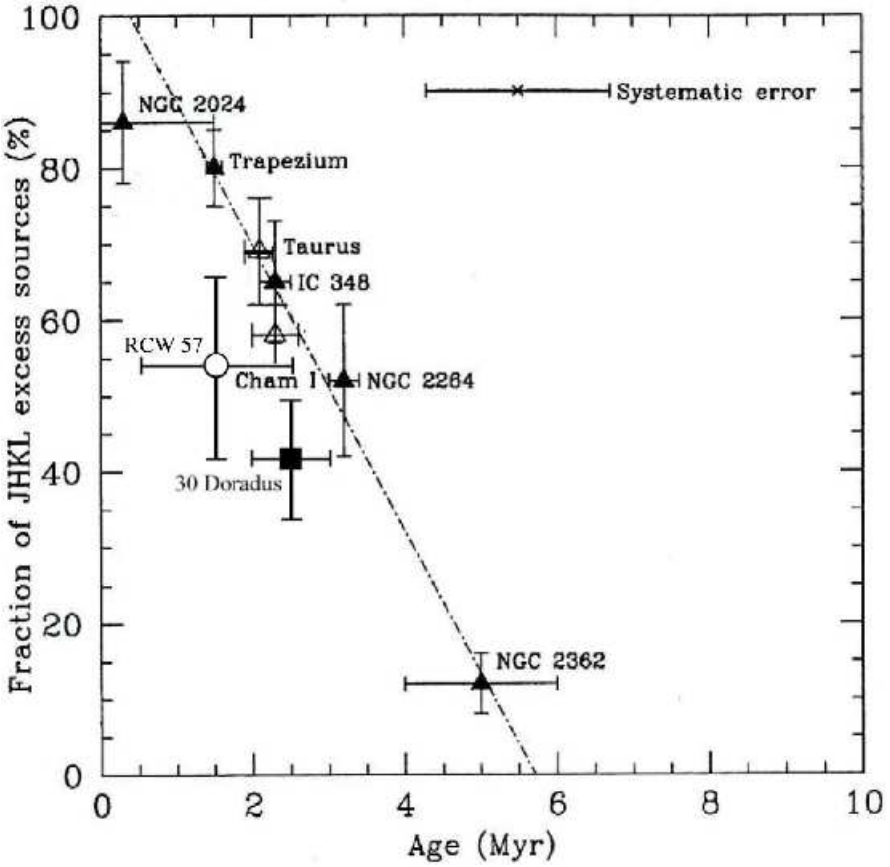

Figure 1.5: Observed fraction of young stars with protoplanetary disks as a function of time as can be found in Haisch et al. (2001).

the fraction of young stars with disks as a function of time as found by Haisch et al. (2001). According to these observational results, 50% of young stars are disk free after 3 Myrs. If the stellar age is larger than 6 Myrs, no young star in the observed sample shows evidence for a disk. These observational time scales for disk dispersal agree with theoretically expected times for disk evaporation suggested by numerical simulations (Alexander et al. 2006).

1.2 Turbulence in protoplanetary disks

There is an intriguing riddle regarding the angular momentum of dense cloud cores, which at some point might form planetary systems, and the angular momentum of our own solar system. Observations of ^{13}CO line emission in the Taurus molecular cloud suggest an angular momentum of dense cores of $\sim 10^{53}$ g cm^2/s (Heyer 1988). Models of protostar spectra compared with observed embedded infrared sources lead to similar angular momentum values (Adams et al. 1987). The angular momentum of our solar system, on the other hand, is only 3×10^{50} g cm^2/s. Hence, a significant fraction of the initial angular momentum must have been lost during the process of planet formation. The missing angular momentum, and how exactly is was lost, is usually called the "Angular momentum problem".

It is reasonable to assume that the angular momentum of a dense core is conserved

during cloud collapse (Bodenheimer et al. 1990). If this is the case, then a large fraction of the collapsing mass will form a disk which carries most of the initial angular momentum. Theoretical calculations of cloud collapse and disk formation suggest that if typical values for dense cores are assumed, then roughly half of the initial core mass will form a protostar (Terebey et al. 1984). The remaining gas forms a disk with a mass of the order of the central star mass, i.e. a very high mass disk. However, this is not what is observed. Disk masses are usually in the order of $\sim 10^{-2}\ M_\odot$ (Beckwith et al. 1990; Akeson et al. 2002; Andrews & Williams 2007; Pinte et al. 2008), i.e. only a minor mass fraction of the central star. Therefore, a significant fraction of mass (and angular momentum) must have been redistributed during disk evolution.

Drastic photometric light variability of classical T Tauri stars (Herbst et al. 1994), the occurence of an UV excess (Calvet & Gullbring 1998), and Hα observations (Gullbring et al. 1996) indicate ongoing mass accretion from the circumstellar disk onto the young star (Ménard & Bertout 1999). This infall of material can be explained by viscous stresses which act in the disk. Viscosity, on principle, transports angular momentum from the inner regions to the outer regions of the disk. This transport mechanism is associated with disk spreading and significant mass accretion (Lüst 1952; Lynden-Bell & Pringle 1974; Nakamoto & Nakagawa 1994; Hueso & Guillot 2005). Theoretically, the system will evolve towards a state where infinitely small mass is at $r = \infty$ carrying all the angular momentum, while the bulk of material has fallen onto the star (Lynden-Bell & Pringle 1974). The infalling material from the disk onto the star may lose its angular momentum via the formation of disk winds and jets (Pudritz & Norman 1983; Pudritz et al. 2007) which carry the angular momentum away. Recent observations of jets validate current magneto-centrifugal models for jet launching and even provide evidence for jet rotation, i.e. angular momentum transport (Bacciotti et al. 2003). This hints towards the fact that disk viscosity and jets may play a key role in solving the angular momentum problem.

It is still a matter of debate what mechanism is responsible for this viscosity. Molecular viscosity is far too small to account for the observed large accretion rates. If thermal viscosity was responsible for mass accretion in the disk, the observed accretion luminosities would be roughly $6-7$ orders of magnitude lower[1]. However, several anomalous sources of viscosity have been proposed to explain the observations. If weak magnetic fields are present then the disk can be unstable to magneto rotational instability (MRI) (Balbus & Hawley 1991; Stone & Pringle 2001). Non-magnetic mechanism for viscosity are, for example, baroclinic instabilities (Klahr & Bodenheimer 2003; Klahr et al. 2006), shear instabilities (Dubrulle et al. 2005) or gravitational torques (Laughlin & Bodenheimer 1994). It was also argued that convection could play an non-negligible role for angular momentum transport in disks. However, if at all, convection will transports angular momentum inwards (Balbus 2000).

In this thesis we will make use of the so-called α-prescription (Shakura & Sunyaev 1973). This parameterisation to describe turbulence is purely phenomenological and ignores most details of turbulence. However, this simplification has the advantage that it makes a treatment of turbulence manageable without extensive hydrodynamical simulations. One may ask the question why we need a description for turbulence in this thesis at all since we are not interested in viscous disk evolution, for example. The answer is that turbulence is a major source for relative velocities between particles in disks (see Section 4.1.2). Relative velocities lead to particle collisions and, hence, to particle growth. For this reason, a reliable description for turbulence is essential for the work presented here. In the following, I will briefly describe

[1]This is easily seen considering that $L_{\rm mol} \propto \dot{M} \propto \alpha_{\rm mol} \propto {\rm Re}^{-1}\alpha_{\rm turb} \propto 10^{-6}\alpha_{\rm turb} \propto 10^{-6}L_{\rm turb}$.

this turbulence α-model.

Turbulence acts like a kind of diffusion on very large scales. A diffusion coefficient D can be written as a product of a velocity scale V_0 and a length scale L_0,

$$D = V_0 \times L_0 \ . \tag{1.4}$$

A typical velocity scale in the disks is the isothermal soundspeed $c_\mathrm{s} \equiv \sqrt{kT_\mathrm{gas}/\mu}$, with T_gas the gas temperature, k the Boltzmann constant, μ the mean molecular weight of the gas (which we take 2.3 times the proton mass for a standard mixture of molecular hydrogen and atomic helium). A characteristic length scale is given by the pressure scale height of the gas $H = c_s/\Omega_k$, where $\Omega_k \equiv \sqrt{GM_*/r^3}$. Regarding these typical scales at a certain radius in the protoplanetary disk, we can alternatively express the diffusion coefficient for the gas as follows

$$D = \alpha c_s H \ . \tag{1.5}$$

The value of the parameter α reflects the amount of turbulence in the disk. It can range from 10^{-6} (Weidenschilling 1980) up to observationally suggested values of 10^{-2} (Hartmann et al. 1998). Extensive hydrodynamical simulations show typical α values of about 10^{-3} (Brandenburg et al. 1995, Johansen & Klahr 2005).

So far, the turbulence parameter α does not provide any information about the two turbulence scales V_0 and L_0 individually. This can be seen in a better way by introducing a further turbulence parameter q

$$D = \alpha c_s H = \alpha^q c_s \times \alpha^{1-q} H \ , \tag{1.6}$$

which ranges between 0 and 1. Now we can identify the terms of equation (1.4) by defining $V_0 = \alpha^q c_s$ and $L_0 = \alpha^{1-q} H$. The physical interpretation of q is as follows. A certain diffusion can be realized by big eddies which move slowly ($q = 1$) or by small eddies moving quickly ($q = 0$). Both possibilities result in the same diffusion coefficient. However, the dust reacts differently in these two scenarios as we will see later. The actual value of q is still a matter of debate. To give some examples, in self-induced turbulence, q tends to be slighly smaller than 1/2 (Weidenschilling 2006). Another possibility is that big convective cells of scale H exists (Klahr & Henning 1997) which would imply $q = 1$. While Morfill (1988), Weidenschilling (1988) or Weidenschilling & Cuzzi (1993) use turbulent gas velocities of αc_s, which also implies $q = 1$, more recent publications analytically derive $q = 1/2$ which leads to $v_t = \sqrt{\alpha} c_\mathrm{s}$ (Dubrulle et al. 1995; Cuzzi et al. 2001; Cuzzi & Weidenschilling 2006). If q exceeds 1/2 then the time scale of the largest eddy, the so-called turn-over time, becomes larger than an orbital time scale since $\tau_\mathrm{ed} \sim \alpha^{1-2q}/\Omega_\mathrm{k}$. Turn over frequencies smaller than the Kepler frequency appear rather unphysical. Therefore, we follow Cuzzi et al. (2001) and adopt $q = 1/2$.

The fundamental importance of knowledge about q can be understood by calculating the eddy-turn-over-time τ_ed

$$\tau_\mathrm{ed} = \frac{L_0}{V_0} = \frac{2\pi}{\Omega_\mathrm{ed}} = \alpha^{1-2q} \frac{1}{\Omega_k} \ . \tag{1.7}$$

Here, Ω_ed is the eddy turn-over frequency. Comparing the two extreme cases $q = 0$ and $q = 1$, the timescales τ_ed differ by a factor of α^2. For a typical α-value in MRI of 10^{-3}, these two time scales differ by 6 orders of magnitude. In the next sections we will see that the effect of the turbulent gas on the dust, especially on the vertical dust particle distribution, is highly dependent on this timescale τ_ed. For this reason knowledge about q is an essential requirement.

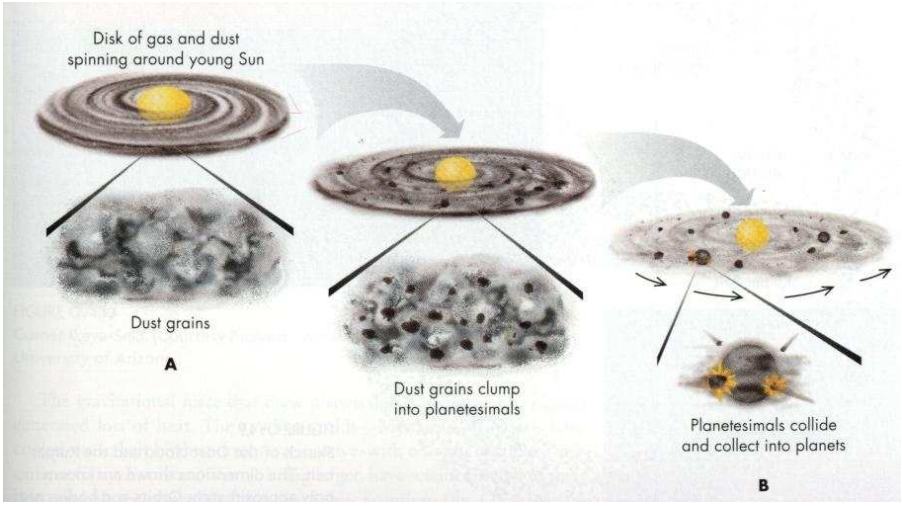

Figure 1.6: The paradigm of planetesimal formation in protoplanetary disks. Dust particle agglomeration of sub-μm dust grains leads to the formation of larger aggregates. Due to this growth mechanism, it is believed that even m-sized rocks, planetesimals and even planets can form over large time scales. To investigate the correctness of this theory is the main subject of this thesis.

1.3 Dust particle growth

The analysis of the interstellar extinction tells us that dust grains in the interstellar medium have radii ranging from a few nm up to a fraction of a μm (Mathis et al. 1977; Clayton et al. 2003). Simulations of the collapse of molecular clouds which leads to the formation of protoplanetary disks suggest that the maximum grain size does not significantly change during this collapse (Ossenkopf 1993). Hence, we expect dust grains in the disk to have radii slighly smaller than a micrometer at the time the disk has formed. Planets, on the other hand, have radii of several thousand kilometers. The question is, how do we get from tiny sub-μm sized dust grains to the planets we see today?

One pathway from tiny dust grains to larger bodies in the protoplanetary disk is hierarchical growth of solid material. The basic idea is the following. Dust grains in protoplanetary disks do not move all in the same direction, but rather have relative particle velocities due to various effects, e.g. Brownian motion, relative velocities caused by turbulent motions of the gas (Völk et al. 1980; Ormel & Cuzzi 2007) and systematic radial and vertical drift velocities (Weidenschilling 1977a; Dubrulle et al. 1995). These relative particle velocities can lead to occasional collisions and, under certain circumstances, to particle sticking due to van der Waals forces (Dominik & Tielens 1997; Blum et al. 1998; Kempf et al. 2000). We believe today that on the basis of this hit and stick mechanism, μm-sized grains could evolve into cm-sized particles and even into planetesimals[2] of km size over time scales of several Myrs, representing the initial stages of planet formation. To find out if this particle growth scenario from sub-micron grains to km-sized objects is actually plausible is the main subject of this thesis. An illustration of this planetesimal formation paradigm is shown in Fig. 1.6.

For several years now, there is observational evidence for dust particle grain growth in

[2]In this thesis, planetesimals are regarded as objects which have grown to such large radii that the effect of gas drag on their motion through the disk is negligible.

protoplanetary disks. This evidence is gathered by mid-infrared spectroscopy of disks by use of, for example, the *Infrared Space Observatory* (ISO), the *Spitzer Space Telescope* (SST), or with MIDI at the Very Large Telescope Interferometer (VLTI). Although the interpretation of these spectroscopic data is not always unambiguous, some information can be obtained by analysis of the shape and the strength of the 10 μm silicate emission feature. This wavelength probes the warm silicate grains in the disk atmosphere high above the midplane in the inner regions of the disk. Bouwman et al. (2001) and van Boekel et al. (2003) analysed the 10 μm spectral region of a sample of Herbig Ae/Be stars. They found that the silicate feature is consistent with dust particle grain growth from sub-μm to some μm in size. Evidence for dust grain evolution beyond sizes that are found in the interstellar medium was not only found in disks around Herbig Ae/Be stars (Bouwman et al. 2001; van Boekel et al. 2003), but also T Tauri stars (Przygodda et al. 2003; Kessler-Silacci et al. 2007) and even in disks around brown dwarfs (Apai et al. 2004, 2005, 2007; Sicilia-Aguilar et al. 2007).

Dust particle growth to radii of several μm leads to flatter silicate emission features. An example of this flattening is shown in Fig. 1.7. If particles grow even larger, i.e. to grain sizes of several 10 μm, the silicate feature would disappear in the mid-IR spectra. Interestingly, this is only observed in a few objects. Moreover, there seems to be no significant correlation between the presence of the 10 μm silicate feature and the age of the system (Natta et al. 2007a). This could suggest that dust particle growth stops for some reason when particles reach sizes of several micron. However, Dullemond & Dominik (2005) find that dust particles grow far beyond 10 μm size within very short time scales, i.e. within 10^2 yrs at 1 AU in the disk if no fragmentation is included. Since the source of the spectrum is usually unresolved with current 8 m class telescopes, one may argue that the observed silicate emission comes from the outer parts of the disk, i.e. originating from 50 AU or even further out where dust particle growth takes much longer than in the inner parts of the disk (Dullemond & Dominik 2005; Brauer et al. 2008). However, dust temperatures are far too low at these disk radii to produce any significant silicate emission in the mid-IR.

A possible explanation for the constant 10 μm emission feature over several Myrs of disk evolution is dust particle fragmentation. If the environment of the disk is very turbulent for example, then solid particles can have very high relative velocities. This can lead to high speed collisions between larger bodies and to massive particle destruction. Particle fragmentation produces a broad particle size distribution from sub-μm size up to sizes of the order of the parent bodies and, hence, involves a constant replenishment of tiny dust grains. These small debris grains would then explain the long-lived 10 μm feature.

Although particle fragmentation explains the observations, it also means that destructive collisions in the disk constantly prevent solid material to form larger bodies. It becomes apparent that particle fragmentation must occur, considering model predictions of relative particle velocities in protoplanetary disks. These models suggest that dust particles of meter size can have relative velocities of more than 50 m/s (Weidenschilling 1977a; Völk et al. 1980; Ormel & Cuzzi 2007). Meter-sized boulders colliding with such high relative velocities do not stick to each other. On the contrary, they will undergo massive destruction. Typical experimental threshold fragmentation velocities of m-sized boulders are of the order of some m/s (Blum 2004). This means that relative velocities between meter-sized particles are typically one order of magnitude larger than typical threshold fragmentation velocities. This raises the question of how larger bodies of e.g. km size can form at all in the disk. This growth problem is usually denoted as the fragmentation barrier.

We assume for the moment that the observed steady presence of the 10 μm feature in disk spectra is due to ongoing particle fragmentation. Destructive collisions in protoplanetary

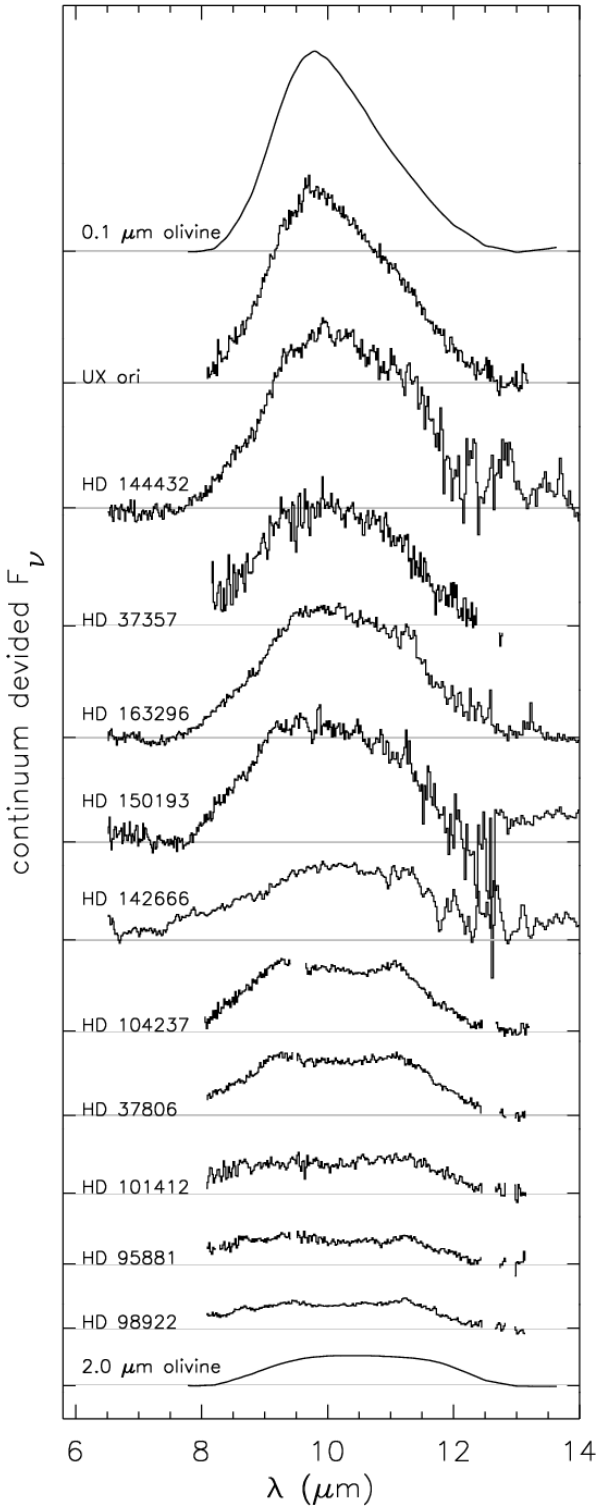

Figure 1.7: Mid-IR spectra of a sample of Herbig Ae/Be stars taken from van Boekel et al. (2003). The two solid curves on the top and on the bottom show the theoretically expected 10 μm feature for olivine grains ($[Mg,Fe]_2SiO_4$) for 0.1 μm and 2 μm, respectively. For larger grains, the silicate feature is flatter than for smaller dust grains. These mid-IR spectra, hence, suggest that particles in the observed disks have grown to radii of ~ 2 μm, i.e. to grain radii larger than typically found in the ISM.

disks primarily occur for solid particles which have already grown to some meters in size, i.e. boulders which have sufficiently high relative velocities to destroy each other. This raises the question if these meter-sized objects can be observed in protoplanetary disks. However, the observation of large m-sized boulders in disks is unfortunately not possible for two reasons. First, the opacities of m-sized bodies are far too low for the boulders to emit a substantial observable flux. Second, from some cm wavelengths on, the radio continuum of young stars is expected to be dominated by free-free radiation from ionized winds or outflows (Rodmann et al. 2006). This makes it impossible to observe bodies larger than a few centimeters in radius. It is, however, observationally possible to use millimeter interferometry to explore if slighly smaller particles, i.e. cm-sized pebbles, are present in the disk. This was done by Testi et al. (2003) and also Wilner et al. (2005) who performed millimeter observations of CQ Tau and TW Hya, respectively. Their results indicate the the dust must indeed have grown to at least cm size. This observation supports the idea that particle fragmentation is responsible for the long-lived 10 μm silicate feature. It also shows that particle growth towards cm-size is in fact possible at these radii.

But there is another problem concerning particles of roughly a meter in size which is quite as severe for the formation of planetesimals as destructive particle collisions. This second obstacle is radial inward motion of dust in the disk. The fundamental cause for inward drift of the dust is the difference in azimuthal velocity between gas and dust. While the dust moves with Keplerian velocity the gas moves slightly sub-Keplerian. This is due to the fact that the gas is not only affected by the gravitational and the centrifugal force but additionally feels a radial pressure force that does not act on dust particles. This extra force is caused by the decrease of gas pressure in the radial direction. Since this force, which exclusively acts on the gas, partly compensates gravitation, the gas moves slower than Kepler speed and therefore slower than any dust particle in the disk. Hence, the dust particle feels a continuous headwind from the gas. This headwind causes the dust particle to lose its angular momentum and to spiral inward. When the dust reaches the inner parts of the disk where the temperature exceeds roughly 1400 K, the dust evaporates and it is lost for the process of planetesimal formation. For this reason, there is a constant dust mass loss. There is the possibility that solid particles recondensate again in form of tiny dust grains, but this only replenishes the very inner disk regions, not the Earth-forming regions. Therefore, we will ignore this effect here.

For meter-sized boulders, this radial inward motion can be very rapid. Typical radial inward drift speeds can be of the order of 100 m/s. This means that radial inward drift happens over extremely short time scales compared to typical gas disk life times which are of the order of several Myrs (Weidenschilling 1977a). To give an example, the time for m-sized boulders to drift from 1 AU into the dust evaporation zone is only of the order of $\sim 10^2$ yrs. Meter-sized boulders only need $\sim 10^4$ yrs to drift across the whole early solar system on spatial scales of 10^2 AU. This estimate shows, that the lifetime of a dust disk which only consists of meter-sized objects might be less than only 10^5 yrs.

Fortunately, dust particles may leave the regime of fast radial drift by growing to larger sizes. While meter-sized boulders have radial drift speeds of 100 m/s, boulders of a few 100 m in radius are not longer influenced by gas drag and, hence, show negligible radial drift motion. Particle growth time scales for m-sized rocks, however, usually exceed radial drift time scales by far (Weidenschilling 1977a; Dullemond & Dominik 2005; Takeuchi & Lin 2005). At 1 AU, drift time scales are of the order of 10^2 yrs while coagulation time scales are typically of the order of 10^4 yrs (Dullemond & Dominik 2005), i.e. two orders of magnitude larger. Even if the dust somehow manages to grow to meter size and circumvent fragmentation due to

destructive collisions, the time to grow further in radius and leave the regime of fast radial inward drift is exceedingly larger than the radial drift survival time until evaporation. This obstacle is usually called the radial drift barrier. Interestingly, the particle size for which particle fragmentation plays an important role is exactly the regime where radial inward motion poses a major abstacle. For this reason, the fragmentation barrier and the radial drift barrier are usually altogether called the meter size barrier. If the dust can somehow manage to circumvent this barrier is discussed extensively in Chapter 4. A sketch of the meter size barrier problem is shown in Fig. 1.8.

1.4 Dust-gas coupling and the dust scale height

Before I come to the outline of the thesis, it seems appropriate to introduce an important dimensionless particle parameter, the Stokes number, which is used throughout this thesis. This quantity does not only determine how dust particles correpond to the motions of the gas, but it also determines the entire radial drift behaviour of the particle. From this characteristic number, we can also calculate relative velocities of dust particles in the disk. These velocities are highly important because they will determine the growth time scales of the dust in the disk. Moreover, these velocities will determine if particles will stick to each other and grow or if they undergo destructive particle fragmentation. Another important quantity which depends on the Stokes number is the dust scale height, i.e. the vertical extent of the dust particle distribution in the disk. Since the dust scale height is very closely related to turbulence in the disk (which was introduced in the last sections) and the Stokes number, we will also introduce this quantity at this point.

The Stokes number

A moving particle in a gas at rest loses a significant fraction of its momentum within a time called stopping time $\tau_{\rm s}$. This time depends on the friction between the particle and the gas. A strong friction means a small $\tau_{\rm s}$, and vice versa. The friction depends on the particle cross section $\sigma_{\rm p} = \pi a^2$ and, therefore, the particle radius[3] a, the relative velocity $v_{\rm p}$ with respect to the gas and the properties of the gas (mainly gas density $\rho_{\rm g}$, isothermal sound speed $c_{\rm s}$ and molecular mean free path l). For particles, with a size smaller than the molecular mean free path, the friction can be expressed by a simple formula:

$$F_e = \frac{4}{3}\rho_{\rm g} c_{\rm s} \sigma_{\rm p} v_{\rm p} \,. \tag{1.8}$$

This is the "Epstein drag law". In this regime the stopping time equals:

$$\tau_{\rm s} = \frac{m_{\rm p} v_{\rm p}}{F_e} \overset{\rm Ep.}{=} \frac{\rho_{\rm s} a}{\rho_{\rm g} c_{\rm s}} \,, \tag{1.9}$$

where $m_{\rm p}$ is the particle mass, which can be expressed with the particle material density $\rho_{\rm s}$ as $m_{\rm p} = (4\pi/3)\rho_{\rm s} a^3$. For particles larger than the mean free path the drag law is much more complex. This regime is characterized by the "Stokes drag law". In this thesis, we mainly focus on particles that are always smaller than the mean free path and can ignore the Stokes regime. Only in Chapter 6 we will modify this drag law because of high gas densities.

If the stopping time $\tau_{\rm s}$ is much smaller than the turn-over-eddy time $\tau_{\rm ed}$, the particles are strongly coupled to the gas having the same motions and the same behaviour with regard to

[3] We will always assume the particles to be spherical.

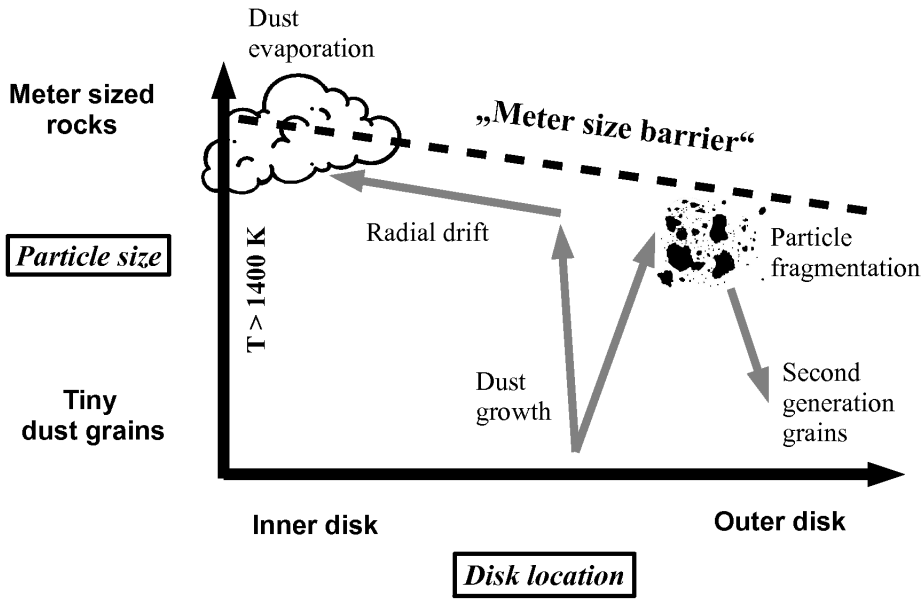

Figure 1.8: The meter size barrier problem as discussed in the introduction. This growth obstacle involves two sub-problems: radial particle drift and particle fragmentation. Particle drift leads to a continuous dust mass loss in the disk. If this particle loss is not prevented by some means then most of the dust material is lost due to dust evaporation after a few Myrs of disk evolution. Moreover, particle fragmentation prevents solid material to grow to larger sizes. This raises the question how larger objects, e.g. planetesimals of km-size, can actually form in the disk. The meter size barrier is extensively studied in Chapter 4 in this thesis. We emphasize at this point that the particle growth barrier due to radial drift and fragmentation is around 1 m at 1 AU only if the MMSN model is assumed. Different disk models shift the growth barrier to larger (smaller) particle radii. The growth barrier is also dependent on which disk region is focused on. Therefore, the critical particle radius of 1 m should be kept in mind with caution.

diffusion. When τ_s exceeds τ_ed by far, the dust decouples from the gas and is hardly influenced by the turbulence of the gas. The stopping time characterizes the dynamic properties of the particle as it moves through the disk. Therefore, we can replace all microphysical particle properties like a, ρ_s, m_p by τ_s. Particles with vastly different properties (e.g. size), but the same τ_s behave *entirely* the same. Instead of using the stopping time τ_s, an even more convenient parameter is the so-called "Stokes number" St_L. It is defined by:

$$\mathrm{St}_L = \frac{\tau_\mathrm{s}}{\tau_\mathrm{ed}} = \tau_\mathrm{s}\Omega_\mathrm{k}\alpha^{2q-1}\,. \tag{1.10}$$

The particles are strongly coupled for $\mathrm{St}_L \ll 1$ and hardly influenced by the gas for $\mathrm{St}_L \gg 1$. For the case $q = 1/2$ the Stokes number does not depend on α. For this specific case, we will denote the Stokes number simply as $\mathrm{St} = \mathrm{St}_L(q = 1/2) = \tau_\mathrm{s}\Omega_\mathrm{k}$. It is worthwile to note that in our disk model, the Stokes number is not dependent on the temperature in the disk. According to Eq. (1.9), the Stokes number only depends on the product $\rho_\mathrm{g}c_\mathrm{s}$. In vertical hydrostatic gas equilibrium, this product is only proportional to the gas surface density.

Particles show the fastest radial inward drift and the highest relative velocities if the Stokes number equals unity. It is exactly these particles which will drift into the evaporation zone over very short time scales and also undergo massive particle fragmentation. For this reason, the meter size barrier can be identified with the criterion $\mathrm{St} = 1$. Interestingly, particles close to this barrier are also most susceptible to the motions of the gas and the gravitational effects of the dust. For example, particles of that specific size can be easily trapped in very elongated gas vortices in magnetorotational turbulence (Balbus & Hawley 1991; Barge & Sommeria 1995). These effects can also slow down the radial drift by a factor of around two (Johansen et al. 2006b). Under certain conditions, the radial particle flow in the disk may become unstable to the streaming instablity (Youdin & Goodman 2005; Youdin & Johansen 2007) which leads to particle clumping, and possibly also to a gravitational collapse of the dust. In high dust density regions, the particle swarms contract due to their own gravity and may form a planetesimal within only a few orbits (Johansen et al. 2007). Apparently, the meter size barrier is not only connected to the radial motion and the fragmentation of the dust particles, but involves various other important effects as well. For this reason, it is vital to answer the question if particles can actually reach by coagulation the size regime at which these non-linear effects become of importance.

Dust scale height

We will now calculate the vertical thickness of the dust layer. We need this quantity to calculate the dust particle density in the disk which is one of the main input parameters of the coagulation equation. The dust density will determine how fast the dust will grow in the protoplanetary disk, i.e. the dust particle growth time scales. This vertical extent of the dust layer is determined by an equilibrium between dust particles which settles towards the midplane and turbulent diffusion which stirs the dust up again (Dubrulle et al. 1995; Schräpler & Henning 2004; Dullemond & Dominik 2004b). The settling can be described by the equation of motion for a dust particle,

$$\ddot{z} = -\Omega_\mathrm{k}^2 z - \frac{1}{\tau_\mathrm{s}}\dot{z}\,. \tag{1.11}$$

For $\mathrm{St} > 1/2$ the particle describes a damped oscillation around the midplane, corresponding to an orbit inclined with respect to the midplane. For $\mathrm{St} \ll 1/2$ the particle is so well

bound to the gas, that the downward motion equals to an equilibrium settling motion with magnitude:

$$v_{\rm sett} = -z{\rm St}\Omega_{\rm k}\,, \tag{1.12}$$

so that the second order differential equation Eq. (1.11) reduces to a first order differential equation:

$$\dot{z} = -v_{\rm sett}\,. \tag{1.13}$$

In order to calculate the dust scale height, we have to consider the diffusion coefficient for the dust. This quantity can be expressed as the product of a typical length and a relative average velocity which the particles aquire in the turbulent medium,

$$D_{\rm d} = Lv_{\rm t}\ . \tag{1.14}$$

For particles with Stokes numbers greater than unity the relative turbulent velocity between the dust particles is given by $v_{\rm t} = V_0/{\rm St_L}$ (Völk et al. 1980; Suttner & Yorke 2001). The velocity V_0 denotes the turbulent velocity of the largest gas eddy which was introduced before. With the typical length scale $L = \tau_{\rm s}v_{\rm t}$, the diffusion of the dust is given by

$$D_{\rm d} = \frac{D}{{\rm St_L}} \qquad \text{for} \qquad {\rm St_L} > 1\ , \tag{1.15}$$

where we used the Eq. (1.5).

Now, for Stokes numbers smaller than unity the dust particles are well coupled to the gas, i.e. both disk components, gas and dust, behave more like one single fluid than two different types of matter. For this reason, we will assume that the dust diffusivity equals the gas diffusivity for small St. Considering this, the diffusion coefficient for the dust in all coupling regimes, ${\rm St_L} > 1$ and ${\rm St_L} < 1$, is then given by (Schräpler & Henning 2004)

$$D_{\rm d} = \frac{D}{1+{\rm St_L}}\ . \tag{1.16}$$

In the intermediate regime ${\rm St_L} \approx 1$, we expect this equation to hold approximately.

From the numbers D_d and $\tau_{\rm sett} = z/\dot{z}$, representing settling and diffusion, we can construct a length scale by $h^2 = D_d\tau_{\rm sett}$. This leads to the expression for the dust layer thickness:

$$h^2 = D_d\,\max(\tau_{\rm sett}, 1/2\Omega_{\rm k}) \tag{1.17}$$

We resticted the settling time scale to be at least half an orbital time scale. For a particle with no initial vertical velocity at a certain height above the midplane and a Stokes number larger than unity, the motion of the particle corresponds to a damped inclined orbit. The time for the particle to cross the midplane can not be significantly smaller than an orbital time scale. However, the dynamics of bodies in quasi-Keplerian orbits in turbulence may be not well described by diffusion, and the approach of Eq. (1.17) is used with caution. Also the vertical distribution of the dust for the case of inclined orbits (i.e. for large Stokes number) is not Gaussian but rather bimodal, but we will ignore this effect. With Eq. (1.5), as well as the expression for the gas scale height $H = c_{\rm s}/\Omega_{\rm k}$, one can rewrite Eq. (1.17) as:

$$\left(\frac{h}{H}\right)^2 = \frac{\alpha}{\min({\rm St}, 1/2)\ (1+{\rm St}_L)}\ . \tag{1.18}$$

This is the most general description of the dust layer. The Stokes numbers St and ${\rm St}_L$ allow us to calculate the thickness of the dust layer and, therefore, the dust mass densities.

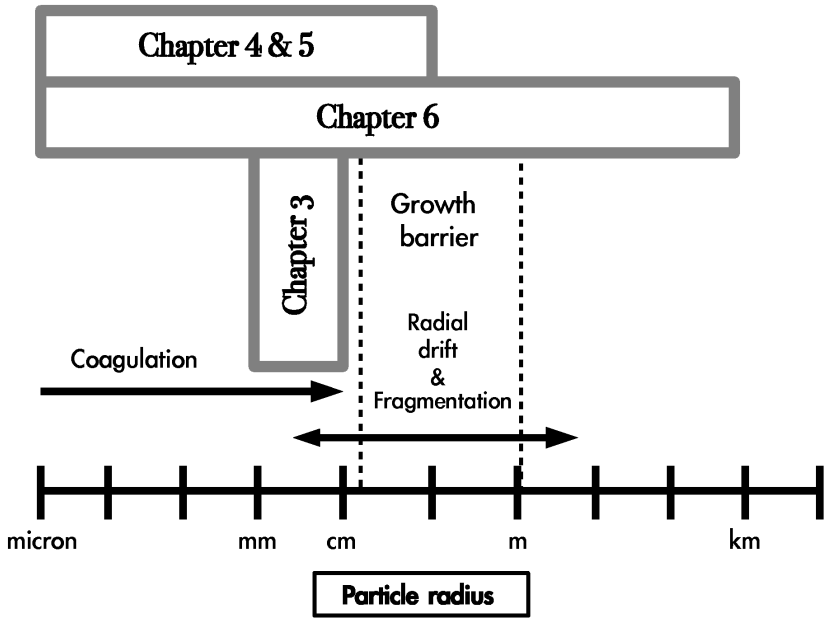

Figure 1.9: Thesis outline. This plot shows the range of particle sizes we consider in this thesis. The regions of coagulation, fragmentation and radial motion are indicated. This figure also shows the sub-range of particle sizes each chapter deals with.

With these densities we are able to calculate radial drift velocities to estimate particle radial drift times in the outer parts of the disk in Chapter 3.

We will always assume that the gas and the dust densities in the vertical direction in the disk have a gaussian profile with a half-width of H and h, respectively. For example, the dust density as a function of height above the midplane is then given by

$$\rho_{\rm d} = \frac{\Sigma_{\rm d}}{\sqrt{2\pi}h} \exp\left[-\frac{1}{2}\left(\frac{z}{h}\right)^2\right] . \tag{1.19}$$

This assumption might be put into question if the turbulence is self-induced (Weidenschilling 1979). This shear-instability can occur if the dust particles settle into a thin midplane layer in which the dust-to-gas ratio exceeds unity. Although Johansen et al. (2006a) showed that the vertical dust density in self-induced turbulence has a gaussian shape for canonical dust-to-gas ratios, the vertical structure can show a different shape especially when the dust-to-gas ratio is increased for instance through photoevaporation (Weidenschilling 2006).

1.5 Outline of this thesis

I give a brief outine of what the following chapters are about and how these chapter are scientifically connected (c.f. Fig. 1.9).

Chapter 2

This first part of the thesis is a rather technical chapter. It introduces the equations which

describe particle growth and particle fragmentation – the Smoluchowski equation, and its analytical solutions. Most importantly, it describes the computer algorithms which were used to solve the coagulation/fragmentation equation. It also explains the implicit differencing scheme used in the simulations and a trick which saves a remarkable amount of computational time in numerical simulations of protoplanetary disks. This chapter is less connected to the rest of the thesis since it rather deals with technical issues and, hence, is not required for the understanding of further chapters.

Chapter 3
The second chapter tries to solve a riddle. There are conflicting results from theoretical models of dust particle evolution in protoplanetary disks and observational findings provided by millimeter interferometry. Observations indicates large amounts of mm to cm-sized pebbles in the outer regions of T Tauri disks. However, considering the age of the disks observed, i.e. several Myrs, the dust should long have drifted away from the outer disk regions into the inner regions of the disk. This chapter extensively studies the radial drift behaviour of dust in protoplanetary disks in order to explain these observations.

As already discussed already earlier in the introduction, the same drift problem is present for the theory of planetesimal formation. The drift problem for mm/cm-sized particles at 100 AU, that will be investigated Chapter 3, similarly shows up for meter-sized particles at 1 AU. The radial drift of these large bodies in the inner parts of the disk is so high that they should drift into the evaporation zone over time scales of 100 yrs. This is one of the fundamental and unresolved problems of planet formation (Dominik et al. 2007). In that sense, the cm problem at 100 AU is a proxy for the meter problem at 1 AU, and figuring out a solution at 100 AU may give important clues to what happens at 1 AU.

Chapter 4
The meter size barrier, i.e. dust mass loss due to radial inward drift and particle fragmentation due to high speed collision, is a severe obstacle for planetesimal formation. This part of the thesis tries to unveil the magnitude of this problem. We investigate if it is, under certain circumstances, possible for the dust particles to circumvent this barrier and to form objects which exceed a meter in radius by far. In order to do so, a fully self-consistent 2+1 dimensional dust particle evolution model is developed, including radial motion of solid material and particle coagulation and fragmentation. The radial drift expressions of Chapter 3 serve as an input for these calculations.

Our dust evolution model – consistent with current beliefs – shows that it is indeed very hard to grow particles in protoplanetary disks larger than some centimeters in size. There are at least two different approaches to circumvent the meter size barrier and, nevertheless, to form planetesimals in disks. The first approach attempts to overcome this barrier by considering more realistic particle properties like, for example, the fractal structure of dust aggregates or the properties of the building blocks of larger aggregates. The second approach considers a more realistic disk environment which might favour dust particle growth. In Chapter 5 and Chapter 6, we will investigate these two approaches.

Chapter 5
One of the underlying assumptions in the dust particle evolution model in Chapter 4 is that the threshold velocity for dust particle fragmentation is independent of particle mass. Although this is a good first approach, laboratory experiments show that this is not true in detail. For example, sub-μm dust grains show fragmentation velocities of several 10 m/s, while threshold velocities for meter-sized boulders are only of the order of some m/s. In this chapter, we improve on this issue. We develop an analytical model which predicts threshold velocities for particle fragmentation. It will be investigated, how a more realistic particle fragmentation model influences the simulation results of Chapter 4.

Chapter 6
The snow line, i.e. the location in the disk where the temperature is sufficient to evaporate water ice, has tremendous influence on the motion of solid particles. The water evaporation front, hence, also affects relative dust particle velocities which determine the growth of solid material. In this last chapter, we include the snow line into our dust particle evolution model. It is investigated if this specific disk environment favours dust particle growth and if the dust is able to overcome the meter size barrier in the presence of such evaporation fronts. The results of this chapter are exemplary for the effect of local gas density maxima on dust particle cogulation and, hence, provide a first insight how strong such density fluctuations influence the evolution of the dust.

Chapter 2

Coagulation equation

The first attempt to describe particle growth took place nearly a century ago. Smoluchowski (1916) was the first to present an equation which was supposed to describe the agglomeration of colloidal particles due to Brownian motion. For this reason, the coagulation equation is often referred to as the 'Smoluchowski equation'. Remarkably unnoticed for more than 50 years, this equation became popular again in the early sixties when meteorologists realised its importance for atmospheric models of rain formation (Twomey 1966; Warshaw 1967). A very elegant algorithm for particle coagulation, i.e. the Podolak algorithm which we will discuss later, was formulated during these years (Kovetz & Olund 1969). Roughly a decade later, the Smoluchowski equation first became widely attractive for astronomical purposes. Particle growth as the initial step for planet formation in protoplanetary disks was investigated by Weidenschilling (1980). Although Safronov already made some simple estimates considering dust particle growth in disks in 1969, Weidenschilling was one of the first to solve the complete coagulation equation numerically. He found that particle growth in disks happens surprisingly fast, i.e. that particles can grow from μm to cm size within only 10^3 orbital time scales. With the discovery of the first exoplanet around a solar type star fifteen years later (Mayor & Queloz 1995) and observational evidence for dust particle growth in protoplanetary disks (Bouwman et al. 2001; van Boekel et al. 2003), the motivation to understand particle growth led to the development of quite sophisticated algorithms to solve the Smoluchowski equation (Dullemond & Dominik 2005).

In this chapter, we discuss the coagulation equation which describes particle growth. We investigate three classes of particle growth, we present the known analytical solutions to the coagulation equation and we also introduce a monodisperse particle growth model which will turn out to be very useful in the further parts of this thesis. Most importantly, the computer algorithms which we will use to predict dust particle growth in disks will be explained. In addition, we present substantial improvements to existing algorithms which speed up the numerical scheme by a factor of 10^4. To illustrate this, while the computer simulations performed by Dullemond & Dominik (2005) took a week to predict dust distributions after 1 Myr of disk evolution including particle fragmentation, the numerical schemes presented here answer the same question in about ten minutes.

2.1 The coagulation equation

The Smoluchowski equation for a continuous particle distribution $f(m,t)$ as a function of mass m and time t has the form (Smoluchowski 1916)

$$\begin{aligned}\partial_t f(m,t) = \frac{1}{2}\int_0^m f(m-m',t)f(m',t)K(m-m',m')\,\mathrm{d}m' \\ -f(m,t)\int_0^\infty f(m',t)K(m,m')\,\mathrm{d}m'\,.\end{aligned} \tag{2.1}$$

The mass distribution function f is defined in a way that $f \cdot m \cdot \mathrm{d}m$ is the spatial mass density for solid particles in the mass interval $[m, m+\mathrm{d}m]$ in units og g/cm^3. The first term on the right-hand side of Eq. (2.1) is a positive source for particles of mass m arising from the agglomeration of particles with masses smaller than m. The second term corresponds to particles of mass m which coagulate with particles of any size and, hence, grow to particle masses larger than m. Therefore, this second term is a sink for particles of mass m. The quantity $K(m,m')$ denotes the so-called coagulation kernel. It describes the rate at which particles grow to larger sizes. All physics concerning particle collision rates in disk environments, fractal growth as well as particle sticking probabilities enter this quantity. This means that the process of particle growth is completely determined if the function K is known. If spherical particles without intrinsic structure are considered (raindrops for example) then the corresponding kernels are relatively simple and Eq. (2.1) can be solved easily without comprising the power of super-computers as needed for hydrodynamical simulations for example. We will mainly consider this 'raindrop' simplification in the course of this thesis. However, in general the coagulation kernel can have a vastly complicated structure, especially if fractal properties of particle aggregates are taken into account (Ossenkopf 1993; Ormel et al. 2007). In this case, the particle distribution f additionally becomes dependent on parameters like fractal dimension or porosity. Alternative coagulation algorithms from those presented here – for example Monte Carlo schemes – then provide an interesting alternative approach to the solution of the Smoluchowski equation (Zsom & Dullemond 2008). We will discuss the analytical expressions for the coagulation kernel $K(m,m')$ after introducing the complete coagulation/fragmentation equation in Sec. 2.3.

A distinct class of coagulation kernels shows the interesting property that it leads to a time independent shape of the distribution function f. The mean particle mass increases with time. The shape of the distribution function, however, remains unchanged. An example of such an evolution is shown in Fig. 2.1. Because of the persistent shape of f, this class of solutions is usually referred to as self-similar solutions. The literature on the Smoluchowsky equation does not clearly state the conditions on the coagulation kernel which lead to self-similarity. Nevertheless, it can be shown that homogeneous kernels lead to self-similarity. We consider a homogeneous kernel such that the condition

$$K(\gamma m, \gamma m') = \gamma^s K(m,m') \tag{2.2}$$

holds for any m and m'. The constant s is the degree of the coagulation kernel. A self-similar solution can always be expressed in the form

$$f(m,t) = \frac{1}{\bar{m}(t)^2}\, g\left(\frac{m}{\bar{m}(t)}\right)\,. \tag{2.3}$$

The quantity $\bar{m}$ can be interpreted as the mean particle mass as a function of time. The function g determines the shape of the distribution function. If we combine Eq. (2.3) and

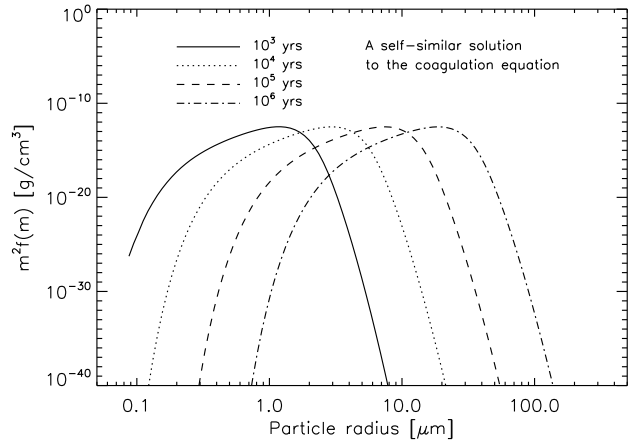

Figure 2.1: An example for a self-similar solution to the coagulation equation as discussed in Sec. 2.1. Shown is the numerically calculated evolution of the particle distribution in the midplane of a protoplanetary disk at 1 AU. The temperature at this point in the disk is assumed to be 204 K. In this simulation, particles coagulate via collisions induced by relative Brownian motion. The figure shows, that the average particle size increases while the shape of the distribution remains unchanged in time.

the coagulation equation (2.1) and introduce a normalised mass $u(t) = m/\bar{m}(t)$, then we can rewrite the Smoluchowski equation as

$$\frac{\dot{\bar{m}}}{\bar{m}^s} = -\frac{\mathscr{F}\left[g(u)\right]}{(2g + ug')} \,, \tag{2.4}$$

with the functional $\mathscr{F}$ given by

$$\mathscr{F}\left[g(u)\right] = \frac{1}{2}\int_0^u K(u-u',u')g(u-u')g(u')\mathrm{d}u' - g(u)\int_0^\infty K(u,u')g(u')\mathrm{d}u' \,. \tag{2.5}$$

In these last expressions, the symbols $\dot{}$ and $'$ denote the time derivative and the derivative with respect to u, respectively. While the left-hand side of Eq. (2.4) is only a function of time, the right-hand side is exclusively dependent on u. This means that both sides must equal a constant c, leading to

$$\dot{\bar{m}} = c\bar{m}^s \,. \tag{2.6}$$

For $s \neq 1$, the mass $\bar{m}$, which corresponds to the peak of the particle distribution g, increases according to

$$\bar{m}(t) = \left[c(t-t_0) + \bar{m}_0^{1-s}\right]^{1/(1-s)} \,. \tag{2.7}$$

The shape of the distribution is given by the equation

$$\mathscr{F}\left[g(u)\right] = -c\left(2g + ug'\right) \,. \tag{2.8}$$

The Smoluchowski equation is roughly one hundred years old, but there are only three known analytical solutions to the last expression. This disappointment gives an idea about the complexity of this equation. We introduce the exact solutions to the coagulation equation,

which are useful for tests of computer coagulation algorithms, in Sec. 2.2. Fortunately, we do not have to solve Eq. (2.8) to acquire information about how fast particles grow to larger sizes, because this equation only determines the shape of the function g. Information about growth time scales is solely provided by expression (2.7) which can be distinguished in three different cases:

1. $s < 1$: In this case, Eq. (2.6) leads to an average mass $\bar{m}$ which is proportional to $t^{1/(1-s)}$. The mass as a function of time, therefore, shows a polynomial behaviour. An example for this case is particle coagulation due to Brownian motion for which $s = -1/2$.

2. $s = 1$: The particle mass increases exponentially with time, i.e. Eq. (2.6) leads to $\bar{m} \propto \exp(ct)$. A property of this particular class of solutions is that the time evolution of $\bar{m}$ is very sensitive to the coagulation parameter c. This means for astronomical applications that coagulation time scales are very sensitive to disk parameters which influence particle growth. An example for this special case is coagulation of solid particles due to relative turbulent motions under the influence of vertical gravity in a protoplanetary disk. The later chapters will shown that it is this growth mechanism with $s = 1$ which makes the formation of planetesimals possible in the disk. Due to this rapid exponential growth of dust, particles are able to circumvent the radial drift barrier which is one of the major obstacles in planet formation.

3. $s > 1$: If we introduce the positive parameter $\varsigma = 1/(s-1)$ and set $t_0 = 0$ then the mass $\bar{m}$ as a function of time is given by

$$\bar{m}(t) \propto \left(\frac{1}{\bar{m}_0^{-1/\varsigma} - ct} \right)^{\varsigma} \qquad \text{and} \qquad c > 0 \,. \tag{2.9}$$

   This expression shows that particles grow hyperbolically for $s > 1$. An interesting property of this solution is that particles can grow to infinite mass in the finite time $t_\infty = \bar{m}_0^{-1/\varsigma}/c$. This effect is called runaway-growth. An example for this $s > 1$ case is charge-induced particle coagulation (Mokler & Morfill 2005) in which charged particles attract each other due to Coulomb forces. Since runaway growth is an interesting possibility to form large particles over short time scales, this family of solutions is attractive for dust growth models in protoplanetary disks. For example, Mokler et al. (2008 in prep.) show that charge-induced particle coagulation leads to the formation of meter-sized bodies within only a few years at 100 AU in the disk. This growth time scale is 10^5 times shorter than typical particle growth time scales of type $s < 1$, as will be shown in Chapter 4. However, this fast growth mechanism is a fragile process which does not work if relative particle velocities exceed a certain critical threshold velocity which corresponds to the Coulomb energy of the charged particle distribution. If protoplanetary disks are a suitable environment which provides a sufficiently small velocity field for this process to work is still highly debated.

Let us consider a simplification to the Smoluchowski equation which will turn out to be very useful in the later chapters. Even though Fig. 2.1 indicates a broad particle distribution which spans more than one order of magnitude in particle radius, this is actually not the case. This misleading impression arises from the fact that the vertical axis is logarithmic. A linear plot would unveil a quite narrow distribution. For this reason, it is legitimate

to approximate the entire particle distribution function f by a peak distribution, i.e. a monodisperse distribution. We make the ansatz

$$f(m,t) = \frac{\rho}{m_0(t)}\delta_{\mathrm{D}}\left(m - m_0(t)\right) \ , \tag{2.10}$$

in which δ_{D} denotes the Dirac function which peaks at $m = m_0(t)$. The factor $1/m_0$ ensures mass conservation. The quantity ρ is a constant spatial particle density. With this ansatz, the Smoluchowski equation (2.1) simplifies to

$$\dot{N}(m) = K(m,m)N(m)^2 \qquad \text{in which} \qquad N = \int_0^\infty f(m,t)\mathrm{d}m = \frac{\rho}{m_0(t)} \ . \tag{2.11}$$

The last two expressions directly lead to the time evolution of the monodisperse distribution,

$$\dot{m}_0(t) = K(m_0,m_0)\rho \ . \tag{2.12}$$

This equation is far easier to solve than the full coagulation equation which allows us to calculate typical growth time scales in protoplanetary disks without large expenditure of time. Hence, we can get a first impression of particle coagulation without performing extensive numerical simulations. In the forthcoming chapters, we will find that this analytical estimate, despite of completely neglecting the particle dispersion, impressively mirrors the numerical solutions to the full coagulation equation if particle growth due to Brownian motion is assumed. However, the monodisperse distribution ansatz does not hold if particle fragmentation is taken into account. The outcome of particle fragmentation due to destructive particle collisions involves particle sizes of the order of the parent bodies as well as tiny dust grains of micrometer size, i.e. a broad dust particle distribution. Therefore, fragmentation is in contradiction with the monodisperse ansatz Eq. (2.10) raising the inevitable need to solve the complete coagulation/fragmentation equation (cf. Chap. 2.3) in all its beauty.

For numerical purposes, we have to consider a discretized form of the coagulation equation Eq. (2.1) in the following way. First, we artificially include two more integrals into the equation using the δ-function,

$$\dot{f}(m,t) = \int_{\mathrm{m,m'}} f(m')f(m'')K(m',m'')\left[\frac{1}{2}\delta(m'+m''-m) - \delta(m-m'')\right]\mathrm{d}m'\mathrm{d}m'' \ . \tag{2.13}$$

Then we introduce a mass grid $\{m_{\mathrm{k}}\}$ with its measure $\{\mathrm{d}m_{\mathrm{k}}\}$. With these definitions, we can introduce the particle number density N_{k} on a mass grid by $N_{\mathrm{k}} = f(m_{\mathrm{k}})\mathrm{d}m_{\mathrm{k}}$. With the transition from integrals to sums and the latter definitions, the Smoluchowski equation on a mass grid is then given by

$$\partial_{\mathrm{t}} N_{\mathrm{i}} = \sum_{\mathrm{jk}} N_{\mathrm{j}} N_{\mathrm{k}} M_{\mathrm{ijk}}^{\mathrm{coag}} \ . \tag{2.14}$$

The exact form of the coagulation matrix M_{ijk} depends on the choice of the mass grid and the coagulation algorithm. This matrix will be discussed in Sec. 2.4. It is worthwhile to note that this discrete formulation of the coagulation equation in terms of particle number densities is not the only possible choice. We later discuss an algorithm which rather involves the quantity f instead of the number density N. This has the advantage that f is independent of how the mass grid is defined, while discrete number densities are directly proportional to $\mathrm{d}m$.

2.2 Exact solutions to the coagulation equation

Even though the coagulation equation is a challenge to physicists and mathematicians for as long as a century, there are only three known analytical solutions to the Smoluchowski equation which mirrors its complexity. Since two of these three solutions can be transformed into each other we will only introduce the two independent ones, namely the solutions for a constant kernel and a linear kernel. The solutions and its derivations can be found in Safronov (1963, 1969) and Ohtsuki et al. (1989). Here, we do not recapitulate the rather extensive derivations. We merely remark that the coagulation equation can be solved more easily after Laplace transformation which is used to attain the following analytical expressions.

1. Linear kernel. We consider a coagulation kernel which is linear in mass,

$$K(m, m') = A(m + m') \; . \tag{2.15}$$

The solution to Eq. (2.1) is given by

$$f(m,t) = \frac{g\rho}{m\sqrt{1-g}} \exp\left((g-2)\frac{m}{m_0}\right) I_1\left(2\frac{m}{m_0}\sqrt{1-g}\right) \quad \text{with} \quad g = \exp\left(-tA\rho\right) \; . \tag{2.16}$$

The quantities ρ and I_1 denote the spatial particle mass density and the first modified Bessel function, respectively. The constant m_0 is the mass of the particles at the time $t = 0$.

We remark a numerical problem which appears when the analytical expression Eq. (2.16) is implemented into a computer codes. The right hand side of this equation is the product of a small number (the exponential factor) and a large number (the Bessel function factor). Computers run into problems when they try to evaluate this expression which typically results in arbitrary numbers with no longer physical meaning. To illustrate this problem, the ratio m/m_0 for km-sized planetesimals of mass m and micrometer sized dust grains of mass m_0 is of the order of $\sim 10^{27}$. While the number $\exp(-10^{27})$ in Eq. (2.16) surely exists in a mathematical sense, it is, however, identically zero regarding any computer maschine accuracy today. To avoid this numerical problem, we consider the asymptotic behaviour of the Bessel function I_1 for large arguments,

$$I_1(x) \to \frac{1}{\sqrt{2\pi x}} \exp(x) \qquad \text{for} \qquad x = \frac{m}{m_0} \gg \frac{3}{4} \; . \tag{2.17}$$

The analytical solution for the linear kernel for large m/m_0 ratios then becomes

$$f(m,t) = \frac{g\rho}{m\sqrt{2\pi x(1-g)}} \exp\left(x(g + 2\sqrt{1-g} - 2)\right) \; . \tag{2.18}$$

For large times, i.e. for $t \gg 1/A\rho$, this last equation simplifies to

$$f(m,t) = \frac{g\rho}{m\sqrt{2\pi x}} \exp(xg) \; . \tag{2.19}$$

Before we come to the constant kernel, we calculate the average mass which most of the particles are present in. In other words, we look for the typical dust grain mass which represents the whole particle distribution given by the last equation. Therefore, we consider the specific particle density $mf(m,t)$ and we calculate the particle

mass m_p for which $mf(m,t)$ has a maximum. This particle mass is easily found to be $m_\mathrm{p} = m_0 g^{-1} = m_0 \exp(A\rho t)$. Interestingly, this mass m_p is (up to a factor of 2) the typical particle mass predicted by the monodisperse model Eq. (2.12). This shows that the monodisperse distribution evolution mirrors the evolution of the full particle distribution quite nicely.

2. Constant kernel. We consider a coagulation kernel of the form

$$K(m,m') = A\,, \tag{2.20}$$

where A is an arbitrary constant. Safronov (1969) first calculated the solution to the Smoluchowski equation for this kernel in its discrete version Eq. (2.14) which is

$$N_\mathrm{k}(\tau) = N_\mathrm{ini}\, g^2\, (1-g)^{\tilde{k}-1} \qquad \text{and} \qquad g = \left(1+\frac{\tau}{2}\right)^{-1}\,. \tag{2.21}$$

The normalised time τ is given by $A\rho t/m_{\mathrm{m}_0}$. The initial conditions are $N_1(\tau=0) = N_\mathrm{ini}$ and $N_\mathrm{k} = 0$ for $k > 1$. The quantity $\tilde{k}$ is given by $\tilde{k} = m_\mathrm{k}/m_{\mathrm{m}_0}$.

Unfortunately, the two analytical solutions presented here are generally not applicable to dust particle growth models in protoplanetary disks. This is due to the following fact. Particle number densities of a specific particle mass at a certain point in a disk are not exclusively altered by particle coagulation. Number densities are also changed by vertical and radial particle motion through the disk. An example for systematic dust motion is the radial inward drift of solid particles due to gas drag forces (Weidenschilling 1977a). Particle motion corresponds to advection terms which are missing in Eq. (2.1) and, hence, the analytical solutions Eqs. (2.16) and (2.21) do not hold.

2.3 Coagulation - fragmentation equation

Particle collisions do not necessarily lead to particle growth. Two meter-sized objects of solid rock which collide with a relative speed of 100 m/s supposably do not stick to each other. Instead, they undergo catastrophic destruction which results in a broad particle size distribution. Relative particle velocities in disks can be as high as ~ 100 m/s (Weidenschilling 1977a; Ormel & Cuzzi 2007). Particle destruction due to high speed collisions is, therefore, likely to occur and an important process in protoplanetary disks. The coagulation equation discussed in the last sections does not include the effect of particle fragmentation. For this reason, we have to introduce the equation which describes particle coagulation *and* particle fragmentation, namely

$$\begin{aligned}\partial_\mathrm{t} f(m,t) = &\frac{1}{2}\int_0^m f(m')f(m-m')K(m',m-m')\mathrm{d}m' - \int_0^\infty f(m)f(m')K(m,m')\mathrm{d}m' \\ &+\frac{1}{2}\int_0^\infty\int_0^\infty f(m')f(m'')L(m',m'')S(m,m',m'')\mathrm{d}m'\mathrm{d}m'' \\ &-\int_0^\infty f(m)f(m')L(m,m')\mathrm{d}m'\,.\end{aligned} \tag{2.22}$$

The first line of this equation is the coagulation equation which was already discussed. The two additive source terms on the right-hand side line describe particle fragmentation. The

quantity $L(m, m')$ describes the rate of particle fragmentation. This quantity can be regarded as the counterpart to the coagulation kernel K. The function $S(m, m', m'')$ describes the material outcome of a destructive collision between two bodies of mass m' and m'' as a function of the mass m after the collision. This re-distribution function contains all the information which concerns the shattering results of a destructive collision. We discuss its exact analytical form in Chapter 4 when we come to include particle fragmentation into our dust evolution model. The term which includes the redistribution function in Eq. (2.22) also comprises a double integral over mass. We already note here that from a numerical computational point of view, this is the most time consuming term which will slow down any computer simulation that includes particle fragmentation. In Chapter. 2.4, we present a procedure to circumvent this problem.

Up to this point, there is no connection between the coagulation and fragmentation kernels, K and L, and physical particle characteristics like collisional cross-section or relative particle velocities. To associate these physical quantities, we consider two particle species, i.e. two particles with mass m_1 and m_2. The number of collisions per second between these two particle species at a certain point in space can be calculated to be

$$\frac{\text{collisions}}{\text{second} \cdot \text{cm}^3} = N_1 N_2 \Delta v_{12} \sigma_{12} \; . \tag{2.23}$$

The quantities N_1 and N_2 denote the number densities of the particle species. The quantities Δv_{12} and σ_{12} are the average relative velocity and the collisional cross-section between the particles of species 1 and 2, respectively. There are at least three different possible events which can occur during a particle collision.

1. The collision results in dust particle growth. We assume this to occur with a certain probability p_c. This probability is usually higher for low velocity impacts than for high velocity impacts.

2. The impact can result in catastrophic fragmentation with a probability p_f.

3. A third possibility is that nothing happens and the colliding particles simply bounce with a probability p_b.

We assume that these are the only possible outcomes, so the sum of all probabilities must equal unity, i.e. $p_\mathrm{c} + p_\mathrm{f} + p_\mathrm{b} = 1$. A comparison between the coagulation/fragmentation Equation (2.22) and the collision rates given by Eq. (2.23) leads to the kernels

$$K(m, m') = p_\mathrm{c}(m, m') \Delta v_{mm'} \sigma_{mm'} \quad \text{and} \quad L(m, m') = p_\mathrm{f}(m, m') \Delta v_{mm'} \sigma_{mm'} \; . \tag{2.24}$$

In general, the sticking probabilities, the collision velocities, and the geometrical particle cross-section are complicated functions of the projectile and the target mass. We illustrate this complexity by giving two examples.

First, relative particle velocities in protoplanetary disks are highly dependent on the particle mass and the geometrical particle cross-section (Cuzzi & Weidenschilling 2006; Ormel & Cuzzi 2007). The ratio between these two quantities determines how strong the dust grains couple to the motions of the turbulent gas. This coupling strength, i.e. the Stokes number St, is the only particle parameter which is important for the calculation of relative dust velocities. Dust particles of sub-μm size, i.e. particles of Stokes number $\sim 10^{-6}$, typically have relative velocities of the order of some cm/s. Meter-sized bodies of St $= 1$ can have relative speeds of 10% of the sound speed.

Second, realistic particle cross-sections are complicated function of the particle mass. This is due to the fact that in ballistic particle growth models, the particle density is dependent on the growth history of the dust grain (Dominik & Tielens 1997; Blum & Wurm 2000; Wurm et al. 2005). Dust particles can either grow by forming particle-cluster aggregates (PCA) or cluster-cluster aggregates (CCA) (Meakin & Donn 1988; Ossenkopf 1993; Kempf et al. 1999). If particles grow mainly via collisions with dust grains of different sizes then PCA's form which have comparatively large material densities (Blum & Wurm 2008). Particle growth via collisions of aggregates of the same size leads to open fractal structures, whose porosity can be very low. These two growth mechanisms lead to quite different collisional cross-sections. The cross-section strongly influences relative dust particle velocities in disks and, hence in turn, dust particle growth (Ormel et al. 2007).

Particle coagulation, fragmentation and bouncing are not the only events that can happen during particle collisions. There are more subtle effects and we give two examples.

First, consider a collision experiment in which small projectile grains hit a large target particle. The velocity of the small projectile particles falls into a regime in which bouncing is observed. Interestingly, in lab experiments some small dust grains show a non-linear flight trajectory after bouncing (Poppe et al. 2000a). Small dust grains first rebound from the target. However, they returned to the target and would finally stick. A reasonable explanation is that the the dust grains are electrically charged (Harper 1967; Pilipp et al. 1992; Poppe et al. 2000b) and electric forces lead to dust growth due to an increased effective particle cross-section. This coagulation mechanism involves particle bouncing, associated with a loss of kinetic energy, and charge separation which finally leads to particle growth.

Second, Wurm et al. (2005) investigated the growth of dust particles at impact speeds of ~ 25 m/s. At these high velocities, a certain mass fraction of the projectile particle sticks to the target while another fraction suffers complete fragmentation. This process involves coagulation and fragmentation at the same time. The possible outcomes of particle collisions as investigated here, i.e. coagulation, fragmentation and bouncing, are surely a proper first step towards an understanding of dust particle growth. Nevertheless, the microphysical effects described above could play an important role.

2.4 Numerical coagulation algorithms

We present two computer algorithms which numerically solve the coagulation equation. The first algorithm was developed by Dullemond & Dominik (2005). The second algorithm, the so-called "Podolak algorithm", was invented in meteorological science by Kovetz & Olund (1969). Before we discuss the numerical schemes to solve the Smoluchowski equation, we note two problems which appear in this context and which should be kept in mind.

We consider a mass grid m_k with $k = 1 \ldots n$. In protoplanetary dust particle growth models, the particle mass m_1 typically has values of $\sim 10^{-14}$ g which corresponds to dust grains of $\sim \mu$m radii, i.e. grain sizes which can be found in disks at the very early stages of disk evolution. The maximum grid mass $m_{\rm n}$ is of the order of 10^{16} g which corresponds to planetesimals of km size. The range of the grid spans over 30 orders of magnitude in mass. Linear mass grids, i.e. mass grids of the form $m_{\rm k} = a + {\rm k}b$, require a number of grid points of the same order of magnitude to span this large mass interval. Numerical simulations which involve 10^{30} grid points are far beyond any computational power today. To circumvent this problem, we adopt a logarithmic mass grid of the form

$$\log_{10} m_{\rm k} = a + {\rm k}b \; . \tag{2.25}$$

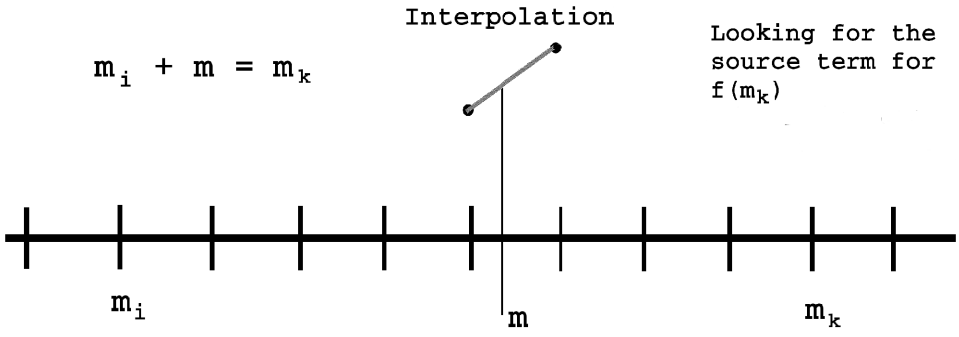

Figure 2.2: The Dullemond & Dominik algorithm as discussed in Sec. 2.4.1. The sketch illustrates the calculation of a positive source term for the particle distribution function at $m = m_\mathrm{k}$. In order to form a particle of mass m_k, the smaller particle m_i has to coagulate with a particle of mass m which usually does not correspond to any mass grid point. Hence, the distribution function has to be interpolated.

This grid has the advantage to cover the whole mass interval with only ~ 200 grid points. However, it has the disadvantage that the sum $m_\mathrm{i} + m_\mathrm{j}$ lies generally not exactly at a discrete mass point. In other words, if a particle of mass m_i and a particle of mass m_j coagulate, into which grid cell do we put the particle of mass $m_\mathrm{i} + m_\mathrm{j}$ if there is no such grid point? Different answers to this question lead to different coagulation algorithms.

A second problem is that intrinsic computer variables, so-called double precision variables, have an accuracy of only up to 14 digits. Assuming that a μm-sized dust grain of mass $m_\mathrm{g} = 10^{-14}$ g coagulates with a km-sized planetesimal of mass $m_\mathrm{p} = 10^{16}$ g. The mass difference of these two bodies is so extremely large that the numerical calculation of the sum $m_\mathrm{g} + m_\mathrm{p}$ exceeds numerical accuracy. For a computer, the equation $m_\mathrm{g} + m_\mathrm{p} = m_\mathrm{p}$ is numerically correct, even though the mass m_g is not zero. In other words, the coagulation of very large and very small bodies leads to the numerical disappearance of the small particle and neglecting this numerical problem in coagulation algorithms can lead to significant mass loss.

2.4.1 Dullemond & Dominik algorithm

We recapitulate the algorithm which is the basis for the dust particle coagulation simulations performed by Dullemond & Dominik (2005), and which is illustrated in Fig. 2.2. To solve the coagulation equation, i.e. to find the new particle distribution function at the mass grid point m_k, we have to calculate the source term $s(m_\mathrm{k}) = \partial_t f(m_\mathrm{k}, t)$. This quantity is given by two terms, i.e. a positive source term and a negative source term (c.f. Eq. 2.1). For the moment, we only consider the positive source term.

For all grid points $m_\mathrm{i} < m_\mathrm{k}/2$ (corresponding to the integral in the coagulation equation), we calculate the mass m which by coagulation with a particle of mass m_i results in a particle of mass m_k, i.e. $m_\mathrm{i} + m = m_\mathrm{k}$. This mass m typically lies in between two gridpoints since we adopt a logarithmic mass grid. Hence, the particle distribution function f has to be

interpolated. Since the function f can vary significantly from one mass grid point to another, the interpolation is best done in $\log f$ instead of f. After this interpolation, the collision rates are calculated from the values of $f(m_\mathrm{i})$ and $f(m)$ according to Eq. (2.1) which directly leads to the positive source terms. For the negative source terms, i.e. the right hand side of Eq. (2.1), no interpolation is needed.

This algorithm as presented so far does not conserve mass. This is due to the numerical problem of coagulation between small and large particles as discussed in the last section. To cope with this problem, Dullemond & Dominik (2005) consider the following renormalisation. At each time step, the gain term and the loss term, i.e. the positive and negative sources of the coagulation equation, are calculated simultaneously for each m_i. If the ratio between these two terms is different from unity, no numerical problem appears. However, if the two terms produce near cancellation, the difference between the terms can result in an arbitrary number without any physical meaning. In this case, we calculate the difference between the two terms using l'Hospital's rule,

$$\begin{aligned} & f(m') \left[f(m-m') K(m', m-m') - f(m) K(m, m') \right] \\ \approx & -f(m')(m-m') \partial_{m''} \left[f(m'') K(m', m'') \right] . \end{aligned} \tag{2.26}$$

We note that this renormalisation is only valid if the gain and the loss term are numerically nearly equal. Using this renormalisation circumvents the problems of numerical accuracy in an elegant manner, but it also makes it difficult to formulate an implicit version of this algorithm (see section 2.4.4).

Even with the renormalisation technique described above, the algorithm does still not conserve mass, because of the interpolation of the particle distribution function between two grid points. The simulations show that this mass change at every time step is typically negligible, but to prevent unphysical build-ups or loss of matter, we consider the following mass conservation scheme. After the new distribution function f_new is calculated from the old distribution f_old, we compute the ratio

$$\chi = \int_m m f_\mathrm{old}(m) \mathrm{d}m \quad / \quad \int_m m f_\mathrm{new}(m) \mathrm{d}m . \tag{2.27}$$

If the particle distribution function f_new is multiplied by the factor χ then the algorithm also conserves mass up to numerical accuracy.

2.4.2 Podolak algorithm

We present an algorithm which was described by Kovetz & Olund (1969) in meteorological science. Contrary to the Dullemond & Dominik scheme, this algorithm automatically conserves particle mass up to numerical accurary and it is more easily implemented into computer codes.

We consider a mass grid m_i, $i = 1 \ldots n$, and a particle size distribution f. From this distribution, we can calculate the number densities $N_\mathrm{i} = f(i)\mathrm{d}m_\mathrm{i}$. Two particles with masses m_i and m_j coagulate with a rate $K_\mathrm{ij} = K(m_\mathrm{i}, m_\mathrm{j})$ which leads to a source term Q_ij given by

$$Q_\mathrm{ij} = N_\mathrm{i} N_\mathrm{j} K_\mathrm{ij} . \tag{2.28}$$

If non-linear mass grids are considered, the mass $m = m_\mathrm{i} + m_\mathrm{j}$ does not match with any of the mass grid points. Therefore, we have to divide the source term Q_ij between the nearest mass grid points close to m (cf. Fig. 2.3).

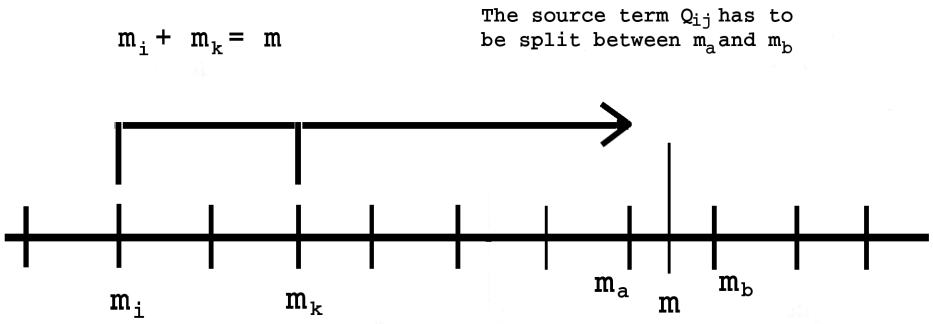

Figure 2.3: Illustration of the Podolak algorithm as discussed in Sec. 2.4.2. The plot shows the coagulation of two particles with mass m_i and m_j. The source term for the mass $m = m_\mathrm{i} + m_\mathrm{j}$ has to be distributed between the mass bin m_a and m_b.

We assume that the nearest neighbours are given by $m_\mathrm{m} < m < m_\mathrm{n}$. With a linear ansatz, we split the source term Q_ij into a source term for the mass m_m and a source term for the mass m_n,

$$Q_\mathrm{m} = \epsilon\, Q_\mathrm{ij} \quad \text{and} \quad Q_\mathrm{n} = (1-\epsilon)\, Q_\mathrm{ij}\ . \tag{2.29}$$

To fix the free parameter ϵ, we consider the conservation of mass which can be expressed as

$$Q_\mathrm{m} m_\mathrm{m} + Q_\mathrm{n} m_\mathrm{n} = Q_\mathrm{ij}(m_\mathrm{i} + m_\mathrm{j})\ . \tag{2.30}$$

Inserting the Eqs. (2.29) into Eq. (2.30), we find that ϵ has the form

$$\epsilon = \frac{m_\mathrm{n} - (m_\mathrm{i} + m_\mathrm{j})}{m_\mathrm{n} - m_\mathrm{m}}\ . \tag{2.31}$$

For every mass triple $(m_\mathrm{i}, m_\mathrm{j}, m_\mathrm{k})$, we can find the ϵ-parameter which ensures mass conservation, so that the coagulation equation can be written as

$$\dot{N}_\mathrm{k} = \frac{1}{2}\sum_\mathrm{ij} Q_\mathrm{ij} C_\mathrm{ijk} - \sum_\mathrm{i} Q_\mathrm{ik}\ . \tag{2.32}$$

The matrix C is given by

$$C_\mathrm{ijk} = \begin{cases} \epsilon & \text{if } m_\mathrm{k} \text{ is the largest mass grid point} < m_\mathrm{i} + m_\mathrm{j}, \\ 1-\epsilon & \text{if } m_\mathrm{k} \text{ is the smallest mass grid point} > m_\mathrm{i} + m_\mathrm{j}, \text{and} \\ 0 & \text{otherwise.} \end{cases}$$

In general, more than 90% of the elements in the matrix C are zero. Therefore, a lot of computer calculation time can be saved if only the non-zero elements in Eq. (2.32) are summed up.

We introduced the analytical solution to the coagulation equation for a constant kernel in Chap. 2.2. Hence, we can check the reliability of our coagulation algorithms in this case.

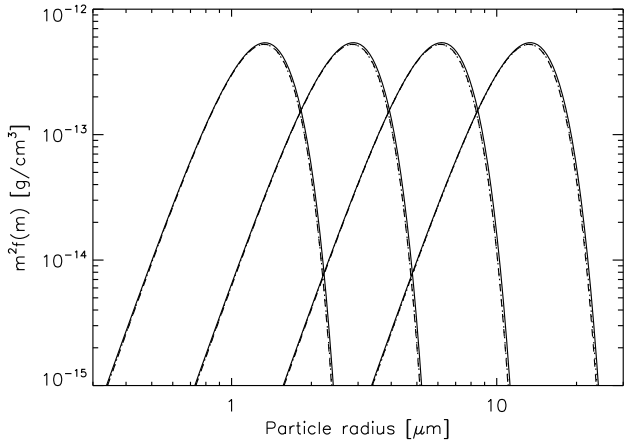

Figure 2.4: Comparison between an analytical solution to the coagulation equation with numerical solutions using different coagulation algorithms. Shown is the analytical solution implementing the constant kernel $K = 1$ (solid), the numerical solution using the Dullemond & Dominik algorithm (dotted) and the Podolak algorithm (dashed) as discussed in Sec. 2.4.2. We find no significant difference between the solutions.

The solid line in Fig. 2.4 indicates the analytical solution to the coagulation equation with the constant kernel $K = 1$. This figure also shows the numerical solutions adopting the Dullemond & Dominik algorithm (dotted) and the Podolak algorithm (dashed). The mass grid ranges from $m_{\rm min} = 10^{-14}$ g to $m_{\rm max} = 10^{-7}$ g using $N = 200$ grid points. We calculate the particle distribution for four different times, i.e. for $\tau = 10^3$, 10^4, 10^5 and 10^6. Considering the constant kernel, we do not find significant differences in the analytical and the numerical solutions to the coagulation equation.

We can compare the two algorithms for a more relevant case. We consider dust particle coagulation due to Brownian motion at 1 AU in the midplane of the disk. The temperature is 204 K and the dust particle density is $\rho_{\rm d} = 2.6 \times 10^{-12}$ g/cm^3. We adopt 200 grid points ranging from 10^{-14} to 10^2 g. Fig. 2.5 shows the dust particle distribution for three different times, i.e. $t = 10^5$, 10^6 and 10^7 yrs. The solid line and the dotted line indicate the particle distributions as predicted by the Dullemond & Dominik algorithm and the Podolak algorithm, respectively. Although the particle distribution for both algorithms peaks at the same particle radius for each time, we find that the Podolak algorithm is more diffusive than the Dullemond & Dominik algorithm. This is due to the fact that the latter algorithm interpolates the particle distribution in $\log f$, while the former algorithm uses linear interpolation. Apart from this small diffusivity which makes the Dullemond & Dominik algorithm more favourable, we do not find convincing physicial reasons to prefer one algorithm over the other. The algorithm invented by Dullemond & Dominik is somewhat faster than the Podolal algorithm. In coagulation simulations, computational times which differ by a factor of ~ 2 were not unusual. On the other hand, the Podolak algorithm can easily be reformulated for implicit integration which is at least challenging for the Dullemond & Dominik algorithm. We come back to this point in Sec. 2.4.4.

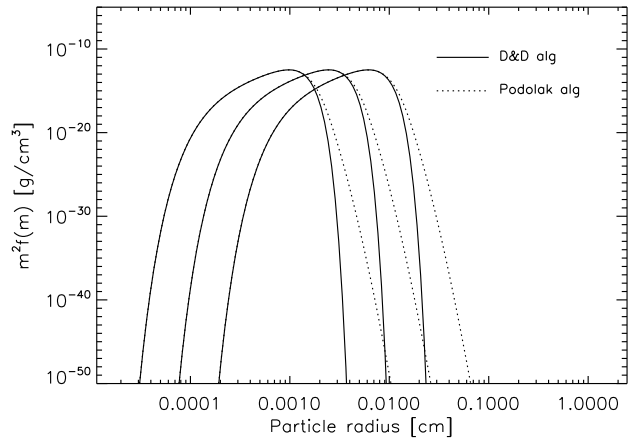

Figure 2.5: Comparison between two numerical solutions to the coagulation equation as discussed in Sec. 2.4.2. Shown is the dust particle density in the midplane of the disk at 1 AU as predicted by the Dullemond & Dominik algorithm (solid) and the Podolak algorithm (dotted) for three different times, i.e. $t = 10^5$, 10^6 and 10^7 yrs. Dust particles grow due to relative thermal velocity fluctuations (Brownian motion). This figure indicates that although the particle distribution peaks at the same particle radius for the different algorithms for each time, the Podolak algorithm is more diffusive than the Dullemond & Dominik algorithm.

2.4.3 Modified Podolak algorithm

The numerical accuracy needed for simulations of particle coagulation in protoplanetary disks exceeds the accuracy provided by the computer. One solution is the introduction of quadrupole precision computer variables but this would slow down the simulation speed significantly. In order to perform the coagulation simulations with double precision variables nevertheless, we have to rewrite the Podolak algorithm at certain points of the numerical scheme.

We introduce a number c_e in the following way. We consider the neighboring mass grid points $m_{\mathrm{k}-1}$ and m_{k}. c_e is now defined in a way that

$$m_{\mathrm{k}-1} + m_{\mathrm{i}} < m_{\mathrm{k}} \qquad \bigvee \mathrm{i} \ : \ \mathrm{i} \leq \mathrm{k} - c_e \ . \tag{2.33}$$

In general, the value of c_e is dependent on the index k.

After introducing this number, we can now reformulate the algorithm. We start from Eq. (2.32) and we formally separate the diagonal elements from the non-diagonal elements.

$$\dot{N_{\mathrm{k}}} = \frac{1}{2} \sum_{\mathrm{i}=1}^{\mathrm{k}} N_{\mathrm{i}}^2 C_{\mathrm{iik}} K_{\mathrm{ii}} + \sum_{\mathrm{i}=1}^{\mathrm{k}} \sum_{\mathrm{j}=1}^{\mathrm{i}-1} N_{\mathrm{i}} N_{\mathrm{j}} C_{\mathrm{ijk}} K_{\mathrm{ij}} - \sum_{\mathrm{j}=1}^{N} N_{\mathrm{j}} N_{\mathrm{k}} K_{\mathrm{jk}} \ . \tag{2.34}$$

In the next step, we consider the second and third term of the last expression. In the second term we separate the case i = k which leads to

$$\sum_{\mathrm{i}=1}^{\mathrm{k}-1} \sum_{\mathrm{j}=1}^{\mathrm{i}-1} N_{\mathrm{i}} N_{\mathrm{j}} C_{\mathrm{ijk}} K_{\mathrm{ij}} + \sum_{\mathrm{j}=1}^{\mathrm{k}+1-c_e} N_{\mathrm{k}} N_{\mathrm{j}} C_{\mathrm{kjk}} K_{\mathrm{kj}} - \sum_{\mathrm{j}}^{N} N_{\mathrm{j}} N_{\mathrm{k}} K_{\mathrm{jk}} \ . \tag{2.35}$$

This can be rewritten as

$$\begin{aligned}
&\sum_{\mathrm{i}=1}^{\mathrm{k}-1}\sum_{\mathrm{j}=1}^{\mathrm{i}-1} N_\mathrm{i}N_\mathrm{j}C_\mathrm{ijk}K_\mathrm{ij} + \sum_{\mathrm{j}=1}^{\mathrm{k}+1-c_e} (N_\mathrm{k}N_\mathrm{j}C_\mathrm{kjk}K_\mathrm{kj} - N_\mathrm{j}N_\mathrm{k}K_\mathrm{jk}) - \sum_{\mathrm{j}=\mathrm{k}+2-c_e}^{N} N_\mathrm{j}N_\mathrm{k}K_\mathrm{jk} \\
&= \sum_{\mathrm{i}=1}^{\mathrm{k}-1}\sum_{\mathrm{j}=1}^{\mathrm{i}-1} N_\mathrm{i}N_\mathrm{j}C_\mathrm{ijk}K_\mathrm{ij} - \sum_{\mathrm{j}=1}^{\mathrm{k}+1-c_e} N_\mathrm{k}N_\mathrm{j}K_\mathrm{kj}\frac{m_\mathrm{j}}{m_{\mathrm{k}+1}-m_\mathrm{k}} - \sum_{\mathrm{j}=\mathrm{k}+2-c_e}^{N} N_\mathrm{j}N_\mathrm{k}K_\mathrm{jk} \\
&= \sum_{\mathrm{i}=1}^{\mathrm{k}-1}\sum_{\mathrm{j}=1}^{\mathrm{i}-1} N_\mathrm{i}N_\mathrm{j}C_\mathrm{ijk}K_\mathrm{ij} + \sum_{\mathrm{j}=1}^{N} N_\mathrm{k}N_\mathrm{j}K_\mathrm{kj}D_\mathrm{jk}\ , \qquad (2.36)
\end{aligned}$$

where the matrix D is given by

$$D_\mathrm{jk} = \begin{cases} -\frac{m_\mathrm{j}}{m_{\mathrm{k}+1}-m_\mathrm{k}} & \text{if } \mathrm{j} \le \mathrm{k}+1-c_e, \text{ and} \\ -1 & \text{if } \mathrm{j} > \mathrm{k}+1-c_e\ . \end{cases}$$

The new coagulation equation now reads

$$\dot{N}_\mathrm{k} = \frac{1}{2}\sum_{\mathrm{i}=1}^{\mathrm{k}} N_\mathrm{i}^2 C_\mathrm{iik}K_\mathrm{ii} + \sum_{\mathrm{i}=1}^{\mathrm{k}-1}\sum_{\mathrm{j}=1}^{\mathrm{i}-1} N_\mathrm{i}N_\mathrm{j}C_\mathrm{ijk}K_\mathrm{ij} + \sum_{\mathrm{j}=1}^{N} N_\mathrm{k}N_\mathrm{j}K_\mathrm{kj}D_\mathrm{jk}\ . \qquad (2.37)$$

This was one part of rewriting the algorithm. For the other part we regard the second term of the last expression, especially the term $\mathrm{i} = \mathrm{k}-1$. We can rewrite this term as follows,

$$\begin{aligned}
&\sum_{\mathrm{j}=1}^{\mathrm{k}-2} N_{\mathrm{k}-1}N_\mathrm{j}C_{\mathrm{k}-1,\mathrm{j},\mathrm{k}}K_{\mathrm{k}-1,\mathrm{j}} \\
&= \sum_{\mathrm{j}=1}^{\mathrm{k}-c_e} N_{\mathrm{k}-1}N_\mathrm{j}C_{\mathrm{k}-1,\mathrm{j},\mathrm{k}}K_{\mathrm{k}-1,\mathrm{j}} + \sum_{\mathrm{k}-c_e+1}^{k-2} N_{\mathrm{k}-1}N_\mathrm{j}C_{\mathrm{k}-1,\mathrm{j},\mathrm{k}}K_{\mathrm{k}-1,\mathrm{j}} \\
&= \sum_{\mathrm{j}=1}^{\mathrm{k}-c_e} N_{\mathrm{k}-1}N_\mathrm{j}\frac{m_\mathrm{j}}{m_\mathrm{k}-m_{\mathrm{k}-1}}K_{\mathrm{k}-1,\mathrm{j}} + \sum_{\mathrm{k}-c_e+1}^{\mathrm{k}-2} N_{\mathrm{k}-1}N_\mathrm{j}C_{\mathrm{k}-1,\mathrm{j},\mathrm{k}}K_{\mathrm{k}-1,\mathrm{j}} \\
&= \sum_{\mathrm{j}=1}^{\mathrm{k}-2} N_{\mathrm{k}-1}N_\mathrm{j}K_{\mathrm{k}-1,\mathrm{j}}E_\mathrm{jk} \\
&= \sum_{\mathrm{i}=1}^{N}\sum_{\mathrm{j}=1}^{N} N_\mathrm{i}N_\mathrm{j}K_\mathrm{ij}E_{\mathrm{j},\mathrm{i}+1}\theta\left(\mathrm{k}-\mathrm{j}-\frac{3}{2}\right)\delta_{\mathrm{i},\mathrm{k}-1}\ . \qquad (2.38)
\end{aligned}$$

In this Equation the matrix E is given by

$$E_\mathrm{jk} = \begin{cases} \frac{m_\mathrm{j}}{m_\mathrm{k}-m_{\mathrm{k}-1}} & \text{if } \mathrm{j} \le \mathrm{k}-c_e, \text{ and} \\ \left[1-\frac{m_\mathrm{j}+m_{\mathrm{k}-1}-m_\mathrm{k}}{m_{\mathrm{k}+1}-m_\mathrm{k}}\right]\theta\left(m_{\mathrm{k}+1}-m_\mathrm{j}-m_{\mathrm{k}-1}\right) & \text{if } \mathrm{j} > \mathrm{k}-c_e\ . \end{cases}$$

With these two reformulations the coagulation equation can be written in the form

$$\dot{N}_\mathrm{k} = \sum_{\mathrm{ij}} N_\mathrm{i}N_\mathrm{j}K_\mathrm{ij}M_\mathrm{ij}\ , \qquad (2.39)$$

wherein the new coagulation matrix M is given by

$$M_{\mathrm{ij}} = \frac{1}{2}\delta_{\mathrm{ij}} C_{\mathrm{ijk}} + C_{\mathrm{ijk}} \Theta\left(\mathrm{k} - \mathrm{i} - \frac{3}{2}\right) \Theta\left(\mathrm{i} - \mathrm{j} - \frac{1}{2}\right) + \delta_{\mathrm{ik}} D_{\mathrm{ji}} + \delta_{\mathrm{i,k-1}} E_{\mathrm{j,i+1}} \Theta\left(\mathrm{k} - \mathrm{j} - \frac{3}{2}\right) \ .$$

In this expression $\Theta(x)$ denotes the Heaviside distribution, which is zero for $x < 0$ and unity for $x > 1$.

The last equation is easily implemented into computer codes. This formulation of the coagulation equation circumvents all problems of numerical accuracy by simply altering the coagulations matrix. Hence, no additional computational time is required.

2.4.4 Implicit differencing

If fragmentation is included into the simulations then the limiting time step for the coagulation/fragmentation process tends to be small. Fragmentation leads to a permanent amount of small particles. Small particles, however, are associated with short time scales. Taking these short time scales into account, the time step of the numerical simulation can not be chosen to be very large. This argumentation only holds for explicit numerical solvers. For this reason we have implemented an implicit solver for the coagulation/fragmentation equation which we will describe in the following.

The coagulation/fragmentation equation can be written in the form

$$\dot{\bar{f}} = \bar{F}(\bar{f}) \ , \tag{2.40}$$

where $\bar{f}$ denotes the particle distribution vector on the mass grid and the function $\bar{F}$ describes the time evolution. In one time step Δt at a certain time t, we want to calculate the new particle distribution $\bar{f}_n = \bar{f}(t + \Delta t)$ from the old distribution $\bar{f}_o = \bar{f}(t)$. Therefore we rewrite Eq. (2.40) as

$$\bar{\epsilon} = \Delta t \bar{F}(\bar{f}_i), \tag{2.41}$$

where $\bar{\epsilon} = \bar{f}_n - \bar{f}_o$ and $\bar{f}_i = \xi \bar{f}_o + (1 - \xi)\bar{f}_n$. The time evolution of the function $\bar{f}$ with $\xi = 1$ is called "explicit", while the time evolution with $\xi = 0$ is usually called "implicit". Choosing $\xi = 0$ in our case, we can perform a Taylor expansion of the right-hand side of Eq. (2.41) which leads to

$$\bar{\epsilon} = \Delta t \bar{F}(\bar{f}_o) + \Delta t \tilde{J} \bar{\epsilon} \ . \tag{2.42}$$

The Matrix $\tilde{J}$ denotes the Jacobi matrix which is definded as $\tilde{J}_{ij} = \partial F_i / \partial f_j$. Solving Eq. (2.42) for $\bar{\epsilon}$ leads to

$$\bar{\epsilon} = \left[1 - \Delta t \tilde{J}\right]^{-1} \Delta t \bar{F}(\bar{f}_o) \ . \tag{2.43}$$

Hence, the evolution of the implicit time step reduces to a solution to a matrix equation which can be done easily.

I remark two points here. First, even though this implicit differencing scheme appears to be rather simple, there are several technical pitfalls which may trouble even an experienced programmer. For example, instead of solving for the difference vector $\bar{\epsilon}$, one could also directly solve for the new distribution function $\bar{f}_n$. However, this usually leads to numerical instabilities and unphysical particle distribution functions.[1] Second, since the mass grid on which the coagulation calculations are based on can range over 30 orders of magitude

[1] It took several weeks to recognize this pitfall, which reminds of the nice saying: The difference between 'Try' and 'Triumph' is just a little 'umph'.

in mass, the coagulation equation matrix elements also vary extremely. In order to invert the matrix with sufficient numerical accuracy, the matrix has to be preconditioned. Online *Lapack* routines intrinsically provide this feature. Nevertheless, even with preconditioning schemes, numerical mistakes in matrix inversions are the most common reason for numerical instabilities. Smaller mass grids and more grid points usually solve this problem.

While the Podolak algorithm can be easily formulated implicitly, this task is challenging for the Dullemond & Dominik algorithm. This is mainly due to the renormalisation scheme described by Eq. (2.26). While the coagulation matrix of the Podolak algorithm can be rewritten analytically to avoid numerical accuracy problems, the Dullemond & Dominik algorithm requires a distinction of cases if the renormalisation is actually needed or not. This differentiation is complicated – if not impossible – to include into an implicit coagulation algorithm. Thus, we chose the Podolak algorithm as a basis for our dust evolution models.

2.4.5 Vertical integration

Coagulation and fragmentation are local processes. This means that the equations described in the last section have to be solved for every point in space. The more space grid points are considered the more time-consuming the computer simulations become. However, under certain conditions the situation simplifies. In the following we describe a scheme that can save a remarkable amount of computational time.

We consider the coagulation/fragmentation equation at a certain space point z_p

$$\dot{N}_\mathrm{k}(z_\mathrm{p}) = \sum_\mathrm{ij} G_\mathrm{ijk}(z_\mathrm{p}) N_\mathrm{i}(z_\mathrm{p}) N_\mathrm{j}(z_\mathrm{p}) \; . \tag{2.44}$$

Since we are interested in particle growth in protoplanetary disks we can adapt the number densities to this special problem. We assume that at any given time the vertical particle distribution of any given particle size is given by a settling-mixing equilibrium distribution. This leads to a density N_i of a particle of size a_i which depends on the height above the midplane z as

$$N_\mathrm{i}(z) = \frac{\omega_\mathrm{i}}{\sqrt{2\pi} h_\mathrm{i}} \exp\left[-\frac{1}{2} \left(\frac{z}{h_\mathrm{i}} \right)^2 \right] \; . \tag{2.45}$$

In this expression the variable h_i denotes the dust scale height of the particles with mass m_i. The quantity ω_i is the surface number density of the particles with that certain mass. Inserting Eq. (2.45) into Eq. (2.44) and integrating over height above the midplane z yields

$$\dot{\omega}_\mathrm{k} = \sum_\mathrm{ij} \omega_\mathrm{i} \omega_\mathrm{j} \sum_\mathrm{p} \frac{G_\mathrm{ijk}(z_\mathrm{p})}{2\pi h_\mathrm{i} h_\mathrm{j}} \exp\left[-\frac{1}{2} \left(\frac{z_\mathrm{p}}{h_\mathrm{i}} \right)^2 \right] \exp\left[-\frac{1}{2} \left(\frac{z_\mathrm{p}}{h_\mathrm{j}} \right)^2 \right] \Delta z_\mathrm{p} \; . \tag{2.46}$$

If we define

$$\tilde{G}_\mathrm{ijk} = \sum_\mathrm{p} \frac{G_\mathrm{ijk}(z_\mathrm{p})}{2\pi h_\mathrm{i} h_\mathrm{j}} \exp\left[-\frac{1}{2} \left(\frac{z_\mathrm{p}}{h_\mathrm{i}} \right)^2 \right] \exp\left[-\frac{1}{2} \left(\frac{z_\mathrm{p}}{h_\mathrm{j}} \right)^2 \right] \Delta z_\mathrm{p} \; , \tag{2.47}$$

then the integrated coagulation equation can be written as

$$\dot{\omega}_\mathrm{k} = \sum_\mathrm{ij} \omega_\mathrm{i} \omega_\mathrm{j} \tilde{G}_\mathrm{ijk} \; . \tag{2.48}$$

In this way we have integrated the z-dimension out without a single approximation, only with the assumption that the vertical redistribution goes faster than the coagulation/fragmentation

process. This reformulation of the coagulation equation has an obvious advantage. Instead of solving the coagulation equation at every point in z, Eq. (2.48) enables us to describe the growth of dust for every height above the midplane simultaneously. If we assume a vertical grid with 60 grid points the vertical integration speeds up the computer simulation routine by a factor of 60. We only need to evaluate the kernel at every z once, i.e. at the start of the simulation, and integrate it over z to obtain $\tilde{G}_{\rm ijk}$, and then for the rest of the simulation we only solve the coagulation equation (2.48).

Chapter 3

Radial drift of solid particles

The main subject of this thesis is the agglomeration and growth of dust particles. But before we come to this topic, it is inevitable to discuss the radial motion of solid particles in disks first. This is because radial particle motion is strongly associated with particle growth. Radial drift speeds strongly depend on the dust particle radius. Particles of unequal size, hence, have a relative radial drift velocity. This leads to particle collisions and, hence, to dust coagulation. However, relative radial speeds can be as high as 100 m/s. Particle growth at these collision velocities is improbable and radial motion may also lead to dust particle fragmentation. We will later find, that high speed collisions caused by relative radial motion are the main reason for severe particle destruction in low turbulent disks. Even though radial motion can trigger particle growth in some cases, radial drift of solid particles will turn out to be a grave obstacle for planetesimal formation.

Another implication of radial particle drift is the loss of solid material. Particles drift into the inner regions of the disk where the temperature is very high. Around this inner disk rim, the temperature is sufficient to evaporate solid material which leads to a continuous loss of solid particles. After a certain time which is of the order of a few Myrs, the remnant disk contains not enough solid material to form planets. For example, in Sec. 4 we will find, that only ~ 1 % of the dust is still present in the disk after 1 Myr. At present, it appears that either the radial drift of solid material in disks is smaller than predicted by dust evolution models, or planets – or at least planetary precursores – indeed form over time scales of significantly less than ~ 10 Myrs. A recent observation of a 10 Jupiter mass planet around TW Hydrae (Setiawan et al. 2008), i.e. a planetary system with an age of less than 10 Myrs, suggests that rapid planet formation is indeed possible. Numerical simulations of dust in MRI driven turbulent disks also hint towards rapid planetesimal formation. Johansen et al. (2007) have shown that gravitationally bound clumps of the mass of Ceres can form within only a few orbits.

Interestingly, there is another problem related to the radial drift of solid particles in disks with ages of several Myrs. Millimeter and sub-millimeter observations have shown the presence of large amounts of millimeter to centimeter-sized grains in the outer regions ($\sim$ 100 AU) of disks around Herbig Ae and T Tauri stars (Testi et al. 2003; Rodmann et al. 2006; Wilner et al. 2005; Natta et al. 2007b). The presence of these grains, which are much larger than the grains typically found in the interstellar medium, is often regarded

as evidence that the first steps of planet formation are taking place in these disks. The presence of such large grains, however, also poses a major problem. As already mentioned above, dust grains undergo a rapid radial drift (Whipple 1972; Weidenschilling 1977a), which causes them to disappear from the outer disk in a very short time (Takeuchi & Lin 2005; Klahr & Bodenheimer 2006; Alexander & Armitage 2007). According to simple theoretical considerations, mm-cm size dust particle should drift into the inner regions of the disk over times of the order of $\sim 10^4$ yrs. However, the typical age of protoplanetary disks that are observed at millimeter wavelengths is a few million years, which is much longer than this radial drift time scale. Takeuchi & Lin propose that the grains could be the collision products of a population of even larger bodies ($\gtrsim$ 10 m) which do not undergo radial drift. However, this explanation requires that in addition to the grain population that is observed at mm wavelengths, there is a population of larger bodies which act as a reservoir of solid material from which mm/cm-sized grains are continuously produced. The problem is that if the drift time scale is, for example, 20 times shorter than the disk life time, this reservoir of larger bodies must contain at least 20 times more mass than the observed dust mass. If it is assumed that the particle size distribution follows a powerlaw then the total mass of the disk and the minimum upper particle size of this distribution can directly be calculated from the slope of the mm flux of the protoplanetary disk. This analysis shows that the amount of dust responsible for the millimeter fluxes of these disks is in many cases already very high, of the order of $10^{-3} M_\odot$ or even higher (Testi et al. 2003; Natta et al. 2004; Wilner et al. 2005; Rodmann et al. 2006; Rodmann 2006). A 20 times more massive reservoir of larger (non-observable) bodies is then clearly unrealistic. These arguments suggest that perhaps the standard theoretical estimate of the radial drift may be not applicable.

The goal of this chapter is to study the radial drift of solid particles in more detail. We will introduce the equations which describe radial particle drift and which we will use to predict particle coagulation in the further part of this thesis. Moreover, we will investigate the magnitude of the radial drift problem described above, and which effects might keep the dust grains for a few Myrs in the outer parts of the disk. In order to demonstrate the physics behind the calculations and its implications on the radial drift velocities we will proceed in certain steps. In every step, more effects are included to demonstrate the influence on the drift velocities (cf. Fig. 3.1). In the first step we will review the radial drift of individual particles in a gaseous disk (Whipple 1972; Weidenschilling 1977a). These results are valid when the dust and the gas are well mixed. This section will show that the drift time scale of such particles is orders of magnitude smaller than the age of the disks observed (5 to 10 Myrs). In a second step, we explore the possibility that collective effects of the dust might slow down the drift. Collective effects take place when the dust settles into a thin midplane layer (Dubrulle et al. 1995; Garaud et al. 2004; Schräpler & Henning 2004). This can happen if either the disk is low turbulent or large particles are considered. This process increases locally the dust-to-gas ratio, and the dynamics of the dust starts to affect the gas motion (Nakagawa et al. 1986; Johansen et al. 2006a). This may, in turn, reduce the relative velocities between the dust and the gas, and hence reduce the head wind that causes radial drift. We will investigate the magnitude of the reduction and if thin midplane layers yield a possibility to increase the drift time scales to some Myrs. In the third step we improve on these calculations by including vertical angular momentum exchanges in the disk through turbulent viscosity. In order to do so, we numerically solve the Navier Stokes equation, i.e. a system of four coupled differential equations which describes the motion of fluids including viscosity. Finally, we speculate on other potential ways in which mm/cm-sized grains could be prevented from drifting inward on a time scale shorter than the life time of the disk:

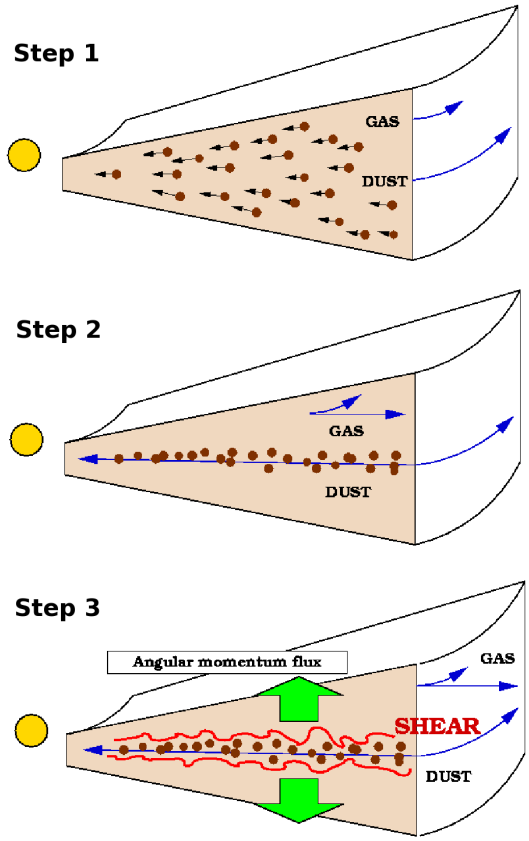

Figure 3.1: This figure shows the three scenarios we will investigate in this part of the thesis. In step 1, we consider the radial drift of individual particles. The results of this section is valid when the gas and the dust are well mixed. In step 2, we investigate the influence of collective effects on the particle drift. These effects become of importance if the particles settle into a thin midplane layer. This may occur when low turbulent disks or large dust particles are considered. Finally, in step 3 we will investigate what happens if we include turbulent viscosity in our simulations. In this case, angular momentum is exchanged between the dusty midplane layer and the gaseous layers above the midplane. The horizontal arrows indicate the radial velocity of gas and dust. The curved arrows indicate the azimuthal velocities.

particle trapping in vortices and gas pressure maxima (Barge & Sommeria 1995; Klahr & Henning 1997; Fromang & Nelson 2005; Johansen et al. 2006b), spiral arms (Rice et al. 2004) and photoevaporation of the gas leaving the dust behind (Alexander et al. 2006).

Over the last decades, various papers determined the radial drift of dust particles which necessarily also involves the investigation of the structure and dynamics of thin midplane dust layers. In particular the latter problem has attracted much attention, but for an entirely different reason than ours: Gravitational instabilities in thin midplane dust layers are thought to be a possible origin of planetesimals (Goldreich & Ward 1973). A lively debate has since appeared about the viability of this concept, spurring various papers including models of midplane dust layers (Weidenschilling 1980; Sekiya 1998; Weidenschilling 2006; Youdin & Shu 2002; Youdin & Chiang 2004; Johansen et al. 2006a). The richness of this literature gives an indication of the complexity of the problem (cf. table 3.1). Hence, due to this complexity only a sub-set of the possible physical effects are considered in these dust layer models. In particular the collective effects of the dust and the effects of vertical and radial viscosity have not been studied yet in combination. Therefore, besides the investigation of radial drift and the mm-particle survival time problem, this chapter also presents a model of dense dust midplane layers that include a multitude of physical effects, albeit still in the form of a 1-D vertical model.

3.1 Step 1 - Radial drift of individual particles

3.1.1 Equations

The fundamental cause for inward drift of the dust is the difference in azimuthal velocity between gas and dust. While the dust moves with Keplerian velocity the gas moves slightly sub-Keplerian. This is due to the fact that the gas is not only affected by the gravitational and the centrifugal force but additionally feels a radial pressure force that does not act on dust particles. This extra force is caused by the decrease of gas pressure in the radial direction. Since this force, which exclusively acts on the gas, partly compensates gravitation, the gas moves slower than Kepler speed and therefore slower than any dust particle in the disk. Hence, the dust particle feels a continuous headwind from the gas. This headwind causes the dust particle to lose its angular momentum and to spiral inward.

Whipple (1972) formulated the first equations for the radial drift of very small and very large particles. Weidenschilling (1977a) later derived a set of equations with a general drag force to calculate the radial drift of solid particles of any size. We will introduce all equations in the dimensionless Stokes number formulation which was described in the introduction. Just to remind, the Stokes number mirrors the coupling between the dust and the gas and it can be regarded as a measure of grain size (see Fig. 3.2). In terms of this dimensionless formulation, the radial drift equations of dust aquire the form

$$\begin{aligned} 0 &= \frac{w_\varphi}{\mathrm{St}} + \frac{w_r}{2} \,, \\ 0 &= w_\varphi^2 + v_\mathrm{N} w_\varphi + \frac{w_r^2}{4} \,. \end{aligned} \tag{3.1}$$

The variables w_r and w_φ denote the radial and azimuthal velocity of the dust, respectively. The form of the drag law is implicitly included in the Stokes number. The quantity v_N is the velocity by which the gas moves azimuthally slower than Keplerian velocity V_k, i.e. $v_\mathrm{gas} = V_\mathrm{k} - v_\mathrm{N}$. The velocity v_N will also turn out to be the maximum radial drift velocity

	Vertical structure of the gas	Vertical structure of the dust	Viscosity of the gas	Viscosity of the dust in r	Viscosity of the dust in φ	Kind of turbulence	Considering the q degeneracy	Solving continuity eq. in radial direction	Drag force	Considering vertical oszillations of dust	Individual particles drift	Backreactions / collective effects	Vertical angular momentum transport	Gas evaporation	Dust particle regime
Weidenschilling (1977a)	-	-	-	-	-	-	-	-	B	-	x	-	-	-	all
Nakagawa et al. (1986)	x	x	-	-	-	-	-	-	B	x	x	x	-	-	all
Takeuchi & Lin (2002)	x	x	x	-	-	α	-	-	E	-	x	-	x	-	Epstein
Youdin & Shu (2002)	-	x	(x)	(x)	(x)	SI	-	x	E	-	x	-	x	-	St$\ll 1$
Youdin & Chiang (2004)	-	x	(x)	(x)	(x)	SI	-	x	E	-	x	x	x	-	St$\ll 1$
Takeuchi et al. (2005)	-	-	x	x	-	α	-	x	E	-	x	-	x	x	St$\ll 1$
Takeuchi & Lin (2005)	-	-	x	x	-	α	-	x	E	-	x	-	x	-	Epstein
Weidenschilling (2006)	-	x	(x)	-	(x)	SI	x	-	B	-	x	x	x	-	all
Johansen et al. (2006b)	x	x	(x)	(x)	(x)	MRI	n.a.	-	B	x	x	x	(x)	-	all
Brauer et al. (2007)	x	x	x	x	x	α	x	-	E	-	x	x	x	-	Epstein

Table 3.1: This table lists various effects that were investigated in the last decades affecting the radial drift of dust particles. The shortcuts α and SI indicate the general α prescription by Shakura & Sunyaev (1973) and the Self-induced turbulence due to vertical shear (Weidenschilling 1979; Cuzzi & Weidenschilling 2006), respectively. MRI stands for magneto rotational instability (Balbus & Hawley 1991). The letter E denotes the Epstein regime, B(oth) indicates that the Epstein regime as well as the Stokes regime were taken into account. Tokens in parathesis indicate that this effect is included implicitly. We remark that collective effects between the gas and the dust together with vertical exchange of angular momentum using a general α-pescription was never investigated before.

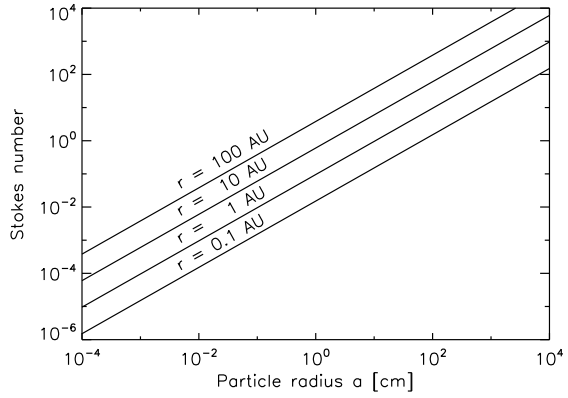

Figure 3.2: The Stokes number St as a function of particle radius a at different radii in the disk. In this calculation the solid particle density of the dust is 1.6 g/cm^3 and the stellar mass is 0.5 $M_\odot$. The innner and the outer radius of the disk are 0.03 AU and 150 AU, respectively. The disk mass is $10^{-2} M_\odot$.

of the dust. We will take v_N from here on as our "standard velocity" scale apart from the Keplerian velocity V_k. The quantity v_N is given by (Weidenschilling 1977a; Nakagawa et al. 1986)

$$v_\mathrm{N} = \eta V_\mathrm{k} = -\frac{\partial_\mathrm{r} p_\mathrm{g}}{2\rho_\mathrm{g} r \Omega_\mathrm{k}^2} V_\mathrm{k} = \frac{c_\mathrm{s}^2}{2V_\mathrm{k}} \left(\frac{3}{2} + \frac{\xi}{2} + \delta \right) . \tag{3.2}$$

The quantity η is the ratio between the radial pressure force and the radial gravity force. The pressure is assumed to be $p_\mathrm{g} = \rho_\mathrm{g} c_\mathrm{s}^2$. We adopt a disk temperature profile of $\xi = 1/2$ which corresponds to a passively irradiated disk. A power law index of $\delta = 0.8$ (Kitamura et al. 2002; Andrews & Williams 2007) the leads to

$$v_\mathrm{N} = 1.28 \, \frac{c_\mathrm{s}^2}{V_\mathrm{k}} . \tag{3.3}$$

Note that the velocity scale v_N does not depend on the disk mass. In our disk model this quantity is also not dependent on the location r in the disk. This is easily seen by

$$\frac{c_\mathrm{s}^2}{V_\mathrm{k}} \propto \frac{T}{r^{-1/2}} \propto \frac{r^{-1/2}}{r^{-1/2}} \propto 1 . \tag{3.4}$$

The set of equations (3.1) is generally difficult to solve and only numerical methods provide information about the drift velocity. However, in some cases the situation simplifies. If the Stokes number is not dependent on the particle velocity, the equations (3.1) can be solved analytically. Assuming this independency, a straightforward calculation yields

$$w_r = \frac{2}{\mathrm{St} + \frac{1}{\mathrm{St}}} v_\mathrm{N} . \tag{3.5}$$

This equation directly shows that the drift velocity has a maximum when the Stokes number is unity and the maximal drift velocity is v_N. The drift velocity as a function of Stokes number is shown in Fig. (3.3). If we adopt a sound speed of $c_\mathrm{s} = 860$ m/s corresponding to

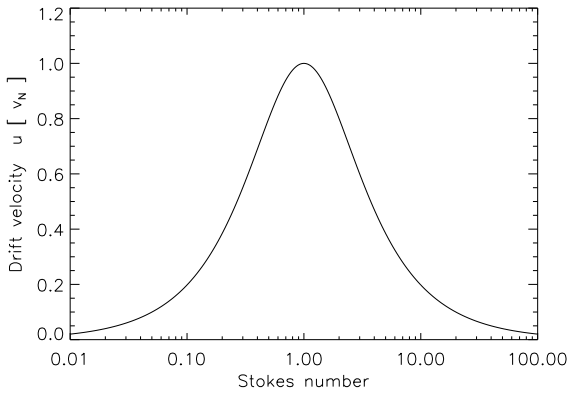

Figure 3.3: The radial drift velocity of individual particles w_r in units of $v_{\rm N}$ as a function of Stokes number.

a temperature of 204 K and a Kepler velocity of 21 km/s at 1 AU for a central star of half a solar mass, then the maximum drift velocity is given by 45 m/s.

The radial particle drift velocity is directly proportional to the radial pressure gradient (cf. Eq. 3.2). If a smooth disk is assumed, i.e. a disk which involves no local gas density fluctuations, no velocity maxima or dust particle enhancements, then the radial drift velocity is a constant throughout the disk and of the order of $\sim$ 100 m/s. However, as far as we know today, disks have to be turbulent in order to explain the observed mass accretion onto the central star (Gullbring et al. 1997; Hartmann et al. 1998). Turbulence can lead to gas density fluctuations and, hence, to pressure maxima. These fluctuations may change the local particle drift behaviour significantly. Johansen et al. (2006b) have shown that local gas pressure fluctuations may reduce the radial drift speed by 40% in average. Temporary speed reductions of more than 90% were observed in the simulations. Moreover, some regions in the disk can show constant pressure maxima independent of the amount of turbulence in the disk. Evaporation fronts in the inner parts of the disk – for example the Snow line – can involve gas density jumps associated with pressure maxima. Theoretical modeling of evaporation fronts predicts radial *outward* drift in some parts of the disk which can even lead to dust grain retention (Kretke & Lin 2007). We will discuss the effect of gas pressure maxima in the last part of this thesis, and their influence on planetesimal formation.

3.1.2 Drift time scales for individual particles

We focus on the radial drift times of individual particles in the outer parts of the disk. More specifically, we are interested in the conditions on particle radius and particle porosity that provide time scales larger than a few Myrs.

The drift timescale $\tau_{\rm drift}$ equals

$$\tau_{\rm drift} = \frac{r}{w_r} \, , \tag{3.6}$$

which should correspond to the age $\tau_{\rm age}$ of the disks observed, thus a few Myrs. While calculating the radial drift time scales, we focus on the radius of $r = 100$ AU. To find the critical Stokes numbers for which the radial drift time scale equals the age of the disk, we replace $\tau_{\rm drift}$ in Eq. (3.6) by $\tau_{\rm age}$. We then insert Eq. (3.5) into Eq. (3.6), and solve for St.

This yields two critical Stokes numbers:

$$\mathrm{St}_{\pm} = \frac{\tau_{\mathrm{age}} v_{\mathrm{N}}}{r} \pm \sqrt{\left(\frac{\tau_{\mathrm{age}} v_{\mathrm{N}}}{r}\right)^2 - 1}\,. \tag{3.7}$$

The interpretation of these two numbers is the following: If the Stokes number of the dust particle falls into the interval $[\mathrm{St}_-, \mathrm{St}_+]$, then the drift timescale is shorter than τ_{age}. If it falls outside of this interval, then the drift time scale is long enough that these particles can be observed in the protoplanetary disk of age τ_{age}. Since the Stokes number interval is a rather abstract depiction we reformulated it into a particle radius interval with a similar meaning.

The region of too short time scales at 100 AU is shown in Fig. 3.4 as a function of disk mass M_{disk} and surface density Σ. In this diagram we applied a dust material density[1] $\rho_{\mathrm{s}} = 1.6$ g/cm^3, a Kepler frequency $\Omega_{\mathrm{k}} = 10^{-10}$/s and $c_{\mathrm{s}} = 2.6 \times 10^4$ cm/s (corresponding to a temperature of 20 K). We take as the age of the disk $\tau_{\mathrm{age}} = 2$ Myrs. We will make use of these values at all times in this section unless otherwise noted. The two Stokes numbers $\mathrm{St}_{\pm}$ that are implied by these values are $\mathrm{St}_- = 0.002$ and $\mathrm{St}_+ = 474$, corresponding to the lower and upper edge of the grey zone in Fig. 3.4 respectively.

The figure shows that the particle radius interval in which the time scale of individual particles is shorter than 2 Myrs ranges over more than 5 orders of magnitude in radius. Particles ranging from mm to cm in size are completely included in this region independent of disk mass.

The Stokes number as the crucial value for radial drift is not only affected by particle radius but also by particle properties like porosity or fractal growth (Kempf et al. 2000). This effect of noncompact growth may be considered by introducing the filling factor of the particle f defined by $m_{\mathrm{p}} = V_{\mathrm{p}} \rho_{\mathrm{s}} f$, where m_{p} and V_{p} are the mass and the volume of the particle, respectively. In Fig. (3.4) we also calculated the critical particle radius interval for a filling factor of $f = 10^{-1}$ (dotted lines).

The lower filling factor shifts the critical particle radius interval towards higher particle radii. The drift time scale of mm size particles exceeds 2 Myrs when disk masses higher then 0.2 $M_\star$ are considered. For cm size particles the time scale never exceeds 2 Myrs. For filling factors lower than 10^{-3} the drift time scales of mm and cm size particles exceed 2 Myrs for any disk mass higher than 10^{-3} $M_\star$. However, particles of mass 1 g and filling factors of 10^{-3} would imply a particle diameter of 5 cm. Since this particle size falls into the regime where compaction is thought to occur (Blum & Wurm 2000) this filling factor represents an unlikely case.

3.2 Step 2 - Collective effects

The scope of the previous subsection can be expanded by including the back-reactions from the dust to the gas. We do no longer consider a single particle, but include how the entire swarm of dust particles can affect the gas motion. The modified gas motion has the effect of reducing the rate by which the gas extracts angular momentum from the dust, and thereby reduces the radial drift of the dust. Such collective effects play the strongest role for low α-values so that a thin midplane dust layer can form in which the dust density is high. This scenario of reduction of radial drift was described by Nakagawa et al. (1986).

The necessity to take this additional effect into account may be illustrated by regarding the following extreme scenario. We consider a hypothetical disk in which the dust density is

[1] 10% silicate, 30% carbonaceous material and 60% ice

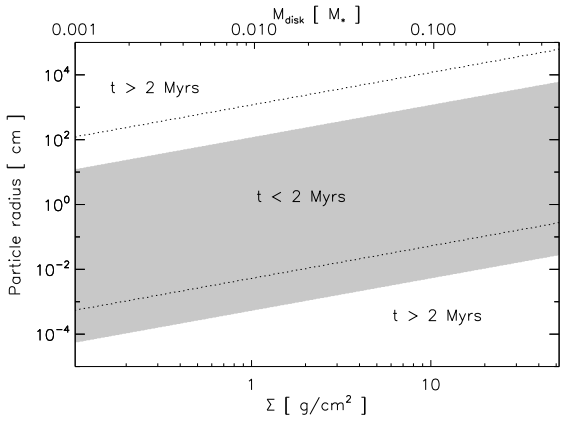

Figure 3.4: The particle radius interval in which the individual drift time scale at r =100 AU becomes shorter than 2 Myrs as a function of surface density or equivalently disk mass (shaded region) as discussed in Sec. 3.1.2. To illustrate the effect of noncompact growth we also calculated the interval for a filling factor of 10^{-1} (dotted lines).

much higher than the gas density. In such a dust-dominated disk the dust is hardly influenced by the gas. The gas, which tends to move sub-Keplerian, is dragged along with the dust since it feels a continuous tailwind of dust particles. Therefore, the gas perpetually gains angular momentum from the dust and spirals outward. The radial drift of the dust is negligible because the dust-to-gas ratio is much higher than unity. This is the reverse situation of the case described in Subsection 3.1. In general, though, we neither have a perfectly dust-dominated nor gas-dominated situation. We then have to solve the following set of equations (Nakagawa et al. 1986)

$$\begin{aligned} 0 &= 2\Omega_{\rm k} u_\varphi - A\rho_{\rm d}(u_r - w_r) - \frac{1}{\rho_{\rm g}}\partial_r p_{\rm g} \\ 0 &= -\frac{1}{2}\Omega_{\rm k} u_r - A\rho_{\rm d}(u_\varphi - w_\varphi) \\ 0 &= 2\Omega_{\rm k} w_\varphi - A\rho_{\rm g}(w_r - u_r) \\ 0 &= -\frac{1}{2}\Omega_{\rm k} w_r - A\rho_{\rm g}(w_\varphi - u_\varphi)\ . \end{aligned} \tag{3.8}$$

The quantities u and w denote the velocity of the gas and the dust in a Keplerian comoving frame, respectively. The subscripts r and φ indicate the radial and the azimuthal components of the velocities. The variables $\rho_{\rm g,d}$ denote the mass densities of gas and dust, and the quantity A is defined as $A = \Omega_{\rm k}/\rho_{\rm g}{\rm St}$. We are primarily interested in the radial dust velocity of the Nakagawa-Sekiya-Hayashi solution (NSHs) implied by Eqs. (3.8) which has the form

$$u^{\rm NSH} = \frac{2}{\psi{\rm St} + \frac{1}{\psi{\rm St}}}\psi v_{\rm N} \qquad \text{and} \qquad \psi = \frac{1}{1+\epsilon}\ . \tag{3.9}$$

The quantity $\epsilon \equiv \rho_d/\rho_g$ denotes the local dust-to-gas ratio. When $\psi \to 1$, i.e., when the dust-to-gas ratio is approaching zero, Eq. (3.9) reduces to the corresponding equation for single-particle drift, Eq. (3.5). The difference between these two equations is the additional factor ψ that modifies the Stokes number St and the maximum drift velocity $v_{\rm N}$. Since ψ is

always smaller than one, the collective radial drift of the dust will always be smaller than the individual particle drift.

Taking collective effects into account requires knowledge about the dust density. Therefore, certain disk parameters, i.e. the turbulence parameter α as well as the initial dust-to-gas ratio ϵ_0 before sedimentation, become of importance. Another dimensionless number, which now comes into play, is the turbulence parameter q. This number determines whether turbulent diffusion is realised by small turbulent eddies moving fast or by big eddies moving slow. These quantities determine the thickness of the dust layer h and, hence, the dust density. In these equations we assume that the dust density in the vertical direction has a gaussian shape. This ansatz might be put into question if the turbulence is self-induced (Weidenschilling 1979). Although Johansen et al. (2006a) showed that the vertical dust density in self-induced turbulence has a gaussian shape for canonical dust-to-gas ratios, the vertical structure can show a different shape especially when ϵ is increased for instance through photoevaporation (Weidenschilling 2006).

Since the dust density is a function of height above the midplane z, the radial drift velocities are dependent on z as well. This vertical dependency is shown in Fig. (3.5) for an exemplary NSH solution. In this calculation we applied the values $\mathrm{St} = 1$, $\alpha = 10^{-5}$, $q = 1/2$ and $\epsilon_0 = 10^{-2}$.

The plot shows that the dust moves inwards while the gas moves outwards which is generally the case in the NSH solution. In the higher regions of the disk ($|z| > 3\,h$) the dust-to-gas ratio is much smaller than unity causing the collective drift behaviour to match the individual particle drift. However, closer to the midplane of the disk collective effects become important. With increasing dust-to-gas ratio towards the midplane, the radial inward drift of the dust decreases while the gas starts to move outwards. The clear difference in velocities between the collective drift and the individual drift around the midplane along with the fact that most of the dust is located in this region demonstrates the importance of collective effects for disks with low turbulence.

The radial velocities as a function of height above the midplane do not directly tell something about the entire radial flow of the dust since the dust itself is vertically distributed in a certain way. For this reason we will now calculate the vertically averaged radial velocity of the dust. This integrated velocity is given by

$$\bar{u}^{\mathrm{NSH}} = \frac{1}{\Sigma_{\mathrm{d}}} \int_z \rho_{\mathrm{d}}(z) u^{\mathrm{NSH}}(z)\, \mathrm{d}z \; . \tag{3.10}$$

A contour plot of this quantity as a function of the turbulence parameter α and the Stokes number St is shown in Fig. (3.6). The drift velocities in this diagram were expressed in terms of the corresponding individual particle drift velocity in order to explicitly point out the differences between these two models.

The figure shows that for fixed Stokes numbers the deviation increases continuously with lower turbulence in the disk. Lower α values imply thinner dust layers and, therefore, higher dust-to-gas ratios. With higher dust-to-gas ratios the back reaction of the dust to the gas increases, and hence the deviation between individual and collective drift velocities. One obvious solution to the whole radial drift problem of grains in the outer parts of the disk would be to continuously decrease the amount of turbulence in the disk or even to set α to zero. However, Weidenschilling (1979) has shown that a shear-instability between the dust layer and the gas induces a weak, but non-negligible level of turbulence. This turbulence is called 'self-induced turbulence' which constrains the α-value to be at least of the order of $\sim 10^{-6}$ (Cuzzi & Weidenschilling 2006).

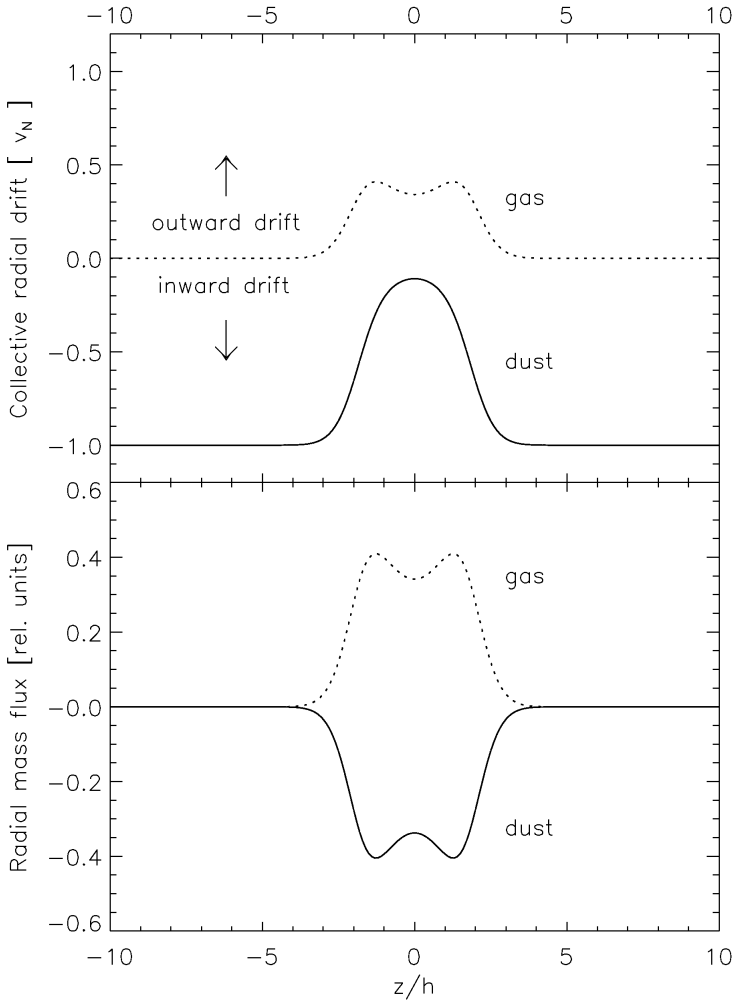

Figure 3.5: The upper figure shows the collective radial velocities of gas and dust of the laminar NSH solution in terms of $v_{\rm N}$ as a function of height above the midplane as discussed in Sec. 3.2. The lower figure shows the radial mass flux of gas and dust in arbitrary units. The values applied in this calculation are $\mathrm{St} = 1$, $\alpha = 10^{-5}$, $q = 1/2$ and $\epsilon_0 = 10^{-2}$.

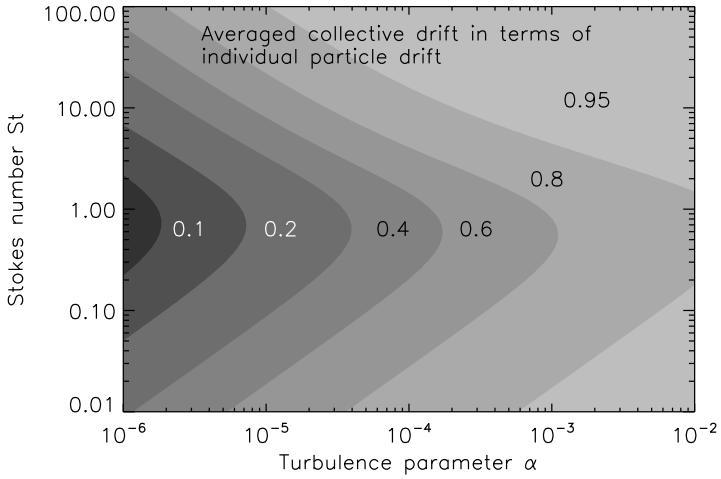

Figure 3.6: A contour plot of the vertically averaged collective radial drift velocities of the dust in terms of the individual particle drift velocity as a function of turbulence parameter α and Stokes number St as discussed in Sec. 3.2. The numbers in the diagram indicate the contour level and are related to the line on the left, respectively. The parameters for this calculation are $q = 1/2$ and $\epsilon_0 = 10^{-2}$.

For fixed α, Fig. 3.6 shows that for low Stokes numbers (small grains) the drift behavior approaches the individual particle drift. Low Stokes numbers imply thick dust layers, causing low dust-to-gas ratios. For high Stokes numbers (large grains), very thin dust layers are obtained. One would intuitively think that this maximizes the collective effects. However, as can be seen from Eq. (3.9), in the limit of $\mathrm{St} \to \infty$ one gets $u^{\mathrm{NSH}} \to 2v_{\mathrm{N}}/\mathrm{St}$ which is equal to the individual particle drift of Eq. (3.5). So for large St the radial drift indeed drops, but not due to collective effects.

For a Stokes number of unity and a turbulence parameter of 10^{-6} the dust-to-gas ratio in the midplane is given by

$$\epsilon_{\mathrm{mid}} = \epsilon_0 \frac{H}{h} = \epsilon_0 \sqrt{\frac{\mathrm{St}}{\alpha}} = 10. \tag{3.11}$$

Therefore, the collective radial drift in the midplane in terms of the individual particle drift according to Eq. (3.9) is $u^{\mathrm{NSH}}_{\mathrm{mid}}/v_{\mathrm{N}} = (1+\epsilon)^{-2} = 0.008$. However, the vertically averaged drift velocity of the dust in terms of the individual particle drift in Fig. (3.6) is only 0.07, which is almost one order of magnitude higher. The reason for this is that the largest radial dust mass flux is not in the midplane, but slightly above the midplane (see Fig. 3.5). The mass flux is the product of dust density ρ_{d} and dust radial velocity u^{NSH}. Although ρ_{d} drops strongly slightly above the midplane, the radial velocity u^{NSH} increases even faster, so that the product $\rho_{\mathrm{d}}\, u^{\mathrm{NSH}}$ has a maximum slightly above the midplane. While the formation of a dense dust layer can reduce the radial drift velocity in the midplane by a factor of 100, the vertically averaged radial drift velocity can be only reduced by a factor of at most 10.

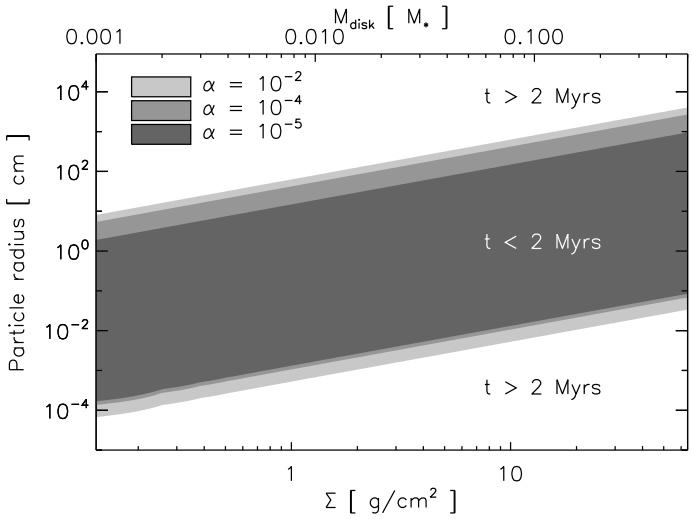

Figure 3.7: As Fig. 3.4, but now with collective effects of the dust and the gas included, at $r = 100$ AU as discussed in Sec. 3.2.1. Different grey scales are the results for different levels of turbulence, hence different thicknesses of the dust midplane layer. Note that for $\alpha = 10^{-2}$ the results are virtually identical to the single-particle case (Fig. 3.4), since in this case the dust layer is so thick that the dust-to-gas ratio is much less than unity.

3.2.1 Radial drift times including collective effects

Armed with the above drift velocity expressions we now calculate the conditions on particle radius and particle porosity that provide time scales larger than 2 Myrs taking into account collective effects.

At first we focus on the conditions on the particle radius. The interval of this particle property that corresponds to time scales shorter than 2 Myrs is shown in Fig. (3.7) for different α-parameters. The second turbulence parameter q is fixed at 1/2 at all times, the initial dust-to-gas ratio is 10^{-2} and the filling factor f is unity. All other parameters were already mentioned in the last section and are not changed throughout this part of the thesis unless directly stated.

According to this plot, the critical particle radii that provide the requested time scales hardly differ from the critical particle radii of the individual particle drift calculated in the last section. Even for small turbulence parameters which favour collective effects the time scales for mm to cm size particles are shorter than 2 Myrs for any disk mass considered. The reason for this is that for very high and very low Stokes numbers, like the two critical numbers St_- and St_+ representing the boundaries of the grey areas in Fig 3.7, collective effects play a minor role (see Fig. 3.6, and discussion in the last subsection). The Stokes numbers for which the collective effects play the strongest role lie in the middle of these grey areas, i.e. where the drift time scales are anyway much too short to be compatible with the observations of mm-sized particles in protoplanetary disks.

So what about the effects of fractal or porous growth? For simplicity we set the mass of the dust particle to be 1 g and then calculate the particle filling factor that provides time scales larger than 2 Myrs. For a filling factor of unity a dust particle of 1 g corresponds to a particle radius of 1/2 cm. For $f = 10^{-4}$ the particle radius can be calculated to be 11 cm.

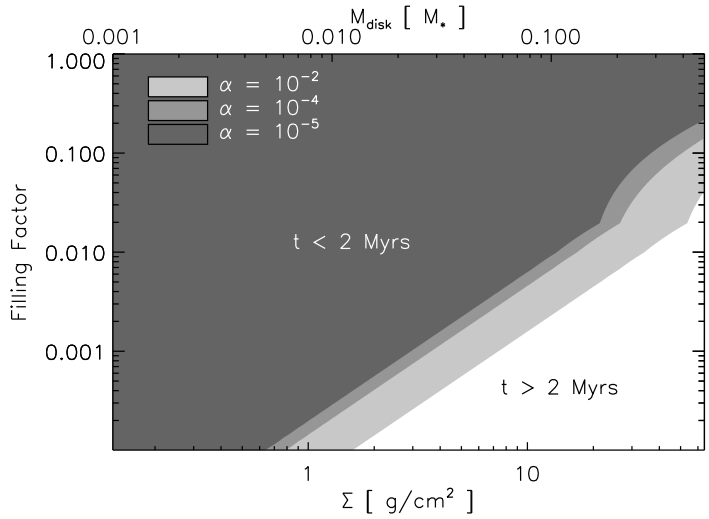

Figure 3.8: The dust particle filling factor that provides time scales larger than 2 Myrs as a function of disk mass for different turbulence parameters at $r = 100$ AU in the disk as discussed in Sec. 3.2.1. In this calculation collective effects of dust and gas are taken into account.

Like in the last paragraph we will perform the time scale calculation in dependency on the disk mass. The results of this calculation is shown in Fig. (3.8) for different values of the turbulence parameter α. This diagram shows that for filling factors lower than 10^{-2} the time scale exceeds 2 Myrs subject to the condition that the disk mass is higher than $\sim 0.2\ M_\star$. For even higher disk masses the filling factor may exceed 0.1 for certain turbulent α parameters. This filling factor corresponds to a particle radius of 1 cm. Ormel & Cuzzi (2007) showed that particle growth in protoplanetary disks can be associated with filling factors of less than $\sim 10^{-1}$. Therefore fractal growth seems to be an actual possibility to considerably increase the radial drift time scales of the dust.

3.3 Step 3 - Effect of turbulent viscosity

We will now investigate the role of turbulent viscosity in addition to the effects studied so far. Including viscosity terms will have the opposite effect on the drift velocities than the collective effects. It will increase the radial drift of the dust and shorten the drift time scales. We will give the Navier-Stokes equation (NSe) including collective effects and viscosity terms and solve these equations numerically. However, we would like to discuss first why turbulent viscosity increases the radial drift of the dust.

Under certain conditions, i.e. small turbulence parameters α or high Stokes numbers St, the previous sections have shown that the dust may settle into a thin midplane layer. When the dust-to-gas ratio inside this layer exceeds unity the gas is dragged along with the dust. Both components, dust and gas, tend to move with Keplerian velocity. Above the dust layer, however, the dust-to-gas ratio is much smaller than unity. In this region the dust particles still feel a continuous head wind which forces them to move with slightly sub-Keplerian velocity. This vertical decrease in azimuthal velocity from Keplerian velocity in the midplane to sub-Keplerian velocity in the higher regions of the disk produces a nonlinear velocity gradient in

both the gas and the dust.

Viscosity generally attempts to damp nonlinear spatial velocity differences. The vertical velocity gradient described above represents such a difference. Turbulent viscosity now acts in such a manner that it transports angular momentum from the midplane to the higher regions of the disk. While the midplane, the region where most of the dust is located, loses angular momentum and falls inward, the regions above the midplane gain angular momentum and move outward (cf. Fig. 3.1). This mechanism of vertical angular momentum exchange was first investigated by Youdin & Chiang (2004).

3.3.1 Navier-Stokes equations

The Navier-Stokes equations for this problem are basically the set of equations (3.8) plus some second order derivative terms due to the inclusion of viscosity

$$\begin{aligned}
0 &= 2\Omega_{\rm k} u_\varphi \quad - A\rho_{\rm d}(u_r - w_r) \; + \; \nu_{\rm g}\partial_z^2 u_r - \frac{1}{\rho_{\rm g}}\partial_r p_{\rm g} \\
0 &= -\frac{1}{2}\Omega_{\rm k} u_r - A\rho_{\rm d}(u_\varphi - w_\varphi) + \; \nu_{\rm g}\partial_z^2 u_\varphi \\
0 &= 2\Omega_{\rm k} w_\varphi \quad - A\rho_{\rm g}(w_r - u_r) \; + \; \frac{\nu_{\rm d}}{\rho_{\rm d}}\partial_z\left(\rho_{\rm d}\partial_z w_r\right) \\
0 &= -\frac{1}{2}\Omega_{\rm k} w_r - A\rho_{\rm g}(w_\varphi - u_\varphi) + \; \frac{\nu_{\rm d}}{\rho_{\rm d}}\partial_z\left(\rho_{\rm d}\partial_z w_\varphi\right) \; . \qquad (3.12)
\end{aligned}$$

Hence, the algebraic Eqs. (3.8) turn into four coupled, differential equations of second order. The left hand side of the Navier-Stokes equations representing the time dependencies are set to be zero since we are interested in steady state solutions. The vectors $\vec{u}$ and $\vec{w}$ denote the velocities of the gas and the dust, respectively. The first terms on the right side correspond to the Coriolis force. These terms arise from the fact that the equations are formulated in a comoving frame. The second term represents the drag force coupling between the gas and the dust. The effects of viscosity show up in the third terms. The expressions for the viscosity of the gas and the dust were introduced in the introduction. In the following we will denote viscosity terms which involve derivatives of radial (azimuthal) velocities as 'radial (azimuthal) viscosity terms'. The very last term in the first line is an extra force acting on the gas which is caused by a radial pressure gradient. This term is responsible for the gas moving slower than the dust and causes the radial drift. The densities of gas and dust serve as input for the Navier-Stokes equations.

Takeuchi & Lin (2002) also investigated the effect of gas viscosity on the drift of dust particles, but they neglected collective effects. This allowed to solve the equations analytically. The drift of the dust particles in their calculations was a superposition of two different effects: The individual dust particle velocity with respect to the gas and the velocity of the gas itself. The former part of the dust particle drift was discussed in detail in Section 3.1. The second part of the dust particle drift investigated by Takeuchi and Lin was due to the gas accretion process. This process of the gas is associated with a certain radial accretion velocity. Since the dust is to some extent coupled to the motions of the gas the dust is carried along with the accreting gas which leads to an extra source of radial particle drift.

In the beginning of this section we described that gas viscosity also increases the radial drift of the dust when collective effects come into play, i.e. when the dust settles into a thin midplane layer and starts to affect the motions of the gas. This process is different from the single particle considerations discussed by Takeuchi and Lin since it is caused by collective

effects and not by gas accretion. In the following, we estimate the ratio of these two radial drift velocities.

The additional drift due to the accretion process may be estimated by a characteristic accretion velocity of the gas which is given by $v_{\rm acc} \propto \alpha c_{\rm s}^2/V_{\rm k}$ (Shakura & Sunyaev 1973). Viscous collective effects imply drift velocities of order $v_{\rm coll} = c_{\rm s}^3/V_{\rm k}^2 \epsilon_0 {\rm Re}^\star$ (Weidenschilling 2003). The ratio

$$\xi = \frac{v_{\rm acc}}{v_{\rm coll}} = \alpha \epsilon_0 {\rm Re}^\star \frac{V_{\rm k}}{c_{\rm s}} \tag{3.13}$$

has values of at most $\approx 10^{-1}$ for[2] $\alpha = 10^{-2}$, $\epsilon_0 = 10^{-2}$, ${\rm Re}^\star = 10^2$, $V_{\rm k} = 3 \times 10^5$ cm/s and $c_{\rm s} = 3 \times 10^4$ cm/s. For smaller turbulence parameters which we will consider here the influence of gas accretion will be even lower.

3.3.2 Numerical results

The parameters for the simulation are St = 1.2, $\alpha = 10^{-6}$, $q = 1/2$, $\epsilon_0 = 10^{-2}$. The results are shown in Fig. 3.9. The two parameters α and St are chosen in a way that effects of viscosity become visible. These values imply a dust-to-gas ratio of 5 in the midplane of the disk and a half thickness of the dusty midplane layer which is $\approx 0.002\ H$. The turbulent motions of the gas have a speed of $0.005\ v_{\rm N}$. The dotted lines in the Fig. 3.9 indicate the analytical solution of the laminar NSH equations ($\nu = 0$) which were discussed in the last section. The solid lines in Fig. 3.9 indicate the numerical solution including viscosity which differs significantly from the NSH solution.

Let us focus on the radial dust velocity since we are primarily interested in radial drift time scales. The radial flow of the dust is significantly affected by turbulent viscosity if α is smaller than 10^{-4}. In this regime the effect is largest for Stokes numbers ≈ 5. For $\alpha > 10^{-4}$ the radial flow is approximately the flow predicted by Nakagawa et al. and viscosity seems to play a minor role. The radial dust velocities in the midplane with and without viscosity terms may differ by a factor of 5 for small α parameters and St ≈ 5.

The azimuthal dust and gas velocities as a function of height above the midplane vary in a complex manner. However, for Stokes numbers smaller than unity the situation with regard to the azimuthal velocities simplifies. In this regime these velocities do hardly differ from the expression given by Nakagawa et al. and viscosity seems to be negligible. The radial outflow of the gas, which is shown in Fig. (3.9), is reduced if turbulent viscosity is included. This decrease may be up to a factor of 30 for small St and α parameters. For turbulence parameters higher than 10^{-4} the radial net outflow of the gas differs less than 10% from the outflow predicted by the NSH equations.

3.3.3 Width of the azimuthal gas velocity layer

The calculation of radial drift velocities in protoplanetary disks including collective effects and effects of viscosity are a challenging topic. Most equations can not be solved analytically and only numerical solutions provide information on the evolution of these disks. Therefore, disk model simplifications often come into play.

One simplification is that the dust sub-disk is assumed to be extremely thin and thought to behave, to some extent, like a solid disk. This approximation is called "plate drag approximation" (Goldreich & Ward 1973). Under this condition, the gas layer above the dust layer can be described by an Ekman layer: The gas in the midplane is forced to move along

[2] Estimated values at 100 AU

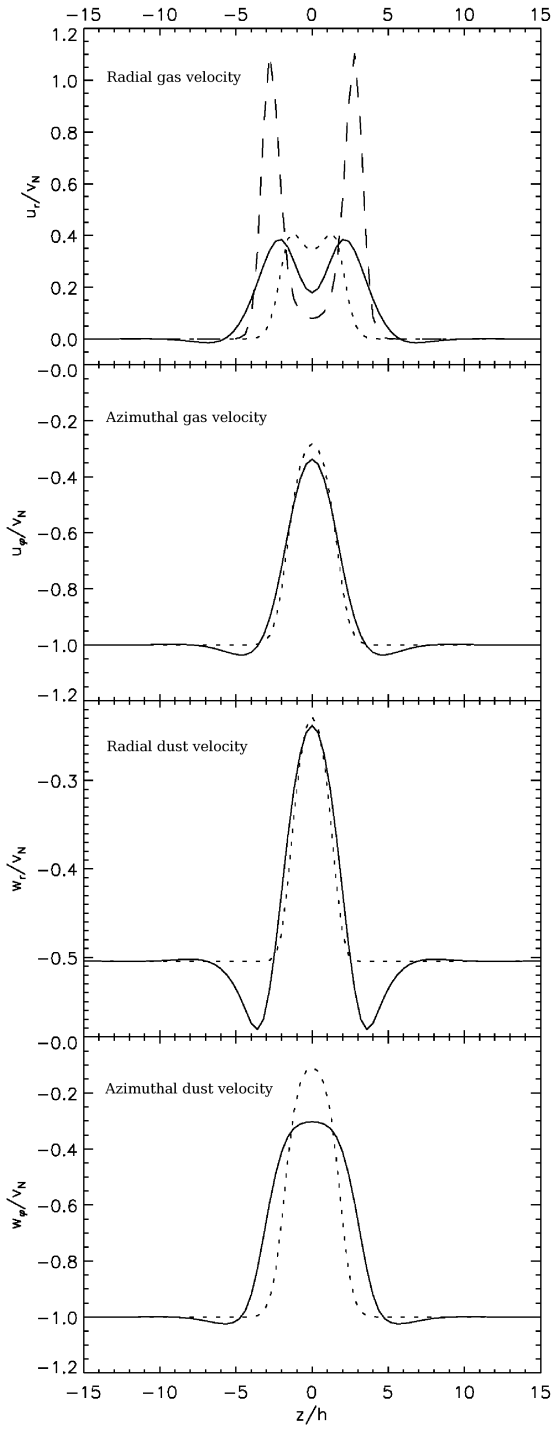

Figure 3.9: The azimuthal and radial gas and dust velocities as a function of height above the midplane as discussed in Sec. 3.3.2. The dotted lines denote the analytical normalised NSH solution without viscosity ($\nu = 0$) as discussed in Section 3.2. The solid lines indicate the numerical solution of the Navier-Stokes equations including azimuthal and radial viscosity terms. The dashed line in the top diagram shows the radial velocity of the gas if radial viscosity terms are neglected. The values for this simulation are St $= 1.2$, $\alpha = 10^{-6}$, $q = 0.5$ and $\epsilon_0 = 0.01$. Note that more than 80% of the dust in within the $z-$interval $[-2h, 2h]$.

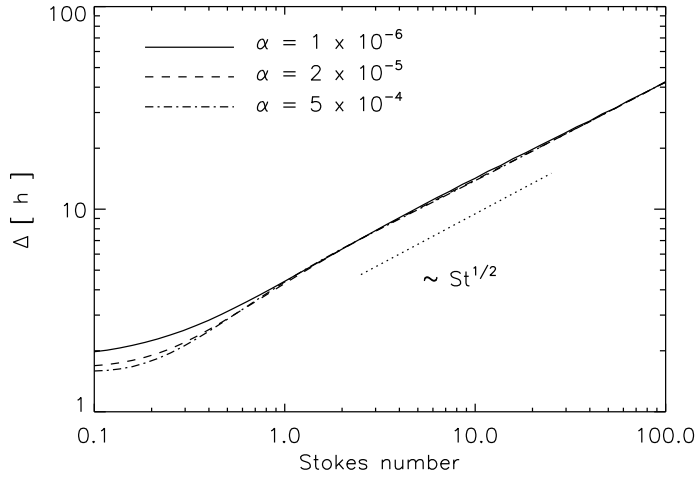

Figure 3.10: The width of the azimuthal gas velocity distribution in units of the dust scale height h as a function of Stokes number St for 3 different turbulence parameters α as discussed in Sec. 3.3.3. The dotted line indicates the $\sim \mathrm{St}^{1/2}$ dependency of the Ekman layer.

with the Keplerian rotating solid equatorial subdisk. High above the midplane the gas is in equilibrium with the radial gas pressure gradient, yielding a slightly sub-Keplerian rotational velocity. The Ekman layer is the transitional region between these two extremes. The thickness of this layer depends on the viscosity of the gas.

In this subsection, we will compare our results with the predictions of the simplified model described above. We want to know the extent of the region where gas and dust affect each other and effects of viscosity become of importance. The comparison with regard to the drift velocities implied by this approximation, however, will be discussed in Section 3.3.6.

To quantify the length scale over which viscous collective effects play an important role, we define a measure Δ by

$$\Delta(\alpha, \mathrm{St}) = \int g(z)|z| \, dz. \tag{3.14}$$

The function $g(z)$ is given by

$$g(z) = c_\mathrm{N}|u_\varphi + v_\mathrm{N}|z^2 \, . \tag{3.15}$$

The constant c_N provides the normalization of g. With this distribution function, deviations from the single particle solution $u_\varphi + v_\mathrm{N}$ are weighted in a way that differences high above the midplane are more important than differences close to the midplane. Therefore, Δ provides informations about the width of the vertical azimuthal velocity distribution of the gas. The dependence of this quantity as a function of St is shown in Fig. (3.10) for 3 different α-values.

According to this diagram the value of the length scale Δ is a few dust scale heights as long as the Stokes number is smaller than unity. For higher St values this quantity increases exponentially up to more than 40 h for $\mathrm{St} = 100$. We also find that Δ is hardly dependent on the turbulence parameter α. This behaviour may be understood by investigating the length

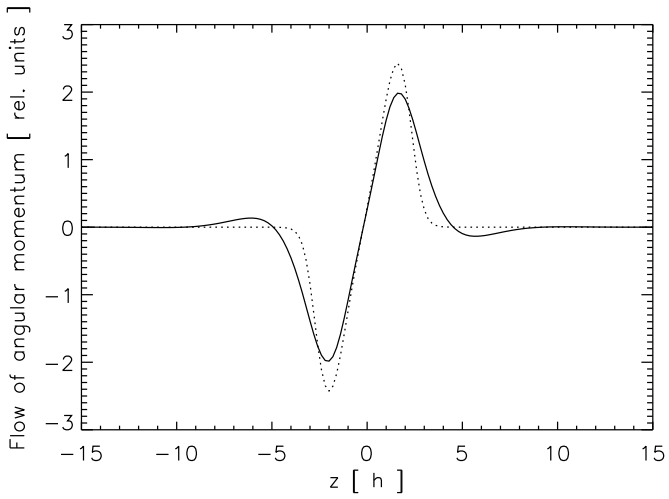

Figure 3.11: This graph shows $\partial_z u_\varphi$ which indicates the flow of angular momentum in the vertical direction as discussed in Sec. 3.3.4. The solid and the dotted lines show the flow of momentum with and without radial viscosity terms, respectively. The azimuthal viscosity terms are included at all times.

scale of the classical Ekman layer

$$\frac{\Delta_\mathrm{E}}{h} \sim \frac{1}{h}\sqrt{\frac{\nu_\mathrm{g}}{\Omega_\mathrm{k}}} \sim \sqrt{\alpha}\frac{H}{h} \sim \sqrt{\mathrm{St}}\,. \tag{3.16}$$

The dotted line in Fig. (3.10) indicates this dependency which shows that the gas layer in fact acts like an Ekman layer when the Stokes number exceeds unity.

3.3.4 Vertical flow of angular momentum

A remarkable effect of the viscosity is the radial inward drift of the gas which is impossible in the laminar NSH solution. At certain heights above the midplane the gas moves inwards (see Fig. 3.9 at $z = \pm 8h$ for example). To understand this effect, we provide the basic scenario. The gas in the midplane of the disk dragged by the dust moves azimuthally faster than the gas outside the dust layer, which causes a vertical velocity gradient. Since viscosity tries to equalize such velocity gradients the gas in the higher regions of the disk is accelerated, decelerating the gas in the midplane. Therefore, viscosity transports angular momentum from the midplane to the higher regions of the disk.

To substantiate this effect we calculate the flow of angular momentum of the gas in the vertical direction. The structure of this flow can be analysed by calculating $\partial_z u_\varphi$ (see Fig. 3.11). This calculation was performed with the same parameter values as used in the last section. The results show that the maximum vertical upward flow of angular momentum takes place at $\pm 2h$. It also shows that there is a vertical downward flow of angular momentum at about $\pm 6h$. This flow is strongly associated with the radial inward drift of the gas at certain heights of the disk and the inclusion of radial viscosity terms. This behaviour can be understood by performing simulations without radial viscosity terms: If only azimuthal viscosity terms are included the azimuthal gas velocities continuously decrease with increasing

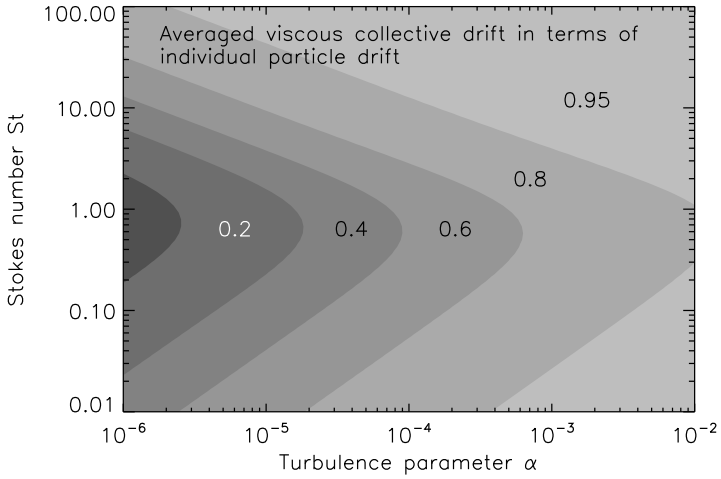

Figure 3.12: A contour plot of the integrated radial dust velocity $\bar{u}^{\mathrm{V}}$ under the influence of viscosity as a function of turbulence parameter α and Stokes number St as discussed in Sec. 3.3.5. The numbers related to the contour lines on the left side, respectively, indicate the net drift velocity in units the individual particle drift u.

distance from the midplane. This means that angular momentum is generally transported in the higher regions of the disk and never towards the midplane. This suggests that the vertical downward flow of angular momentum is an effect caused by radial viscosity. To substantiate this assumption Fig. (3.11) also shows the vertical flow of angular momentum when radial viscosity terms are neglected (dotted lines). The inflow vanishes in this case.

We also calculated the radial velocity of the gas without radial viscosity terms included. The results of this calculation indeed demonstrate that the radial inward drift of the gas vanishes in this case (see Fig. 3.9). The results also show the occurrence of two narrow peaks in the vertical velocity distribution of the radial gas velocity without radial viscosity terms. These peaks imply high velocity gradients. Radial viscosity, once included in the simulation, reduces these velocity differences by radially accelerating the neighbouring regions. This acceleration leads to a decrease in the azimuthal velocities since $\dot{u}_\varphi \sim -u_{\mathrm{r}}$ due to Coriolis forces. This again causes the gas to drift inward. Figure 3.9 also shows that the radial outflow of the gas may be faster than v_{N} if radial viscosity terms are neglected. The azimuthal velocity differences in gas and dust that initially cause any drift behaviour are of the same order of magnitude. Therefore, it appears unjustified to neglect radial viscosity terms as often implicitly done by using the plate drag approximation for example.

3.3.5 Integrated radial velocities

We now calculate the net flow of the dust $\bar{u}^{\mathrm{V}}$ according to Eq. (3.10). The result is shown in Fig. (3.12) expressed in terms of the individual particle drift velocity. According to these results the drift behaviour for high turbulence parameters is that of individual particles and neither collective effects nor effects of viscosity seem to play a major role in this part of the diagram. The net dust velocity has values of about $-v_{\mathrm{N}}$ for $\mathrm{St} \approx 1/2$ (cf. Fig. 3.12) and decreases with lower α values and with growing distance from $\mathrm{St} \approx 1/2$.

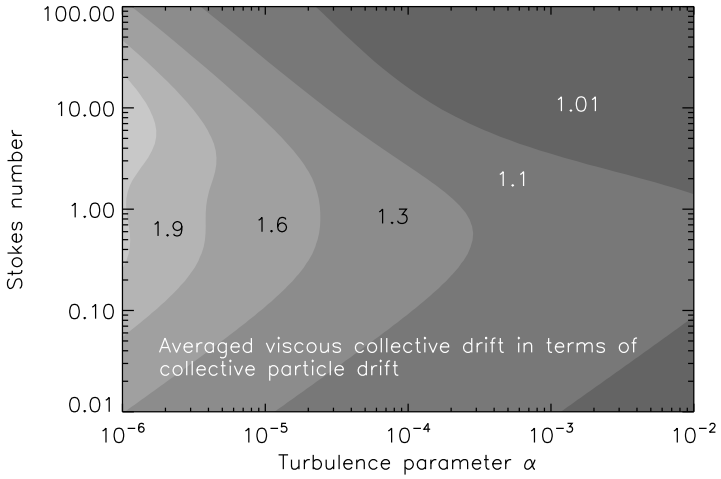

Figure 3.13: A contour plot of the integrated radial dust velocity $\bar{u}^{\mathrm{V}}$ under the influence of viscosity as a function of turbulence parameter α and Stokes number St as discussed in Sec. 3.3.5. The numbers related to the contour lines on the left side, respectively, indicate the net drift velocity in units of the NSH drift $\bar{u}^{\mathrm{NSH}}$ without viscosity.

To demonstrate how viscosity changes the collective drift behaviour investigated in step 2, it is suggestive to express the viscous collective drift $\bar{u}^{\mathrm{V}}$ in terms of the NSH drift $\bar{u}^{\mathrm{NSH}}$. A contour plot of this ratio can be seen in Fig. (3.13). This plot shows that the radial velocities calculated in this section exceed the drift due to collective effects by a factor of 2 at most if very low turbulence parameters are considered. For α parameters higher than 10^{-4} viscosity alters the drift scales by a factor of 1.2 in the most extreme case. The deviation from individual particle velocities due to collective effects were more pronounced than those due to viscosity. Therefore, we conclude that the drift behaviour is predominantly determined by collective effects and not by effects of viscosity.

3.3.6 Plate drag approximation

Here we will compare our results with previous work. We will consider the predictions of the "plate drag approximation". We would like to investigate if these two drift models predict the same radial velocities in certain parameter regimes.

In the plate drag approximation the drift induced by viscosity is given by (Goldreich & Ward 1973; Weidenschilling 2003)

$$u_{\mathrm{PD}} = \frac{\eta V_{\mathrm{k}}}{c_{\mathrm{s}}\epsilon_0 \mathrm{Re}_\star \sqrt{2\pi}} \,. \tag{3.17}$$

The derivation of this expression is based on the assumption that the dust sublayer behaves like a solid disk subject to viscous stress on its surface by a turbulent boundary layer. This stress extracts angular momentum from the dust layer which implies radial drift of the dust (Weidenschilling 2006). The quantity $\mathrm{Re}_\star$ denotes the critical Reynolds number which indicates the transition point between laminar and turbulent flow. The value of this number depends on the geometry of the flow and is usually determined experimentally. We calculated the viscous drift for two different critical Reynolds numbers $\mathrm{Re}_\star = 100$ and $\mathrm{Re}_\star = 200$.

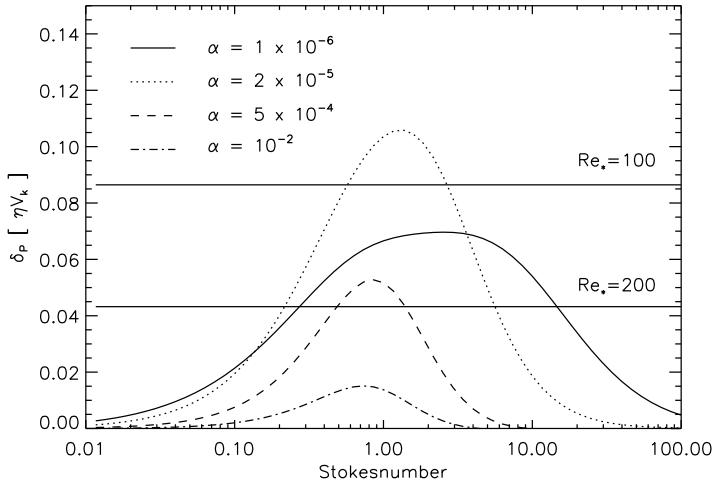

Figure 3.14: The radial velocity deviation induced by the inclusion of viscosity as a function of Stokes number St for different turbulence parameters α as discussed in Sec. 3.3.6. The horizontal lines indicate the viscous radial drift predicted by the plate drag approximation for two different critical Reynolds numbers.

We will measure the radial drift due to the inclusion of viscosity by the deviation

$$\delta_{\rm p} = \bar{u}^{\rm V} - \bar{u}^{\rm NSH} \,. \tag{3.18}$$

This difference velocity $\delta_{\rm p}$ as well as the predictions of the plate drag approximation $u_{\rm PD}$ are shown in Fig. (3.14) as a function of the Stokes number for different turbulence parameters α. This figure shows that the predictions of these two models are roughly of the same order of magnitude if the Stokes number is about unity. For Stokes numbers much smaller/larger than unity the results of the numerical integration of the Navier-Stokes equations deviates from the predictions of the plate drag model. Already Youdin and Chiang (2004) put the plate drag approximation in question. They found that the plate drag overestimates turbulent stresses and that vertical shear and buoyancy are important elements missing in this description. While the plate drag model involves a radial drift velocity which is inversely proportional to the surface density of the layer and not explicitly dependent on particle size Weidenschilling (2006) found the very contrary. In his simulations, the drift velocity shows no significant variation with surface density, but is dependent on particle size which clearly speaks against the validity of the plate drag model.

3.3.7 Fitting formula

A simple fitting formula that reproduces the results might be useful for forthcoming purposes for example investigations of drift time scales or radial mixing. For this reason we fitted the vertically averaged radial dust velocities given by the numerical solution of Eq. (3.12). This solution includes all effects investigated here, i.e. collective effects and effects of turbulent viscosity, and it is shown in Fig. (3.15).

i	c^Γ	c^ξ	c^μ
0	1.89082	2.06164×10^{-2}	0.57083
1	0.14763	4.69938×10^{-3}	-0.41644
2	0.20912	-4.05442×10^{-3}	-0.12910
3	8.25120×10^{-2}	–	-1.24036×10^{-2}
4	7.38181×10^{-3}	–	-4.09782×10^{-4}

Table 3.2: Coefficients for the polynomical fit of the simulated integrated dust velocities as discussed in Sec. 3.3.7.

For the fit we use an expression of the form

$$u_{\rm fit} = \frac{\Gamma(\alpha)}{x(\alpha, {\rm St}) + \frac{1}{x(\alpha,{\rm St})}} \ , \tag{3.19}$$

following Eq. (3.5) for individual particle drift. In this expression the amplitude Γ is solely a function of the turbulence parameter α. The quantity $\Gamma/2$ matches the maximum occuring radial dust velocity in units of $-v_{\rm N}$ when α is fixed. The parameter x is given by

$$x(\alpha, {\rm St}) = 10^{\xi(\alpha)} {\rm St}^{\mu(\alpha)} \ . \tag{3.20}$$

The two functions ξ and μ are only dependent on α. The parameter ξ determines the location of the maximum of the velocity distribution, the parameter μ determines the width of the velocity distribution. The fits for the three functions Γ, ξ and μ were performed with polynomials of the form

$$\Gamma = \sum_{\rm j=0}^{4} c_{\rm j}^{\Gamma} y^{\rm n} \ , \quad \xi = \sum_{\rm j=0}^{2} c_{\rm j}^{\xi} y^{\rm n} \ , \quad \mu = \sum_{\rm j=0}^{4} c_{\rm j}^{\mu} y^{\rm n} \ , \tag{3.21}$$

in which y is given by $y = \log_{10} \alpha$. For the dependency of ξ on α a second order polynomial turned out to be sufficient. For the quantities Γ and μ a fourth order polynomial provided a satisfying fit to the simulation results. The coefficients for all these polynomials are listed in table 3.2. The deviation between the fitting function and the simulation within the parameter intervalls ${\rm St} \in [10^{-2}, 10^2]$ and $\alpha \in [10^{-6}, 10^{-2}]$ is always smaller than 0.01 $v_{\rm N}$.

3.3.8 Radial drift times including effects of viscosity

While collective effects reduce the radial drift of the dust the additional inclusion of viscosity into the disk model again increases it. For this reason, the time scales implied by collective effects and effects of viscosity represent an intermediate regime between the time scales of individual particles and the time scales implied by collective effects. In other words, neither collective effects nor effects of viscosity can prevent the dust particle to drift away from 100 AU in short time scales. Hence, the observations of mm-cm size grains do not constrain the α-parameter in the outer parts of the disk as one may have hoped for. Nevertheless, there are various other disk parameters which still can provide a solution to this drift problem.

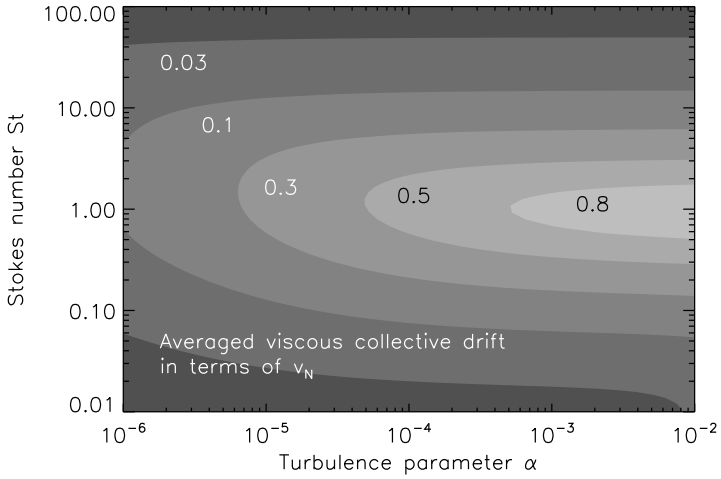

Figure 3.15: A contour plot of the integrated radial dust velocity $\bar{u}^{\mathrm{V}}$ under the influence of viscosity as a function of turbulence parameter α and Stokes number St. The numbers related to the contour lines on the left side, respectively, indicate the net drift velocity in units of $-v_{\mathrm{N}}$.

3.4 Other possibilities to increase the drift timescale

We have seen that even with the creation of very dense midplane layers for very low α the radial drift is too fast to explain the observed millimeter flux of these disks. We now discuss other possible solutions to this problem. We first consider the effect of the dust-to-gas ratio on the drift time scales. With this particular calculation, we try to mirror the later stages of disk evolution when gas evaporation becomes of importance. A large number of the disks observed have ages of more than 5 Myrs (Testi et al. 2003; Natta et al. 2004). If we regard the onset of disk clearing typically after ~ 6 Myrs (Alexander et al. 2006) and the rather larger error bars in the stellar age determination[3], some of the disks may already have suffered significant gas mass loss. We also investigate the importance of the turbulence parameter q and consider the possibility of non-linear effects which could play an important role.

3.4.1 Dust-to-gas ratio

What influence does the dust-to-gas ratio have on the drift time scales? To change this quantity to larger values we will remove a certain fraction of the gas from the disk. This approach mirrors the later stages of disk evolution when disk clearing becomes of importance. The drop in gas density has severe implications for the drift time scales: When gas is removed from the disk then the dust particles are less affected by the motions of the gas. This leads to thinner dust layers and hence to higher dust-to-gas ratios. For this reason collective effects become of importance which reduces the radial drift velocities according to Eq. (3.9). In this paragraph, we will investigate how much gas we have to remove from the disk to provide time scales larger than 2 Myrs.

As in the last sections we calculate the particle radius interval in which the drift time

[3]Priv. com. with J. Setiawan

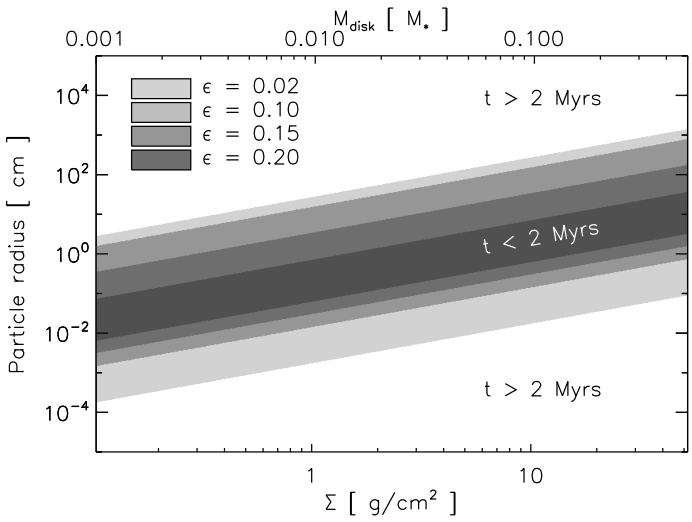

Figure 3.16: This figure shows the effect of the dust-to-gas ratio on the drift time scales for a turbulence parameter of $\alpha = 10^{-6}$ as discussed in Sec. 3.4.1. The figure gives the particle radius interval for which the drift time scale is smaller than 2 Myr as a function of disk mass and surface density for different total vertical dust-to-gas ratios $\epsilon = \Sigma_d/\Sigma_g$. The surface density is given at 100 AU. The disk mass and the surface density in this figure are the 'original' mass and surface density of the disk before the gas depletion that is invoked to alter the dust-to-gas ratio.

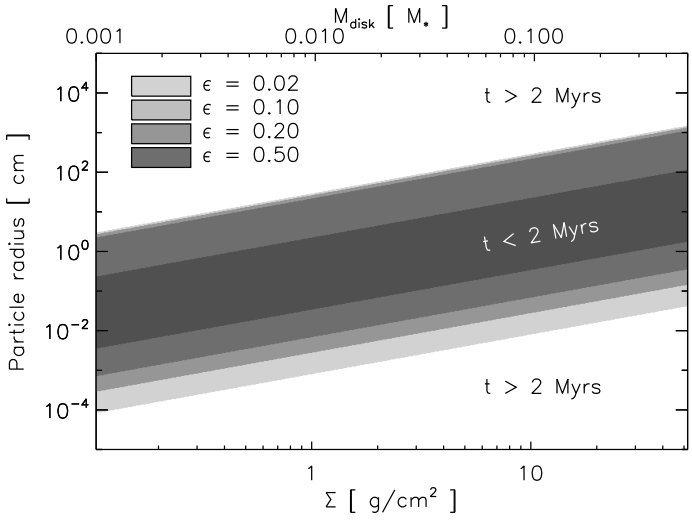

Figure 3.17: This plot is the same as Fig. 3.16. But here the turbulent α parameter is 10^{-5}.

scale is shorter than 2 Myr. These calculations were performed for two different turbulence parameters $\alpha = 10^{-5}$ and $\alpha = 10^{-6}$. The results of these simulations are shown in Fig. (3.16)-(3.17). In these figures the disk mass and the surface density are the 'original' mass and surface density of the disk before the assumed gas depletion that is invoked to alter the dust-to-gas ratio.

The drift behaviour of the dust particles hardly changes if only a small fraction of the gas is removed. Both figures show that the critical particle radius interval is little affected by removing 50% of the gas, cf. Fig. 3.7. However, for higher dust-to-gas ratios the critical interval decreases continuously. Considering the case $\alpha = 10^{-6}$ we find that cm particles are able to stay in the outer parts of the disk for 'original' disk masses $< 0.05 M_\star$ and $> 0.2 M_\star$ if only 5% of the gas is left. The critical interval disappears completely if the total vertical dust-to-gas ratio $\epsilon = \Sigma_d / \Sigma_g$ exceeds 0.40. For higher turbulence parameters the critical radius interval decreases slower with higher dust-to-gas ratios. We find that for $\alpha = 10^{-5}$ the interval disappears for a dust-to-gas ratio of $\epsilon = 0.75$. We conclude that removing the gas may be a possibility to preserve mm to cm particles in the outer part of the disk.

3.4.2 Turbulence parameter q

Little attention was given to the turbulence parameter q until now. A certain diffusion coefficient of the gas may be realized by big gas eddies moving slow or by small gas eddies moving fast. These two extreme cases are represented by $q = 1$ and $q = 0$, respectively. To illustrate how strongly q may influence the thickness of the dust layer we consider the following numerical example. We assume a Stokes number of unity and a turbulent α parameter of 10^{-3}. For the extreme case $q = 0$ we calculate a dust scale height of $h/H = 10^{-3}$ and for $q = 1$ we obtain $h/H = 3 \times 10^{-2}$. These two dust scale heights differ by a factor of 30 which possibly influences the drift time scales.

We calculated the effect of the turbulence parameter q on the drift velocity for two different turbulence parameters α, i.e. $\alpha = 10^{-6}$ and $\alpha = 10^{-5}$. The Stokes number was chosen in a way the the drift velocity for $q = 1/2$ corresponds to a timescale of 1 Myr. For $\alpha = 10^{-6}$ and $\alpha = 10^{-5}$ this implies St = 225 and St = 235, respectively. The results of these simulations are shown in Fig. 3.18. This figure shows that the integrated drift velocities of the dust vary by 3% for $\alpha = 10^{-6}$ and by 1% for $\alpha = 10^{-5}$ when q is changed from zero to unity. We find that for higher α parameters this variation is always less than 0.4%. We conclude that q has a very minor effect on the radial drift velocities.

A small h/H ratio leads to a high dust-to-gas ratio in the midplane of the disk. This causes the radial drift of the dust in the midplane to decrease due to collective effects. One would now intuitively think that a continuously decreasing h/H ratio leads to smaller and smaller radial drift velocities but this is not the case for the following reason: When the ratio h/H decreases the vertical gradients of the azimuthal gas and dust velocities increase. Therefore, more angular momentum is transported in the higher regions of the disk. The midplane loses angular momentum which directly causes the radial velocity of the dust to increase. Finally both effects, the decrease in radial velocity due to collective effects and the increase of velocity due to the vertical transport of angular momentum, seem to cancel each other (or at most result in a negligible change in radial velocity) when small h/H ratios are considered.

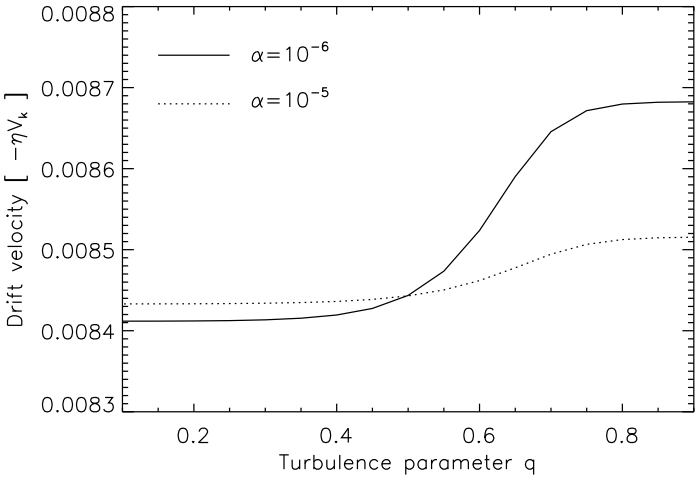

Figure 3.18: This figure shows the effect of the turbulence parameter q on the radial drift velocity for two different turbulence parameters α as discussed in Sec. 3.4.2. The Stokes number was chosen in a way that the radial drift velocity for $q = 1/2$ corresponds to a timescale of 1 Myr with regard to 100 AU assuming that $v_{\rm N} = 60$ m/s. For $\alpha = 10^{-6}$ and $\alpha = 10^{-5}$ this implies St = 225 and St = 235, respectively.

3.4.3 Effects of non-linear dynamics

So far we have considered different equilibrium states that would potentially allow solid particles to reside at large orbital radii for a longer time than a single test particle. It is however also possible for dynamical effects, such as spiral arms, turbulence or vortices, to reduce the radial drift.

Dust particles are forced to climb up the local gas pressure gradient. In the simple case of a gas pressure that falls monotonically with radius the particles fall into the inner disk, but the particles may end up in any local gas overdensity that they encounter on their way (Klahr & Lin 2001; Haghighipour & Boss 2003). If the disk is massive enough to be gravitationally unstable, its spiral arms may act as such local density maxima (Rice et al. 2004). Transient overdensities that occur in magnetorotational turbulence, in a way very elongated vortices, have the same effect (Johansen et al. 2006b), slowing down radial drift by a factor of two. The important parameter for reducing the overall radial drift is the life-time of the gas overdensity. Spiral arms would from this perspective be a good candidate, since turbulent overdensities tend to live no longer than a few local orbits of the disk.

The coupled flow of gas and dust is in itself unstable to the streaming instability (Youdin & Goodman 2005), leading to particle clumping in the non-linear state (Johansen et al. 2006b). These local dust overdensities drag the gas along with their orbital motion, thus reducing the sub-Keplerian head wind and the radial drift. The effect of the streaming instability on the radial drift can be as high as a factor two in reduction (Johansen & Youdin 2007).

3.4.4 Temperature and surface density profiles

We also investigated to which extent the radial drift time scales of the dust particles depend on the temperature and the surface density profile. These quantities were found to play a

minor role which can be reasoned as follows. If the temperature is decreased by a factor of 2 then the maximum radial drift velocity v_N decreases by the same factor since $v_\mathrm{N} \propto c_\mathrm{s}^2$. This means that if the temperature at 100 AU is decreased from 20 K to a rather low value of 10 K then the drift time scales would only increase by a factor of 2. Since the radial drift problem spans at least one order of magnitude a change in temperature does not provide a solution. A change in the surface density index from $\delta = 0.8$ towards $\delta = 0$ changes the maximum drift velocity v_N by a factor of 1.5 according to Eq. (3.2) which also does not solve the problem.

However, a change in the power law index for the surface density δ does not only change the maximum radial drift velocity of solid material according to Eq. (3.2). It also changes the actual surface density at 100 AU since the mass is distributed differently. This leads to different particle Stokes numbers and, hence, to different radial drift velocities (cf. Eq. 3.5). We can calculate the change in the surface density at 100 AU when we go from the MMSN model ($\delta = 1.5$) to models based on recent observations (Kitamura et al. 2002; Andrews & Williams 2007), i.e. shallower mass profiles with a median power law index of $\delta = 0.5$. These two models represent the most extreme cases of how we think today that the mass in a protoplanetary disk is distributed. The ratio between the two surface densities at 100 AU can be easily calculated to be

$$\frac{\Sigma(\delta_1 = 0.5)}{\Sigma(\delta_2 = 1.5)} = \frac{2-\delta_1}{2-\delta_2} \left(\frac{100\,\mathrm{AU}}{r_\mathrm{out}} \right)^{\delta_2 - \delta_1} = \frac{3}{2} \,. \tag{3.22}$$

If we assume an outer disk radius of $r_\mathrm{out} = 200$ AU then the surface density of the gas changes by a factor of 1.5 when going from one extreme to the other. We see that the power law index has hardly any effect on the gas density in the outer parts of the disk. Also the gas densities, the Stokes number and the radial drift velocities are altered by the same factor. Since the value of 1.5 is too low to explain the observationally determined long survival times of the dust, we conclude that mass redistribution does not provide a solution to this drift problem.

3.5 Summary and conclusions

We discussed two main subjects in this chapter. First, we investigated the velocity field within the dust and gas layer in protoplanetary disks. By regarding the interaction of gas and dust, we were able to calculate averaged radial drift velocities of the dust including various effects, i.e. collective effects and effects due to turbulent viscosity. The results of this first part enabled us to estimate characteristic drift time scales of dust. This was the second main subject of this chapter. These survival time calculations were performed in order to explain interferometric millimeter observations that indicate the presence of mm to cm size particles in the outer part of disks with ages up to 10 Myrs.

We first summarize our findings regarding the velocity structure of the gas and the dust layer. For turbulence parameters α larger than a threshold value of $\sim 10^{-4}$, collective effects as well as effects of turbulent viscosity play a minor role. The dust is stirred up away from the midplane in such a way that the dust-to-gas ratio is too low for these effects to become of importance. The radial drift velocities of individual particles and those in the full model including all effects investigated in this chapter differed by a factor of 1.3 at most. For this reason, both effects can be disregarded for large α-values. Numerical simulations of MRI induced turbulence in disks predict α-values of the order of 10^{-3} (Hawley et al. 1995; Sano et al. 2004) which is one order of magnitude larger than the treshold value given above. Turbulence levels implied by observed accretion rates onto T Tauri stars suggest that the disk

is even more turbulent than seen in numerical simulations (Hartmann et al. 1998; King et al. 2007). This suggests that the individual particle drift model is the approproate description for radial dust motion in disks.

In the calculations of this chapter, we did not include the back-effect of the velocity field on the spatial distribution of the dust. Johansen et al. (2006b) found that if this back-reaction is included, particle pile-ups may arise which involve high dust-to-gas ratios. These overdensities in the dust can lead to a reduction factor of about 2 in the radial drift velocities. We also remark that for very large α-values the accretion velocity of the gas is not negligible. The dust is dragged along with the gas which leads to an extra source of radial velocity which was not discussed here.

We find that in the case of low turbulent disks with $\alpha \sim 10^{-6}$, the collective radial drift velocity of the dust in the local surrounding of the disk midplane is reduced by a factor of 100. This reduction factor would be quite sufficient to explain the presence of dust pebbles in the outer parts of protoplanetary disks. Our calculations, however, show that the vertically averaged radial dust velocity, i.e. the velocity which determines the survival time of the dust population, is only an order of magnitude lower than the corresponding individual particle drift. If turbulent viscosity is included in the simulations as well, then the radial drift of dust even higher due to the vertical transport of angular momentum. Taking collective and viscous effects into account, the radial drift speed could not be reduced by more than $\sim 90\%$.

This reduction factor led to radial drift time scales which were only in agreement with the observations if very high/low mass disks or very porous particles were considered. Except for these two cases, the drift time scales of the dust turned out to be far too short to explain the millimeter observations. For this reason, we investigated several other possibilities in order to increase the drift time scales. We found that one possible way out of the survival time problem is to remove a significant fraction of the gas from the disk. This increased the radial drift time scales up to several Myrs. Gas might be removed in the later stages of disk evolution when photoevaporation sets in. While the gas is evaporated from the disk the dust particles > 20 μm (Takeuchi & Lin 2005; Bally et al. 2005) remain in the outer parts of the disk. However, current photoevaporation models remove the gas from the disk rather abruptly (Alexander et al. 2006). This would lead to rather high relative particle velocities in the disk. Hence, the dust particles would collide and destructive collisions would play an important role. Centimeter particles would be destroyed in short time scales which is not in agreement with the observations.

Nevertheless, let us for the moment assume that photoevaporation is the correct explanation for the survival of these mm-cm size pebbles in the outer parts of protoplanetary disks. Is the presence of such thin midplane layers then consistent with observations of e.g. edge-on disks? To answer this question we consider that the infrared emission from protoplanetary disks originates from smaller ($\ll 3$ mm) dust grains. These grains must be smaller than 3 micrometer, as can be inferred from the presence of a 10 micron silicate feature in emission in most sources. Even with relatively little vertical mixing (low turbulence) the very smallest dust particles can still be mixed up to intermediate height above the midplane (Dullemond & Dominik 2004a), although we admit that the disk should look significantly less flared in such a case, i.e. the disk should be of Group II in the Meeus et al. (2001) classification. Interestingly, Acke et al. (2004) have shown that there is indeed a correlation between the presence of large grains in the outer regions of disks around Herbig stars and the type of SED of the disk: disks with large amounts of large (mm/cm) grains appear on average to also have SEDs consistent with flatter disk geometry. This seems to substantiate at least qualitatively the idea of low turbulent disks.

For larger grains, which can be observed at mm/cm wavelengths, there have not been observations of edge-on disk with very thin mm disks so far. However, this has two reasons. The first reason is that if the mm/cm disk is very thin, then the chance to observe it sufficiently precisely edge-on is very small. This reduces the number of potential candidates for such measurements drastically. The second reason is that current state-of-the-art interferometers do not yet have the spatial resolution to resolve such thin disks. For instance, the Butterfly Nebula (a well-studied nearly perfectly edge-on disk), was resolved with OVRO by Wolf et al. (2003), but the vertical extent of the observed disk was as large as the beam size, i.e. unresolved in vertical direction.

There is one important effects that we did not include in this section, namely the growth of dust particles. Coagulation time scales of dust to reach centimeter size could be of the order of 1 Myr considering the outer parts of the disk. This growth delay time might explain the observations. A model including both processes, radial drift and coagulation, would clarify this issue. Recent work about the drift time scales in comparison to the growth time scales was done by Klahr & Bodenheimer (2006). According to their calculations, the dust would long have drifted away from 100 AU before the particles even reach the size of about a centimeter. These findings raise the questions of how these mm- to cm-sized pebbles form in the first place. Not only the effect of particle coagulation, also dust fragmentation could change the situation. Even though particle fragmentation destroys particles, it could finally, contrary to intuition, help for the process of coagulation. Particle fragmentation leads to a permanent amount of small particles as a result of collisions. These small particles may be swept up by larger particles due to their high relative velocity. Although some particles are destroyed, the sum of both effects, particle growth and destruction, could finally lead to a net growth.

In the next chapter, we construct a disk model which involves radial particle motion, dust particle coagulation and the effect of particle fragmentation alltogether. Though this chapter casually gives also more insight into the survival time problem of dust discussed so far, the main subject will be the growth of dust and the formation of planetesimals. We will try to answer the question if larger objects can actually form in the disk, or if the paradigm of planetesimal formation due to dust particle sticking is simply wrong.

Chapter 4

Particle growth and the meter size barrier

The amazing number of 313 extrasolar planets around 267 stars were found[1] since the first discovery of an exosolar planet around a star by Mayor & Queloz (1995). Some of these planetary systems, e.g. some members of the TW Hydrae association and the system TW Hydrae itself (Chauvin et al. 2005; Setiawan et al. 2008), have ages of less than 10 Myrs. These observations suggest that planets can form over short astronomical time scales of only a few Myrs. It is widely accepted today that the very initial step in the formation of planetesimals, which are the building blocks for planets, is the coagulation of sub-μm dust particles to some meters in size (Klahr & Brandner 2006; Natta et al. 2007a). Such large objects are hard to observe in disks. However, the presence of μm-sized dust grains, i.e. particle which are at least one order of magnitude larger than grains in the interstellar medium, was inferred by mid-infrared spectroscopy of disks around Herbig Ae/Be stars (Bouwman et al. 2001; van Boekel et al. 2003), T Tauri stars (Przygodda et al. 2003; Kessler-Silacci et al. 2007) and also around brown dwarfs (Apai et al. 2004, 2005, 2007; Sicilia-Aguilar et al. 2007). Millimeter interferometry even indicates large populations of particles which have grown to sizes up to several centimeters (Testi et al. 2003; Wilner et al. 2005; Rodmann et al. 2006).

All these observations, i.e. the discovery of exoplanets and the inferred growth of dust particles up to cm size, give reason to model the evolution of solid particles in protoplanetary disks in order to explain the observational data (Dullemond & Dominik 2004b, 2005; Tanaka et al. 2005; Nomura & Nakagawa 2006; D'Alessio et al. 2006; Ormel & Cuzzi 2007). These theoretical models do not only describe the evolution of protoplanetary disks. They also unveil certain obstacles in the formation of planetesimals by particle coagulation (Youdin 2004; Dominik et al. 2007; Brauer et al. 2007). One major obstacle is the meter-sized barrier as described in the introduction. We briefly remind what this obstacle is about.

Solid particles drift towards the central star as first dicussed by Whipple (1972) and Weidenschilling (1977a). Radial drift time scales for meter-sized bodies at 1 AU are of the order of $\sim 10^2$ yrs. In this time, these boulders drift 1 AU into the inner regions of the disk and evaporate. A possible way out of this problem is particle growth since the radial drift velocity is fairly dependent on the particle radius. For example, the drift velocity of meter-sized particles at 1 AU is ~ 50 m/s. The radial drift velocity of 10 meter-sized bodies is already

[1]Number given by the *Jet Propulsion Laboratory* of the CIT on Oct 28th, 2008. http://planetquest.jpl.nasa.gov/

10 times lower. Therefore, swift particle growth could prevent the particles from drifting into the evaporation zone. However, the general disk evolution comprises a considerable particle loss due to evaporation which is hard to prevent. This mass loss problem is one topic of this chapter. Other sublimation zones of the disk, e.g. the snow line at ~ 2 AU (Lecar et al. 2006), could also play a role for particle drift and coagulation processes. However, we will for now neglect this issue and we will come back to this topic in the last chapter.

Another obstacle is the fragmentation of solid particles. While low-velocity collisions lead to particle growth, high velocity impacts lead to destruction (Blum et al. 1998; Poppe et al. 1999; Blum & Wurm 2000). For example, the relative particle velocity of meter-sized bodies in a protoplanetary disk can be more than ~ 50 m/s (Weidenschilling 1977a; Markiewicz et al. 1991). Benz (2000) found that meter-sized rocks appear unlikely to survive an impact with a relative low collision velocity of some cm/s. For this reason, the particle size of roughly a meter seems to pose an upper limit for particle coagulation.

These two obstacles, the radial drift barrier and the fragmentation barrier, are the main topic of this chapter. We investigate under which conditions the dust can overcome these barriers and form larger objects. We consider a disk model including the growth, the radial drift and the fragmentation of solid particles. In order to show how these three effects change the evolution of the disk, we will include them step by step.

1. In the first step we only consider particle coagulation due to Brownian motion, vertical settling and turbulent mixing. This step shows to which sizes particles can grow if radial drift and fragmentation are neglected.

2. The second step includes the radial drift and the radial mixing of dust. Particles are now allowed to move inwards and to disappear into the evaporation zone. However, we investigate which disk parameters influence the drift time scales and for which parameters the dust particles overcome the drift barrier.

3. The last step also includes particle fragmentation. We show under which conditions, i.e. in which regions of the disk and for which disk parameters, it is possible for the dust to overcome this barrier.

The meter-sized barrier is not only of interest for the radial drift itself. Particles close to this barrier are most susceptible to the motions of the gas and the gravitational effects of the dust. For example, particles can be trapped in very elongated gas vortices in magnetorotational turbulence (Balbus & Hawley 1991; Barge & Sommeria 1995). These effects can slow down the radial drift by a factor of two (Johansen et al. 2006b). Under certain conditions the solid particle layer itself may become gravitationally unstable (Johansen & Youdin 2007). In high dust density regions, the particles contract due to their own gravity and may form a planetesimal within a few orbits (Johansen et al. 2007). Moreover, the flow of the gas and the dust can be unstable to the streaming instablity (Youdin & Goodman 2005) which leads to particle clumping, and possibly also to a gravitational collapse of the dust. Apparently, the radial drift barrier is not only connected to the radial motion of the dust particles, but involves various other important effects as well. For this reason, it is vital to answer the question if particles can actually reach the size regime at which these non-linear effects become of importance.

Throughout the whole chapter, a computer code is used which includes a 2+1 dimensional disk evolution model. The first dimension is the radial coordinate of the disk r, the second one is the height above the midplane z and the third coordinate is the mass of the dust

particles m. The dust can move radially due to radial drift and radial mixing. We will numerically solve the continuity equation for this problem for each particle species. In order to do so, we implement a one dimensional hydro solver using an implicit version of the *Donor Cell algorithm*.[2] The time evolution for the particle size distribution is determined by the coagulation equation which was extensively discussed in Chapter 2. We will numerically solve this equation using the modified Podolak algorithm as presented in Sec. 2.4.3. In the vertical direction, we will always assume that each particle species is in vertical sedimentation/mixing equilibrium (Dubrulle et al. 1995; Cuzzi & Weidenschilling 2006). Hence, we will not solve the time dependent continuity equation in the vertical direction as done for example by Dullemond & Dominik (2005). Nor do we need to solve the coagulation equation at all z explicitly. Instead, we solve the vertically integrated coagulation equation, which significantly saves computational time (cf. Sec. 2.4.5). We also formulated the coagulation equation in an implicit way (cf. Sec. 2.4.4) which saves another factor of ~ 100 of computer simulation time.

4.1 Step 1 - Dust particle coagulation

4.1.1 Mass profile controversy

Before discussing the growth of dust particles, there is the need to distinctly point out that the radial surface density distribution of gas and dust in the disk, on which the dust particle coagulation calculations in this section are based upon, differs significantly from the disk model which is usually referred to as the minimum mass solar nebula (MMSN) model (Weidenschilling 1977b; Hayashi 1981). As we will see in the later sections, this variation from the – im some sense – standart model of protoplanetary disks has severe implications for the dust particle evolution. The fundamental difference can be found in the distribution of the mass of gas and dust in the disk. In the MMSN disk model, the power law index of the surface density is $\delta = 1.5$, while the disk model in this section adopts a much shallower value of $\delta = 0.8$. Fig. 4.1 shows the surface densities as a function of disk location for both disk models assuming a disk mass of 0.01 $M_\star$. The MMSN model implies surface densities of ~ 600 g/cm^2 at 1 AU in the disk. With the disk model adopting $\delta = 0.8$, we yield surface density values of ~ 20 g/cm^2 which is more than one order of magnitude lower.

The actual distribution of mass in a protoplanetary nebula is still a matter of debate. There is evidence from meteoritics that the densities in the protosolar nebula in the planet forming region have been very high, implying disk masses much larger than the MMSN (Desch et al. 2002). On the other hand, resolved millimeter dust emission maps of protoplanetary nebula seem to indicate much lower surface densities (Andrews & Williams 2007). However, millimeter dust observations of disks may not trace the radial profile of the gas mass density correctly since particle growth to larger sizes is expected to proceed more quickly in the inner parts of the disk than in the outer parts. For this reason, the dust continuum emission becomes flat even though the radial profile of the surface density might have a steep radial behaviour. Hence, analysing dust emission maps assuming a constant dust particle size throughout the disk likely leads to power law indices δ which are systematically shifted towards lower values.

The actual surface density distribution probably lies in between these two extreme cases, i.e. the MMSN model with $\delta = 1.5$ and the observational median of $\delta = 0.5$ (Andrews &

[2] Confer the lecture notes of "Numerical hydrodynamics" by C. P. Dullemond.
www.mpia.de/homes/dullemon/lectures/hydrodynamicsII/index.html

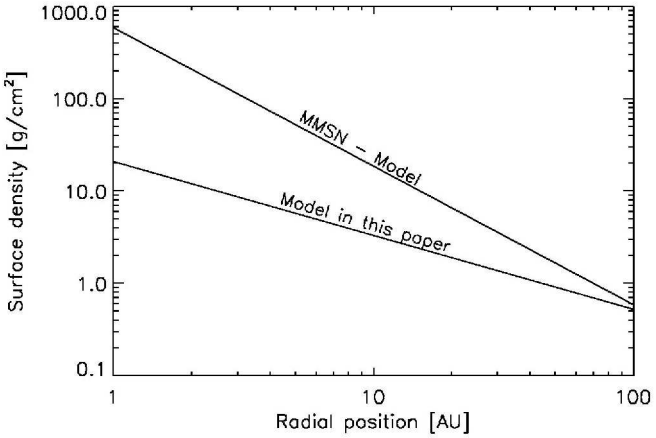

Figure 4.1: The surface density distribution of the gas as a function of disk radius for the disk model discussed here and the MMSN model as discussed in Sec. 4.1.1. Note, that the surface densities at 1 AU differ by more than one order of magnitude. In the outer parts of the disk, the difference in the surface densities is much smaller. This effect was already considered in Sec. 3.4.4 when we discussed the survial times of dust grains in the outer parts of the disk.

Williams 2007). The surface density profile adopted in this section is chosen to be between these two extremes. The goal is to gain insight in dust disk evolution in an environment which has not been investigated yet and which might well be a likely scenario considering the δ range under discussion. We will come back to this important point in Sec. 4.3.5.

I would like to remark one more word about the gaseous background in the disk. It is assumed that the gas in the disk is in a steady state, even for times as long as 1 Myr. Hence, the gas densities in our model do not change in time. We only focus on the dust component in the disk which evolves on a steady gas background. To unveil the robustness of this assumption, we compare the following time scales. Particle growth time scales are of the order of $\sim 10^2$ orbital times before fragmentation prevents further particle growth (c.f. Sec. 4.3). Radial gas accretion velocities are of the order of $\sim 1 \ldots 10$ cm/s at 1 AU in the disk (Takeuchi & Lin 2002). With regard to 1 AU, this leads to accretion time scales of the order of 10^5 yrs, which is much larger than typical particle growth time scales. For example, Takeuchi & Lin (2002) find that in the first $10^{4...5}$ yrs, the gas surface density between 1 and 100 AU is hardly affected by viscous evolution. However, after 10^5 yrs, the surface density of the gas may change significantly over time scales of several Myrs (Reyes-Ruiz 2007). This introduces a systematic uncertainty in the dust evolution model presented here regarding late evolutionary stages of T Tauri disks.

4.1.2 Relative dust particle velocities

Dust particles have to have relative velocities to enable dust growth. The main sources for relative particle velocities in protoplanetary disks are Brownian motion, differential settling, turbulence and radial drift. All these sources are described shortly in the following.

1. Brownian motion. Two particles of mass m_1 and m_2 in a region of the disk with temperature T have an average statistical relative velocity due to Brownian motion

given by

$$\Delta v_{\rm bm} = \sqrt{\frac{8kT(m_1+m_2)}{\pi m_1 m_2}} \; . \tag{4.1}$$

This expression shows that relative thermal velocities are higher for smaller dust particles than for larger dust particles. Hence, the growth process due to Brownian motion is more effective for small particles than for large particles. For example, if we assume a temperature of 200 K, a solid particle density of 1 g/cm^3 and micrometer-sized particles then the relative particle velocity due to Brownian motion is 0.2 cm/s. Particles of centimeter in size lead to a relative velocity of 10^{-7} cm/s. This particular example shows that there is practically no coagulation due to Brownian motion for particles much larger than micrometer size. In general, growth by Brownian motion leads to fractal structures and 'fluffy' aggregates (cluster-cluster aggregates) (Ossenkopf 1993; Kempf et al. 1999). However, we will ignore these intrinsic properties of the dust particles here and assume a constant solid material density. See, however, Schmitt et al. (1997) or Ormel et al. (2007) for dust particle coagulation models including porosity at a fixed radius in the disk.

2. Differential settling is the second process that leads to relative velocities. Solid particles which do not feel a vertical pressure gradient settle to the midplane of the disk due to vertical gravity. If we assume that the solid particles are smaller than the mean free path of the gas then the equilibrium settling velocity is given by $z{\rm St}\Omega_{\rm k}$ (Dullemond & Dominik 2004b). We have to take into account that for Stokes numbers larger than unity, the equilibrium settling velocity model loses validity. Very large bodies (${\rm St} \rightarrow \infty$) above or below the midplane follow an orbit that is tilted with respect to the midplane. The settling time towards the midplane can not exceed an orbital time scale. For this reason we restrict the settling velocity to be the projected Kepler velocity $zV_{\rm k}/r$ at most. Hence, we adopt the following settling velocity in our model,

$$v_{\rm ds} = \frac{z{\rm St}\Omega_{\rm k}}{1+{\rm St}} \; . \tag{4.2}$$

The relative settling velocity between two particles of mass $m_{\rm i}$ and $m_{\rm j}$ at a height z above the midplane then reads

$$\Delta v_{\rm ds} = z\Omega_{\rm k} \left| \frac{{\rm St_i}}{1+{\rm St_i}} - \frac{{\rm St_j}}{1+{\rm St_j}} \right| \; . \tag{4.3}$$

3. Radial drift is the third source for relative velocities of particles in disks (c.f. Chapter 3). The relative velocity in this case is simply the difference in the drift velocities

$$\Delta v_{\rm rd} = |v_{\rm r}^{\rm i} - v_{\rm r}^{\rm j}| \; . \tag{4.4}$$

We apply the radial drift model for individual particles, because Chapter 3 has shown that collective viscous effects only play a role for disks with α-values less than 10^{-4}. In this chapter, our turbulence degree will always be higher than this critical value.

4. Turbulence in the disk is the cause for the fourth relative velocity between dust particles. Relative particle velocities produced by turbulence were calculated numerically by Völk et al. (1980) and Mizuno et al. (1988). Weidenschilling (1984) fitted these results with analytical formulas. Current work by Ormel & Cuzzi (2007) shows that these

expressions underestimate the turbulent relative velocities for particles with large Stokes numbers. In this thesis, we will use the state-of-the-art expressions calculated by Ormel & Cuzzi (2007), in which we have to distinguish between three cases.

Consider two dust particles with stopping times τ_1 and τ_2. If both response times are less than the Kolmogorov time scale τ_η, i.e. $\tau_1, \tau_2 \leq \tau_\eta$, then the relative turbulent velocity of the two dust grains is given by

$$\Delta v_{\rm t}^2 = \frac{3}{2} V_0 \, \frac{{\rm St}_1 - {\rm St}_2}{{\rm St}_1 + {\rm St}_2} \left(\frac{{\rm St}_1^2}{{\rm St}_1 + {\rm Re}^{-1/2}} - \frac{{\rm St}_2^2}{{\rm St}_2 + {\rm Re}^{-1/2}} \right) . \tag{4.5}$$

${\rm St}_{1,2}$ denotes the Stokes number of the two particles. $V_0 = \sqrt{\alpha} c_{\rm s}$ is the turbulent velocity of the gas introduced in the introduction. The Reynolds number Re is given by the ratio $\nu_{\rm t}/\nu_{\rm m}$, where $\nu_{\rm t}$ and $\nu_{\rm m}$ is the turbulent and molecular viscosity of the gas, respectively. The Kolmogoroff time scale is given by $\tau_\eta = \tau_{\rm ed}/\sqrt{\rm Re}$. It is interesting to note that two equal-sized particles do not have a relative velocity in this regime.

If the stopping time of the larger particle τ_1 is in the intermediate regime $\tau_\eta \leq \tau_1 \leq \tau_{\rm ed}$, where $\tau_{\rm ed}$ is the large eddie turn-over time introduced in Chapter 1, then the relative turbulent velocity is

$$\Delta v_{\rm t}^2 = \frac{3}{2} V_0^2 \, {\rm St}_1 \, \left[\frac{13}{5} - \epsilon_t + \frac{2}{1+\epsilon_t} \left(\frac{5}{13} + \frac{\epsilon_t^3}{\frac{8}{5} + \epsilon_t} \right) \right] , \tag{4.6}$$

where the quantity ϵ_t is given by the ratio $\epsilon_t = {\rm St}_2/{\rm St}_1$.

For $\tau_1 \geq \tau_{\rm ed}$, the relative turbulent velocity between the two particles is simply

$$\Delta v_{\rm t}^2 = \frac{3}{2} \, V_0^2 \, \left(\frac{1}{1+{\rm St}_1} + \frac{1}{1+{\rm St}_2} \right) . \tag{4.7}$$

To give an impression of full relative dust particle velocities in a protoplanetary disk,

$$\Delta v(\tau_1, \tau_2)^2 = \Delta v_{\rm bm}^2 + \Delta v_{\rm ds}^2 + \Delta v_{\rm rd}^2 + \Delta v_{\rm t}^2 \, , \tag{4.8}$$

Fig. 4.2 shows a contour plot of this quantity at 1 AU including Brownian motion, differential settling, relative turbulent velocities and relative particle drift velocities. The same calculation at 10 AU is shown in Fig. 4.3.

In this model, two particles at a certain point in space with a certain mass will always collide with the same constant velocity. For example, two 5 cm size pebbles at 1 AU in the disk midplane will always collide with the average relative velocity of 44.3 m/s. This is apparently not true. In principal, relative velocities have stochastic variations. If we consider turbulent velocity fluctuations it may well be that particles do not only collide with the average relative velocity $\bar{v}$ but sometimes also with a speed of ≈ 0 m/s or $2\bar{v}$. This surely influences the particle growth during the evolution of the disk. We will come back to this point at the very end of this chapter.

4.1.3 Time evolution of the dust

What are the growth time scales of the solid particles at different radii in the disk? To answer this question, we will not allow any radial motion of the particles. We glue the dust to a certain radial position even though the radial drift of the dust is potentially very high. We

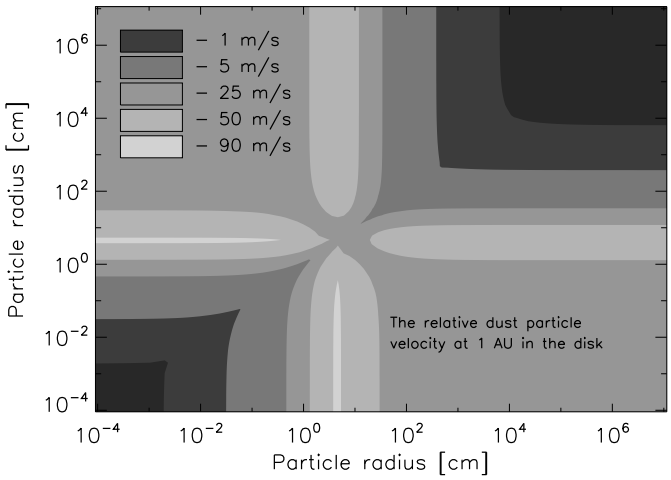

Figure 4.2: Relative velocities of dust particles at 1 AU in the disk as discussed in Sec. 4.1.2. This calculation includes Brownian motion, differential settling, relative radial and relative turbulent velocities. In this calculation we adopted a turbulent α value of 10^{-3}.

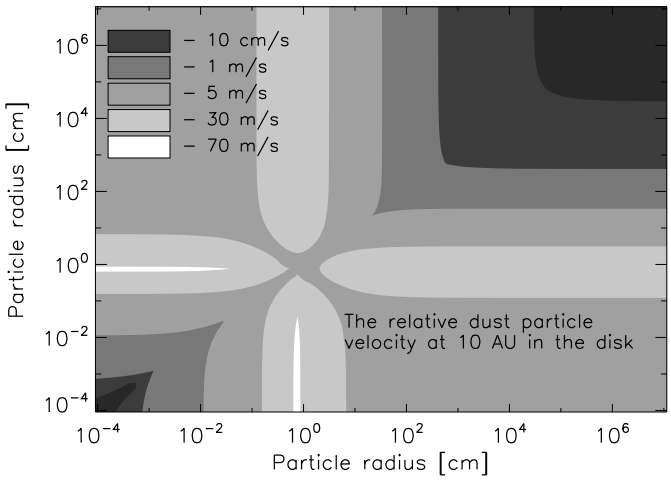

Figure 4.3: As Fig. 4.2, but now at 10 AU in the disk.

also do not allow particle fragmentation. The coagulation of solid particles at a fixed radius in the disk was for example also treated by Schmitt et al. (1997) and Dullemond & Dominik (2005), Nakagawa et al. (1981), Tanaka et al. (2005) and recently Ciesla (2007). We assume that the mass of the disk is 1% of the central mass, an initial dust-to-gas ratio of $\epsilon_0 = 10^{-2}$ and a solid material density[3] of $\rho_\mathrm{s} = 1.6$ g/cm^3. The turbulent α parameter is 10^{-3} and the turbulent q parameter is set to be 1/2. At the beginning of each simulation the dust is equally distributed between a dust particle size of 0.5 μm and 0.8 μm.

Let us first focus on the particle growth due to Brownian motion at different radii in the disk. The result of this simulation, i.e. the particle size distribution after 1 Myr, is shown in the upper panel of Fig. 4.4. According to these results, dust particles grow from sub-micrometer to ~ 30 μm in radius in 1 Myr at 1 AU in the disk. At 10 AU the particle distribution has a maximum for $a \sim 4$ μm. At 100 AU most of the dust is roughly a micrometer in size. We conclude that particle growth due to Brownian motion is not very effective, which is a well known result (Ossenkopf 1993; Schmitt et al. 1997; Dullemond & Dominik 2005). However, Brownian motion is an important effect for the following reason. We calculate the relative velocities due to Browian motion, differential settling and turbulence for $a = 0.6$ μm equal-sized particles at 1 AU in the disk. While the relative particle velocity due to Brownian motion is 0.4 cm/s the relative turbulent velocity is in the order of 10^{-8} cm/s. The relative velocity due to differential settling is practically zero. Dust particle growth due to differential settling or turbulence gets of importance only for larger particles. Therefore, Brownian motion is a trigger mechanism for the entire coagulation process which was noted before by Weidenschilling (1984).

In Sec. 2.1 we introduced the cogulation equation for a monodisperse distribution. This evolution Eq. (2.12) can be written in the form

$$\dot{a} = \frac{\rho_\mathrm{d}}{\rho_\mathrm{s}} \Delta v \; . \tag{4.9}$$

In this derivation we assumed that the collisional cross section of two equal sized particles of radius a is given by $\sigma = 4\pi a^2$. If we assume that Brownian motion is the source for the relative velocities Δv (c.f. Eq. 4.1) then the solution of this simplified growth equation is

$$a(t) = \left[\frac{5}{2} c_\mathrm{BM} (t - t_0) + a_0^{5/2} \right]^{2/5} \; . \tag{4.10}$$

The quantity a_0 is the initial grain radius and the constant c_BM can be calculated to be

$$c_\mathrm{BM} = \frac{2\epsilon_0 \rho_\mathrm{g}}{\pi} \sqrt{\frac{3kT}{\rho_\mathrm{s}^3}} \; . \tag{4.11}$$

Assuming the disk model values mentioned above, i.e. $\rho_\mathrm{g} = 1.4 \times 10^{-11}$ g/cm^3 and a temperature of 204 K then the constant c_BM has the value 1.3×10^{-20} cm$^{5/2}$/s. The particle radius after 1 Myr is then ~ 40 μm which is in good agreement with the simulation results shown in Fig. 4.4.

Now, we will additionally include coagulation due to differential settling into our model. The result of this simulation is shown in the second panel of Fig. 4.4. This plot shows that particles have grown to more than 10^4 cm in radius at 1 AU in the disk after 1 Myr. This particle size is more than 6 orders of magnitude larger than the grain size after 1 Myr caused

[3] 10% silicate, 30% carbonaceous material and 60% ice

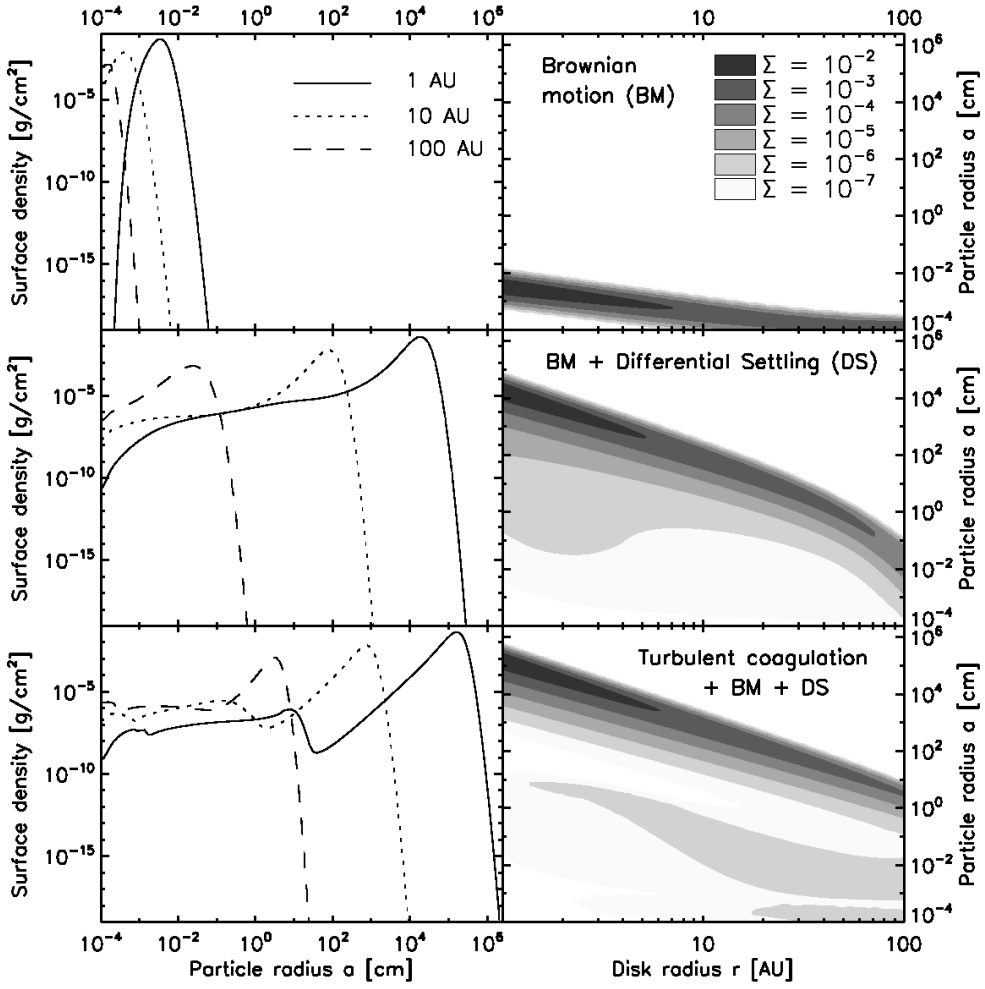

Figure 4.4: These plots show the particle size distribution at different radii in the disk after 1 Myr of disk evolution as discussed in Sec. 4.1.3. The left and the right plot always belong together. From top to bottom more and more growth mechanisms are included in the simulations. The upper panel shows coagulation only due to Brownian motion (BM). The second panel shows BM and differential settling (DS). Finally, BM + DS and turbulent coagulation (TC) are shown in the lowest panel. The left plots show the surface density of the dust at 1, 10 and 100 AU as a function of particle radius. On the right side the corresponding contour plots of the dust surface density are shown as a function of the radial location in the disk and the particle radius. In these simulations the radial drift as well as the fragmentation of the dust particles were neglected.

by Brownian motion. Most particles at 10 AU and 100 AU have grown to sizes of about 1 m and 100 μm, respectively. We conclude that differential settling is an effective growth mechanism which can create large boulders in the inner parts of the disk. Note that in our model the vertical mixing continuously allows the grains to go back up again and grow again by differential settling. Therefore, the maximal size formula of Safronov (1969) does not apply here.

Apart from the fact that particles grow to much larger sizes if differential settling is included, Fig. 4.4 also shows that there is always a certain amount of small particles that remains in the disk and that does not coagulate for at least 1 Myr. After this time, roughly 6% of the dust between 1 and 75 AU is still present in grains < 1 mm. The reason for this is the following. Not all of the dust particles coagulate at the same time. While a certain fraction of the dust has already grown to larger sizes and formed a thinner dust layer, another certain fraction of small dust remains in the higher regions above the midplane. These small dust particles high above the midplane are subject to a rather slow coagulation process. The dust densities above the midplane are low after most of the dust already settled closer to the midplane. This leads to long growth time scales. Larger particles close to the midplane can not sweep up the smaller particles above the midplane since turbulence is not able to stir them up so far. For this reason small particles remain in the disk for a long time.

We will now also include relative velocities of the particles caused by random turbulent motions. The result of this simulation is shown in Fig. 4.4 in the lower panel. This plot indicates that the dominant grain size at 1 AU, i.e. the grain size corresponding to the surface density maximum, changes by a factor of ~ 10 if turbulent coagulation is included in the simulation. The dominant particle radius at 1 AU is $\sim 10^5$ cm. At 100 AU, random turbulent motions also speed up the coagulation process which leads to particles of a few centimeters in radius after 1 Myr of disk evolution. Without relative turbulent velocities included in the simulation, the particle radius was two orders of magnitude smaller.

4.2 Step 2 - Dust particle coagulation and radial motion

We will now include radial motion, both as transport and as extra source of relative velocities for coagulation. This significantly changes the results of the last section. We find that the radial drift of solid particles is so high that the dust drift into the evaporation zone long before larger particles in the disk can possibly form. This happens even though an additional source for coagulation is introduced which decreases the coagulation time scales. We will investigate if particles can in some way "break through" the radial drift barrier. Before we come to the results, we introduce the continuity equation.

4.2.1 Continuity equation

In Chapter 3 we extensively discussed the radial motion of dust in a disk. In order to include this radial motion into our disk model, we have to solve the continuity equation in the radial direction for every particle species $m_{\rm k}$. This equation is given by

$$r\dot{\Sigma}_{\rm k} + \partial_r \left(r F_{\rm k} \right) = 0 \; . \tag{4.12}$$

The factors r account for the fact that we solve the equation in cylindrical coordinates. The quantity $F_{\rm k}$ is the dust mass flux of particles of mass $m_{\rm k}$ and it is given by

$$F_{\rm k} = \Sigma_{\rm k} v_{\rm r}^{\rm k} - D_{\rm k} \Sigma_{\rm g} \partial_r \left(\frac{\Sigma_{\rm k}}{\Sigma_{\rm g}} \right) \; . \tag{4.13}$$

The first term on the right side is the mass flux for the radial drift of individual particles. The second term is the mass flux due to turbulent diffusion (radial mixing). The radial drift velocity of a particle with mass m_k is

$$v_\mathrm{r}^\mathrm{k} = \frac{v_\mathrm{gas} - 2v_\mathrm{N}\mathrm{St}_\mathrm{k}}{1 + \mathrm{St}_\mathrm{k}^2} \,. \tag{4.14}$$

The standart velocity scale v_N was introduced in Chapter 3 and the gas velocity can be calculated to be $v_\mathrm{gas} = -84\alpha v_\mathrm{N}/51 \approx -1.65\alpha v_\mathrm{N}$. The unusual factor arises from the specifications of our disk model. The diffusion coefficient for solid particles D_k was already mentioned in the introduction.

In the expression for the radial drift of dust we neglect collective and viscous effects between the gas and the dust. This has several reasons. First, if collective effects are taken into account then the radial drift velocity is dependent on the local dust to gas ratio. If so, then the vertical integration techique as presented in Chapter 2 is not applicable and the computer simulation time increases by a factor of 100. Second, collective and viscous effects only get of importance for turbulent α-values lower than 10^{-4}. Since we generally consider disks with higher degrees of turbulence in this chapter, these effects play a minor role. Third, particle fragmentation in the later sections will show that dust grains can not grow to sizes where collective and viscous effects are important.

4.2.2 Time evolution of the disk

Fig. 4.5 shows the time evolution of the dust if now particle coagulation and radial motion are taken into account. This plot indicates that cm-dm-sized particles form in the inner regions of the disk (< 2 AU) within the first 10^3 yrs. Compared to the outer parts of the disk the formation of these particles appears rather quickly due to comparatively high gas and dust densities and high temperatures. However, before the dust particles can reach more than dm size they rapiply drift radially inwards. The radial motion is so fast, that solid particles do not cross the $\mathrm{St} = 1$ line, i.e. the line of maximum radial drift. With increasing distance from the central star the formation of larger particles gets more and more difficult. At 10 AU in the disk, it is still possible to form mm-sized particles in 10^4 yrs according to Fig. 4.5. However, in the outer parts of the disk (> 100 AU) the dominant particle size of the dust never exceeds 0.1 mm at any time. The disregard of radial drift in the previous section led to particle sizes of more than a centimeter at 100 AU after 1 Myr, which is orders of magnitude larger.

The neglect of radial drift, as discussed in section 4.1.3, involved a permanent amount of small particles which was present throughout the disk for at least 1 Myr. These small particles were located high above the midplane and were subject to a rather slow coagulation process due to relatively low dust densities. Fig. 4.5 indicates that there is a smaller remaining amount of small dust if radial motion is taken into account. This is due to the following reason. Even the small particles in the higher regions of the disk can have relative radial velocities of the order of some mm/s or even cm/s. These higher relative velocites lead to higher collision rates and, hence, to a depletion of the small dust grains.

After 10^5 yrs of disk evolution, the average particle size at a certain radius in the disk starts to decrease in time. To give an example, after 10^5 yrs the dominant dust grain radius at 1 AU is ~ 1 cm. After 1 Myr this value is about an order of magnitude lower. While particles drift inward from a certain radial position they are replaced by other particles from the outer parts of the disk. The coagulation time scales are larger in the outer parts of the disk which

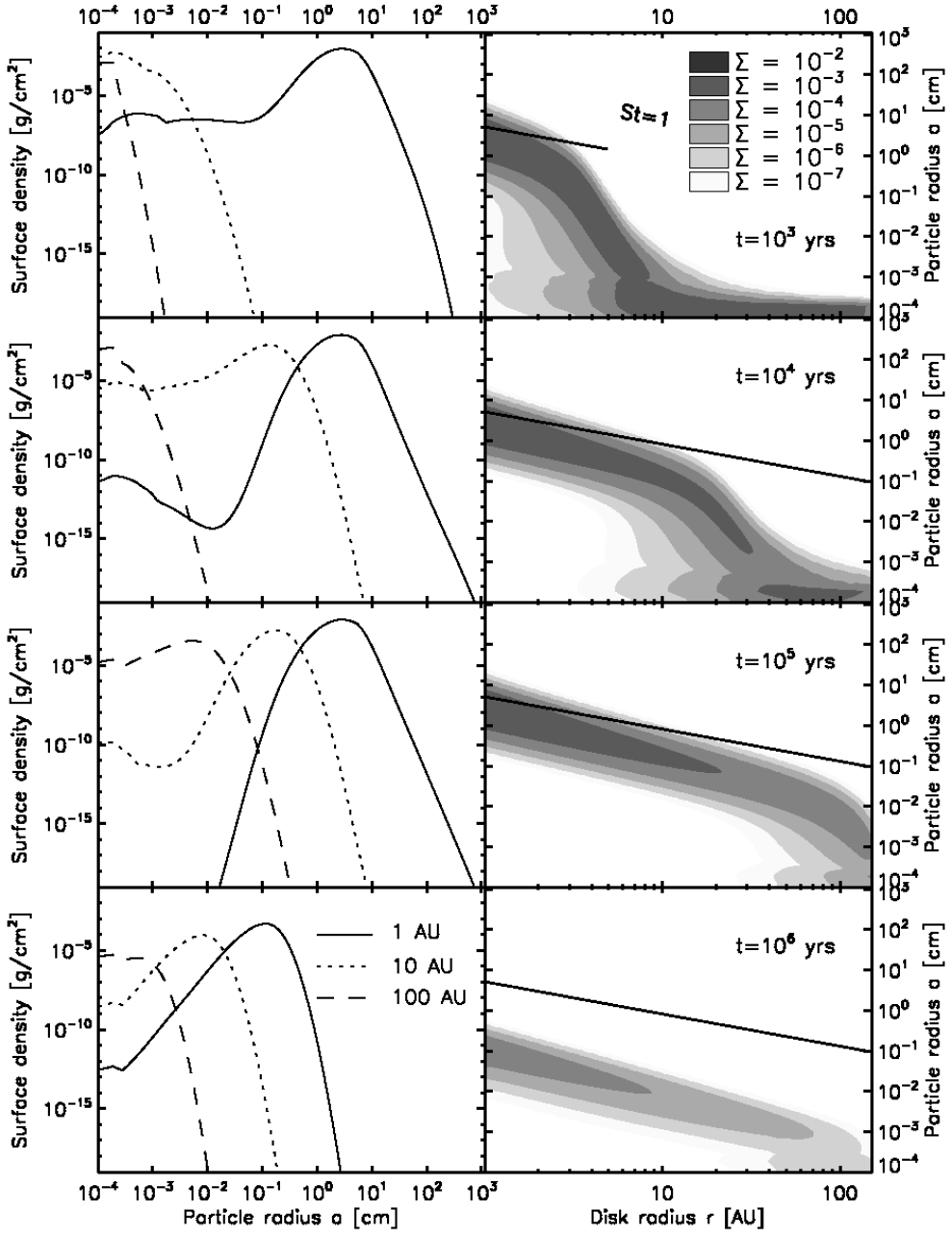

Figure 4.5: The particle size distribution at different radii in the disk at different times of disk evolution as discussed in Sec. 4.2.2. In this simulation all particle gowth mechanisms are included as well as the radial motion of the dust. The fragmentation of particles is neglected. The left and the right plots always belong together. The left column shows the surface density as a function of particle radius at 1, 10 and 100 AU. The right column shows the corresponding contour plots of the surface density as a function of disk radius and particle radius. The white lines in the contour plots denotes the particle radius for which the Stokes number is unity (i.e. largest radial drift and largest radial velocities).

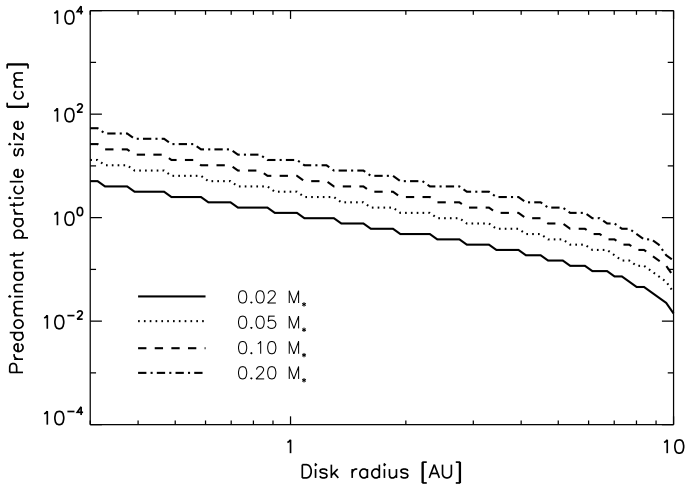

Figure 4.6: The effect of disk mass on the particle growth as discussed in Sec. 4.2.3. Shown is the dominant dust particles radius after 10^4 yrs of disk evolution for different disk masses between 0.2 and 10 AU. The turbulent α parameter is 10^{-3} and the initial dust-to-gas ratio is 10^{-2}.

means that particles grow to smaller sizes in the same time. Therefore, the particles that reach a certain position are smaller than the particles that drift away and, hence, the average dust particle size decreases.

In these simulation results, we see that the particle size at 100 AU is always smaller than a millimeter. This is in contradiction with millimeter interferometry data (c.f. last chapter) which suggests the presence of mm to cm-sized pebbles in the outer parts of the disk. This hints towards the point that there is a planetesimal formation mechanism missing in these calculations. Possible explanations for this inconsistency will be discussed in the last Chapter.

4.2.3 Effect of disk mass

We investigate the effect of disk mass on the particle growth. The result of this investigation can be seen in Fig. 4.6. This plot shows the dominant dust particle size for different disk masses after 10^4 yrs of disk evolution as a function of disk radius. We find that the particle size increases by an order of magnitude if the disk mass is increased from 1% to 20% of the central mass. Larger disk masses lead to higher gas and dust densities and, hence, to higher collision rates according to Eq. (2.23). Therefore, dust particles can grow to larger sizes over the same time interval.

The Stokes number of the dominant particles is always smaller than unity. Of course, particles may grow to larger sizes which increases the Stokes number since $\mathrm{St} \propto a$. However, larger disk masses also lead to higher gas densities which again decreases the Stokes number because $\mathrm{St} \propto 1/\rho_\mathrm{g}$. Finally, both effects cancel out and the disk mass seems to plays a minor role in breaking the radial drift barrier.

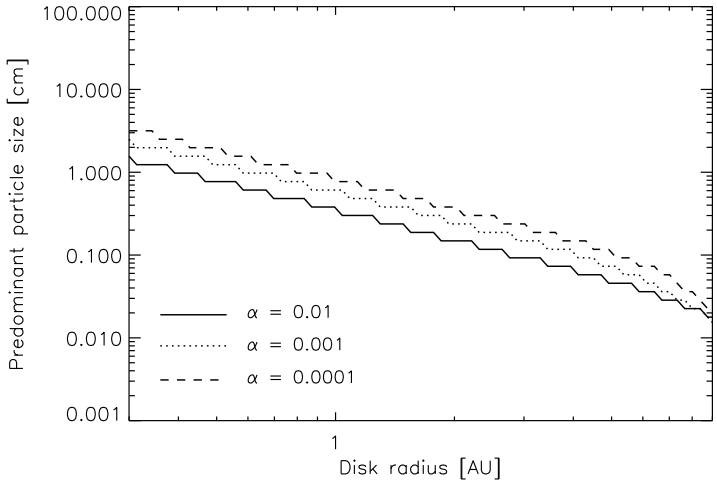

Figure 4.7: Same plot as Fig. 4.6 but now showing the effect of turbulence on the particle growth as discussed in Sec. 4.2.4. Shown is the dominant particles size after 10^4 yrs of disk evolution for different turbulent α parameters between 0.2 and 10 AU. The disk mass is 10^{-2} $M_\star$ and the initial dust-to-gas ratio is 10^{-2}.

4.2.4 Effect of turbulence

As in the last section, we calculate the dominant particle size after 10^4 years but now for different turbulent α-parameters instead of different disk masses. The initial dust-to-gas ratio in this simulation is 10^{-2}, the disk mass is 10^{-2} $M_\star$ and the result is shown in Fig. 4.7. One would intuitively think that in a certain time particles can grow to larger sizes in highly turbulent disks than in low-turbulent disks. Fig. 4.7 shows, however, that the dominant particle size after 10^4 yrs is only weakly dependent on the turbulence parameter α. If α changes by two orders of magnitude then the dominant particle size only changes by a factor of two. This can be understood by the following consideration.

A high amount of turbulence in the disk leads to high relative turbulent particle velocities (Völk et al. 1980; Weidenschilling 1984; Cuzzi et al. 2001). These high relative velocities cause high collision rates, cf. Eq. (2.23), which favour the process of coagulation. For this reason particles should have grown to larger sizes in highly turbulent disks. On the other hand, a large amount of turbulence leads to thick particle layers. The dust is stirred up in the higher regions of the disk which causes the average dust densities to decrease. The collision rates in Eq. (2.23) are proportional to the particle number densities. Lower dust particle densities lead to longer coagulation time scales.

The two determining factors for the growth time scales, the relative turbulent particle velocity and the dust density, seem to cancel out if the amount of turbulence in the disk is varied. Hence, different α-parameters lead to the same particle size over the same time interval.

4.2.5 Effect of the initial dust-to-gas ratio

We now investigate the effect of the initial dust-to-gas ratio on the growth time scales and the particle size distribution. We consider a disk mass of 10^{-2} $M_\star$ and a turbulence parameter

α of 10^{-3}. Fig. 4.8 shows the surface density of the particle distribution as a function of disk location and particle radius for four different initial dust-to-gas ratios after 10^4 yrs of disk evolution. These results indicate that $10^4 - 10^5$ cm sized boulders can form in the inner parts of the disk (< 3 AU) subject to the condition that the initial dust-to-gas ratio of the disk is higher than 1%. This means that the dust particles may overcome the radial drift barrier if the dust-to-gas ratio is slighly higher than usually assumed. A contour plot of the surface density distribution with $\epsilon_0 = 0.03$, i.e. in the case where the particles are able to break through the radial drift barrier for disk radii < 3 AU, as a function of time is shown in Fig. 4.9.

To understand the importance of the initial dust-to-gas ratio we consider the growth rate of the dust particles (cf. Eq. 4.9),

$$\dot{a} = \frac{\rho_\mathrm{d}}{\rho_\mathrm{s}} \Delta v \; . \tag{4.15}$$

If we assume that the particles have Stokes numbers smaller than unity then the relative turbulent particle velocity is given by (Cuzzi et al. 2001; Weidenschilling & Cuzzi 1993)

$$\Delta v_\mathrm{turb} \propto \sqrt{\alpha \mathrm{St}}\, c_\mathrm{s} \; . \tag{4.16}$$

The dust mass density can be approximated by $\rho_\mathrm{d} \propto \Sigma_\mathrm{d}/h$ so that we obtain

$$\dot{a} = \frac{1}{\rho_\mathrm{s}} \frac{\Sigma_\mathrm{d}}{h} \sqrt{\alpha \mathrm{St}}\, c_\mathrm{s} \; . \tag{4.17}$$

With the height of the dust layer $h/H = \sqrt{\alpha/\mathrm{St}}$, the last expression can be written as (for $\mathrm{St} < 1$)

$$\dot{a} = \frac{1}{\rho_\mathrm{s}} \epsilon_0 \Sigma_\mathrm{g} \mathrm{St} \Omega_\mathrm{k} \; . \tag{4.18}$$

If we also take into account the definition of the Stokes number as discussed in the introduction, then most quantities cancel each other out, particularly the gas surface density Σ_g, leading to

$$\dot{a} = a \epsilon_0 \Omega_\mathrm{k} \tag{4.19}$$

with the solution

$$a = a_0 e^{\epsilon_0 \Omega_\mathrm{k} t} \; . \tag{4.20}$$

This expression shows that only the initial dust-to-gas ratio ϵ_0 and the Kepler frequency Ω_k determine the turbulent growth time scales as long as $\mathrm{St} < 1$. According to Eq. (4.20), the time scales are not linear dependent on the initial dust-to-gas ratio. An increase of ϵ_0 leads to an exponential decrease of the growth time scales. This strong dependency unveils the crucial importance of this initial parameter. Eq. (4.20) also shows that turbulent coagulation occurs faster in the inner parts of the disk than in the outer parts since $\Omega_\mathrm{k} \propto r^{-1.5}$. For this reason, the particles first break through the radial drift barrier in the inner parts of the disk (cf. Fig. 4.8).

In Section 4.2.3 and 4.2.4 we have seen that the dominant particle size only shows a weak dependency on the disk mass and the amount of turbulence in the disk. This can also be explained by Eq. (4.18). The turbulent growth rate of the dust is neither dependent on the disk mass nor on the turbulent α parameter. Moreover, this expression also indicates that the disk temperature and intrinsic particle properties like solid density are rather unimportant as long as the Stokes number of the particles is smaller than unity and turbulence is the leading process that triggers coagulation. However, Ormel et al. (2007) have shown that the porosity

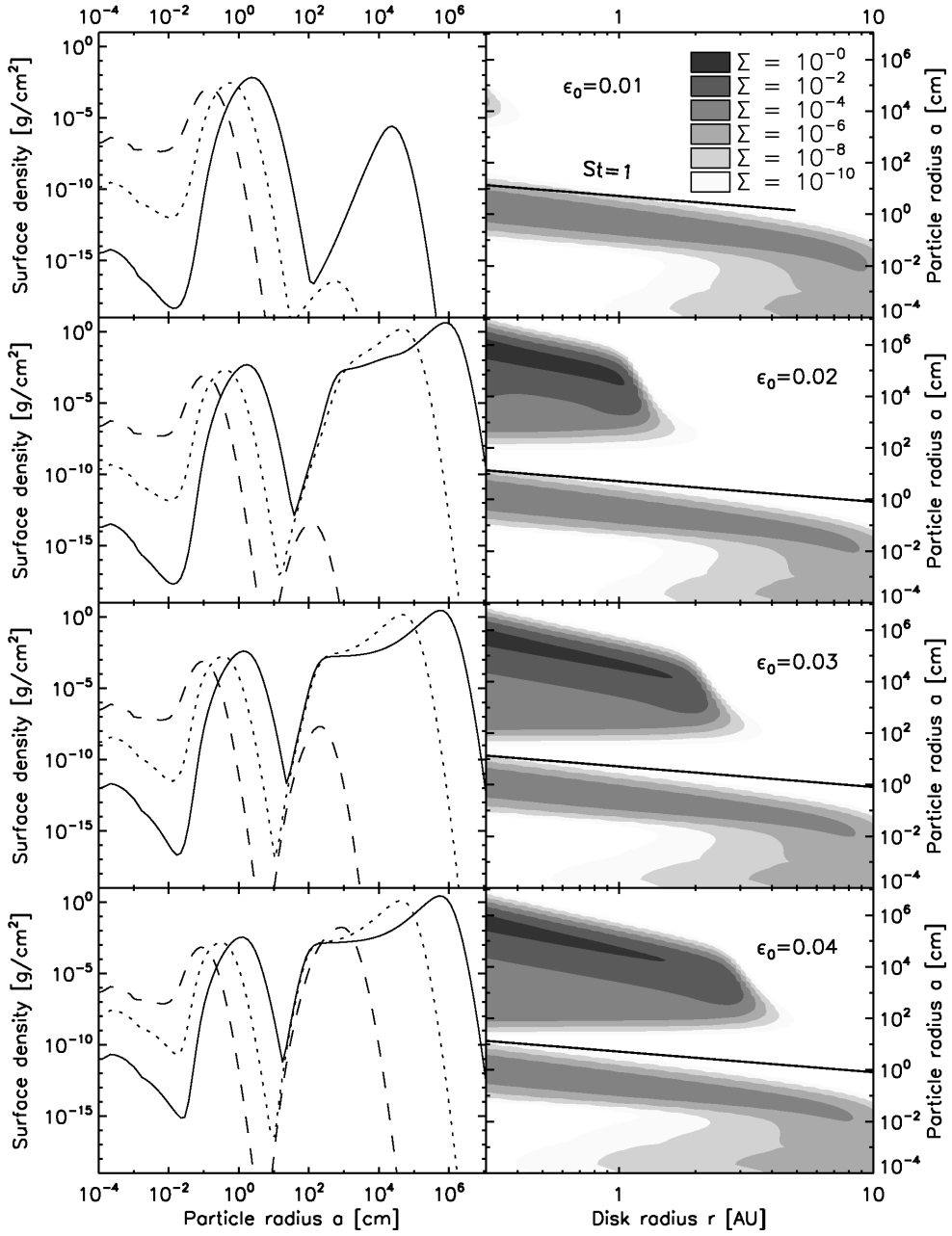

Figure 4.8: These plots shows the effect of the initial dust-to-gas ratio on the particle growth as discussed in Sec. 4.2.5. The right side shows contour plots of the surface density as a function of disk location and particle radius for 4 different initial dust-to-gas ratios after 10^4 yrs of disk evolution. The corresponding left plots show the surface density as a function of particle radius for 3 different locations in the disk (0.3 AU - solid, 1 AU - dotted, 3 AU - dashed) after the same time. The disk mass is 10^{-2} $M_\star$ and the turbulent α parameter is 10^{-3}. For initial dust-to-gas ratios which are slighly higher than 1% the particles break through the radial drift barrier.

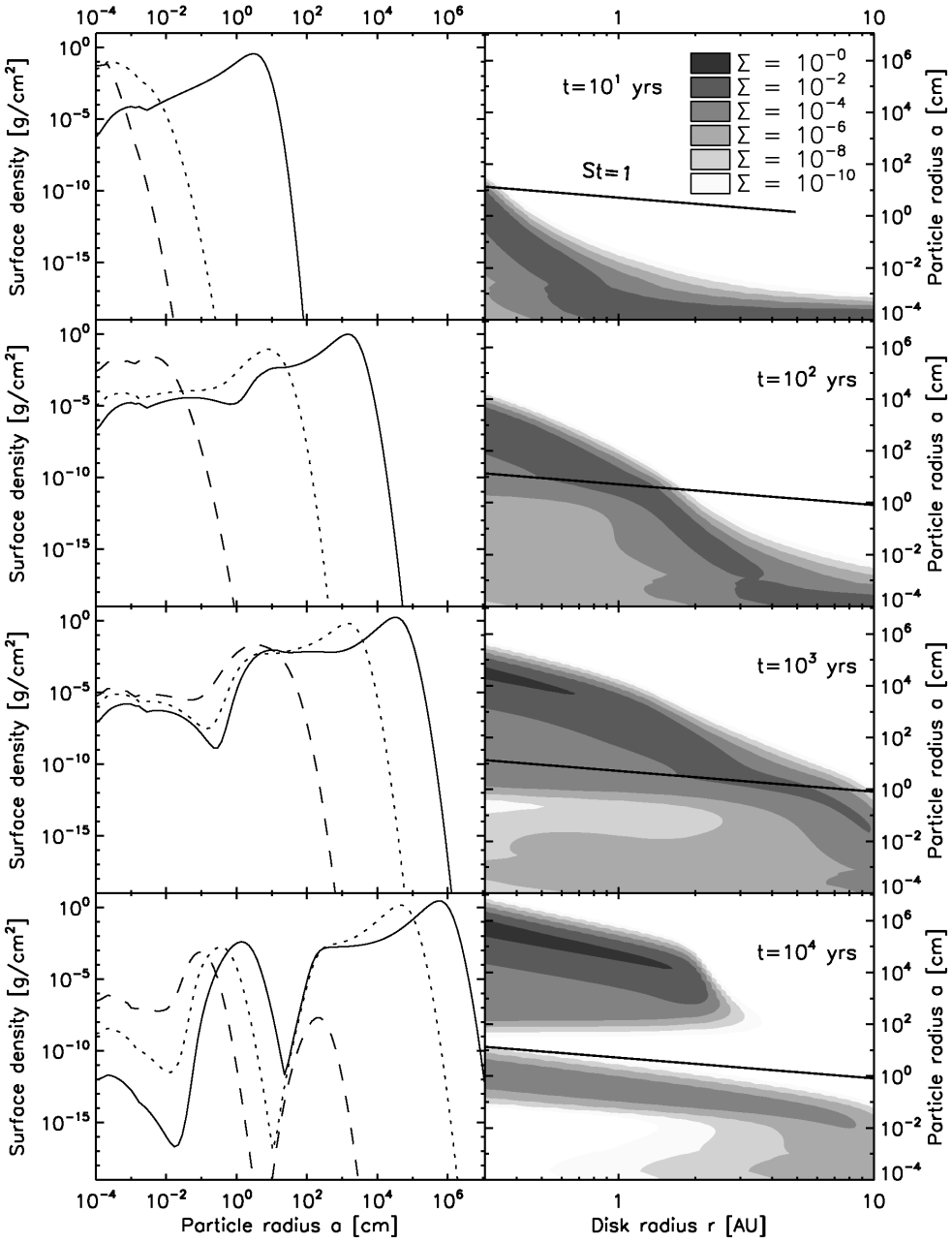

Figure 4.9: This plot shows the results of a simulation in which the particles can break through the radial drift barrier as discussed in Sec. 4.2.5. Particle fragmentation is neglected in this simulation. Shown is the surface density distribution for the first 10^4 yrs of disk evolution for an initial dust-to-gas ratio of 0.03 as a function of disk radius and particle radius. The disk mass is 10^{-2} $M_\star$ and the turbulent α parameter is 10^{-3}. The right side is a contour plot of the surface density. The left side shows the absolute values of the surface density for 3 different disk radii (solid - 0.3 AU, dotted - 1 AU, dashed - 3 AU).

of dust particles actually matters in the early phases of disk evolution. This discrepancy is due to the fact that the Eq. (4.20) only holds if $\mathrm{St} > \alpha$ while Ormel et al. (2007) considered particles with $\mathrm{St} < \alpha$. Moreover, Brownian motion is the main source for relative particle velocities for small dust grains in the early disk evolution while the derivation of Eq. (4.20) assumes that turbulence is the major source for relative particle velocities.

4.2.6 The radial drift barrier

We estimate in which regions of the disk and under which conditions solid particles can theoretically overcome the radial drift barrier. In section 4.2.5 we have seen that particle coagulation due to turbulence in the disk can be described by $\dot{a} = a\Omega_\mathrm{k}\epsilon_0$. We define a particle growth time scale τ_g by

$$\tau_\mathrm{g} = \gamma\frac{a}{\dot{a}} = \frac{\gamma}{\Omega_\mathrm{k}\epsilon_0} \,. \tag{4.21}$$

The parameter γ measures how much the solid particle has to grow to cross the particle size region of fast radial drift, i.e. to overcome the radial drift barrier. We assume this parameter to have a certain value determined by the disk model and to be a constant throughout the disk. The largest radial drift velocity in the disk is approximately given by $c_\mathrm{s}^2/V_\mathrm{k}$. We define a radial drift time scale τ_d by

$$\tau_\mathrm{d} = \frac{r}{c_\mathrm{s}^2/V_\mathrm{k}} \,. \tag{4.22}$$

The ratio between these two time scales is given by

$$\frac{\tau_\mathrm{g}}{\tau_\mathrm{d}} = \frac{\gamma}{\epsilon_0}\left(\frac{H}{r}\right)^2 \,. \tag{4.23}$$

Now, the particles may overcome the radial drift barrier if the ratio $\tau_\mathrm{g}/\tau_\mathrm{d}$ is smaller than unity, i.e. if the growth time scales are smaller than the radial drift time scales. The parameter γ is still indefinite. To specify this parameter we consider Fig. 4.8 in Section 4.2.5. These simulation results show for which initial dust-to-gas ratio ϵ_0 the particles break through the meter size barrier at a certain radius in the disk. We chose the parameter γ in a way that the condition $\tau_\mathrm{d} > \tau_\mathrm{g}$ is in agreement with the results shown in this figure. This leads to $\gamma \approx 12$. With this value, the particles should overcome the radial drift barrier if the inequality

$$\epsilon_0 \gtrsim 12\left(\frac{H}{r}\right)^2 \tag{4.24}$$

holds.

The particles, which break through the radial drift barrier in Fig. 4.8, have already drifted inwards. For this reason, the critical value given by Eq. 4.24 indicates the initial dust-to-gas ratio for which the particles most likely break through the radial drift barrier. The sufficient ϵ_0-value to overcome the radial drift barrier is presumably even lower than this value.

4.2.7 Dust mass loss in the disk

When particles drift into the evaporation zone, they are lost for the process of planetesimal formation. Hence, the question of how much solid material is actually lost due to its drift into the inner regions is of essential importance. We calculate the mass which is present in small ($\mathrm{St} < 1$) and large ($\mathrm{St} > 1$) particles between 0.5 AU and 150 AU as a function of time for different initial dust-to-gas ratios. The result of this calculation can be seen in Fig. 4.10.

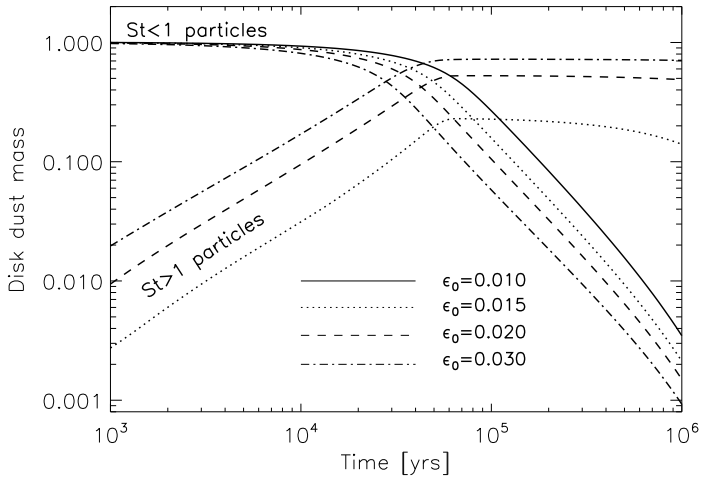

Figure 4.10: The mass of the dust disk for small (St < 1) and large (St > 1) particles between 0.5 AU and 150 AU as a function of time for different initial dust-to-gas ratios as discussed in Sec. 4.2.7. In this simulation only the particle coagulation and the radial motion of the dust were considered. Particle fragmentation was neglected.

This plot shows, that the mass of the dust disk does not change significantly within the first 10^4 yrs for every initial dust-to-gas ratio considered. Since the power law index of the surface density is -0.8, most of the solid particles are in the outer regions of the disk. Fast radial drift in the inner disk regions which takes place in $\sim 10^3$ yrs does not change the total dust mass in the disk.

After a few 10^4 yrs, the mass present in small grains starts to decrease. After 1 Myr of disk evolution, this mass is less than 1% of the initial dust mass. The amount in small grains, i.e. St < 1 particles, is dependent on the initial dust-to-gas ratio. For $\epsilon_0 = 0.01$ roughly 0.4% of the initial particle mass is present in small grains. For $\epsilon_0 = 0.03$ this mass is a factor of 4 lower. Hence, higher initial dust-to-gas ratios lead to lower dust masses in small grains after 1 Myr. In the last section we showed that particles grow faster with increasing dust-to-gas ratio. Therefore, particles can grow to larger sizes while moving radially inwards. However, larger sizes also lead to higher radial drift velocities. For this reason, the mass which is present in small particles in the disk decreases faster for increasing dust-to-gas ratios. We will find the same behaviour for the small particles in step 3 where fragmentation is also taken into account.

For an initial dust-to-gas ratio of 1%, the mass of the entire dust disk, i.e. the mass in small and large particles, after 1 Myr between 0.5 AU and 150 AU is 0.4% of the initial dust mass. Most of the dust has drifted into the evaporation zone. For higher initial dust-to-gas ratios, i.e. higher than 0.015, the particles in the inner regions of the disk can break through the radial drift barrier. These larger boulders around 1 AU then sweep up smaller particles which drift inwards from larger radii (cf. Fig. 4.10 between 10^3 yrs and $\sim 5 \times 10^4$ yrs). After $\sim 5 \times 10^4$ yrs most of the dust mass is present in large boulders. While for $\epsilon_0 = 0.015$ roughly 20% of the initial dust mass is present in St > 1 particles after 1 Myr, the remaining mass in large boulders is a factor of ~ 4 higher for $\epsilon_0 = 0.03$. Note that the mass of the remnant dust disk after 1 Myr changes by a factor of ~ 200 by changing the initial dust-to-gas ratio from

1% to 3%. We conclude that the initial dust-to-gas ratio is a crucial parameter which has an important influence on how much solid material remains in the disk after 1 Myr. However, the mass present in small grains is always less than 0.4% of the initial dust mass after 1 Myr no matter the value of ϵ. Note that this finding is in agreement with observationally inferred dust disk life times of less than a few Myrs (Haisch et al. 2001).

4.3 Step 3 - Coagulation, radial motion and fragmentation

Collisions between particle aggregates do not necessarily lead to particle growth. For sufficiently high relative collision velocities, the aggregates may fragment into smaller bodies. Fragmentation velocities of aggregates are usually of the order of a few cm/s up to several 10 m/s. While smaller particles tend to stick to each other up to high relative particle velocities (Dominik & Tielens 1997) larger bodies show the tendency to fragment even for small relative velocities (Benz 2000). For simplicity, we will assume a fixed threshold velocity for particle destruction $v_{\rm f}$ which does not depend on the mass of the particles. We will investigate how the results of the simulations change if $v_{\rm f}$ is varied over a wide parameter range.

The result of destructive collisions between solid particles, i.e. the exact particle distribution after fragmentation, is still a matter of debate. Usually this particle distribution is described by a power-law,

$$n(m)\,{\rm d}m \propto m^{-\xi}{\rm d}m\,. \tag{4.25}$$

In this expression $n(m){\rm d}m$ is the number of particles per unit volume within the mass range $[m, m + {\rm d}m]$. The last decades involved various attempts to determine the fragmentation parameter ξ. Mathis et al. (1977) and also Draine & Lee (1984) showed that the extinction and scattering of starlight by interstellar dust can be reproduced by a power-law dependency following $\xi = 1.83$. Experimental studies found values for ξ ranging between 1.3 (low-velocity impacts) and 2 (catastrophic impacts) (Davis & Ryan 1990; Blum & Muench 1993). Steady state solutions between coagulation and fragmentation lead to $\xi = 1.83$ as shown by Dohnanyi (1969). More recently, Tanaka et al. (1996) argued that the very general result $\xi = 1.83$ is a direct implication of the self-similarity of the particle size distribution. In this section we will assume the ξ-value 1.83 if not otherwise noted.

The process of fragmentation between particles which have the same mass is different from the fragmentation of particles whose mass differ by orders of magnitude. Two bodies of equal mass may destroy each other. Small dust grains, however, are not able to destruct a meter-sized body. But they can excavate a small crater in the larger target. This process is usually called 'cratering'. We will assume that cratering sets in if the mass of the colliding bodies differs by more than one order of magnitude. In this case, the smaller dust particle m_s excavates a crater which contains a factor χ times its own mass, i.e. $m_{\rm crater} = \chi m_s$. The parameter χ is set to unity if not otherwise noted. The mass of the smaller body and the crater ejecta are then redistributed according to Eq. (4.25). On the other hand, if the mass of the colliding particles differs by less than an order of magnitude, i.e. in the non-cratering case, then the total mass is redistributed following Eq. (4.25). To illustrate the results of fragmentation Fig. 4.11 shows the outcome of a destructive collision as modeled here. The solid line shows the outcome of fragmentation in the case of cratering. The dotted line corresponds to the fragmentation results of two particles with the same mass.

In this section, we will assume that the probability for fragmentation $p_{\rm f}$ only depends on

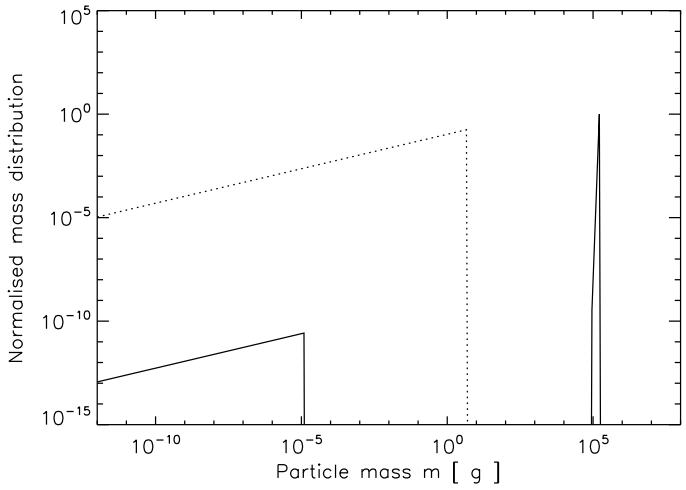

Figure 4.11: The assumed fragmentation results of collisional destruction as discussed in Sec. 4.3. The solid line shows an example for cratering. The larger body has a mass of $\sim 10^5$ g. The smaller dust grain, which is destroyed in this process, had a mass of $\sim 10^{-5}$ g. The dotted line corresponds to the collision of two particles with the same mass. In this calculation the fragmentation parameter ξ is assumed to be 1.83 which means that most of the fragmentation results are at the large end of the particle size distribution.

the relative particle velocity Δv and adopt the following expression for this probability,

$$p_{\rm f}(\Delta v) = \left(\frac{\Delta v}{v_{\rm f}}\right)^{\psi} \Theta\left(v_{\rm f} - v\right) + \Theta\left(v - v_{\rm f}\right) \ . \tag{4.26}$$

The two Heaviside step functions Θ ensure that the particles fragment with 100% probability if the relative particle velocity Δv is larger than the critical fragmentation velocity $v_{\rm f}$. For $\Delta v < v_{\rm f}$ we assume that there is always a possibility for fragmentation given by $(v/v_{\rm f})^{\psi}$. We will investigate the influence of the critical fragmentation velocity $v_{\rm f}$ and the index ψ. The value of ψ is set to unity if not otherwise noted. The probability for coagulation $p_{\rm c}$ is given by $p_{\rm c} = 1 - p_{\rm f}$. The last expression implies that the particles either coagulate or they fragment. We do not allow the particles to collide and not to undergo either the process of coagulation or fragmentation. However, just for the moment let us assume that $p_{\rm f} + p_{\rm c} < 1$. If this last expression holds then the time scales for coagulation and fragmentation increase.

4.3.1 Time evolution

The evolution of the disk in the first 1 Myr including particle growth, radial motion and particle fragmentation is shown in Fig. 4.12. In this calculation, the fragmentation velocity is $v_{\rm f} = 10^3$ cm/s and the fragmentation parameter ξ is 1.83. We adopt a disk mass of $10^{-2}\ M_{\star}$, a turbulent α-value of 10^{-4} and an initial dust-to-gas ratio of 10^{-2}. The cratering-parameter χ is 0.5 and $\psi = 2$.

After 10^3 yrs of disk evolution, most of the particles in the disk < 3 AU have grown to sizes of some millimeters. However, if fragmentation is neglected (cf. Sec. 4.2), the dominant particle size at 1 AU in the disk after 10^3 yrs is an order of magnitude larger. This significant

difference is due to the fragmentation of particles. When the particles reach millimeter size then destructive effects prevent the particles from growing to larger sizes (cf. Fig. 4.2 with 10 m/s). Even after 10^4 yrs, the dominant particle size in the disk < 10 AU is still of the order of a millimeter. Hence, this particle size corresponds to the fragmentation barrier for this specific set of disk parameters. Even for long periods of time the particles are not able to overcome this barrier. Once the particles have reached the fragmentation barrier the particle distribution is characterised by an equilibrium between particle coagulation and particle fragmentation due to destructive collisions. In other words, the amount of particles of a certain mass, which are created by dust particle coagulation, equals the amount of particles, which are destroyed by high velocity collisions. This steady state will be discussed in more detail later in this Section.

Fig. 4.12 indicates that the maximum dominant particle size $a_{\max}$ and the Stokes number St have the same radial behaviour. This is due to the fact that relative particle velocities in our model (except Brownian motion) scale with this dimensionless number. For this reason, the dominant particle size follows $a_{\max} \propto r^{-0.8}$ which we obtain directly from the definition of the Stokes number.

Due to destructive collisions a large amount of dust is present in small grains as can be clearly seen in Fig. 4.12. We calculate the amount of dust which is present in grains larger (smaller) than 10^{-2} cm after 10^5 yrs of disk evolution. While 18% of the dust mass is present in grains larger than 10^{-2} cm, yet 82% of the mass is present in smaller grains. This large population of sub-mm grains should have a strong effect on the spectrum of the protoplanetary disk. However, we will not investigate the influence of the fragmentation parameters, i.e. $v_{\rm f}$ and ξ, on the disk spectrum which goes beyond the scope of this thesis.

4.3.2 Effect of turbulence

Different turbulent α-values and, hence, changing turbulent velocities should lead to different maximum particle sizes due to destructive collisions. To investigate the influence of turbulence on the fragmentation barrier, we calculate the dominant particle size for different α-values after 10^4 yrs of disk evolution. In this simulation the disk mass is $10^{-2}\ M_\star$, the fragmentation velocity is 10^3 cm/s, the initial dust-to-gas ratio is 10^{-2} and the results of the calculation are shown in Fig. 4.13.

According to this plot, the dominant particle size is fairly dependent on α in moderately turbulent disks. If α is changed from 10^{-3} to 10^{-4} then the dominant particle size $a_{\rm dom}$ changes by a factor of ~ 5. We find that less turbulence shifts the fragmentation barrier towards larger particle sizes. Hence, in less turbulent disks particles can grow to larger sizes than in highly turbulent disks.

However, this statement does not hold for extremely low turbulent disks. In these disks, turbulence is not the main source for relative velocities and, hence, the fragmentation barrier should not be dependent on α. If α is smaller than $\sim (c_{\rm s}/2V_{\rm k})^2$ (cf. Eqs. 3.2 and 4.16) which is $\sim 10^{-4}$ at 1 AU then relative particle velocities due to radial motion exceed relative dust particle motions induced by turbulence. To illustrate this independency we calculate the dominant particle size after 10^4 yrs for a practically laminar disk with a very low α-value of 10^{-10}. The result of this calculation is also shown in Fig. 4.13. In this nearly laminar disk, destructive collsions due to relative drift velocities up to 50 m/s prevent particle growth to sizes of more than ~ 2 mm at 1 AU.

Relative radial drift velocities are always due to particle size differences. Monodisperse distributions do not show relative radial motion. The simulation result for extremely low

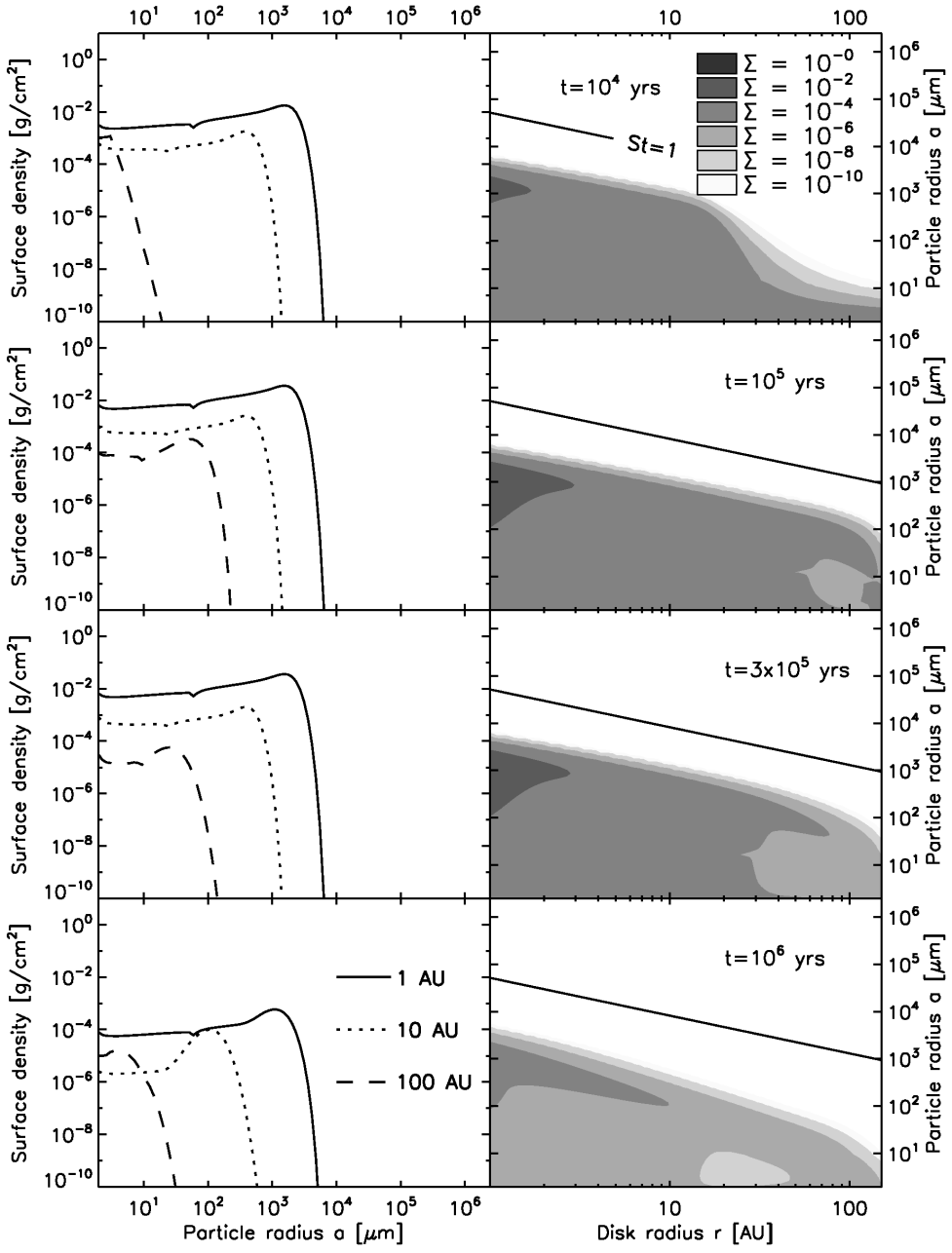

Figure 4.12: As Fig. 4.5, but now also the fragmentation of particles is included in the simulations as discusssed in Sec. 4.3.1. The left column shows the surface density as a function of particle radius at 1, 10 and 100 AU. The right column shows the corresponding contour plots of the surface density as a function of disk radius and particle size.

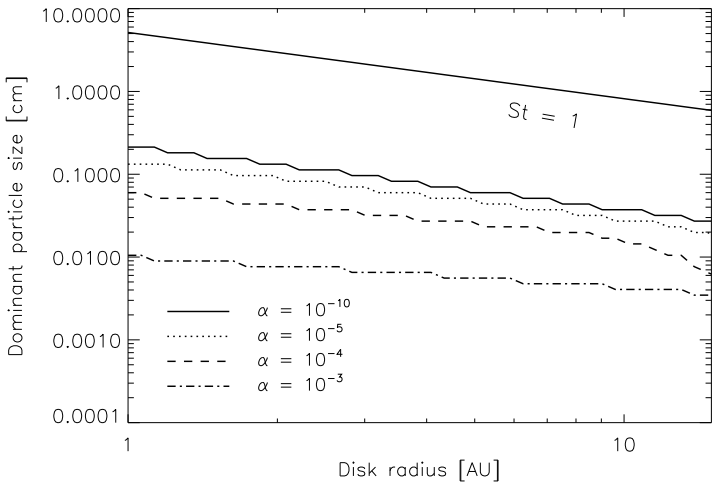

Figure 4.13: The influence of the turbulence parameter α on the dominant particle size after 10^4 yrs of disk evolution for different disk radii between 1 and 20 AU as discussed in Sec. 4.3.2. The disk mass is 10^{-2} $M_\star$, the fragmentation velocity is 10^3 cm/s and the initial dust-to-gas ratio is 10^{-2}. This graph also shows the particle size for which the Stokes number ist unity. The χ parameter is set to 0.5 and $\psi = 1$.

turbulent disks ($\alpha = 10^{-10}$) raises the question how the particle size dispersion of the dust distribution can produce such high relative velocities to inhibit particle growth to larger sizes[4].

We try to answer this question by considering the relative velocities of dust particles at 1 AU in the disk as a function of particle radius, c.f. Fig. 4.14. In this calculation, we adopt an α-value of 10^{-10} which means that relative radial motion is the main source for relative velocities. According to this figure, particle coagulation is only possible in a very narrow particle size interval, i.e. in the dark shaded regions of this plot. If the particle size dispersion is larger than the extent of this 'bottleneck' then particle fragmentation starts to play a non-negligible role. With Eq. (4.14) for the radial velocities, we can estimate the importance of fragmentation for a specific particle size dispersion. We assume a particle size distribution which has a surface density maximum at $a_0 = 3$ cm. If the size dispersion is larger than 1 cm, then particles start to fragment with 100% probability. For a particle size dispersion of 0.5 cm and 0.1 cm, the fragmentation probability decreases to 50% and 10%, respectively. Hence, only for particle size dispersions of some millimeters, particles might have the chance to overcome the fragmentation barrier. For larger size dispersions, the fragmentation probability is far too high to allow the distribution to pass the bottleneck shown in Fig. 4.14.

To investigate if the particle size dispersion is narrow enough to overcome the fragmentation barrier, we consider the following. We simulate 700 yrs of dust particle evolution neglecting fragmentation. The result of this simulation, i.e. the particle distribution at 1 AU in the disk as a function of particle size, is shown in Fig. 4.15 (solid line). The size dispersion of this particle distribution is ~ 1.5 cm. Now, particle fragmentation tends to smear out the

[4]We define the particle size dispersion as the half-width of the size distribution

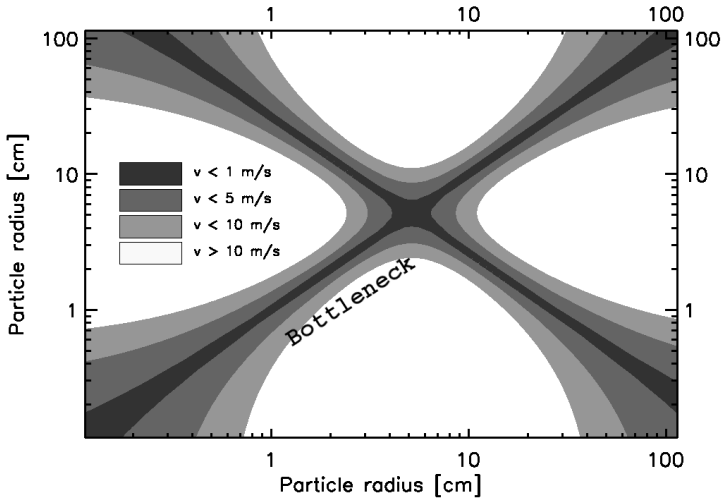

Figure 4.14: The relative particle velocities at 1 AU as a function of particle radius as discussed in Sec. 4.3.2. The turbulence parameter α in this calculation is 10^{-10}. This means that relative radial motion is the main source for relative particle velocities. A critical fragmentation velocity of 10 m/s results in a very narrow band in which particle coagulation is still possible. If the particle size dispersion is larger than the extent of this bottleneck then particle fragmentation starts to play a non-negligible role.

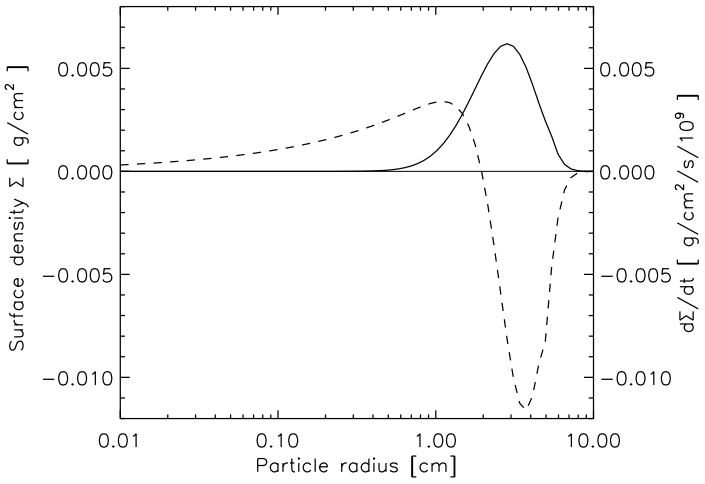

Figure 4.15: The dust particle distribution (solid) and its time derivative (dashed) as a function of particle size after 700 yrs of evolution at 1 AU in the disk as discussed in Sec. 4.3.2. The distribution is located around $a_0 = 3$ cm and it has a size dispersion of ~ 1.5 cm. In these 700 yrs, particle fragmentation was neglected. In the calculation of the source terms, which are shown in this figure, fragmentation is included. These source terms show that destructive collsions would rapidly shift the dominant particle size to smaller values.

dust distribution and it increases the particle size dispersion. Hence, the distribution shown is Fig. 4.15 represents a best case scenario; the distribution can not become narrower. What happens if we now switch on fragmentation? Fig. 4.15 also shows the time derivative of the particle distribution (dashed line) if fragmentation is considered. This curve indicates, that destructive collsions would rapidly shift the dominant particle size towards smaller values. The size dispersion is apparently too large for the particles to pass through the fragmentation bottleneck without undergoing substantial destructive collsions. If fragmentation is included in the simulations from the very beginning, then the size dispersion is even larger and, therefore, the chance of passing the narrow region of coagulation becomes even smaller.

For a fragmentation velocity of 10 m/s, which we adopt in these simulations, the particles never overcome the fragmentation barrier, regardless of the amount of turbulence in the disk since the radial drift always accounts for destruction. We find that this statement also holds for larger ψ-values. We conclude that the amount of turbulence in the disk alone does not determine whether particles can break through the fragmentation barrier or not. Note, that the maximum radial drift velocity of particles is independent of radius, so that these statements hold everywhere in the disk.

4.3.3 Effect of the fragmentation velocity

For which critical fragmentation velocities can particles break through the fragmentation barrier? To answer this question let us consider a best case scenario. We adopt a low turbulent disk, i.e. a disk in which the relative radial velocities exceed the relative turbulent particle velocities, and we neglect the effect of cratering for the moment. We calculate the dominant dust particle size as a function of disk location for three different fragmentation velocities after 10^4 yrs of disk evolution. The results of this calculation can be seen in Fig. 4.16. In this simulation, the α-value is 10^{-5}, $\chi = 0$ (no cratering) and $\psi = 2$.

For a fragmentation velocity of 5 m/s, particles can grow to millimeter size at ~ 1 AU in the disk before destructive collisions prevent further particle growth. In the outer regions, i.e. at 10 AU, the dominant particle radius is a factor of 10 smaller. Even for a relatively high critical velocity of 20 m/s the particles are not able to grow beyond a centimeter at 1 AU.

For even higher fragmentation velocities, i.e. $v_\mathrm{f} \sim 30$ m/s, solid particles start to break through the fragmentation barrier. Fig. 4.17 shows the dust particle distribution for this critical velocity as a function of disk radius and particle radius for four different times of disk evolution. This plot indicates that particles have grown to meter size in the inner parts of the disk after 10^4 yrs. However, a fragmentation velocity of several 10 m/s for centimeter- or even meter-sized boulders is at least questionable. For lower (and probably also more realistic) critical velocities, i.e. velocities of $1 \ldots 10$ m/s, we never find solid particles in our simulations which are able to overcome the fragmentation barrier for any disk parameters considered. For α-parameters, which are higher than the adopted value of 10^{-5} in the simulations of this paragraph, it is even more unlikely that solid particles may grow to larger sizes. This chance does not increase if destructive effects due to cratering are also taken into account.

4.3.4 Disk dust mass

As in Sec. 4.2.7, we calculate the solid material mass in the disk as a function of time, but now with the effect of particle fragmentation included in the simulations. The result of this calculation is shown in Fig. 4.18 which shows that the dust mass does not change significantly within the first 10^5 yrs for any ϵ_0 considered. This is the same behaviour as in the case of no

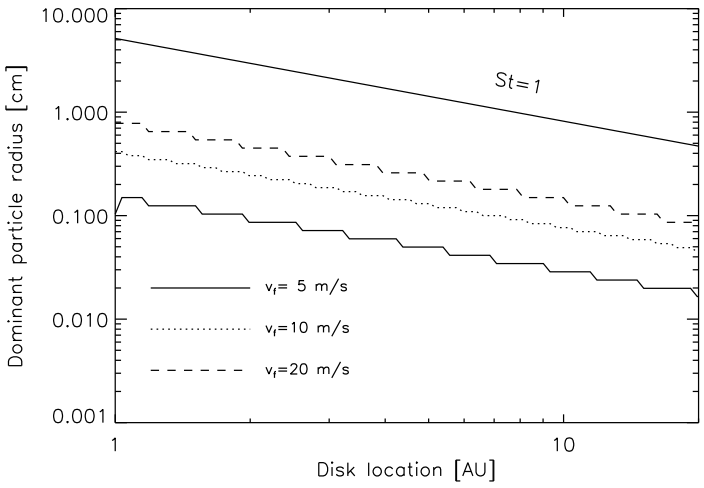

Figure 4.16: The dominant particle size as a function of disk location for three different fragmentation velocities after 10^4 yrs of disk evolution as discussed in Sec. 4.3.3. In this simulation, $\psi = 2$, $\chi = 0$, $\epsilon_0 = 0.03$ and the turbulent α-value is 10^{-5}.

fragmentation. After 10^5 yrs the mass starts to decrease rapidly. For an initial dust-to-gas ratio of 0.01 only 2% of the initial solid material mass between 1 and 150 AU remains after 1 Myr. Higher initial dust-to-gas ratios lead to less solid material after 1 Myr. For example, for $\epsilon = 0.03$ the mass is only 0.7% of the initial dust mass, which is a factor of ~ 3 lower.

Let us compare the solid material mass after 1 Myr for $\epsilon_0 = 0.01$ in the case of fragmentation/no fragmentation. We find that the remaining dust mass is a factor of 5 higher if we allow the particles to destroy each other. This difference is due to destructive collisions which lead to large amounts of small particles in the disk (cf. Sec. 4.3.1). These small dust grains have low radial drift velocities and, hence, long radial drift time scales. In other words, small particles stay much longer in the disk before they evaporate in the inner regions of the disk. For this reason, the solid material mass after 1 Myr is higher in the case of fragmentation than in the case of no fragmentation.

In the previous sections we found that if fragmentation is included in the simulations then the dust particles are not able to break through the meter size barrier. No larger particles in the inner parts of the disk can form which can sweep up smaller dust particles drifting inward from the outer regions. For this reason, most of the solid material after 1 Myr has drifted into the evaporation zone and is lost for the process of planetesimal formation.

4.3.5 Effect of disk model

In the introduction we mentioned that the disk model adopted in this chapter differs significantly from the MMSN model. This leads to the question of how the results of this chapter change if different disk models are considered. In this section, we repeat simulations of Sec. 4.3 with other disk model parameters, attempting to unveil the basic changes in the dust particle distribution. Table 4.1 shows the disk parameters for the simulations in this section. Model A and B are the MMSN model and the disk model in this section, respectively. Model C is our model, but now with 10% disk mass instead of 1% compared to $M_\star$.

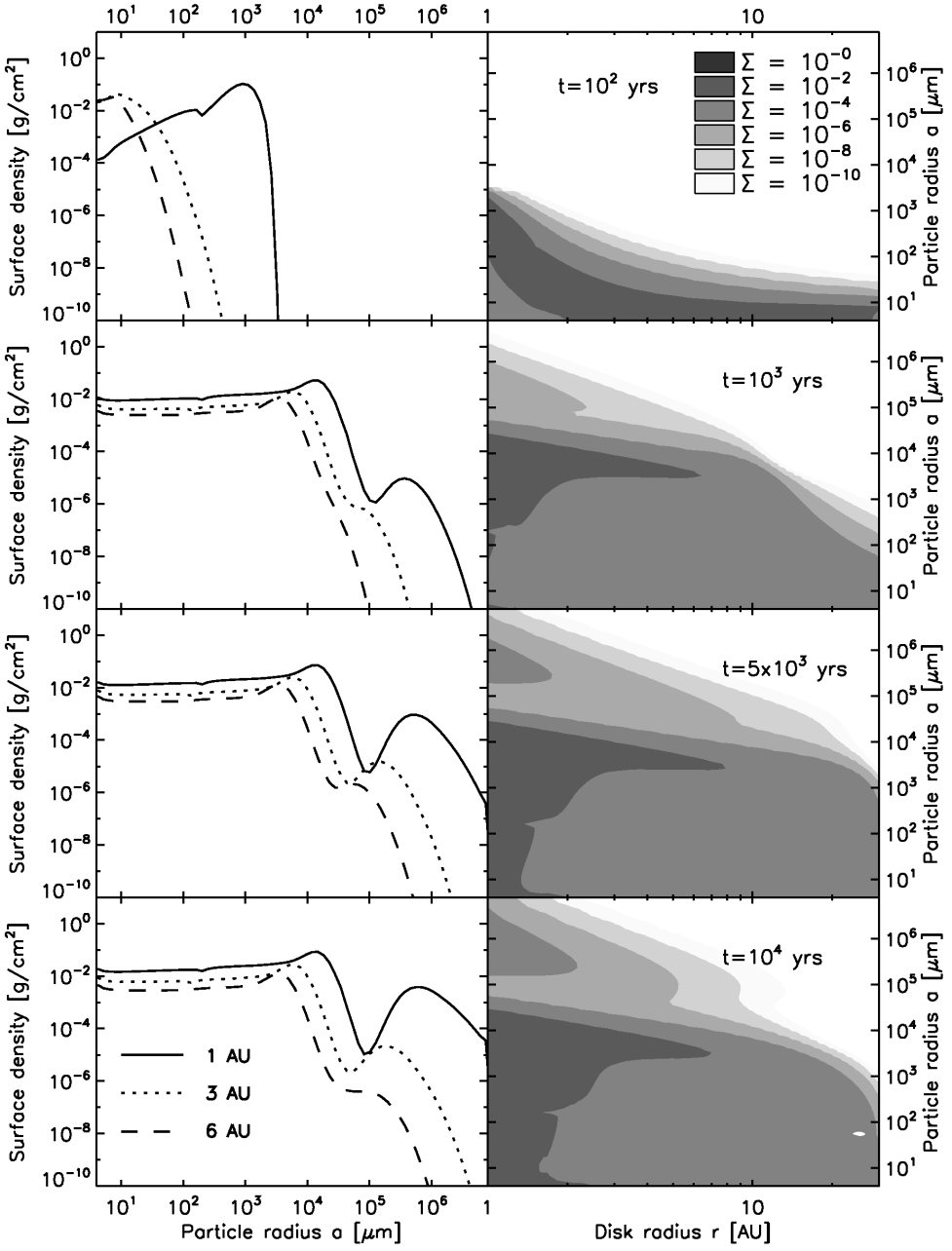

Figure 4.17: These plots show how the particles break through the radial drift barrier and the fragmentation barrier as discussed in Sec. 4.3.3. Shown are contour plots of the surface density as a function of disk radius and particle radius at four different times of disk evolution. The fragmentation velocity is chosen to have the relatively high value of 30 m/s. In this simulation $\psi = 2$ and $\chi = 0$. The initial dust-to-gas ratio is 0.03.

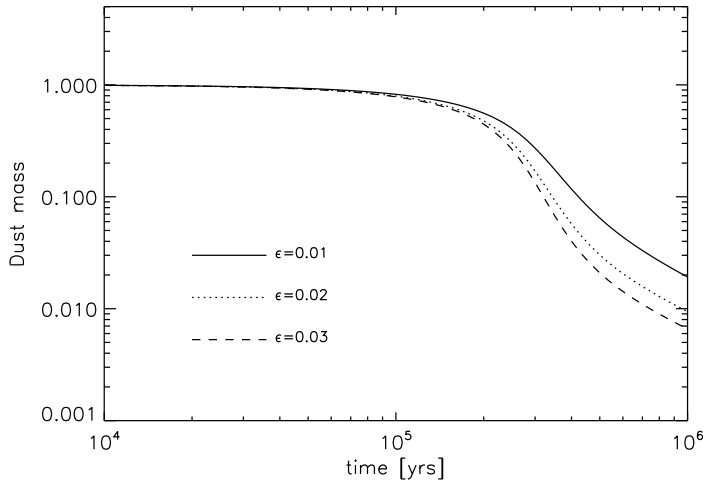

Figure 4.18: The mass of the dust disk between 1 AU and 150 AU as a function of time for 3 different initial dust-to-gas ratios as discussed in Sec. 4.3.4. In this simulation, particle growth particle fragmentation and radial motion are included. The initial disk mass of gas and solid material is 10^{-2} $M_\star$, $\alpha = 10^{-4}$, $\chi = 0.5$, $\psi = 2$ and $v_f = 10$ m/s.

This leads to gas densities which are comparable to those of the MMSN model. The mass distribution, however, has a much flatter radial dependency. The models D to F are the same as A to C, but with a steeper radial temperature dependency. Andrews & Williams (2007) observationally find radial temperature profiles with a median power law index of 0.62. This is slighly higher than the passively irradiated disk profile of 0.5 adopted in our model.

Before we come to the results of the simulations, we will qualitatively discuss the difference between the MMSN model and the model presented here. The gas mass densities of our model are generally smaller than those of the MMSN model. This has the following main implications. First, solid particles are less coupled to the motions of the gas. The coupling between the gas and the dust can be described by the Stokes number St, which is given by $\mathrm{St} = \rho_s a/\Sigma$. If the surface density of the gas Σ decreases, then St is shifted towards higher values. Therefore, the particle growth barrier due to radial drift and particle fragmentation, which is usually referred to as the 'meter size barrier' and which corresponds to the particle radius implied by $\mathrm{St} = 1$, is shifted towards lower particle radii. In the MMSN model, particles with a Stokes number of unity have radii of ~ 2 m at 1 AU in the disk. A surface density slope of $\delta = 0.8$ implies $a \sim 5$ cm for $\mathrm{St} = 1$ particles at 1 AU. While it seems challenging to grow particles larger than meter in size in the MMSN disk model, it is difficult to grow particles larger than centimeter size in the disk model adopted here.

Second, if the Stokes number is shifted towards higher values then all quantities depending on this number are influenced by this change as well. For example, for Stokes numbers smaller than unity the radial drift velocity of solid particles in the disk is proportional to the Stokes number, $v_r \propto \mathrm{St}$ (Weidenschilling 1977a). Now, if the Stokes number is modified due to a change of δ then also the radial drift of the dust is significantly affected. The Stokes number also determines relative dust particle velocities in turbulent disks and, hence, dust particle growth time scales and the maximum dust particle size due to fragmentation.

Fig. 4.19 shows the particle distribution after 1 Myr of disk evolution for the Models A

Model	Surface density power law index δ	Disk mass	Temperature power law index β
A	1.5	0.01	0.50
B	0.8	0.01	0.50
C	0.8	0.10	0.50
D	1.5	0.01	0.62
E	0.8	0.01	0.62
F	0.8	0.10	0.62

Table 4.1: Disk parameters for the simulations performed in Sec. 4.3.5. The quantity β denotes the temperature power law index $T \propto r^{-\beta}$. The Models A and B correspond to the MMSN model and the model adopted in the past sections, respectively. Model C is again the model from the past sections but now with 10% disk mass. The Model D to F are as A to C but with a slighly steeper radial temperature dependency.

to F. In these simulations, particle growth, radial particle motion and destructive collisions are included. The initial dust-to-gas ratio is 10^{-2} and the α-value is 10^{-3}. The ψ-parameter is chosen to be 2 and the cratering parameter $\chi = 0.5$. This figure shows that particles can grow to much larger sizes in model A than in model B in the inner parts of the disk. This is due to higher gas densities in the MMSN model which alter the Stokes number and shift the whole particle growth problem towards larger particle radii. At 1 AU, the gas density in model A is a factor of ~ 15 higher than in model B. The dominant particle size before fragmentation inhibits further particle growth is 3 mm in model A and 0.2 mm in model B. This dominant particle size difference from one model to the other nicely mirrors the gas density difference between the two models. Hence, we find that the dominant particle size is directly proportional to the gas density.

Model C is the same as the model B, but now with 10% disk mass instead of 1% compared to $M_\star$. Fig. 4.19 shows that the dominant particle radius due to destructive collisions is shifted by a factor of 10 towards larger particle sizes. According to these results, particles can grow to a few millimeter in size in high mass disks before particle fragmentation prevents further growth. However, even in these very high mass disks, particles can not overcome the fragmentation barrier. Since the whole coagulation/fragmentation process scales with gas density, higher disk masses do not provide a solution for planetesimal formation. The entire particle growth problem is only shifted towards larger particle radii. The right column shows the results of the three simulations A-C if the radial temperature dependency follows $T \propto r^{-0.62}$ corresponding to the observational median. We do not find a significant difference in the maximum particle size between these two model sets.

We also calculate the mass of the dust disk which is shown in Fig. 4.20. This plot shows that the remaining dust mass after 1 Myr of disk evolution is smaller in the MMSN model than in the model adopted here. This is due to the fact that the maximum radial drift velocity is proportional to the power law index δ of the surface density profile (cf. Eq. 3.2). Since the parameter δ is larger in the MMSN model than in our model, the maximum radial drift speed is also larger. A higher drift speed leads to shorter drift time scales and, hence, reduces the remaining amount of dust after a certain time. In the disk models D-F, the temperature is generally smaller than in the models A-C. Therefore, the radial drift velocity is also smaller since $v_\mathrm{n} \propto T$. Hence, the disk dust mass in the model A-C after a certain time is generally

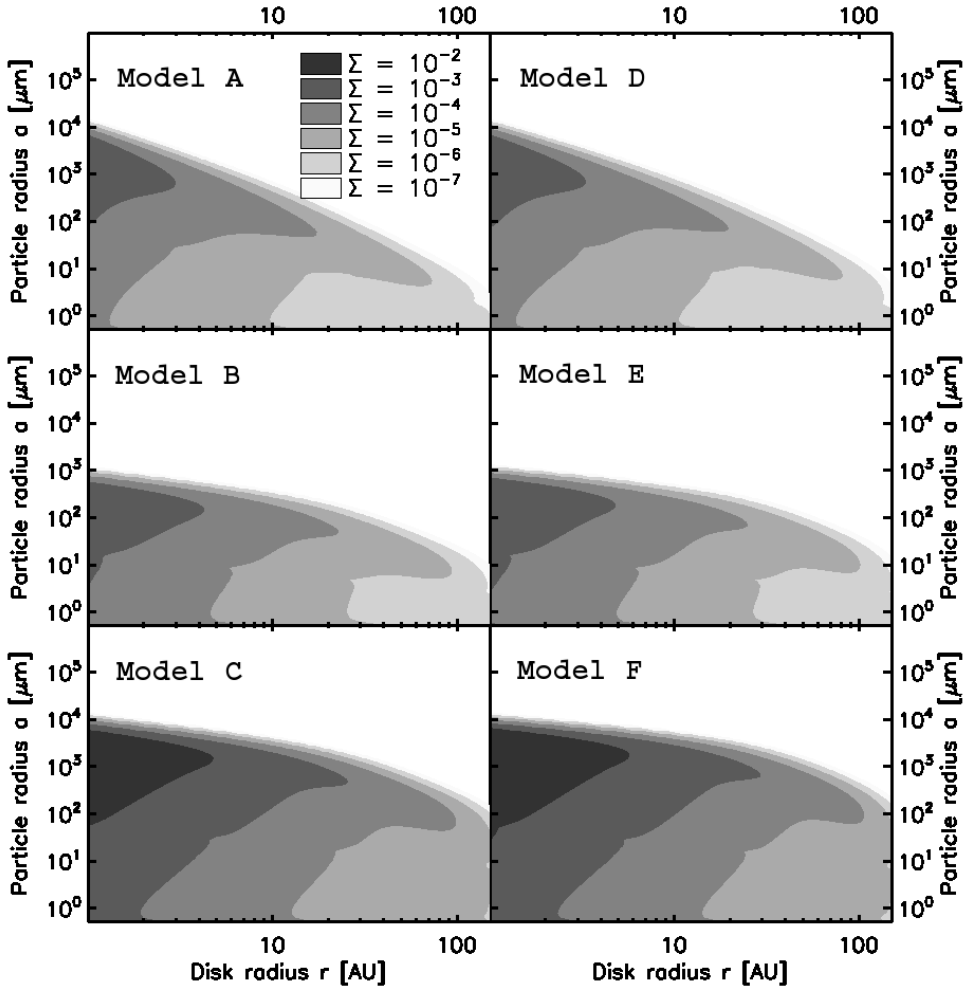

Figure 4.19: The particle distribution in the disk after 1 Myr for the disk models A to F as discussed in Sec. 4.3.5. The Models A and B correspond to the MMSN model and the model adopted in the past sections, respectively. Model C is as the model here but now with 10% disk mass. The Model D to F on the right side have a slighly steeper radial temperature dependency.

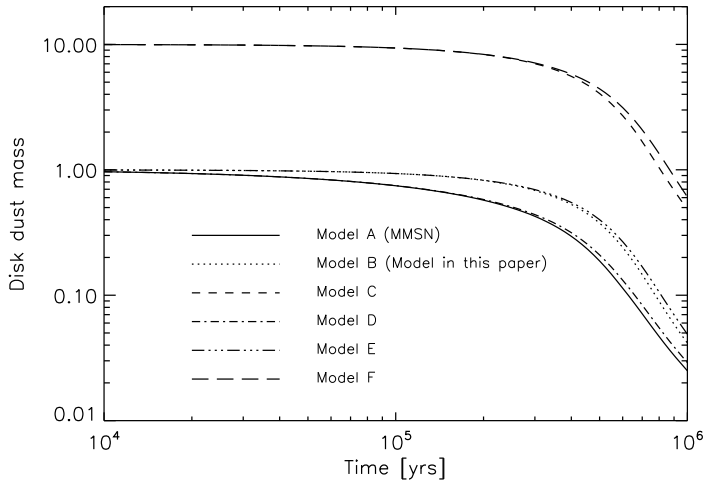

Figure 4.20: The mass of the dust disk as a function of time for the 6 different disk models A to F as discussed in Sec. 4.3.5. The models with 1% disk mass are normalised to unity. The disk models with 10% disk mass are normalised a factor of 10 larger.

smaller than in the models D-F. Finally, we find that less than 6% of the initial dust mass is left after 1 Myrs of disk evolution in any disk model considered.

4.3.6 Effect of cratering

If a smaller particle of mass m_s collides with a larger body at a sufficiently high velocity then the smaller particle does not only fragment due to this destructive collision but it can also excavate a certain amount of matter m_c from the larger body, i.e. $m_c = \chi m_s$. This effect is called cratering. In the following we investigate if this process has an effect on the equilibrium particle distribution between particle coagulation and particle fragmentation.

Fig. 4.21 shows the equilibrium particle distribution at 1 AU in the disk after 10^4 yrs of disk evolution for different cratering-parameters χ. The fragmentation velocity is 20 m/s, $\epsilon = 0.03$, $\alpha = 10^{-5}$ and $\psi = 2$.

This plot shows that the equilibrium distribution is hardly affected whether the effect of cratering is included in the simulations or not. Changing the χ-value from 0 (no cratering) to 1 (the projectile particle excavates a crater corresponding to its own mass) changes the surface density for 50 μm-sized dust grains by a factor of 1.3 at most. The maximum peak of the surface density is shifted from 9 mm to 6 mm by including cratering. We also investigated the effect of cratering for different fragmentation velocities. In any case we found that cratering does not significantly affect the particle distribution. This shows that the main destruction by fragmentation is due to collisions between particles of not large mass ratio.

4.4 Summary and conclusions

We investigated a disk model which includes the effects of dust particle growth, radial motion and particle fragmentation. This model shows that, consistent with current beliefs, that the combination of radial drift and fragmentation is a strong limitation to growth of aggregates in

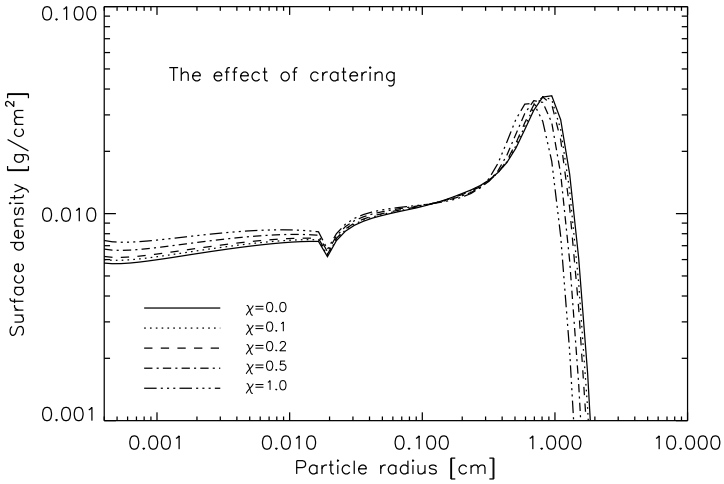

Figure 4.21: The effect of cratering on the equilibrium particle distribution as discussed in Sec. 4.3.6. Shown is the surface density of solid particles at 1 AU in the disk after 10^4 yrs of disk evolution for different cratering-parameters χ. In this simulation, the fragmentation velocity is 20 m/s, $\epsilon = 0.03$, $\alpha = 10^{-5}$ and $\psi = 2$.

disks. Typically, aggregates cannot grow to sizes larger than millimeters throughout the disk if threshold fragmentation velocities up to several m/s are considered. For highly turbulent disks, it is the turbulence-induced relative velocities that cause the damage to aggregates. For nearly non-turbulent disks it is the differential radial drift that limits the growth. Only if the fragmentation threshold velocity is set to the unlikely value of 30 m/s or larger then the fragmentation barrier can be broken and particles grow to larger sizes. Whether this high fragmentation threshold is realistic remains to be verified by high-speed laboratory collision experiments. It has been tentatively shown that high-speed impacts of a small projectile on a large target may result in growth (Wurm et al. 2005), but further study in this direction is imperative.

We find that the maximum particle size before fragmentation prevents further growth is strongly dependent on the gas mass distribution within the disk, i.e. the radial surface density distribution of the gas. Higher gas densities lead to larger maximum particle sizes, and vice versa. The disk model used in this thesis, which involves rather low gas densities in the inner part of the disk, leads to at most mm-sized dust grains at 1 AU. The MMSN model with an order of magnitude higher gas densities at 1 AU already predicts cm-sized particles before fragmentation prevents further growth. We expect even larger particles in the Desch (2008) disk model which involves gas surface densities of more than 50.000 g/cm^2. For comparison, the model used in this thesis involves a gas surface density of 20 g/cm^2 at 1 AU. If such high densities are realistic or not is a matter of debate since they are in contradiction with recent sub-millimeter continuum observations of disks. These surveys suggest gas surface densities of at least three orders of magnitude lower than in the Desch model (Andrews & Williams 2007). Moreover, such high densities also raise the question of gravitational instability of the gas.

It was also investigated what happens when, for some reason, no fragmentation occurs. Even in this reduced model, the particle radius never exceeds several centimeters at any time

at any radius in the disk because of radial particle motion. However, this radial drift barrier problem is very sensitive to slight changes in the initial dust-to-gas ratio. If slighly higher initial dust-to-gas ratios than the canonical value of 1% are adopted in the simulations, then particles can grow to very large sizes in the inner parts of the disk. Interestingly, there is observational evidence hinting towards the importance of this quantity. Santos et al. (2004) and Fischer & Valenti (2005) found a correlation between stellar metallicity and the presence of giant planets. Hence, also observations of planetary systems suggest that the ratio between gas and dust is a crucial parameter which determines the fate of protoplanetary disks.

This strong dependency of particle growth on the dust-to-gas ratio could play an important role also in outer disk regions, subject to the condition that the dust-to-gas ratio is significantly enhanced. This can happen around gas pressure maxima as shown by Kretke & Lin (2007) near the snow line, for example. However, gas pressure maxima are not only of interest for particle growth. It turns out that also particle fragmentation is less likely to occur in gas over-densities. Due to comparetively small relative collision velocities in these gas bumps, solid particles rather grow than destroy each other. The reason for this is that radial drift velocities are caused by radial pressure gradients. Since the pressure gradient is zero in pressure maxima, radial velocities cease. Gas over-densities, therefore, seem to provide an environment in which planetesimal formation could be possible.

Non-linear feedback of the dust back onto the gas was not included in the model. It has been recently shown by Johansen et al. (2007) that such feedback can lead to the rapid formation of gravitationally bound clumps of dust which subsequently form Ceres-size bodies. The 'dust' particles, however, must be large (Stokes number near unity) before this scenario can take place. For low-turbulent disks Stokes numbers larger than 0.1 can be reached, but we need further investigation if the amount of dust present in these large grains is sufficient to trigger such a gravitational collapse in locally overdense regions in the midplane of the disk.

In the full model, most of the solid material has drifted into the evaporation zone after 1 Myrs and the remnant disk contains less than 5% of the initial dust mass. However, there are reasons to believe that the strong radial drift of particles in such disks may be reduced by non-linear hydrodynamic effects. Tentative results from Johansen et al. (2006b) find a reduction by a factor of 3 in MRI turbulence. Moreover, it was shown in Chapter 3 that observations of millimeter grains in the outer regions of protoplanetary disks indicate that the standard radial drift formulae are inconsistent with the observations. This suggests that the current conception of radial drift behaviour of dust in disks could miss some crucial points which might be quite relevant for particle evolution and planetary formation.

In the beginning of this chapter, it was mentioned that the description of relative particle velocities in our dust evolution model involves an ansatz which can be put in question. We neglect stochastic fluctuations of relative turbulent velocities. These velocity variations can change the results of our disk simulations especially if the fragmentation of solid particles is taken into account. This stochastic effect is challenging to implement into the computer code which is used throughout this thesis and other algorithms appear to be better suited to cope with these stochastic effects. Monte Carlo algorithms, for example, have turned out to be a promising approach to this problem (Zsom & Dullemond 2008). To give an example how stochastic fluctuations in the relative velocities change the evolution of the dust, Fig. 4.22 shows two dust distributions at 1 AU in the disk if only Brownian motion and turbulent velocities are considered.[5] The solid line indicates the particle distribution without stochastic

[5]These particle growth simulations were performed by Andras Zsom at the MPIA Heidelberg using a dust particle coagulation code which is based on a Monte Carlo algorithm developed by C. P. Dullemond. The

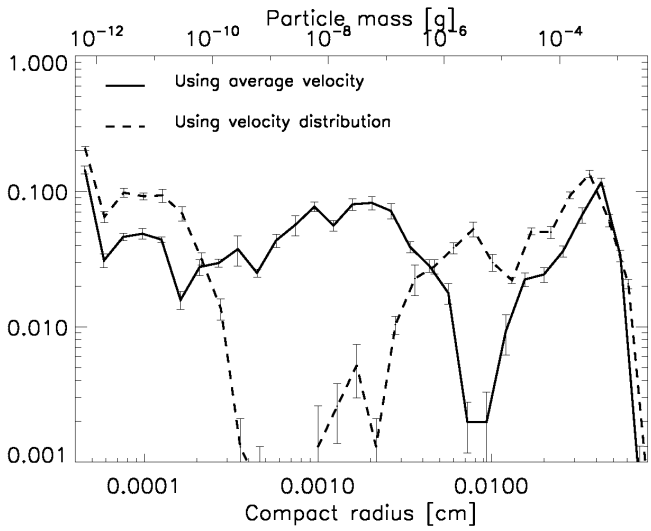

Figure 4.22: The effect of stochastic velocity fluctuations on the dust particle distribution as discussed in Sec. 4.4. Only Brownian motion and turbulent velocities are taken into account. The solid line shows the particle distribution after 3000 yrs of evolution if no stochastic velocity fluctuations are taken into account. The dashed line shows the same setup including particle velocity fluctuations. These simulations were performed by A. Zsom at the MPIA in Heidelberg.

velocity fluctuations. The dashed line represents the simulation result with the same setup if random velocity fluctuations are included. Though the maximum particle radius is very similar in both results, the is a large gap in the dashed dust distribution between 5 to 10 μm, which is not present if velocity fluctuations are neglected. This indicates the importance of stochastic effects.

The particle growth model presented in this chapter involves a constant threshold fragmentation velocity. Laboratory experiments, however, show that this threshold velocity is dependent on particle size (Blum & Muench 1993; Paraskov et al. 2007). While small μm-sized aggregates can have fragmentation velocities of several 10 m/s, meter-sized boulders may already fragment at cm/s relative velocities. Taking this dependency into account could change the evolution of the protoplanetary disk significantly. It might even lead to the formation of planetesimals. Therefore, we seek to improve on this issue in the next chapter. We analytically developed a more sophisticated model for particle fragmentation, which will predict the evolution of dust in disks more realistically.

permission to show these results by courtesy of A. Zsom.

Chapter 5

A particle fragmentation model

The pioneering work of Safronov (1969) and Weidenschilling (1984), as well as current state-of-the-art coagulation models of e.g. Dullemond & Dominik (2005), Nomura & Nakagawa (2006) or Ciesla (2007) have a common consensus. Dust particles reach mm-cm sizes in the inner parts of the disk within a few 10^2 orbital time scales involving a rapid depletion of small micrometer-sized grains. Larger particles sweep up the small dust grains due to rain out effects similar to what happens in the earth's atmosphere. This depletion of tiny dust grains over time scales of only a few 10^4 yrs as anticipated by particle growth models, however, is problematic. Small dust is the source of infrared excess in the spectra of stars with protoplanetary disks (Kenyon & Hartmann 1987; Meeus et al. 2001). The rapidly vanishing population of small grains implies this IR excess to disappear over short time scales < 1 Myr (Dullemond & Dominik 2005) in contrast to observational evidence, e.g. Haisch et al. (2001).

There are various attempts to bring theory and observations into agreement. The surrounding disk envelope could constantly supply the disk with new gas containing small dust particles (Mizuno et al. 1988). The idea of a constant inflow of gas and dust onto the disk surely holds for the early evolutionary phases. It appears, however, problematic at best at time scales of several Myrs. An alternative explanation for the continuous presence of small dust is the fragmentation of larger boulders which have already grown to meter size or larger. Frequent destructive collisions between large rocks would lead to a permanent replenishment of small dust grains. These "second generation grains" would provide an explanation for the observed IR excess for disks with ages $\gtrsim 1$ Myr.

Even though collisional fragmentation may provide a good solution to bring theory and observations into agreement, particle destruction is a genuine problem for planetesimal formation as seen in the previous chapter (cf. also Benz 2000; Schäfer et al. 2007). Typical relative velocities between m-sized boulders due to the turbulent motions of the gas can be more than several 10 m/s (Weidenschilling & Cuzzi 1993; Cuzzi et al. 2001). Constructive collisions at these relative speeds are at least questionable (Youdin 2004; Wilkinson et al. 2007). While the coagulation probability of large boulders at high velocities tends to be negligibly small, collisions between boulders and small dust can still lead to particle growth (Dominik & Tielens 1997). Due to this mechanism, some rocks which are not destroyed in equal-sized particle collisions may grow to larger sizes by sweeping up smaller grains. Larger particles could grow by moving through a dusty disk background as for example investigated

by Haghighipour (2005). This mechanism could lead to planetesimal formation. If this is actually possible is one of the topics of this chapter.

A condition for this scenario to work is that the threshold fragmentation velocity must not be a constant. Dust particle evolution models usually assume this simplification as a first approach (Weidenschilling 1984; Dullemond & Dominik 2005; Brauer et al. 2008) and, therefore, do not allow the growth mechanism described above. Laboratory experiments, however, unveil that the threshold fragmentation velocity indeed depends on the mass of the colliding particles (Blum & Wurm 2000; Blum 2004). In this part of the thesis, we try to improve on this issue. We develop an analytical model to calculate the threshold fragmentation velocity as a function of particle mass. The key parameters of this model are the average interstellar dust particle size and the power law index which describes the particle distribution after a destructive particle collision.

The disk model adopted in these sections is basically the same as investigated in the previous chapter. The only difference is the much more sophisticated treatment of particle fragmentation, which will be described in great detail in the next paragraphs.

5.1 Fragmentation model

Dust particle aggregates in disks are thought to be formed of tiny sub-μm-sized grains, which typically can be found in the interstellar medium (Clayton et al. 2003). These monomer particles hierarchically build up the larger dust particles which are held together by short range van der Waals forces. Every contact point between monomers is associated with a certain contact energy. Therefore, the destruction of dust aggregates, which means to break off the bonds between the monomers, requires energy. For example, the break-off energy of SiO_2 monomers with a radius of 0.95 μm is given by 1.3×10^{-15} J (Heim et al. 1999; Blum 2004). For larger particles, i.e. particles which consist of billions of monomers, one may calculate the total break-off energy $E_{\rm break}$ from the surface area produced during a destructive collision, i.e. $E_{\rm break} = \gamma \Delta O$. The proportionaly factor γ is usually called surface energy.

We can estimate this quantity by the following consideration. The binding energy between two μm-sized dust grains is roughly of the order of 10^{-15} J. If we assume that 1 m^2 involves $\sim 10^{12}$ μm-sized particles then the surface energy is of the order of $\sim 10^{-15} \times 10^{12}$ J/m^2 = 1 erg/cm^2. On the other hand, one may express γ as $\gamma = Tl$, where T is the tensile strength and l the binding length. Blum et al. (2006) have shown that $T = 10^3$ Pa and $l = 10$ μm for SiO_2 monomers with a particle radius of a micrometer which implies $\gamma = 10$ erg/cm^2. Surface energies of the same order of magnitude were also found earlier by Heim et al. (1999). Considering these estimates, we will investigate the influence of γ on dust particle coagulation in the range between $1 \ldots 50$ erg/cm^2.

In the following sections, we will calculate the surface area which is produced during a destructive collision. From this quantity, we can estimate the energy which is required to provoke such a fragmentation. If we relate this energy to the kinetic energy of the collisional partners then we get a critical fragmentation velocity. This threshold velocity will serve as an input for dust evolution models in protoplanetary disks in the further parts. We first discuss the model in the case of cratering and non-cratering. After this, we assume a certain surface energy and show typical fragmentation velocities for particles between sub-micrometer size and meter size.

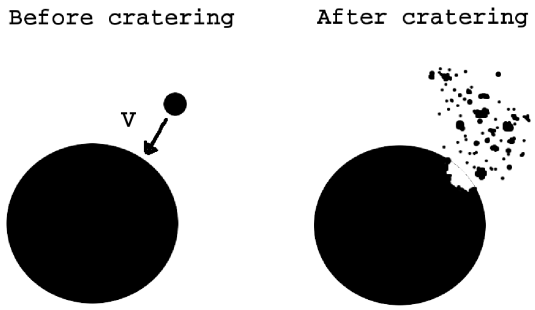

Figure 5.1: This figure shows the effect of cratering as discussed in Section 5.1.1. Two particles, whose mass ratio is very different from unity, collide with a significant high velocity which leads to particle destruction.

5.1.1 Case of cratering

The effect of cratering occurs if the ratio of the masses of the collisional partners is significantly different from unity. We assume that the smaller projectile particle of mass m_p excavates a crater in the larger target particle m_t which roughly corresponds to its own mass (cf. Fig. 5.1). The mass m_p is approximately given by the reduced mass

$$m_p \approx \mu = \frac{m_\mathrm{p} m_\mathrm{t}}{m_\mathrm{p} + m_\mathrm{t}} \,, \tag{5.1}$$

so that the excavated caldera material mass can be written as $m_\mathrm{cal} = \chi\mu$. The cratering parameter χ is a free parameters of the fragmentation model. The solid material mass, which has to be redistributed according to some recipe, we still have to discuss, is then given by

$$m_p + m_\mathrm{cal} = (1+\chi)\mu \,. \tag{5.2}$$

What does the particle distribution after fragmentation look like? Various authors, for example Draine & Lee (1984), Davis & Ryan (1990) or Blum & Muench (1993), have noted that this distribution can be described by a powerlaw. Hence, as in the last chapter we will assume that the particle number densities after fragmentation follow

$$n(m) = C\, m^{-\xi} \,. \tag{5.3}$$

The power law index ξ may range from 1.3 (low-velocity impacts) up to 2 (catastrophic impacts)(Davis & Ryan 1990) and is a free parameter of our model. The usually assumed classical value of $\xi = 1.83$ may be obtained by investigating either steady-state solutions (Dohnanyi 1969) or the self-similarity of coagulation/fragmentation particle distributions (Tanaka et al. 1996). In the case of the "classical" value $\xi = 1.83$, the particle distribution after fragmentation (Eq. 5.3) is more widely known in the form $n(a) \propto a^{-3.5}$, where a is the dust particle radius. The entire redistributed mass equals $(1+\chi)\mu$, i.e.

$$\int_{m_0}^{\mu} n(m) m \,\mathrm{d}m = (1+\chi)\mu \,, \tag{5.4}$$

which leads to the normalisation constant

$$C = (2-\xi)(1+\chi)\mu \left[\mu^{2-\xi} - m_0^{2-\xi}\right]^{-1} . \tag{5.5}$$

The smallest mass which may result from destructive collisions is assumed to be a monomer mass m_0. The radius of these monomer grains is a free parameter of our model. We will investigate the influence of this monomer radius on the simulation results in the radius interval $[0.1, 1]$ μm. Note, that we consider a single monomer size and not a whole monomer size particle distribution. The total surface area of dust fragments is then given by

$$O_{\text{slope}} = \int_{m_0}^{\mu} n(m) O(m)\, \mathrm{d}m , \tag{5.6}$$

in which $O(m)$ is the surface area of a particle with mass m. The quantity O_{slope} can then be calculated to be

$$O_{\text{slope}} = \frac{C\delta}{5/3-\xi}\left[\mu^{5/3-\xi} - m_0^{5/3-\xi}\right] , \tag{5.7}$$

where $\delta = 4\pi(3/4\pi\rho_s)^{2/3}$. The surface area of the crater in the bigger target particle is given by

$$O_{\text{crater}} = \frac{\delta}{2}(2\chi\mu)^{2/3} , \tag{5.8}$$

so that the total surface area after the impact reads

$$O_{\text{after}} = O_{\text{slope}} + O_{\text{crater}} . \tag{5.9}$$

Now, we also have to calculate the surface area before the impact. The surface area of the smaller particle is given by $\delta m_{\text{p}}^{2/3}$. The surface area of the 'crater' before the impact can be calculated to be $\delta(2\chi\mu)^{2/3}/4$. Hence, the total area before the impact is

$$O_{\text{before}} = \delta\mu^{2/3}\left[1 + \frac{(2\chi)^{2/3}}{4}\right] . \tag{5.10}$$

The total amount of surface area which is created due to the destructive collision is then

$$\Delta O = O_{\text{after}} - O_{\text{before}} . \tag{5.11}$$

The energy which is needed to break the contact points between monomers and, hence, to create new surface area is given by

$$\Delta E_{\text{area}} = \gamma \Delta O . \tag{5.12}$$

To calculate the fragmentation velocity, we consider that a certain fraction of the kinetic energy before the impact E_{kin} is used to break the contact points between the monomers and, hence, used to create new surface area,

$$\Delta E_{\text{area}} = (1 - c_{\text{f}}) E_{\text{kin}} . \tag{5.13}$$

The parameter c_{f} accounts for the fact that only a certain fraction of the kinetic energy is used to break certain bonds between the monomers of the dust particles. The rest of the energy remains kinetic and the dust fragments have a certain velocity after the impact. Including

the well-known expression for the kinetic energy of a particle of a certain velocity, the critical fragmentation speed is then given by the expression

$$v_c = \left[\frac{2}{\mu(1-c_\mathrm{f})} \gamma \Delta O \right]^{1/2} . \tag{5.14}$$

The free parameters of this model are the slope of the power law distribution ξ and the monomer mass m_0. Even though the surface energy γ is mainly determined by laboratory experiments, we will also investigate the influence of this parameter on the simulation results. For simplicity, we will set c_f to zero. The investigation of this parameter is in pricipal mirrored by the simulations concerning the surface energy γ.

Particle fragments which result from a destructive collision are not necessarily spherical. The resulting particles could have elongated or even fractal shapes. Non-spherical particles have more surface area than a spherical particle of the same mass. For this reason, the expression for the surface area $O(m)$ as a function of mass in the form

$$O(m) = 4\pi \left(\frac{3m}{4\pi\rho_\mathrm{s}} \right)^{2/3} \tag{5.15}$$

generally underestimates the surface area of a particle of arbitrary shape. Hence, the quantity O_slope in Eq. (5.7) is systematically shifted towards smaller values. In other words, the threshold fragmentation velocity as calculated here is presumably smaller than the value that would be measured in laboratory experiments.

5.1.2 Reformulation

We reformulate the equations given in the last section to investigate some parameter limits. We can write the surface area O_slope (c.f. Eq. 5.7) which is produced by the fragmentation of the smaller projectile particle and the crater material as

$$O_\mathrm{slope} = (1+\chi) O_0 S(\xi) , \tag{5.16}$$

in which O_0 is the surface area of a monomer and S is a structure function given by

$$S(\xi) = \frac{2-\xi}{5/3-\xi} \frac{\left(n^{5/3-\xi}-1\right)}{\left(n^{2-\xi}-1\right)} n . \tag{5.17}$$

In the derivation of the last equation we assumed, that the reduced mass can be written as $\mu = n m_0$, where n is the number of monomers in the projectile particle. The total surface area gain is then

$$\Delta O = O(\mu) \left[(1+\chi) \frac{S}{n^{2/3}} + \frac{(2\chi)^{2/3}}{4} - 1 \right] . \tag{5.18}$$

Now, we investigate the influence of the ξ-parameter on ΔO more closely. This parameter determines whether particle fragmentation more likely results in tiny monomers (large ξ) or in fragments comparable to the size of the parent bodies (small ξ). The former case corresponds to a high velocity impact. The latter case usually involves low relative velocities. One may consider two extreme cases, namely $\xi \to \pm\infty$. In the case $\xi \to -\infty$, the additional surface area produced during an impact shows the following behaviour,

$$\Delta O|_{\xi\to-\infty} \to O(\mu) \left[(1+\chi) + \frac{(2\chi)^{2/3}}{4} - 1 \right] \sim O(\mu) . \tag{5.19}$$

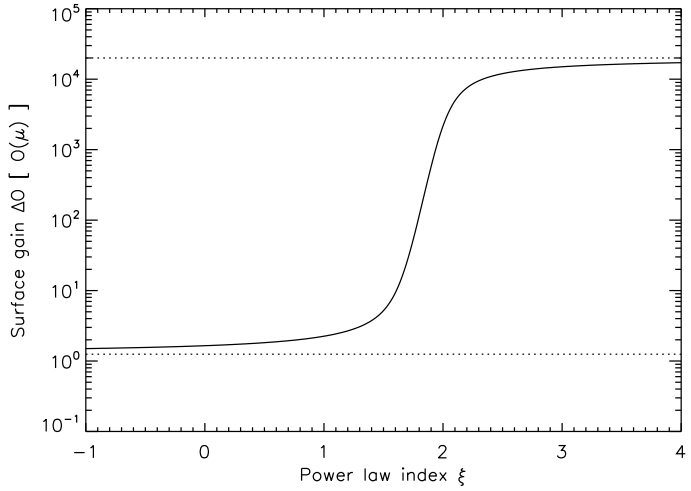

Figure 5.2: Surface area gain in units of $O(\mu)$ as a function of the power law index ξ as discussed in Section 5.1.2. The two limiting cases are $1+2^{2/3}/4$ for $\xi \to -\infty$ and $2nO(m_0)/\pi$ for $\xi \to \infty$. In this calculation $n = 10^{12}$, $\xi = 1$, $m_0 = 8.4 \times 10^{-13}$ g which corresponds to 0.5 μm. $O(m_0) = \pi \times 10^{-8}$ cm^2 and $O(\mu) = \pi$ cm^2.

The difference in surface area before and after the impact is in the order of the surface area of the reduced mass. That is what we expect since most of the mass is in larger bodies corresponding to masses $\sim \mu$. In the other extreme, i.e. for the case $\xi \to \infty$, we find that

$$\Delta O|_{\xi\to\infty} \to O(m_0)\left[(1+\chi)n + \frac{(2n\chi)^{2/3}}{4} - n^{2/3}\right] . \tag{5.20}$$

For very lange n this expression becomes

$$\Delta O|_{\xi\to\infty,n\to\infty} \to n(1+\chi)O(m_0) \sim nO(m_0) . \tag{5.21}$$

The surface area produced during the impact is roughly n times the surface area of a monomer. In this limiting case, the dependency of ΔO on the monomer parameters follows

$$\Delta O \propto nm_0^{2/3} \propto m_0^{-1/3} \propto a_0^{-1} , \tag{5.22}$$

where a_0 is the monomer grain radius. If the monomer radius decreases by a factor of four then the gain in surface area increases by the same factor. This leads to fragmentation velocities which are a factor of two larger according to Eq. (5.14).

To illustrate the influence of the power law index ξ on the gain of surface area between these two limiting cases, we calculate ΔO as a function of ξ (cf. Fig. 5.2). We adopt a solid material density of 1.6 g/cm^3, $n = 10^{12}$, $\chi = 1$ and a monomer mass of $m_0 = 8.4 \times 10^{-13}$ g, which corresponds to a monomer particle radius of 0.5 μm. The reduced mass μ is given by $\mu = nm_0 = 0.84$ g which corresponds to a particle radius of 0.5 cm. The surface area of a monomer is $O(m_0) = \pi \times 10^{-8}$ cm^2 and the surface area of a particle with mass μ is $O(\mu) = \pi$ cm^2.

Fig. 5.2 shows that the gain of surface area during an impact is quite sensitive to the power law index ξ. While for low ξ-values, the gain of surface area is of the order of $O(\mu)$,

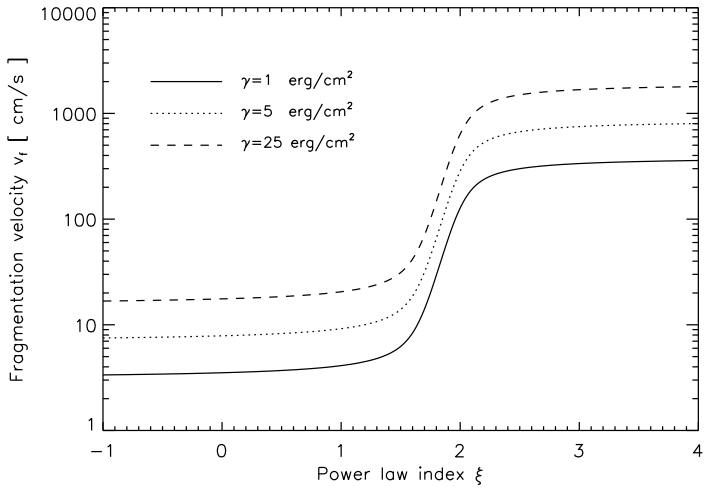

Figure 5.3: Fragmentation velocity v_c as a function of the power law index ξ for three different surface energies as discussed in Section 5.1.2. This simulation involves the same set of parameters as for Fig. 5.2.

the increase in area is roughly four orders of magnitudes if larger ξ-values are considered. The specific value ξ_c for which $\partial_\xi \ln \Delta O(\xi)$ is maximal, i.e. for which the gain in surface area is most sensitive to ξ, can be calculated to be

$$\xi_c = 1 + \frac{1}{2}\partial_{\ln m} \ln \left(\int_m O(m)\, \mathrm{d}m \right) . \tag{5.23}$$

Interestingly, for compact particles which imply $O(m) \propto m^{2/3}$, the value for ξ_c equals the usually assumed power lax index $\xi = 11/6 \approx 1.833$. This finding suggests that there is a connection between the surface area per mass of a particle and the slope of the fragmentation results after destructive collision. Williams & Wetherill (1994) already found that the average steady-state value of ξ is extremely insensitive to the assumed physical parameters of the fragmentation process. This fact can be traced back to geometrical properties of the fragmentation cascade which relates area and mass to particle radius. According to Williams & Wetherill (1994), the value of ξ has not much to do with how rocks break, but instead is determined by the "dimensionality of space".

The dependency of ΔO on the power law index ξ can directly be translated into fragmentation velocities (cf. Eq. 5.14). If we assume a surface energy of 1, 5 and 25 erg/cm^2 then the fragmentation velocities are of the order of $1 \ldots 2000$ cm/s. An illustration of this dependency is shown in Fig. 5.3.

5.1.3 Case of non cratering

In this section, we consider the complete destruction of the particles as shown in Fig. 5.4. The mass distribution of the shattering results also follows the power law $m^{-\xi}$ which we have already assumed in the previous sections. If two particles with masses $m = nm_0$ and $m' = n'm_0$ fragment then we can write the surface area present in this distribution as

$$O_{\mathrm{slope}} = O(m_0)\tilde{S}(\xi) , \tag{5.24}$$

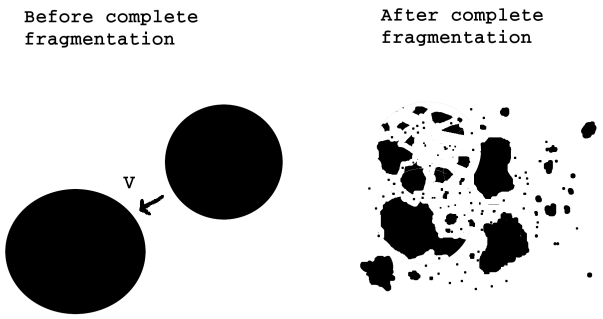

Figure 5.4: This figure shows the effect of complete destruction of the collisional partners as discussed in Section 5.1.3. Two particles, whose mass ratio around unity, collide with a significant high velocity which leads to complete particle fragmentation.

where the structure function $\tilde{S}$ is given by

$$\tilde{S} = \frac{2-\xi}{5/3-\xi}(n+n')\frac{\left[N^{5/3-\xi}-1\right]}{\left[N^{2-\xi}-1\right]} \tag{5.25}$$

and $N = nn'/(n+n')$ is the reduced particle number corresponding to $\mu = Nm_0$. The surface area of the two particles before destruction can be written as

$$O_{\text{before}} = O(m_0)\left[n^{2/3} + n'^{2/3}\right] , \tag{5.26}$$

so that the total surface area gain is then

$$\Delta O = O(m_0)\left[\tilde{S} - (n^{2/3} + n'^{2/3})\right] . \tag{5.27}$$

For $\xi \to -\infty$, the surface area gain becomes

$$\Delta O|_{\xi\to-\infty} = O_0\left[\frac{(n+n')^{4/3}}{(nn')^{1/3}} - (n^{2/3} + n'^{2/3})\right] . \tag{5.28}$$

And for equal sized particles we get

$$\Delta O|_{\xi\to-\infty, n=n'} = 2\left(2^{1/3}-1\right)O(\mu) . \tag{5.29}$$

For the other limiting case, i.e. $\xi \to \infty$, we find

$$\Delta O|_{\xi\to\infty} = O_0\left[(n+n') - (n^{2/3} + n'^{2/3})\right] . \tag{5.30}$$

In the case of equally sized particles and large n, the surface gain becomes

$$\Delta O|_{\xi\to\infty, n=n'} = 2nO(m_0) , \tag{5.31}$$

which corresponds to the complete destruction into small monomers.

Here and in the last section, we developed a particle fragmentation model for the case of cratering, i.e. ΔO_c, and a model for the complete destruction of the collisional partners, ΔO_cd. We can define a function $f(\zeta)$ by

$$f(\zeta) = \frac{4\zeta}{(1+\zeta)^2} \,. \tag{5.32}$$

This function is unity if ζ is unity and it decreases for $\zeta \neq 1$ to zero. With this definition, we can formulate the gain of surface area in both model together by

$$\Delta O = f(\zeta)\Delta O_\mathrm{cd} + [1 - f(\zeta)]\,\Delta O_\mathrm{c} \,. \tag{5.33}$$

In this expression, ζ is given by $\zeta = m/m'$. For $\zeta = 10$ and $\zeta = 50$, the the function f has decreased down to 0.3 and 0.08, respectively. The choice of the transfer function f is somewhat arbitrary which raises the question of how this choice influences the simulation results of the following sections. We performed model simulations with different transfer functions, but we did not find significant differences in the results as long as f decreases to zero for $\zeta \neq 1$.

5.1.4 Fragmentation velocity and critical specific energy

Before we come to the threshold fragmentation velocities implied by our model, let us consider the "traditional" approach to calculate threshold velocities. For this reason, we consider the specific kinetic energy

$$Q = \frac{\frac{1}{2}\mu v_\mathrm{c}^2}{M} \,, \tag{5.34}$$

where M is the material mass which is fragmented during the impact. Fragmentation will occur if the specific energy Q is larger than a critical value $Q^\star$. If we assume that M is given by 2μ and that for two equal sized particles of mass m the reduced mass is given by $m/2$, then the threshold fragmentation velocity which corresponds to the critical value $Q^\star$ is given by

$$v_\mathrm{c} = \sqrt{8Q^\star} \,. \tag{5.35}$$

This critical velocity is independent of the mass of the colliding particles which is often used as a first approach for particle fragmentation models (Weidenschilling 1984; Dullemond & Dominik 2005). Values for $Q^\star$ are typically of the order of $10^5 \ldots 10^6$ erg/g (Weidenschilling 1984; Benz 2000) which leads to threshold velocities of several 10 m/s.

This independency on particle mass also occurs for $\xi = \infty$ in our fragmentation model as described in the previous sections. The gain in surface area for two equal sized particles with n monomers is given by $2nO(m_0)$. Using Eq. (5.14) with $c_\mathrm{f} = 0$ leads to a fragmentation velocity given by

$$v_\mathrm{c} = \sqrt{\frac{24\gamma}{\rho_\mathrm{s} a_0}} \,. \tag{5.36}$$

For a surface energy of 10 erg/cm^2, $a_0 = 0.5$ μm and $\rho_s = 1.6$ g/cm^3, we obtain a threshold velocity of ~ 20 m/s.

The critical threshold velocities Eq. (5.35) and (5.36) are independent on particle mass. This has the following reason. On one hand, the kinetic energy involved in the collision is proportional to the mass of the parent bodies. On the other hand, for $\xi = \infty$, the outcome of fragmentation are solely monomer particles which means that all the van der Waals contacts

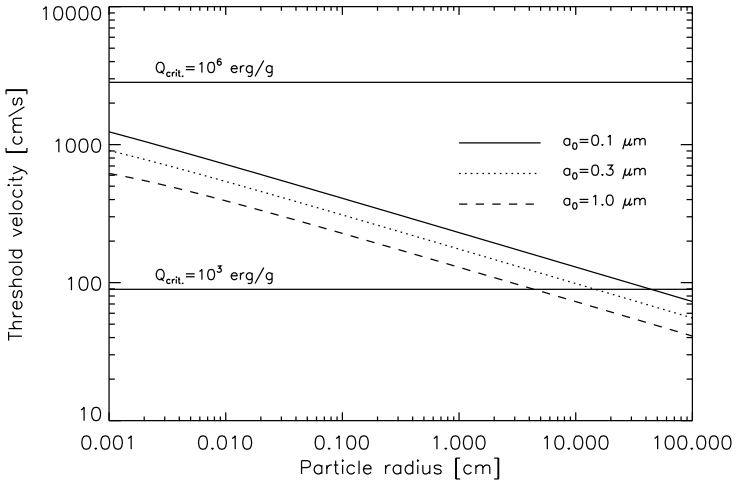

Figure 5.5: Threshold velocity v_c as a function of particle radius for 3 different monomer radii as discussed in Sec. 5.1.4. This plot also shows the threshold velocity for the specific energy approach for two different $Q^\star$.

between monomers in the parent bodies must be broken. Since the number of monomer contacts in the parent bodies is also proportional to the mass of the parent bodies, the threshold velocity is independent of particle mass.

Not all van der Waals contacts n break during fragmentation. A more realistic assumption is that only a certain fraction

$$\Delta E_\mathrm{area} \propto n^\beta \tag{5.37}$$

with $\beta < 1$ contributes to the gain in surface area. The last equation and Eq. (5.14) then imply that the critical fragmentation velocity follows

$$v_\mathrm{c} \propto m^{(\beta-1)/2} \; . \tag{5.38}$$

For $\beta = 1$, i.e. for the specific energy approach in the beginning of this section, the threshold velocity becomes independent of particle mass. For the more realistic case $\beta < 1$, the threshold velocity generally decreases with particle mass. If we consider the canonical value for the particle distribution after fragmentation $\xi = 11/6$, it is easily shown that $\beta = 5/6$ (cf. Eq. 5.25 and 5.27). For this specific case, the threshold fragmentation velocity follows

$$v_{\mathrm{c},\,\xi=11/6} \propto m^{-1/12} \propto a^{-1/4} \; . \tag{5.39}$$

To illustrate this dependency, Fig. 5.5 shows the threshold velocity as a function of particle size for three different monomer radii. This figure also indicates the threshold velocity for two different critical specific kinetic energies according to Eq. (5.35). In this calculation we adopted $\gamma = 10$ erg/cm^2 and $\rho_\mathrm{s} = 1.6$ g/cm^3.

Heim et al. (1999) and Blum (2004) experimentally find values for the surface energy of 14 erg/cm^2 and higher for monomer particles of radius $a_0 = 0.95$ μm. Taking these values and assuming the canonical power law index $\xi = 11/6$, we can calculate the threshold fragmentation velocity as a function of not neccesarily equal-sized particles. The result of this calculation is shown in Fig. 5.6. This plot again indicates that the threshold fragmentation

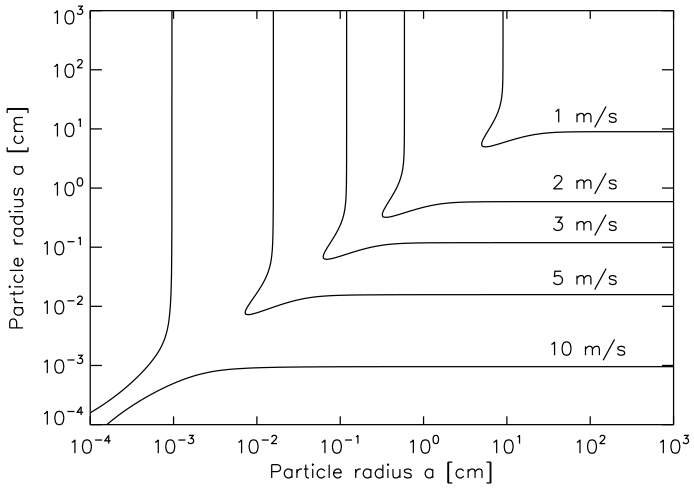

Figure 5.6: Threshold velocity for particle fragmentation v_c as a function of particle radius as discussed in Sec. 5.1.4. The monomer radius is assumed to be 0.95 μm and the power law index $\xi = 11/9$. With our model, we obtain threshold velocities between 10 m/s for μm-size particles and 1 m/s for dm-size particle.

velocity decreases with particle radius. While μm-sized dust grains have threshold velocities of several 10 m/s, this quantity decreases down to 1 m/s for dm-sized aggregates. This figure also unveils that the threshold velocity is determined by the smaller particle of the collisional partners. For example, it does not matter if a 10 μm-sized aggregate collides with a 100 μm-sized grain or a m-sized body. Both collisions involve the same threshold velocity. This is due to the fact that the crucial particle parameters entering our fragmentation model are not the two masses of the colliding bodies, but only the reduced mass μ. For large particle mass differences, this quantity equals the smaller dust particle mass, cf. Eq. (5.1). The contour plot in Fig. 5.6 mirrors this independency of the large target particle.

We will investigate which particles will grow to larger sizes and which particles will fragment and destroy each other. Therefore, we consider the ratio between the relative particle velocity Δv and the threshold fragmentation velocity v_c. For the moment, we will adopt two sources for relative particle velocities, namely relative velocities due to turbulent motions of the gas as calculated by Ormel & Cuzzi (2007) and relative radial drift velocities (Weidenschilling 1977a). We assume a turbulent α-value of 10^{-3} and a sound speed of $c_s = 8.4 \times 10^4$ cm/s, corresponding to a temperature of 204 K at 1 AU in the disk. The result of this calculation is shown in Fig. 5.7.

These results indicate that particles may grow to millimeter size at 1 AU in the disk before particle fragmentation inhibits further growth. This figure also indicates that m-sized bodies will less likely fragment with μm-sized dust grains than with boulders of meter size. Hence, the collisions between very small aggregates and large boulders might play in important role for the growth behaviour of large bodies. We will come back to this point in the next Section.

The maximum particle size of a millimeter is surely dependent on the disk model parameters. For example, mm-sized particles have much higher relative velocities in our model than they would have in the MMSN model. While mm-sized grains still coagulate and grow to larger sizes in the MMSN model, they tend to fragment here. This relative velocity discrep-

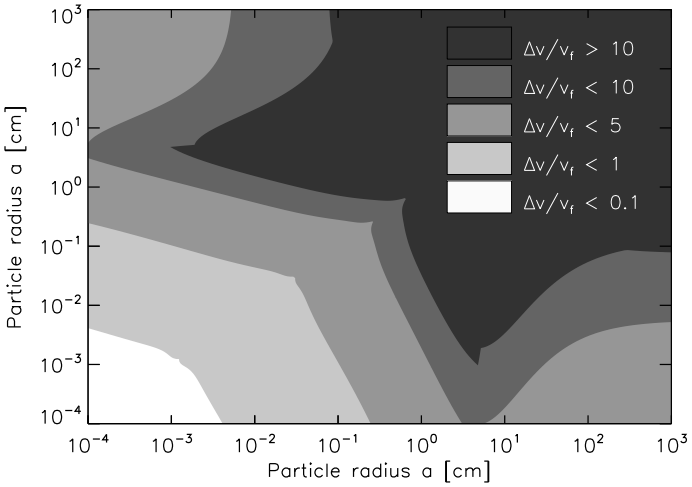

Figure 5.7: The ratio betweeen the relative particle velocity at 1 AU in the disk and the threshold fragmentation velocity $\Delta v/v_\mathrm{f}$ as a function of particle radius as discussed in Sec. 5.1.4. In this calculation we assumed a sound speed of $c_\mathrm{s} = 8.4 \times 10^4$ cm/s and a turbulent α-value of 10^{-3}. We adopted a gas mass density in a way that St = 1 particles correspond to 5 cm size dust aggregates.

ancy is due to the fact that the gas mass densities in the MMSN model at 1 AU are roughly one order of magnitude higher than in our model. In Brauer et al. (2008) we showed, that the maximum particle size before destructive collisions prevent further growth scales with the gas mass density. Therefore, we expect the fragmentation barrier to be around 1 cm in the MMSN model.

5.2 Equilibrium particle distribution

When the dust particles reach the size of ~ 1 mm, they enter a velocity regime where particle fragmentation due to destructive collisions starts to play a significant role. After $\sim 10^4$ yrs at 1 AU in the disk, the particle distribution reaches a steady-state which is characterised by an equilibrium between particle coagulation and particle fragmentation. In this Section, we will neglect radial particle motion and we will only focus on this equilibrium particle distribution at 1 AU in the disk. We investigate the influence of the monomer radius a_0, the power law index ξ and the surface energy γ on this distribution.

To make sure that the particle distribution at 1 AU is in equilibrium between dust coagulation and fragmentation after 10^4 yrs, we consider the following estimate. If the main source for relative particle velocities is due to turbulent motions of the gas then the dust particle radius as a function of time is given by (Brauer et al. 2008)

$$a(t) = a_0 \exp\left(\Omega_\mathrm{k} \epsilon_0 t\right) . \tag{5.40}$$

In this expression, Ω_k denotes the Kepler frequency and ϵ_0 is the initial dust-to-gas ratio in the disk. Expression (5.40) only holds if the Stokes number $\mathrm{St} = a\rho_\mathrm{s}/\Sigma_\mathrm{gas}$ of the dust particle is smaller than unity and the stopping time of the dust larger than the Kolmogoroff

time scale (Weidenschilling & Cuzzi 1993; Cuzzi et al. 2001; Ormel & Cuzzi 2007). Relative turbulent dust particle velocities are given by (Ormel & Cuzzi 2007)

$$\Delta v = \sqrt{\alpha \mathrm{St}}\, c_\mathrm{s} \,. \tag{5.41}$$

With this last expression, we can calculate the growth time scale t_eq for the dust to reach relative velocities corresponding to the threshold fragmentation velocity v_f in terms of the orbital time scale $t_\mathrm{orb} = 1/\Omega_\mathrm{k}$,

$$\frac{t_\mathrm{eq}}{t_\mathrm{orb}} = \frac{2}{\epsilon_0} \ln\left(\frac{v_\mathrm{f}}{\sqrt{\alpha \mathrm{St}_0}\, c_\mathrm{s}}\right) . \tag{5.42}$$

The quantity St_0 denotes the Stokes number of a monomer dust particle in the midplane of the disk. If we adopt an initial dust-to-gas ratio of $\epsilon_0 = 10^{-2}$, a threshold fragmentation velocity $v_\mathrm{f} = 10^3$ cm/s, an α-value of 10^{-3}, $c_\mathrm{s} = 8 \times 10^4$ cm/s and an initial monomer Stokes number of 10^{-5} then the equilibrium time scale is roughly $t_\mathrm{eq} \approx 5 \times 10^3\ t_\mathrm{orb}$. We simulate 10^4 yrs which, hence, should be sufficient for the particle distribution to get into the coagulation/fragmentation equilibrium.

5.2.1 Effect of the surface energy γ

The surface energy γ is usually determined by measuring adhesion forces of SiO_2 microspheres (Heim et al. 1999). However, dust aggregates in a protoplanetary disk do not only consist of silica, but also carbon and water ice which surely influences the surface energy. Moreover, the value of γ also depends on particle characteristics such as surface roughness which is known to decrease adhesion forces (Fuller & Tabor 1975). While Heim et al. (1999) find surface energies between 14 to 18 erg/cm^2 for silica spheres, Kendall et al. (1987) obtain 25 erg/cm^2 from the elastic behaviour of silica powder. Horn et al. (1989) measured a factor of two higher surface energies of 40 erg/cm^2 by a modified surface force apparatus. Due to this parameter variety, we will investigate the effect of γ over a wide parameter range between 1 erg/cm^2 up to 100 erg/cm^2.

In the numerical calculation of the equilibrium distribution, we adopt $\xi = 11/6$, $\chi = 0.5$, $a_0 = 0.4$ μm and $c_\mathrm{f} = 0$. We consider a sound speed of $c_\mathrm{s} = 8.4 \times 10^4$ cm/s, an initial dust-to-gas ratio of 10^{-2} and an α-value of 10^{-3}. The particle distribution after 10^4 yrs as a function of particle size is shown in Fig. 5.8.

This figure indicates that particles can grow to larger sizes if higher surface energies are considered. While for $\gamma = 1$ erg/cm^2 the dominant particle radius is ~ 50 μm, this value increases up to 1 mm if a very high surface energy of 100 erg/cm^2 is considered. This behaviour is due to the relation

$$v_\mathrm{c} \propto \sqrt{\gamma} \,, \tag{5.43}$$

which is implied by Eq. (5.14). Higher surface energies involve higher tensile stresses F to separate adhering particles since $F \propto \gamma$ (Derjaguin et al. 1975). Therefore, higher energies and, hence, higher collision velocities are required to fragment an aggregate into monomers.

5.2.2 Effect of the power law index ξ

The last decades involved various attempts to determine the ξ parameter. Laboratory experiments find values for ξ ranging between 1.3 (low-velocity impacts) and 2 (catastrophic impacts) (Davis & Ryan 1990; Blum & Muench 1993). In this section, we will investigate

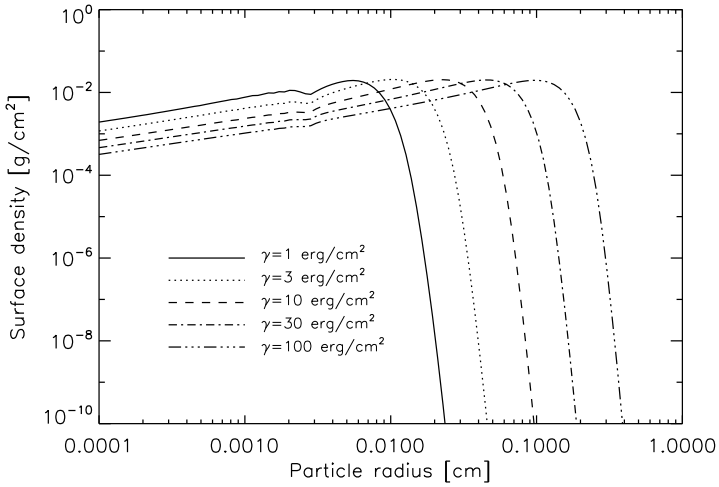

Figure 5.8: The equilibrium particle distribution between dust coagulation and fragmentation after 10^4 yrs as discussed in Sec. 5.2.1. Shown is the surface density at 1 AU in the disk for 5 different surface energies γ. In this simulation, we adopt $\xi = 11/6$, $\chi = 0.5$, $a_0 = 0.4$ μm and $c_\mathrm{f} = 0$. The disk parameters are $c_\mathrm{s} = 8.4 \times 10^4$ cm/s, the initial dust-to-gas ratio is 10^{-2} and $\alpha = 10^{-3}$.

the influence of ξ on the particle distribution in the range $\xi \in [1.3, 2.1]$. The result, i.e. the equilibrium dust particle distribution after 10^4 yrs of disk evolution, is shown in Fig. 5.9. We adopted a surface energy of 10 erg/cm^2 and the same fragmentation and disk parameters as in the last section.

This figure shows that the dominant particle radius is shifted from 70 μm towards 1 mm by changing ξ from 1.3 to 2.1. Higher ξ-values, i.e. collisions resulting in more small particles, lead to higher threshold fragmentation velocities according to Eq. (5.17). Since relative particle velocities in disks increase with particle size[1], larger ξ-values also lead to larger maximum particle sizes before fragmentation prevents further growth. If the condition $5/3 < \xi < 2$ holds, then the leading term of the threshold fragmentation velocity follows

$$\ln v_\mathrm{c} \propto \xi \; . \tag{5.44}$$

Fig. 5.9 also indicates that larger ξ-values significantly change the slope of the dust particle distribution. For $\xi = 1.3$, the surface density increases rapidly with dust particle radius. While for μm-sized dust grains, the surface density is $\sim 10^{-5}$ g/cm^2, this value has increased by more than 3 orders of magnitude for 100 μm-sized grains. If we consider the case $\xi = 2.1$, then the particle distribution shows a rather flat behaviour and the surface density has a much weaker dependency on the dust particle size.

Fig. 5.9 also unveils that the surface density of sub-micrometer dust particles is strongly dependent on the power law index ξ. Disk spectra tend to be very dependent on the presence of these small sub-μm grains and, hence, on the fragmentation parameter ξ. This raises the question if observations of T Tauri disks can provide constraints on this crucial value.

[1]This statement only holds as long as the Stokes number of the particles is smaller than unity.

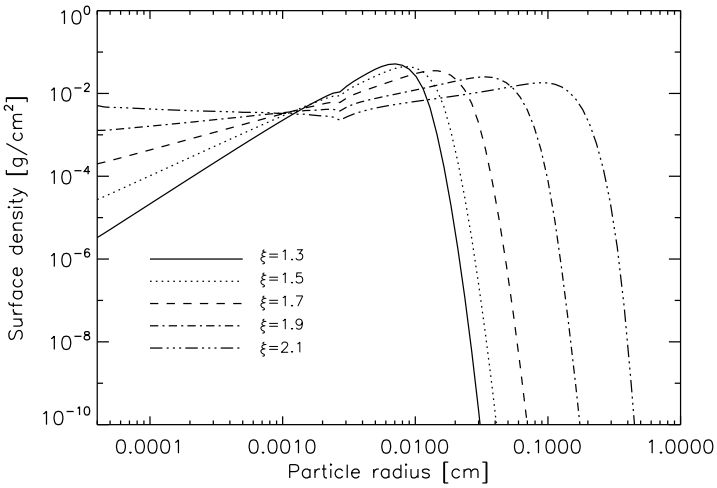

Figure 5.9: The same figure as Fig. 5.8, but now for different power law indices ξ.

5.2.3 Effect of the monomer radius a_0

Smaller monomer particle radii lead to higher tensile forces necessary to separate the adhering particles (Derjaguin et al. 1975). Therefore, smaller monomers lead to higher threshold fragmentation velocities which certainly influences the equilibrium particle distribution between coagulation and fragmentation. This raises the question of what the typical grain size of the interstellar medium (ISM), i.e. the parent material of the dust aggregates in protoplanetary disks, actually is.

Mathis et al. (1977) found a silicate grain size distribution ranging from 0.025 up to 0.25 μm by fitting the interstellar UV and visible extinction. More recently, Clayton et al. (2003), who give a very good overview about the history of grain size distributions, find ISM silicate distributions with an upper cutoff around 1 μm and a bulk density at 0.1 μm using maximum entropy methods to fit the interstellar extinction. Regarding these findings, we will investigate monomer particle radii between 0.1 and 1 μm. The result of this investigation, i.e. the equilibrium dust particle distribution after 10^4 yrs of disk evolution, is shown in Fig. 5.10. In these simulations, we adopted the same fragmentation and disk parameters as in the last section.

This figure indicates that larger monomer particle radii lead to lower maximum particle sizes. For $a_0 = 0.1$ μm for example, we find the bulk material to have a particle size between $a_{\max} = 0.3 \ldots 0.4$ mm. If the monomer radius is increased towards $a_0 = 0.9$ μm, then the dominant particle size decreases to a particle size around 0.2 mm. Hence, the dominant particle size of the equilibrium distribution shows a very weak dependency on the monomer radius.

We try to understand this behaviour by considering the threshold fragmentation velocity (Eqs. 5.14 and 5.18),

$$v_{\mathrm{c}} \propto \sqrt{\Delta O} \propto a_0^{-1/4} \,. \tag{5.45}$$

In this derivation, we adopted $\xi = 11/6$. In the disk model at hand, relative turbulent motions of the gas are the main source for relative dust particle velocities. Hence, these velocities

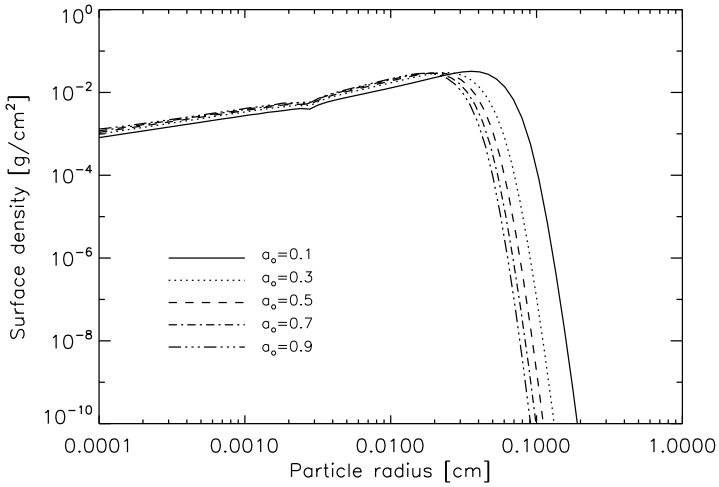

Figure 5.10: The same figure as Fig. 5.8, but now for different monomer particle radii.

follow (Cuzzi et al. 2001; Weidenschilling & Cuzzi 1993)

$$\Delta v_{\rm turb} \propto \sqrt{a_{\rm max}} \, . \tag{5.46}$$

If we equate the last two expression, we obtain the following dependency for the maximum particle size due to fragmentation,

$$a_{\rm max} \propto a_0^{-1/2} \, . \tag{5.47}$$

If the monomer size radius is increased by a factor of 9 then the dominant particle size should decrease by a factor of 3. According to Fig. 5.10, the maxima of the surface density for $a_0 = 0.1$ μm and 0.9 μm differ by a factor of 2.2, which is a bit lower than the estimated value. This is due to the fact, that relative turbulent particle velocities are not the only source for relative velocities. Even though relative radial velocities and relative vertical velocities due to particle settling towards the midplane are much lower than $\Delta v_{\rm turb}$ for St $\approx 10^{-2}$ dust grains, they do shift the dominant particle size to slightly lower values.

The ISM is not a monodisperse dust particle distribution of e.g. μm-sized dust grains. The ISM rather involves many different particle sizes, in particular dust grains much smaller than micrometer size. The binding energy and, hence, the threshold fragmentation velocities of dust aggregates can be different from our model if a broad particle size dispersion of the ISM is assumed. Smaller grains which are much higher in number sit between the larger dust particles can they can strengthen or weaken the dust agglomerate (Blum et al. 2006). The dust aggregate is strengthened if small particles sit in empty space gaps in between larger monomers. On the other hand, the aggregate is weakened if contacts between large grains and small grains are dominant in the dust particle. Blum et al. (2006) have shown that dust agglomerates formed from a broad particle size distribution lead to weaker bound particles than a formation from a monodisperse distribution. Therefore, the energy necessary to fragment the whole dust particle aggregate is probably lower than calculated in this section. Hence, dust particles presumably grow to smaller sizes than calculated here. Further investigation regarding this issue is surely needed.

Interstellar medium dust grains already grow to larger sizes in collapsing molecular clouds which finally form a protoplanetary disk. For this reason, the typical grain size distribution

in the ISM could be significantly different from particles which are present in the very early stages of disk evolution. Simulations of dust coagulation in dense molecular clouds indeed show that tiny dust grains, i.e. particles with radii ~ 10 nm at the lower end of the "typical" ISM distribution (Mathis et al. 1977; Greenberg 1978), are quickly removed from the size spectrum within only 10^5 yrs (Ossenkopf 1993; Ossenkopf & Henning 1994). Hence, we do not consider dust particles smaller than 0.1 μm as building blocks for larger aggregates in this section. Ossenkopf (1993) also shows, that the upper grain size limit is only slighly increased during the cloud collapse. This finding is supported by analytical calculations of dust growth time scales in molecular clouds which typically are of the order of $\sim 10^7$ to 10^8 yrs (Hirashita 2000). Since the life time of molecular clouds is usually less than $\sim 10^7$ yrs (Williams et al. 2000), i.e. smaller than a galactic arm crossing time, dust grains at the upper end of the ISM particle distribution simply do not have the time to undergo significant growth.

While collisions between ∼m-sized bodies lead to destruction for impact velocities less than 1 m/s (c.f. Fig. 5.6), collisions between m-sized bodies and tiny dust grains can still lead to particle growth even if relative velocities up to several 10 m/s are considered. This raises the question if larger particles can grow beyond the meter size barrier by sweeping up smaller dust grains. Figs. 5.8-5.11 show a very sharp cutoff in the particle distribution for larger sizes which suggests that this 'sweeping up scenario' is problematic. This is due to the following reason. From Sec. 5.1.2 we can calculate the threshold fragmentation velocity for $\xi = 11/6$ in the case of cratering which is (up to some tiny surface terms) given by

$$v_\mathrm{c} \approx \left[\frac{16\pi\gamma}{\left(\frac{4}{3}\pi\right)^{5/6}}\right]^{1/2} \mu^{-1/12}\, r_0^{-1/4}\,. \tag{5.48}$$

For $\gamma = 10$ erg/cm^2, $r_0 = 0.1$ μm and $\mu(r_0) \approx 7 \times 10^{-15}$ g, we obtain a critical fragmentation velocity of ~ 40 m/s. Even though this critical threshold velocity for fragmentation to occur is very high, relative particle velocities between micrometer sized dust grains and meter sized bodies usually exceed this value by far. Relative radial drift velocities in protoplanetary disks already have values of typically 50 m/s (Weidenschilling 1977a). If relative particle velocities caused by turbulent motions of the gas are also taken into account, relative speeds of the order of 10^2 m/s may occur around 1 AU in the disk (Weidenschilling & Cuzzi 1993; Ormel & Cuzzi 2007). These high velocities make the coagulation between large boulders and even sub-mircometer dust grains questionable at best and impossible at worst. Future laboratory experiments concerning high speed collisions between sub-μm dust grains and larger targets are needed.

5.2.4 Effect of the disk model

To perform the particle growth simulations of this section, we assumed a certain mass distribution in the disk. However, this distribution of dust and gas mass, i.e. the power law index of the surface density distribution δ, is still a matter of debate. This mass distribution controversy was already mentioned in Sec. 4.1.1. Different power law indices lead to different gas mass densities in the disk. Since Brauer et al. (2008) have shown that the maximum dust particle size before fragmentation inhibits further particle growth is very sensitive to the gas densities, different disk models can lead to quite different maximum particle sizes.

To illustrate this issue, we calculate the dust particle distribution after 10^4 yrs at 1 AU in the disk for 4 different δ-values. The results of this simulation are shown in Fig. 5.11. The solid line indicates the equilibrium particle distribution for the MMSN model. The

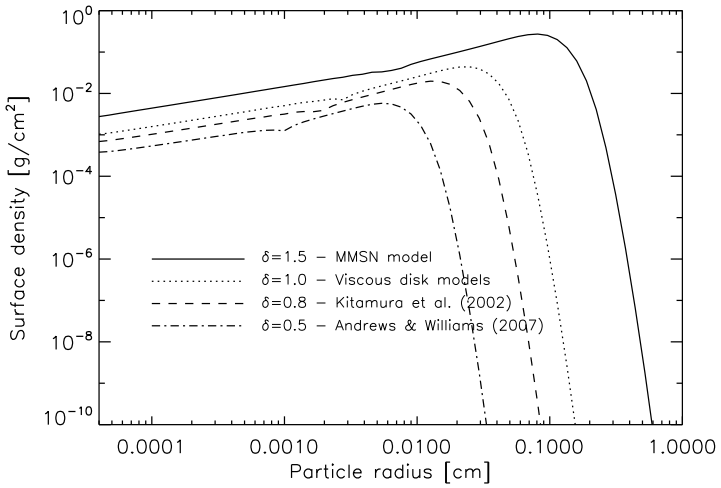

Figure 5.11: The equilibrium dust particle distribution after 10^4 yrs of disk evolution at 1 AU for different disk models as discussed in Sec. 5.2.4.

dotted line denotes the $\delta = 1$ case as suggested by viscous disk evolution models (Hueso & Guillot 2005). The dashed and the dotted-dashed line indicate models based on observational data (Kitamura et al. 2002; Andrews & Williams 2007). In these simulations, we adopted a monomer particle size of 0.4 μm, a power law index $\xi = 11/6$, an α-value of 10^{-3} and a surface energy of 10 erg/cm^2.

This figure shows that the maximum dominant particle radius strongly depends on the power law index δ. While particles can grow to roughly a millimeter in size at 1 AU in the MMSN model, disk models based on observational findings predict particle sizes of ~ 0.1 mm. This particular example shows that knowledge about the gas mass distribution in the disk is of high importance for reliable predictions of dust particle growth. For this reason, dust particle coagulation models including the viscous evolution of the gas, as for example done by Garaud (2007), seem to be the next logical step.

5.3 Particle radii and dust mass

In the last sections, we focused on the equilibrium dust particle distribution between coagulation and fragmentation specifically at 1 AU in the disk. To study particularly the isolated effects of the fragmentation model parameters on the particle distribution, we neglected the radial motion of solid particles to avoid radial mass transfer which also changes the dust particle distribution in time. However, in these next sections we will include the radial motion of dust. We will mainly focus on two disk quantities, namely the dominant particle size in the disk and the mass of the dust disk after 1 Myr.

5.3.1 Effect of the monomer radius

To which sizes can the dust particles grow at most in the disk? To answer this question, we calculate the maximum dominant particle size $a_{\rm m}(r)$ for all times as a function of disk location r. In other words, we first consider a fixed radial position r. Then we consider the

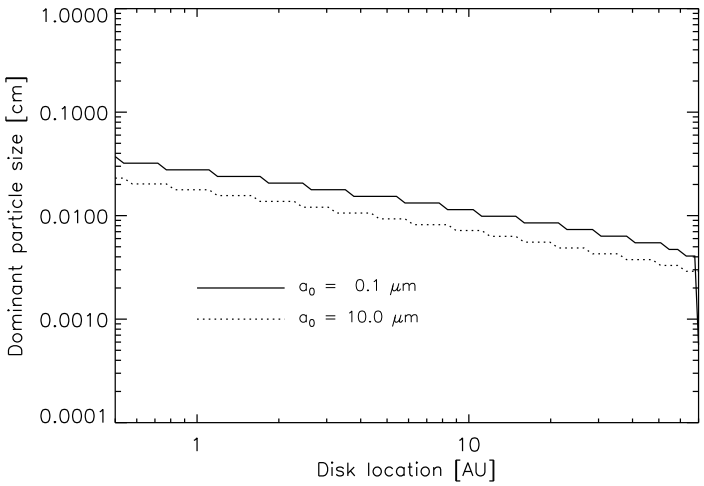

Figure 5.12: The maximum dust particle radius for times < 1 Myr as a function of disk location for two different monomer radii as discussed in Sec. 5.3.1. This figure indicates that the maximum dust grain radius is rather weakly dependent on the size of the monomers.

particle radius $a_{\rm m}(r,t)$ for which the surface density has a maximum at a certain time t. The maximum dominant particle size is then given by

$$a_{\rm m}(r) = \max{}_t \left[a_{\rm m}(r,t)\right] \ . \tag{5.49}$$

Fig. 5.12 shows this quantity for the two monomer radii $a_0 = 0.1$ μm and 10 μm. In Sec. 5.2.3, we already found that the maximum particle size in the equilibrium distribution is rather weakly dependent on the monomer radius. Fig. 5.12 indicates that this situation does not change if radial motion of the dust is included in the simulations. If the monomer radius is changed by an order of magnitude then the dominant particle size is altered by a factor of two at most. We conclude, that the maximum particle size before fragmentation inhibits further particle growth is rather independent on the particle size distribution of the ISM.

Particles in a protoplanetary disk tend to drift radially inwards due to gas drag forces as already discussed in the previous chapters. To investigate how much mass is lost due to radial motion, we calculate the mass of the dust disk after 1 Myr of disk evolution. We performed this calculation for different monomer size radii and different power law indices ξ. The result is shown in Fig. 5.13

This Figure shows that the remnant dust mass after 1 Myr increases with increasing monomer size radii. For monomer particles of radius $a_0 = 0.1$ μm, the remaining dust mass is $\sim 2.5\%$ of the initial dust mass if we consider $\xi = 2$. If we adopt monomers which are one order of magnitude larger, then the remaining dust mass has increased to 4.5%. Larger monomer particles lead to smaller threshold fragmentation velocities and, hence, to smaller particles due to destructive collisions. Smaller particles also have smaller radial inward drift velocities and, hence, longer drift times scales. Therefore, a larger amount of dust mass remains in the disk after a certain time.

Even though we will discuss the influence of the ξ-parameter on the remnant dust mass in the next section, we already want to note one point here. For the particular value $\xi = 1.4$, the remaining mass is very weakly dependent on the monomer radius. This is due to the

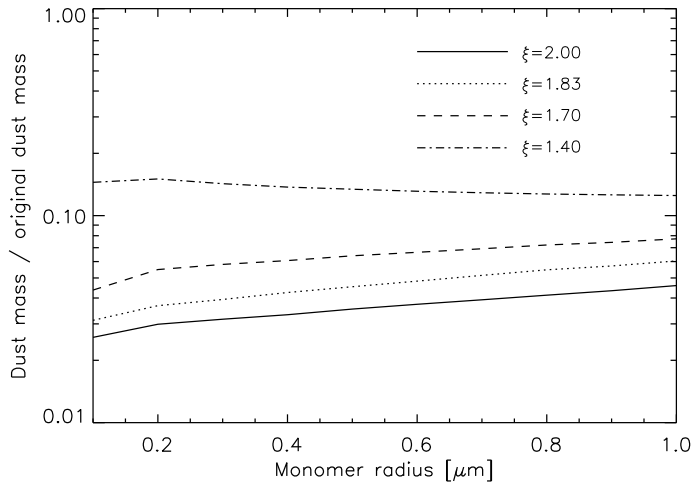

Figure 5.13: The dust mass of the remnant disk after 1 Mys as a function of monomer radius for different fragmentation power law indices ξ as discussed in Sec. 5.3.1.

following reason. For $\xi < 5/3$, the structure function Eq. (5.17) is $\propto n^{2/3}$. Hence, the gain in surface area ΔO becomes independent of n and, hence, independent of the monomer size radius a_0. The physical explanation for this is that for small ξ-values, the fragments after destructive collisions are only slightly smaller than the colliding bodies. Most of the mass is at the large end of the particle distribution. Therefore, the surface area gain is rather determined by the size of the colliding bodies than by the size of the monomer particles. For this reason, the remnant dust mass becomes independent of monomer size for $\xi < 5/3$.

5.3.2 Effect of the power law index ξ

We again calculate the maximum dominant particle radius for times < 1 Myr as a function of disk location between 0.5 and 100 AU. However, this time we adopted different fragmentation power law indices ξ instead of different monomer particle radii. The result of these simulations is shown in Fig. 5.14.

In Sec. 5.2.2, we already found that the maximum particle size in the equilibrium distribution is very dependent on the ξ-value. The results shown in Fig. 5.14, i.e. the simulations including the radial motion of solid material, mirror this strong dependency. For $\xi = 1.3$, only small aggregates of 0.1 mm in radius can form in the inner parts of the disk before fragmentation prevents further particle growth. If we adopt a ξ-value of 2.1, then the dust grains can grow to particle sizes which are roughly one order of magnitude larger.

As in the last section, we also calculate the dust mass of the remnant disk as a function of the power law index ξ for different turbulent α-parameters. The result is shown in Fig. 5.15. This figure indicates that higher ξ-values lead to less remaining mass after 1 Myr. This can be explained by the fact that larger ξ-parameters lead to higher threshold fragmentation velocities, c.f. Fig. 5.2. In other words, particles can grow to larger sizes before fragmentation starts to play a significant role. Larger particle radii lead to higher radial drift velocities and, hence, to less remaining mass after a certain time.

Let us consider the remaining dust mass for different turbulent α-parameters for the case

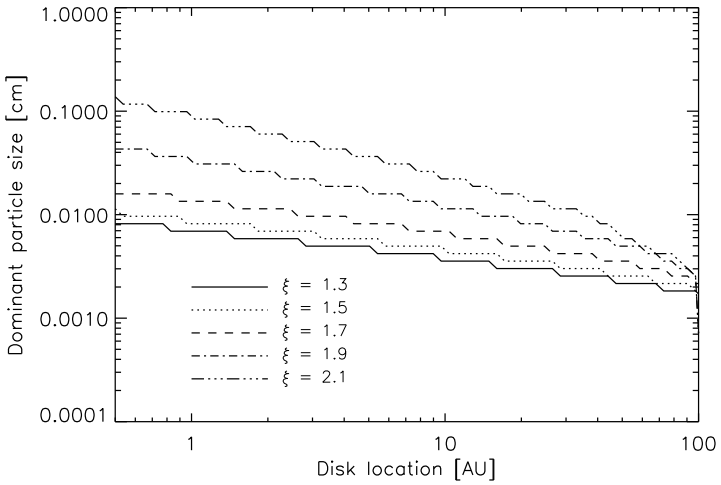

Figure 5.14: The maximum dominant particle radius for times < 1 Myr as a function of disk location for different fragmentation power law indices ξ as discussed in Sec. 5.3.2.

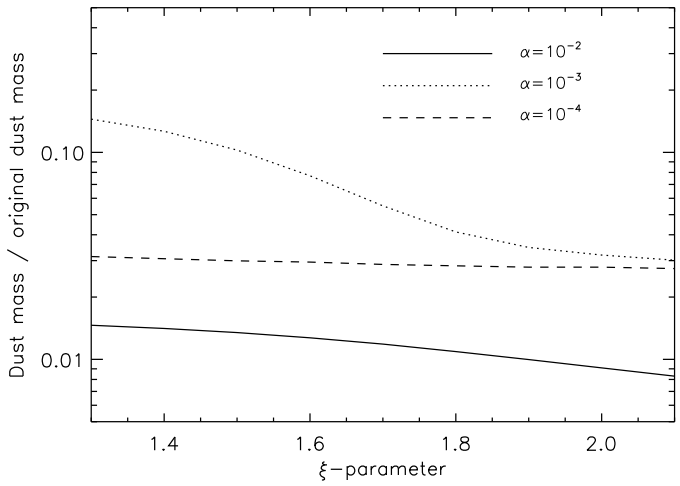

Figure 5.15: The remaining dust mass after 1 Myr normalised to the initial dust mass as a function of the power law index ξ for different turbulent α-values as discussed in Sec. 5.3.2.

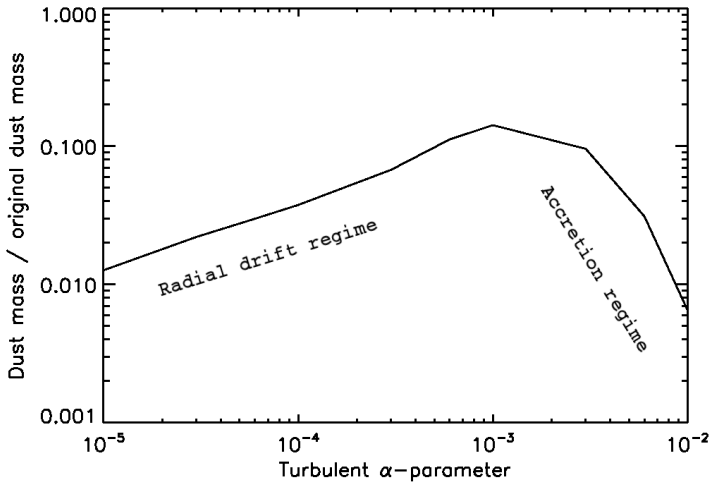

Figure 5.16: The remaining dust mass after 1 Mys normalised to the initial dust mass as a function of the turbulent α-parameter as discussed in Sec. 5.3.2.

$\xi = 1.3$. If $\alpha = 10^{-4}$, then the dust mass after 1 Myr is $\sim 3\%$ of the initial dust mass. For an α-value which is one order of magnitude larger, i.e. $\alpha = 10^{-3}$, the remnant solid material mass has increased towards more than 10% of the initial dust mass. Now, something interesting happens. If we consider even higher turbulent disks, then the remaining dust decreases again. For example, if we adopt $\alpha = 10^{-2}$, then the dust mass after 1 Myr has dropped again to $\sim 3\%$ of the inital mass. To illustrate this issue more clearly, we calculate the solid material mass in the disk after 1 Myr as a function of the turbulent α-value for the case $\xi = 1.3$. The result is shown in Fig. 5.16. This plot again indicates that the turbulence parameter $\alpha = 10^{-3}$ is peculiar for some reason.

To unveil this issue, let us first consider a very low turbulent disk, i.e. with α-value of 10^{-5}. In this low turbulent case, dust particles can grow to comparatively large sizes due to small relative turbulent particle velocities. For this reason, dust particle collisions rather lead to particle growth than to particle fragmentation. Large particles involve high radial drift velocities which explains the little amount of remaining dust mass after a certain time.

With increasing turbulence in the disk, the average size of the dust particles decreases. This leads to lower radial drift velocities and, therefore, to higher disk masses after 1 Myr. For this reason, the remaining dust mass increases with the α-parameter, c.f. Fig. 5.16.

However, if the α-value exceeds 10^{-3} then the remaining dust mass starts to decrease again. This behaviour is due to the viscous accretion of the gas disk itself. Also the gas has a radial inward velocity due to viscous stress. This radial velocity is of the order of some cm/s for $\alpha = 10^{-3}$. Since small dust grains are very strongly coupled to the gas, the dust particles move with the gas towards the inner regions of the disk. More turbulence in the disk, i.e. higher α-values, lead to larger radial gas accretion velocities. This again decreases the remaining dust mass after 1 Myr.

We can estimate for which α-values dust mass loss due to radial gas accretion becomes of significance. Therefore, we consider the radial gas accretion velocity (Takeuchi & Lin 2002;

Brauer et al. 2008)

$$v_{\mathrm{acc.}} = -\frac{6}{5}\alpha v_{\mathrm{n}} \ . \tag{5.50}$$

In this last expression, we already adopted the specific parameters of our disk model. The quantity v_{n} is the maximum radial drift velocity for dust particles due to gas drag (Weidenschilling 1977a). The radial inward velocity of single particles due to the headwind of gas is given by

$$v_{\mathrm{head.}} = 2v_{\mathrm{n}}\mathrm{St} \ . \tag{5.51}$$

The quantity St is the Stokes number of the particles which describes the coupling strength between the dust and the gas. Equating the last two expressions, we find the critical α-value for which accretion becomes more important than single particle drift,

$$\alpha_{\mathrm{crit.}} = \frac{5}{3}\mathrm{St} \ . \tag{5.52}$$

If we consider the case $\xi = 1.3$, then Fig. 5.14 indicates that the dominant particle size is roughly given by 0.1 mm. In our disk model, this particle size corresponds to a Stokes number of $\sim 10^{-3}$. Hence, the critical turbulent α-parameter is approximately 2×10^{-3}, which is in good agreement with the simulation results shown in Fig. 5.16.

5.4 Summary and conclusions

We improved the disk model presented in chapter 4 by developing an analytical model to describe particle fragmentation. This new model enabled us to calculate realistic threshold velocities for particle fragmentation. One major result of this model is a strong correlation between threshold fragmentation velocities and the mass of the colliding particles. This finding is in agreement with laboratory experiments (Blum & Wurm 2000; Wurm et al. 2005). We find that small dust grains stick to each other up to comparatively high relative velocities of several 10 m/s, while treshold fragmentation velocities between m-sized boulders are only of the order of ~ 10 cm/s.

The power law index ξ which describes the outcome of a destructive collision, i.e. the particle distribution after fragmentation, was considered to be an independent input parameter of our model. However, this parameter usually depends on the impact velocity of the colliding bodies. Low velocity impacts usually lead to fragments comparable to the size of the parent bodies. High velocity impacts tend to produce very small fragments. Even though Fig. 5.3 mirrors this behaviour, taking this dependency fully into account would mean to apply the fragmentation model presented in this paper locally at every point in the disk which goes beyond the scope of this work. Nevertheless, this is an important issue and further investigation is surely needed.

We investigated to which particle sizes the dust typically grows in a protoplanetary disk. We find, in agreement with previous studies and current beliefs, that again particle fragmentation is a genuine problem. Even though different model parameters lead to different maximum particle sizes, we never find dust agglomeration to be an effective mechanism to form larger objects of e.g. km-size. Dust particles typically grow to radii of several millimeters before fragmentation start to play a non-negligible role. We also investigated the growth of dust considering different gas mass distributions in the disk. We find that dust particles can grow to larger sizes in the MMSN model than in disk models adopting more moderate radial surface density profiles.

In the beginning of this chapter, we mentioned the possibility that solid particles could overcome the fragmentation barrier by sweeping up smaller dust grains. This formation growth scenario is based on the fact that coagulation between e.g. μm-sized dust grains and meter-sized bolders can result in particle sticking up to relatively high collision velocities of several 10 m/s. Hence, some lucky m-sized particles which are not destroyed in destructive high speed impacts between equal meter-sized bodies could still grow by collecting small dust grains while moving through a dusty disk background. This mechanism might lead to the formation of large boulders with sizes beyond the fragmentation barrier. However, we find this "sweeping up scenario" to be problematic. Even though the fragmentation velocities between small and large particles can be as high as 40 m/s, typical relative particle velocities in disks can be of the order of 100 m/s. These high velocities make the coagulation between large boulders and even sub-micrometer dust grains questionable.

We also calculated the mass of the remnant dust disk after 1 Myr of disk evolution. According to our simulations, the remaining dust mass can range between 0.5% and 20% of the initial dust mass depending on the disk model and fragmentation parameters. This wide range of remaining dust masses unveils that knowledge about particle fragmentation parameters and the possible outcome of destructive collisions are of great importance to predict the evolution of protoplanetary disks emphasising the need for further laboratory experiments regarding dust particle collisions.

There are at least two possible strategies to circumvent massive particle fragmentation in protoplanetary disks and to form planetesimals, nevertheless. These two strategies can be unveiled if we recall that dust particle destruction occurs if *relative particle velocities* exceed a critical *threshold fragmentation velocity.* Apparently, we can overcome this obstacle by looking for a particle size regime in which threshold fragmentation velocities are comparatively high. Wurm et al. (2005) found in 'crossbow' collision experiments that particles can have net growth up to collision velocities of 25 m/s. Even though parts of the dust underwent massive fragmentation, net growth on the target particle was observed. Hence, one possibility is to investigate particle fragmentation properties – either experimental or theoretical – and to hope that particles of certain sizes can stick to each other up to very high velocities.

Lets consider the second possible backdoor. We could alternatively look for regions in protoplanetary disks in which relative particle velocities are significantly lower. This would lead to particle growth which outbalances particle fragmentation. If we regard the two main sources for relative particle velocities in disks, i.e. turbulence and radial drift, we could ask the question: In which regions and in what kind of disks do these relative particle velocities cease?

We first consider relative turbulent velocities. Under certain conditions, disks can have a non-turbulent dead zone around the midplane. While the upper layers of the disk are MRI-active, turbulence ceases in the regions around the equatorial plane. A residual α-value of 10^{-5} in the midplane leads to maximum turbulent velocities of only ~ 3 m/s and particle coagulation at these velocities is not unlikely. A possible mechanism to suppress radial drift, i.e. the second source for high relative velocities, was recently presented by Kretke & Lin (2007). They find that the snow line can be associated with a radial gas pressure maximum in which radial motion basically ceases. Fragmentation, hence, becomes even less likely. In the next chapter, we investigate exactly this scenario. We focus on dust particles growth around the snow line in layered MRI-driven turbulent disks.

There are several other mechanisms in protoplanetary disks involving pressure maxima (Klahr & Lin 2001; Haghighipour & Boss 2003; Rice et al. 2004; Johansen et al. 2006b) which could play a similar key role for the formation of larger boulders which are not included

in the disk evolution models discussed here. In fact, the *a priori* exclusion of local gas density fluctuations in the particle growth models discussed so far, i.e. the consideration of monotonically decreasing gas surface densities in the disk, maybe even prevents the formation of larger objects. In other words, could it be possible that dust particle growth in disks with "smooth" gas density distributions will intrinsically never lead to the formation of larger boulders? The next chapter tries to answer this question.

Chapter 6

Particle growth around the snow line

The previous two chapters have shown that dust particle fragmentation is a severe obstacle for planetesimal formation. Depending on the disk model, dust particle growth is significantly inhibited by high-speed impacts for particles around meter size. Even for times as large as 1 Myr, solid particles are not able to overcome the fragmentation barrier and the formation of planetesimals as precursors for Earth-like or Jovian planets, therefore, poses a major problem.

However, as already mentioned in the discussion of the last chapter, there are several mechanisms in protoplanetary disks which could still lead to planetesimal formation. For example, Johansen et al. (2007) have recently shown that the non-linear feedback of the dust onto the gas can lead to the rapid formation of gravitationally bound clumps of dust which subsequently form Ceres-size bodies. The dust particles, however, must have already grown to some meters in size before this scenario can take place. Another possibility which could provide a solution to this formation problem is particle trapping in gas pressure maxima (Barge & Sommeria 1995; Klahr & Henning 1997). In gas pressure bumps, relative particle velocities are substantially lower and, hence, the collision between large bodies more likely leads to particle growth than to particle disruption.

An intriguing process which can lead to gas pressure maxima and dust particle trapping was recently presented by Kretke & Lin (2007). This particle retention mechanism requires the presence of an evaporation front, for example the snow line, and acts in the following way. When we pass through the snow line away from the central star then the dust-to-gas ratio suddenly increases. In a disk with solar composition, the total mass fraction in grains increases by at least 50% due to the condensation of water vapor exterior to the snow line (Lodders 2003). This dust density jump affects the strength of the magneto-rotational turbulence since the amount of free electrons in the disk strongly depends on the dust densities. With increasing dust density, the amount of turbulence in the disk decreases (Sano et al. 2000; Ilgner & Nelson 2006). We now assume a constant mass accretion rate throughout the disk. The gas surface density then has to be larger in low turbulent disk regions than in high turbulent regions for the gas mass accretion to result in the same value. The jump in the dust densities, hence, could also lead to a jump in the gas densities. For certain accretion rates, Kretke & Lin (2007) found the occurence of a local gas density bump in which solid particles tend to accumulate. In their simulations, dust particle retention led to very high surface dust densities of the order of several 10^3 g/cm^2 which raises the question

of gravitational instability.

However, even with such a particle retention mechanism described above, the growth of solid material towards larger sizes remains an open issue. Gas pressure maxima may decrease relative radial particle velocities triggering coagulation, but the most severe reason for violent particle fragmentation is not radial drift but the turbulent nature of the protoplanetary disk itself. Relative turbulent particle velocities are of the order of several 10 m/s (Ormel & Cuzzi 2007; Völk et al. 1980) and particle sticking at these high speeds is doubtful at best. Nevertheless, Ciesla (2007) found that particles can grow to several 10 m in radius if layered MRI active disks are considered. Under certain circumstances, MRI is only active in the upper layers of the disk while the disk midplane is nearly laminar. Since most of the larger grains are located around the midplane where the disk is basically quiescent, dust growth is not inhibited by high speed collisions resulting in particle fragmentation.

In this last chapter, we combine three ingredients for a planetesimal formation model. We consider dust particle growth, coagulation and fragmentation (Brauer et al. 2008) around the snow line (Kretke & Lin 2007) in a layered MRI active protoplanetary disk (Ciesla 2007). The inclusion of the snow line into our simulations will provide a particle retention mechanism and nearly ceasing radial drift velocities favouring particle growth. We adopt a layered MRI-driven disk to circumvent particle fragmentation in the midplane of the disk due to turbulent motions of the gas. We try to answer the question if solid particles can overcome the fragmentation barrier and form larger objects as possible precursors for planets. We will investigate the influence of two parameters, namely the gas accretion rate $\dot{M}_{\rm acc}$ and the critical theshold velocity for fragmentation $v_{\rm f}$.

6.1 Theoretical background

We consider a background gas disk which is in a steady state and, hence, does not change in time. We also assume that the mass accretion rate is a constant, i.e. that this quantity does not depent on disk location, an assumption which is not necessarily true. The surface gas densities are then given by (Pringle 1981)

$$\Sigma = \frac{\dot{M}}{3\pi\alpha c_{\rm s} H} \, . \tag{6.1}$$

In a layered MRI-driven disk which we consider here, the α-parameter depends on the height above the midplane. While the upper disk surface is fully MRI active (large α), the region around the midplane tends to be quiescent (low α). In order to calculate the surface gas densities, we use the vertically integrated α-value given by

$$\alpha(r) = \frac{\Sigma_{\rm A}(r)}{\Sigma(r)} \alpha_{\rm MRI} + \alpha_0 \, . \tag{6.2}$$

This last expression shows, that the α-parameter is dependent on the disk location r. The $\alpha_{\rm MRI}$-value which corresponds to fully developed MRI turbulence is given by $\alpha_{\rm MRI} = 1.8 \times 10^{-2} (\beta/1000)^{-1}$ (Sano et al. 1998). For the plasma parameter β, we will use $\beta = 1000$ which is a reasonable value for disks with weak magnetic fields (Sano et al. 2000). The residual turbulence value α_0 represents some mechanism of angular momentum in the quiescent part of the disk around the midplane. This low turbulence could be due to either self-induced turbulence (Weidenschilling 1979), baroclinic instability (Klahr & Bodenheimer 2003) or strong MRI turbulence on the surface of the disk which is able to stir up even the hardly

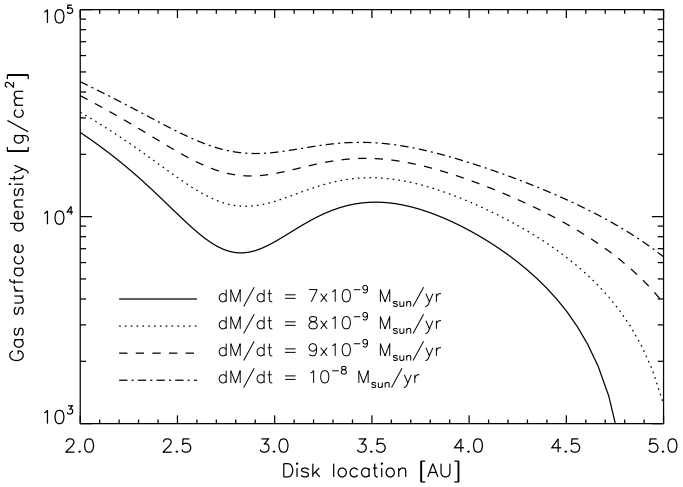

Figure 6.1: The surface gas densities for different gas accretion rates which we will use in our simulations as discussed in Sec. 6.1. The snow line is located at 3 AU.

ionized inner regions of the disk if gas-phase heavy metals, such as magnesium, are present (Ilgner & Nelson 2008). Here, we will set this residual α_0-value to 10^{-5}.

Now, the surface density of the region unstable to MRI turbulence can locally be described by a power law. In our model, we follow Kretke & Lin (2007) and we adopt

$$\Sigma_{\rm A} = \left(\frac{r}{r_0}\right)^p \left[\frac{\Sigma_1 - \Sigma_2}{2}\left(1 + {\rm erf}\left[\frac{r_0 - r}{\Delta r}\right]\right) + \Sigma_2\right] \ . \tag{6.3}$$

The quantities r_0 and Δr denote the location and the width of the snow line. We will adopt $r_0 = 3$ AU (Lecar et al. 2006) and $\Delta r = 0.5$ AU in our simulations. The variables Σ_1 and Σ_2 indicate the column depth of the regions unstable to MRI turbulence diminutive interior and exterior to the snow line, respectively. Closely interior to the snow line where H_2O is in gas form, we adopt a surface density of the active layer of 5 g/cm^2. Closely exterior where H_2O is frozen out, we adopt an active surface layer with a column density of 20 g/cm^2. The power law index p is set to 1.5. The last three expression lead to a gas surface density which is shown in Fig. 6.1.

The occurence of a local gas density maximum is strongly dependent on the gas accretion rate. In the early phases of disk evolution, the mass accretion rates are high (Hartmann et al. 1998) corresponding to large surface gas densities (c.f. Eq. 6.1). The small contribution of the change in the active layer at the snow line, hence, will not be important in these early disks. When the mass accretion rate drops in time, the surface gas densities are more and more affected by the active MRI surface layer. We focus on this evolutionary disk stage in the simulations performed here. Finally, the surface gas densities will decreases to a point where the whole vertical disk extent becomes MRI active and no gas density bump will occur.

Let us focus on the dust component in the disk. As in the last chapters, we include the radial drift motion of solids in our model. The maximum radial inward drift velocity is given by

$$v_{\rm N} = \frac{\partial_r P_{\rm g}}{2\rho_{\rm g}\Omega_{\rm k}} \ . \tag{6.4}$$

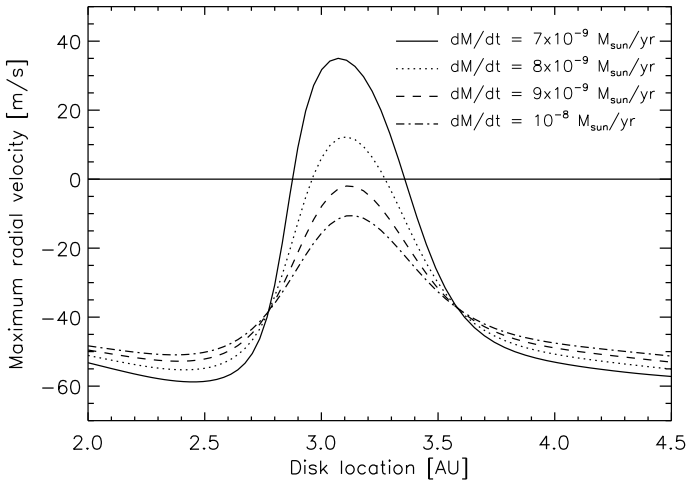

Figure 6.2: Maximum radial drift velocity $v_{\rm N}$ for different gas accretion rates as discussed in Sec. 6.1. The horizontal line indicates zero radial drift. Outward drift occurs for the two accretion rates 7×10^{-9} and 8×10^{-9} $\mathrm{M_{sun}/yr}$. Hence, we expect dust grain retention for these two values. Note as well, that for these two accretion rates, there are two stagnation points in which the radial drift speed vanishes.

This quantity as a function of disk location for different accretion rates is shown in Fig. 6.2. From this maximum radial drift velocity, we can calculate the actual radial drift speed of a particle of a certain size and solve the continuity equation in the radial direction for all dust particle species. Radial diffusion due to turbulent mixing is included in the model as well.

Fig. 6.2 shows, that for sufficiently small accretion rates, grain retention will occur around the snow line near 3 AU in the disk. For dust particle growth, it is even more important to note that there are two radial drift stagnation points, i.e. disk locations at which the radial drift completely vanishes. Relative particle speeds at these radii are too low to induce destructive particle collisions. While solid particles move away from the inner diverging point at ~ 2.9 AU, the dust tends to accumulate in the outer converging point at ~ 3.3 AU.

We also consider that the disk has a vertical structure. The vertical dust distribution is determined by turbulent diffusion and particle settling towards the midplane (Dubrulle et al. 1995; Schräpler & Henning 2004). We solve the sedimentation/diffusion equation with a semi-analytical model, assuming that the particle distribution is in equilibrium between particle settling and turbulent mixing. We consider a dead zone around the midplane in which there is nearly no turbulence present. In this region, we adopt an α-value of 10^{-5}. In the MRI active regions on the surface of the disk, we assume an α parameter of 1.8×10^{-2} (Sano et al. 1998). Little turbulence around the midplane involves small relative turbulent velocities (Ormel & Cuzzi 2007). Hence, in the radial drift stagnation points, *all* relative velocities, i.e. relative turbulent and relative radial velocities, are low and we may expect dust particles to grow to larger sizes and break through the fragmentation barrier in the midplane of the disk.

Since the column density of the MRI active gas is much smaller than the surface density of the total gas, i.e. $\Sigma_{\rm A} \ll \Sigma$, the region in which the α-value is large is confined to high disk surface regions $> 3H$. As dust particles grow, they rapidly settle into the deadzone due

to vertical gravity and escape from the high turbulent regions high above the midplane. For this reason, we find the value for $\alpha_{\rm MRI}$ to play a minor role for the results in this chapter.

At every point in the disk, we allow dust particles to coagulate and to grow to larger sizes or to suffer fragmentation due to high speed collisions. The parameter which distinguishes between these two cases is the collision velocity of the particles. If this quantity is larger than a critical threshold velocity $v_{\rm f}$, fragmentation will occur. Apart from the accretion rate $\dot{M}_{\rm acc}$, the threshold fragmentation velocity is the second parameter which will be investigated in this chapter. In the simulations, we will assume five sources for relative particle velocities in the disk which lead to dust growth, namely Brownian motion, differential settling, relative turbulent velocities and relative radial and azimuthal velocities. All these sources are extensively explained in chapter 4. The numerical schemes to solve the rather complicated coagulation equation, i.e. the Smoluchowski equation, the outcome of fragmentation and the effect of cratering which will also be included in this model are explained in great detail in chapter 2.

In the simulations of the chapters 4 and 5, particles were smaller than the mean free path of the gas at any point in the disk. This is not the case here due to very high gas densities. This means that we have to consider a different drag force regime, namely the Stokes regime instead of the Epstein regime. For our purposes, it is sufficient to implement the Stokes regime for particle Reynolds numbers smaller than unity (Weidenschilling 1977a)

$$\mathrm{St}_{\rm Stokes} = \frac{9}{4}\,\mathrm{St}_{\rm Epstein}\left(\frac{a}{\lambda}\right) \ . \tag{6.5}$$

To avoid confusion, we remark that the particle Reynolds number has nothing to do with the Reynolds number of the turbulent gas.

6.2 Numerical results

Fig. 6.3 shows the particle distribution after 1800 yrs of disk evolution for different accretion rates. In this simulation, we adopt a critical threshold fragmentation velocity of 10 m/s. This plot indicates that particles can grow to some 10^2 m in size around the ice evaporation front subject to the condition that the gas accretion rate is not too high. It also shows that fragmentation inhibits particle growth towards m-sized particles in other disk regions, for example around 4 AU.

According to these results, particles can grow to km-sized planetesimals in very short time scales, i.e. a few 10^3 yrs around 3 AU in the disk. Dullemond & Dominik (2005) and also the numerical results in Chapter 4, however, suggested that the growth time scales for the formation of km-sized objects – without particle fragmentation – is at least of the order of 10^5 yrs. How can this difference be explained? This discrepancy is due to quite different disk models which these dust evolution simulations are based upon. The model of Dullemond & Dominik (2005) and the model in Chapter 4 involve rather low gas surface densities of 100 and 20 g/cm^2, respectively. The disk model presented here has surface densities of the order of 10^4 g/cm^2, which is at least two orders of magnitude larger. Particle growth time scales for $\mathrm{St} > 1$ depend on the gas densities. This can easily be understood by regarding particle growth time scales at a fixed radius in the disk for particles with Stokes numbers larger than unity,

$$\dot{a} \propto \rho_{\rm d} \cdot \Delta v \propto \frac{\Sigma_{\rm d}}{H}\sqrt{\frac{\mathrm{St}}{\alpha}} \cdot \sqrt{\alpha} c_{\rm s} \sqrt{\frac{1}{\mathrm{St}}} \propto \Sigma_{\rm d} \propto \Sigma_{\rm g} \quad \text{and} \quad \mathrm{St} > 1 \ . \tag{6.6}$$

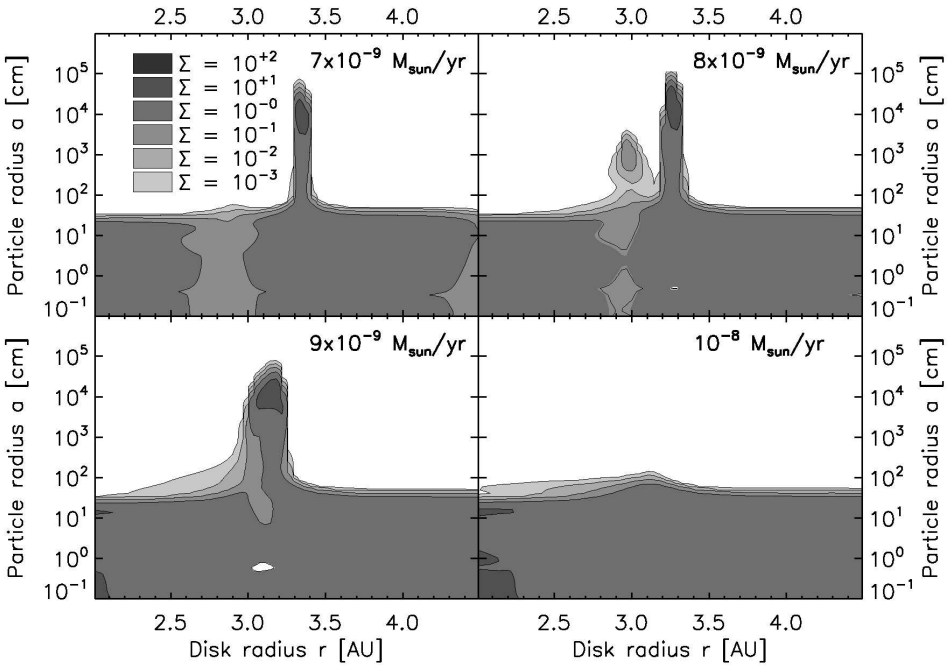

Figure 6.3: The particle distribution after 1800 yrs of disk evolution as discussed in Sec. 6.2. Shown is a contour plot of the surface dust density as a function of disk location and particle radius for four different accretion rates. The figure indicates that particles break through the fragmentation barrier if the accretion rate is not too high. The critical fragmentation velocity is 10 m/s in this simulation.

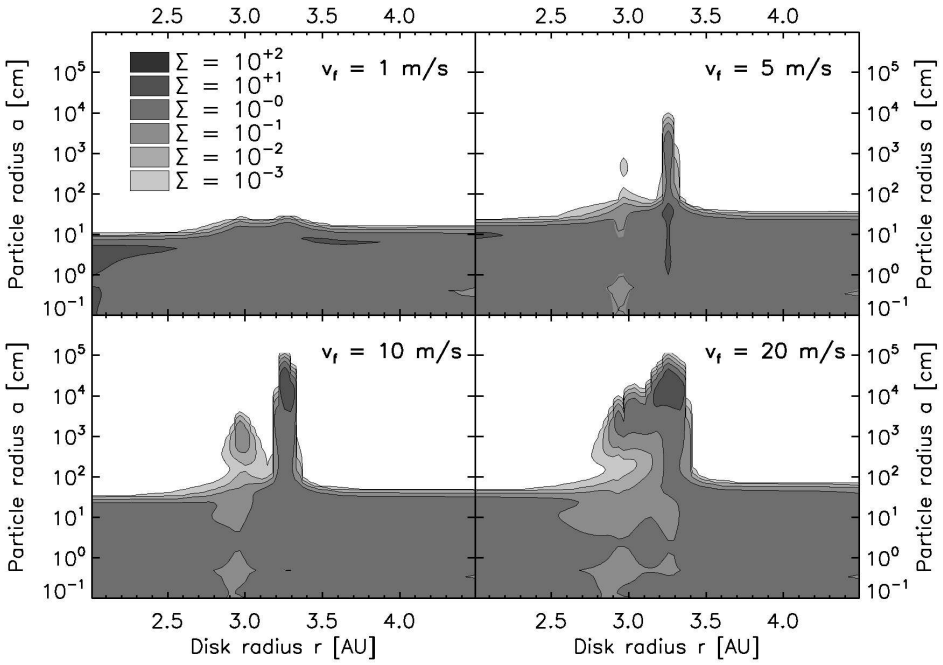

Figure 6.4: As Fig. 6.3, but now for four different critical theshold fragmentation velocities. The figure indicates that dust particles can break through the fragmentation barrier if the theshold fragmentation velocity is at least 5 m/s. In this simulation, we adopted an accretion rate of $\dot{M}_{\rm acc} = 8 \times 10^{-9}\ M_{\rm sun}/{\rm yr}$.

Since the gas surface densities are a factor of ~ 100 larger in the simulations performed in this Chapter, the coagulation time scales decrease accordingly.

The accretion rate of a protoplanetary disk decreases in time (Hartmann et al. 1998). Therefore, Fig. 6.3 also mirrors the virtue of our planetesimal formation mechanism at different stages of disk evolution. As already mentioned in the introduction of this Chapter, in the early stages, the accretion rate is too high for the dip in the dust-to-gas ratio at the snow line to significantly affect the gas surface densities. Hence, we do not find particles to grow to very large objects in this case. With decreasing accretion ratein time, the surface gas density gets more and more affected by the snow line resulting in the formation of large boulders as shown in Fig. 6.3. At this stage of disk evolution, planetesimal formation could take place. At later evolutionary stages, the surface gas densities will have declined towards a level at which the whole disk becomes MRI active and this mechanism does not longer work.

The dust particle distribution after 1800 yrs, but now for different criticial fragmentation velocities, is shown in Fig. 6.4. In this calculation, we considered an accretion rate of $\dot{M}_{\rm acc} = 8 \times 10^{-9}\ M_{\rm sun}/{\rm yr}$. This plot indicates that dust particles can overcome the fragmentation barrier and grow to nearly km-size if the critical theshold velocity is at least 5 m/s. For the case $v_{\rm f} = 1$ m/s, we do not find particles which are able to grow larger than a meter in radius. This is due to the fact that relative turbulent velocities in our quiescent midplane are still of the order of several m/s. Even with a very low residual turbulent α_0-value of 10^{-6}, relative particle velocities will hardly drop below this value.

In the simulation in which a fragmentation velocity of 10 m/s was assumed, it can be

clearly seen that particles manage to break through the fragmentation barrier at both radial drift stagnation points. Even though the amount of mass which coagulates beyond meter size is larger at the outer stagnation point at 3.3 AU, particle can still grow to 10 m size in $\sim$ 2000 yrs at the inner diverging point at $\sim$ 2.9 AU where the radial drift speed is zero. This effect is due to radial turbulent mixing which transports dust particles towards the inner stagnation point even though radial drift attempts to deplete this disk region.

Particle growth beyond the fragmentation barrier in low relative velocity regions does not necessarily mean that the particle will survive the near future and become a planetesimal. The boulder can again be transported into a disk region with high relative particle velocities which can still lead to the destruction of the body. The inclusion of turbulent diffusion into our model provides such a mass transfer mechanisms. The fact that we, nevertheless, find particles which can grow to very large sizes suggests that evaporation fronts may provide a quite favourable environment to form precursors for planets.

The residual turbulent α_0-value around the midplane can be shifted to higher values due to the occurrence of turbulent convection. Klahr & Henning (1997) suggest turbulent gas speeds of $\sim 0.02 c_\mathrm{s}$, which correspond to velocities of $\sim$ 16 m/s at 1 AU and an α-value of $\sim 10^{-4}$. Hence, if convection is a driving source of turbulence in the disk then the results of this Letter might change significantly. Turner et al. (2007) showed that free charges can be mixed into the disk interior, producing a slight coupling between the midplane gas and the magnetic fields. This may generate an active turbulent midlane layer, which could trigger particle fragmentation. Further investigation of the influence of each of these effects is imperative.

6.3 Conclusions

Even though particle fragmentation by high speed collisions is a severe obstacle for the formation of planetesimals, this chapter showed that dust particle growth towards very large boulders is possible under certain circumstances. If dust particle coagulation in the presence of an evaporation front is considered, solid particles can grow to nearly km-sizes within only a few thousand years. Another condition is that the protoplanetary disk involves a dead zone in which turbulence – the main source for relative particle velocities – nearly ceases. The main conclusion is that planetesimal formation due to dust particle agglomeration is a possible mechanism to form large bodies in protoplanetary disks.

Gas density maxima caused by alternative scenarios could affect the dust particle evolution in a similar way. After the mechanism presented in this last chapter has formed a planetesimal around the snow line, the mass accreting body will become so large at some point that it produces spiral waves and vortices due to planet disk interactions (Nelson & Papaloizou 2003). These induced disk structures could lead to further built up of solid material (Bryden et al. 2000; Haghighipour & Boss 2003) which could again trigger further dust particle coagulation. This mechanism could result in the formation of other planetesimals. Lyra et al. (2008b) find that the presence of a Jupiter mass planet in the disk leads to the gravitational collapse of solid material in gas vortices at the edges of the disk gap. Their simulations suggest the formation of a rocky planet of 17 Earth masses in less than 200 orbital time scales.

Chapter 7

Summary and outlook

The topic of this thesis was the evolution of dust during the first 1 Myr in protoplanetary disks. We focused on two main subjects, namely the radial motion and the growth of dust in the disk. One goal was to answer the question of how the dust distribution spatially evolves in time. This investigation was partly motivated by observational findings. Interferrometric millimeter data of circumstellar disks suggest large amounts of mm to cm sized dust pebbles in the outer disk regions which theoretically should not be there (Chapter 3). Another goal was to investigate how large dust grains can grow in disks, what the time scales for particle growth are (Chapter 4 and 5), and if dust particle growth due to hit-and-stick mechanisms can actually lead to the formation of planetesimal, or not (Chapter 6).

Concerning the first topic, i.e. the spatial evolution of dust, we find that systematic inward motion of dust is a genuine problem. It leads to a continuous solid material loss due to dust evaporation at the inner hot rim of the disk. Although the mass of the dust disk stays roughly constant in the first few 10^5 yrs, the dust mass has decreased down to a few percent of its original value after 1 Myr of disk evolution. Without dust, it appears rather challenging to form planets. This suggests that either our understanding of radial motion of particles in disks lacks important physics, or planetesimal formation of rocky cores happens over time scales which are significantly shorter than the life time of the disk.

Theoretical investigation of particle motion in disks suggests that radial drift can not be as efficient as first calculated by Weidenschilling (1977a). In this thesis, we have shown that the radial drift is reduced by a factor of ~ 10 if weakly turbulent disks are considered. This is due to the occurence of collective effects which become of importance if the dust-to-gas ratio exceeds unity (Nakagawa et al. 1986). If particle growth is included in the simulations and particle fragmentation neglected then the solution to the radial drift problem may lie in the dust-to-gas ratio of the disk. If this quantity is increased by a factor of ~ 2 compared to the dust-to-gas ratio of the ISM, then we find that up to 50% of the initial dust mass is still present after 1 Myr of disk evolution. Also gas pressure fluctuations due to MRI turbulence can reduce the radial drift up to a factor of 2 (Johansen et al. 2006b). Simple particle drift models including analytical descriptions of gas overdensities even predict averaged radial drift velocities which are more than an order of magnitude lower.[1] Another effect which inheres the capacity to significantly affect the radial motion of dust grains is photophoresis. Various

[1] Unpublished data of V. Menke.

authors have shown that the dust evolution is strongly influenced by this mechanism if the disk is optically thin (Krauss & Wurm 2005; Herrmann & Krivov 2007; Takeuchi & Krauss 2008). There is even reason to believe that photophoresis could play a non-negligible role in optically thick disks. This is due to the radial temperature gradient in protoplanetary disks which involves a permanent radial radiation flux. Further investigation of this, regrettably sometimes ignored effect, is surely needed.

If radial particle drift and fragmentation is neglected, then dust particle growth happens very fast in protoplanetary disks. Simulation results of this thesis in agreement with earlier studies of particle growth (Weidenschilling 1980; Dullemond & Dominik 2005; Ciesla 2007) suggest the formation of meter-sized objects within only 10^3 yrs at 1 AU in a disk around a solar type star. At 100 AU, this growth time scale increases towards several 10^6 yrs. This shows that dust particle growth time scales are strongly dependent on the disk location. The inclusion of radial drift into the disk model, however, changes the dust growth evolution significantly. If a canonical dust-to-gas ratio of 1% is adopted, then dust particles at 1 AU never grow larger than meter size. This is because radial drift time scales are usually shorter than particle growth time scales. Particles grow to some cm in size and then rapidly drift into the inner regions of the disk where they evaporate. Only for initial dust-to-gas ratios larger than 1.5%, boulders of 100 m size can form in the inner disk < 5 AU within 10^4 yrs. This example shows that particle growth time scales are strongly dependent on the initial dust to gas ratio which is a major result of this thesis. In the outer disk around 100 AU, the maximum dust particle size never exceeds 1 mm.

Let us consider a disk with an initial dust-to-gas ratio sufficient to form meter-sized boulders at 1 AU in the disk in a few 10^3 yrs. The further growth from meter-sized boulders to km-sized objects via collisional sticking takes roughly 1 Myr. However, this is not true if the self-gravity of the dust is taken into account. From meter size on, particle swarms if sufficiently dense can undergo gravitational collapse and basically jump over several orders of magnitude in particle radius in very short time scales. This instability can result in the formation of Ceres-size objects (Johansen et al. 2007) or even large rocky Mars-like planets (Lyra et al. 2008a). Gravitational collapse from meter-sized boulders to planets occurs in less than 10 orbital time scales, which is orders or magnitude less than the formation time scale of meter-sized objects by collisional growth.

So far, one may get the impression that planetesimal formation is no problem in planetary disks. However, this is not the case since we ignored the important effect of dust particle fragmentation so far. The models investigated in this thesis show that it is very hard to grow particles in disks larger than cm-size before destructive high speed collisions prevent further growth. The maximum particle size before fragmentation inhibits further coagulation surely depends on the disk model and particle parameters such as the threshold fragmentation velocity, but for reasonable disk and particle parameters we never find solid material to overcome the fragmentation barrier. Only, for example, in disks with very low turbulence, and for critical threshold fragmentation velocities of 30 m/s or higher, we find planetesimal formation in our simulations. Johansen et al. (2007) and Lyra et al. (2008a) ignore particle destruction in their dust collapse simulations, although Lyra et al. find relative velocities of boulders of more than 20 m/s, with peak velocities of 80 m/s. The investigation of the combined effect of gravitational dust collapse and particle fragmentation is, hence, highly needed.

The gravitational collapse as found by Johansen et al. (2007) is only operating if boulders with Stokes numbers close to unity are present, and if they are abundant enough. If the conditions for this collapse are fulfilled can be answered by the dust growth evolution models

of this thesis. For weakly turbulent disks and high fragmentation velocities ($v_f = 20$ m/s), we find that particles marginally grow to the size regime where gravitational instability of solids becomes of importance (St > 0.1). However, the amount of dust present in these large grains always corresponds to vertically integrated dust-to-gas ratios smaller than the considered canonical value of 0.01 adopted by Johansen and collaborators. This is because significant amounts of dust are present in smaller aggregates due to permanent particle fragmentation in the disk. If this process will work also with lower dust-to-gas ratios remains to be answered. The gravitational collapse of particle swarms as investigated by Lyra et al. (2008a) requires dust particle radii of only 1 cm, corresponding to Stokes numbers of 10^{-2} in their model. Our dust evolution models show that this particle size can be reached without adopting unphysical disk or dust parameters. This makes the mechanism by Lyra et al. more probable for the moment.

In the last chapter, we investigated a possibility to form large objects in protoplanetary disks, nevertheless. We focused on particle growth in layered MRI-driven disks including a non-turbulent dead zone around the ice evaporation front. We chose this specific disk environment since it involves comparatively low relative dust particle velocities, i.e. relative velocities which are in the same order of magnitude than typical particle fragmentation velocities. We indeed find that planetesimal formation is possible in this environment. In our simulations, objects of km-size can form around the snow line in only $\sim 10^3$ yrs of disk evolution. We find, however, that this formation scenario is very dependent on the mass accretion rate in the disk and that planetesimal formation due to this mechanism is only possible in the later evolutionary stages of the disk. Nevertheless, this chapter is examplary for the effect of gas pressure maxima on the growth of solid material. Gas pressure maxima do no neccesarily have to origin in the presence of an evaporation front, like in this thesis. Other possibilities for gas overdensities are spiral waves, long-lived hydrodynamical fluctuations, or gas structures caused by the presence of a Jupiter-like planet, which might as well lead to planetesimal formation due to the same process.

There is another possibility for dust particles to overcome the fragmentation barrier. Before particles reach the velocity regime where fragmentation occurs, the effect of bouncing is thought to play an important role. Particles could grow to dm-size, for example, and then enter a regime where equal-sized particle collisions only lead to particle bouncing. Particles, however, could still grow by sweeping up smaller dust grains. This scenario is strongly dependent on for what particle sizes and in which velocity regime bouncing occurs. Unfortunately, experiments of particle bouncing only cover a small experimental range of collision parameters. More input from particle collision experiments is needed to explore this effect in more detail.

There are various opportunities for future work and I would like to mention some possible projects.

The determination of dust masses of disks via observations is typically based on an assumption about the dust particle size distribution in the disk. However, observationally inferred dust masses can vary significantly if different grain sizes, i.e. different opacities, are assumed. This is because the observed flux is in principle the product between the dust density and the dust opacity. Lower opacities lead to higher dust masses and vice versa, and since the exact dust opacity is not known, the dust mass is poorly constrained as well. Dust particle evolution models as presented in this thesis can give a valuable input for a more realistic interpretation of observational data. Moreover, we discussed in Chapter 4 that sub-millimeter continuum observations of disks suggest radial dust mass distributions which are rather shallow (Andrews & Williams 2007). This could be explained by the fact that

growth time scales of dust vary strongly with disk radius. Further investigation regarding this issue is surely worthwhile.

We have shown that the amount of turbulence in a disk affects the growth of dust significantly. Less turbulent disks lead to larger dust particles and vice versa. However, disk turbulence does not only affect the dust, solid particles also influence the amount of turbulence in the disk in a non-trivial way. The degree of MRI turbulence in disks is very dependent on the amount of free electrons. The electron density, on the other hand, strongly depends on the surface area to mass ratio of the dust particles. This ratio changes by several orders of magnitude during particle growth. Hence, we expect the amount of turbulence in the disk to change significantly during dust growth. The investigation of this back-reaction from the dust on the turbulence in the disk seems to be a next logical step.

In the disk model discussed here, the gaseous background was always assumed to be in a steady state, even for times as long as a Myr. However, disks undergo viscous spreading which changes the surface density distribution of the gas over time scales of 10^5 yrs. Moreover, we ignored the effect of gas and dust infall after the disk has formed. This infall involves a constant supply of small dust grains in the disk for at least the first $\sim 10^5$ yrs. A model which includes the infall of the collapsing cloud on the disk, viscous disk spreading, and dust particle growth at the same time is surely needed.

This thesis was performed under the supervision of Dr. Cornelis P. Dullemond and Prof. Dr. Thomas Henning. Parts of the thesis were published in refereed journals.

"Survival of the mm-cm sized grain population observed in protoplanetary disks" (2007),
F. Brauer, C.P. Dullemond, Th. Henning, A. Johansen, H. Klahr, A. Natta, A&A 469, 1169B

"Coagulation, fragmentation and radial motion of dust in protoplanetary disks" (2008)[2],
F. Brauer, C.P. Dullemond and Th. Henning, A&A 480, 859B

"Planetesimal formation around the snow line in MRI-driven turbulent protoplanetary disks" (2008),
F. Brauer, Th. Henning and C.P. Dullemond, A&A Letters, 487, L1

[2]This paper was awarded the "Patzer Prize" for one of the best refereed publications by a PhD student at the MPIA in 2008.

Bibliography

Acke, B. & van den Ancker, M. E. 2004, A&A, 426, 151

Acke, B., van den Ancker, M. E., Dullemond, C. P., van Boekel, R., & Waters, L. B. F. M. 2004, A&A, 422, 621

Adams, F. C., Lada, C. J., & Shu, F. H. 1987, ApJ, 312, 788

Akeson, R. L., Ciardi, D. R., van Belle, G. T., & Creech-Eakman, M. J. 2002, ApJ, 566, 1124

Alexander, R. D. & Armitage, P. J. 2007, MNRAS, 375, 500

Alexander, R. D., Clarke, C. J., & Pringle, J. E. 2006, MNRAS, 369, 229

Amelin, Y., Krot, A. N., Hutcheon, I. D., & Ulyanov, A. A. 2002, Science, 297, 1678

Andrews, S. M. & Williams, J. P. 2007, ApJ, 659, 705

Apai, D., Luhman, K., & Liu, M. 2007, ArXiv Astrophysics e-prints

Apai, D., Pascucci, I., Bouwman, J., et al. 2005, Science, 310, 834

Apai, D., Pascucci, I., Sterzik, M. F., et al. 2004, A&A, 426, L53

Bacciotti, F., Ray, T. P., Eisloeffel, J., et al. 2003, ApSS, 287, 3

Balbus, S. A. 2000, ApJ, 534, 420

Balbus, S. A. & Hawley, J. F. 1991, ApJ, 376, 214

Bally, J., Moeckel, N., & Throop, H. 2005, in Astronomical Society of the Pacific Conference Series, Vol. 341, Chondrites and the Protoplanetary Disk, ed. A. N. Krot, E. R. D. Scott, & B. Reipurth, 81

Bally, J., Reipurth, B., & Davis, C. J. 2007, in Protostars and Planets V, ed. B. Reipurth, D. Jewitt, & K. Keil, 215–230

Barge, P. & Sommeria, J. 1995, A&A, 295, L1

Beckwith, S. V. W., Sargent, A. I., Chini, R. S., & Guesten, R. 1990, AJ, 99, 924

Benz, W. 2000, Space Science Reviews, 92, 279

Blum, J. 2004, in Astronomical Society of the Pacific Conference Series, Vol. 309, Astrophysics of Dust, ed. A. N. Witt, G. C. Clayton, & B. T. Draine, 369

Blum, J. & Muench, M. 1993, Icarus, 106, 151

Blum, J., Schräpler, R., Davidsson, B. J. R., & Trigo-Rodríguez, J. M. 2006, ApJ, 652, 1768

Blum, J. & Wurm, G. 2000, Icarus, 143, 138

Blum, J. & Wurm, G. 2008, AnnRevA& A, 46, 21

Blum, J., Wurm, G., Poppe, T., & Heim, L.-O. 1998, Earth Moon and Planets, 80, 285

Bodenheimer, P., Yorke, H. W., Rozyczka, M., & Tohline, J. E. 1990, ApJ, 355, 651

Bolatto, A. D., Leroy, A. K., Rosolowsky, E., Walter, F., & Blitz, L. 2008, ApJ, 686, 948

Bouwman, J., de Koter, A., van den Ancker, M. E., & Waters, L. B. F. M. 2000, A&A, 360, 213

Bouwman, J., Meeus, G., de Koter, A., et al. 2001, ApJ, 375, 950

Brandenburg, A., Nordlund, A., Stein, R. F., & Torkelsson, U. 1995, ApJ, 446, 741

Brauer, F., Dullemond, C. P., & Henning, T. 2008, A&A, 480, 859

Brauer, F., Dullemond, C. P., Johansen, A., et al. 2007, A&A, 469, 1169

Bryden, G., Różyczka, M., Lin, D. N. C., & Bodenheimer, P. 2000, ApJ, 540, 1091

Calvet, N. & Gullbring, E. 1998, ApJ, 509, 802

Chauvin, G., Lagrange, A.-M., Dumas, C., et al. 2005, A&A, 438, L25

Ciesla, F. J. 2007, ApJL, 654, L159

Clayton, G. C., Wolff, M. J., Sofia, U. J., Gordon, K. D., & Misselt, K. A. 2003, ApJ, 588, 871

Cuzzi, J. N., Hogan, R. C., Paque, J. M., & Dobrovolskis, A. R. 2001, ApJ, 546, 496

Cuzzi, J. N. & Weidenschilling, S. J. 2006, Particle-Gas Dynamics and Primary Accretion (Meteorites and the Early Solar System II), 353–381

D'Alessio, P., Calvet, N., Hartmann, L., Franco-Hernández, R., & Servín, H. 2006, ApJ, 638, 314

Davis, D. R. & Ryan, E. V. 1990, Icarus, 83, 156

Derjaguin, B. V., Muller, V. M., & Toporov, Y. P. 1975, J. Colloid Interface Sci., 53, 314

Descartes, R. 1644, Principia Philosophiae (Elzevir, Amsterdam)

Desch, S. J. 2007, ApJ, 671, 878

Desch, S. J., Connolly, Jr., H. C., & Moser, D. E. 2002, in Lunar and Planetary Institute Conference Abstracts, Vol. 33, Lunar and Planetary Institute Conference Abstracts, 1768

Dohnanyi, J. W. 1969, J. Geophys. Res., 74, 2531

Dominik, C., Blum, J., Cuzzi, J. N., & Wurm, G. 2007, in Protostars and Planets V (Univ. Arizona Press), 783–800

Dominik, C. & Tielens, A. G. G. M. 1997, ApJ, 480, 647

Draine, B. T. & Lee, H. M. 1984, ApJ, 285, 89

Dubrulle, B., Marié, L., Normand, C., et al. 2005, A&A, 429, 1

Dubrulle, B., Morfill, G., & Sterzik, M. 1995, Icarus, 114, 237

Dullemond, C. P. & Dominik, C. 2004a, A&A, 417, 159

Dullemond, C. P. & Dominik, C. 2004b, A&A, 421, 1075

Dullemond, C. P. & Dominik, C. 2005, A&A, 434, 971

Dutrey, A., Guilloteau, S., Duvert, G., et al. 1996, A&A, 309, 493

Eisner, J. A., Plambeck, R. L., Carpenter, J. M., et al. 2008, ApJ, 683, 304

Fernandez, J. A. & Ip, W.-H. 1984, Icarus, 58, 109

Fischer, D. A. & Valenti, J. 2005, ApJ, 622, 1102

Fromang, S. & Nelson, R. P. 2005, MNRAS, 364, L81

Fuller, K. N. G. & Tabor, D. 1975, Proc. R. Soc. London A, 345, 327

Galilei, G. 1632

Garaud, P. 2007, ArXiv e-prints, 705

Garaud, P., Barrière-Fouchet, L., & Lin, D. N. C. 2004, ApJ, 603, 292

Goldreich, P. & Ward, W. R. 1973, ApJ, 183, 1051

Greenberg, J. M. 1978, Interstellar dust (Cosmic Dust), 187–294

Gullbring, E., Barwig, H., & Schmitt, J. H. M. M. 1997, A&A, 324, 155

Gullbring, E., Petrov, P. P., Ilyin, I., et al. 1996, A&A, 314, 835

Haghighipour, N. 2005, MNRAS, 362, 1015

Haghighipour, N. & Boss, A. P. 2003, ApJ, 583, 996

Haisch, Jr., K. E., Lada, E. A., & Lada, C. J. 2001, ApJL, 553, L153

Harper, W. R. 1967, Contact and Frictional Electrification (Oxford Univ. Press)

Hartmann, L., Calvet, N., Gullbring, E., & D'Alessio, P. 1998, ApJ, 495, 385

Hawley, J. F., Gammie, C. F., & Balbus, S. A. 1995, ApJ, 440, 742

Hayashi, C. 1981, in IAU Symposium, Vol. 93, Fundamental Problems in the Theory of Stellar Evolution (D. Reidel Publishing Co.), 339–342

Heim, L.-O., Blum, J., Preuss, M., & Butt, H.-J. 1999, Physical Review Letters, 83, 3328

Herbst, W., Herbst, D. K., Grossman, E. J., & Weinstein, D. 1994, AJ, 108, 1906

Herrmann, F. & Krivov, A. V. 2007, A&A, 476, 829

Heyer, M. H. 1988, ApJ, 324, 311

Hirashita, H. 2000, Publ. Astron. Soc. Japan, 52, 585

Horn, R. G., Smith, D. T., & Haller, W. 1989, Chem. Phys. Lett., 162, 404

Hueso, R. & Guillot, T. 2005, A&A, 442, 703

Ilgner, M. & Nelson, R. P. 2006, A&A, 445, 205

Ilgner, M. & Nelson, R. P. 2008, ArXiv e-prints, 802

Jeans, J. H. 1902, in A, Vol. 199, Philosophical transactions of the Royal Society of London, 1–53

Johansen, A., Henning, T., & Klahr, H. 2006a, ApJ, 643, 1219

Johansen, A. & Klahr, H. 2005, ApJ, 634, 1353

Johansen, A., Klahr, H., & Henning, T. 2006b, ApJ, 636, 1121

Johansen, A., Oishi, J. S., Low, M.-M. M., et al. 2007, Nature, 448, 1022

Johansen, A. & Youdin, A. 2007, ApJ, 662, 627

Kempf, S., Blum, J., & Wurm, G. 2000, Bulletin of the American Astronomical Society, 32, 1099

Kempf, S., Pfalzner, S., & Henning, T. K. 1999, Icarus, 141, 388

Kendall, K., Alford, N. M., & Birchall, J. D. 1987, Nature (London), 352, 794

Kenyon, S. J. & Hartmann, L. 1987, ApJ, 323, 714

Kessler-Silacci, J. E., Dullemond, C. P., Augereau, J.-C., et al. 2007, ApJ, 659, 680

King, A. R., Pringle, J. E., & Livio, M. 2007, MNRAS, 376, 1740

Kitamura, Y., Momose, M., Yokogawa, S., et al. 2002, ApJ, 581, 357

Klahr, H. & Bodenheimer, P. 2006, ApJ, 639, 432

Klahr, H. & Brandner, W. 2006, Planet Formation (Cambridge University Press)

Klahr, H., Różyczka, M., Dziourkevitch, N., Wünsch, R., & Johansen, A. 2006, Turbulence in protoplanetary accretion disks: driving mechanisms and role in planet formation. (Planet Formation), 42

Klahr, H. H. & Bodenheimer, P. 2003, ApJ, 582, 869

Klahr, H. H. & Henning, T. 1997, Icarus, 128, 213

Klahr, H. H. & Lin, D. N. C. 2001, ApJ, 554, 1095

Koestler, A. 1980, Die Nachtwandler: Die Entstehungsgeschichte unserer Welterkenntnis (Suhrkamp Verlag)

Königl, A. & Pudritz, R. E. 2000, Protostars and Planets IV, 759

Kovetz, A. & Olund, B. 1969, Journal of Atmospheric Sciences, 26, 1060

Krauss, O. & Wurm, G. 2005, ApJ, 630, 1088

Kretke, K. A. & Lin, D. N. C. 2007, ApJL, 664, L55

Lahuis, F., van Dishoeck, E. F., Blake, G. A., et al. 2007, ApJ, 665, 492

Laughlin, G. & Bodenheimer, P. 1994, ApJ, 436, 335

Lecar, M., Podolak, M., Sasselov, D., & Chiang, E. 2006, ApJ, 640, 1115

Lin, D. N. C. & Papaloizou, J. C. B. 1993, in Protostars and Planets III, ed. E. H. Levy & J. I. Lunine, 749–835

Lin, D. N. C., Papaloizou, J. C. B., Terquem, C., Bryden, G., & Ida, S. 2000, Protostars and Planets IV, 1111

Lodders, K. 2003, ApJ, 591, 1220

Lüst, R. 1952, Z. Naturforschung Vol. A, 7, 87

Lynden-Bell, D. & Pringle, J. E. 1974, MNRAS, 168, 603

Lyra, W., Johansen, A., Klahr, H., & Piskunov, N. 2008a, ArXiv e-prints

Lyra, W., Johansen, A., Klahr, H., & Piskunov, N. 2008b, ArXiv e-prints

Markiewicz, W. J., Mizuno, H., & Voelk, H. J. 1991, A&A, 242, 286

Mathis, J. S., Rumpl, W., & Nordsieck, K. H. 1977, ApJ, 217, 425

Mayor, M. & Queloz, D. 1995, Nature, 378, 355

McCaughrean, M. J. & O'Dell, C. R. 1996, AJ, 111, 1977

Meakin, P. & Donn, B. 1988, ApJL, 329, L39

Meeus, G., Waters, L. B. F. M., Bouwman, J., et al. 2001, A&A, 365, 476

Ménard, F. & Bertout, C. 1999, in NATO ASIC Proc. 540: The Origin of Stars and Planetary Systems, ed. C. J. Lada & N. D. Kylafis, 341

Mizuno, H., Markiewicz, W. J., & Voelk, H. J. 1988, A&A, 195, 183

Mokler, F. & Morfill, G. E. 2005, in Protostars and Planets V, 8172

Morfill, G. E. 1988, Icarus, 75, 371

Nakagawa, Y., Nakazawa, K., & Hayashi, C. 1981, Icarus, 45, 517

Nakagawa, Y., Sekiya, M., & Hayashi, C. 1986, Icarus, 67, 375

Nakamoto, T. & Nakagawa, Y. 1994, ApJ, 421, 640

Natta, A., Testi, L., Calvet, N., et al. 2007a, in Protostars and Planets V (Univ. Arizona Press), 767–781

Natta, A., Testi, L., Calvet, N., et al. 2007b, in Protostars and Planets V, ed. B. Reipurth, D. Jewitt, & K. Keil, 767–781

Natta, A., Testi, L., Neri, R., Shepherd, D. S., & Wilner, D. J. 2004, A&A, 416, 179

Nelson, R. P. & Papaloizou, J. C. B. 2003, MNRAS, 339, 993

Nomura, H. & Nakagawa, Y. 2006, ApJ, 640, 1099

O'Dell, C. R. & Wen, Z. 1994, ApJ, 436, 194

O'Dell, C. R., Wen, Z., & Hu, X. 1993, ApJ, 410, 696

Ohtsuki, K., Nakagawa, Y., & Nakazawa, K. 1989, in Lunar and Planetary Inst. Technical Report, Vol. 20, Lunar and Planetary Institute Conference Abstracts, 808

Ormel, C. W. & Cuzzi, J. N. 2007, A&A, 466, 413

Ormel, C. W., Spaans, M., & Tielens, A. G. G. M. 2007, A&A, 461, 215

Ossenkopf, V. 1993, A&A, 280, 617

Ossenkopf, V. & Henning, T. 1994, A&A, 291, 943

Panić, O., Hogerheijde, M. R., Wilner, D., & Qi, C. 2008, ArXiv e-prints

Papaloizou, J. C. B., Nelson, R. P., Kley, W., Masset, F. S., & Artymowicz, P. 2007, in Protostars and Planets V, ed. B. Reipurth, D. Jewitt, & K. Keil, 655–668

Paraskov, G. B., Wurm, G., & Krauss, O. 2007, Icarus, 191, 779

Pilipp, W., Hartquist, T. W., & Morfill, G. E. 1992, ApJ, 387, 364

Pinte, C., Padgett, D. L., Ménard, F., et al. 2008, A&A, 489, 633

Poppe, T., Blum, J., & Henning, T. 1999, Advances in Space Research, 23, 1197

Poppe, T., Blum, J., & Henning, T. 2000a, ApJ, 533, 454

Poppe, T., Blum, J., & Henning, T. 2000b, ApJ, 533, 472

Pringle, J. E. 1981, AnnRevA& A, 19, 137

Przygodda, F., van Boekel, R., Àbrahàm, P., et al. 2003, A&A, 412, L43

Pudritz, R. E. & Norman, C. A. 1983, ApJ, 274, 677

Pudritz, R. E., Ouyed, R., Fendt, C., & Brandenburg, A. 2007, in Protostars and Planets V, ed. B. Reipurth, D. Jewitt, & K. Keil, 277–294

Quine, W. v. O. 1953, From a logical point of view (Harper and Row, New York)

Reyes-Ruiz, M. 2007, MNRAS, 380, 311

Rice, W. K. M., Lodato, G., Pringle, J. E., Armitage, P. J., & Bonnell, I. A. 2004, MNRAS, 355, 543

Rodmann, J. 2006, PhD thesis, PhD Thesis, Combined Faculties for the Natural Sciences and for Mathematics of the University of Heidelberg, Germany. XIII+137 pp. (2006)

Rodmann, J., Henning, T., Chandler, C. J., Mundy, L. G., & Wilner, D. J. 2006, A&A, 446, 211

Rosolowsky, E. 2007, ApJ, 654, 240

Safronov, V. S. 1963, Soviet Physics Doklady, 7, 967

Safronov, V. S. 1969, Evoliutsiia doplanetnogo oblaka. (1969.)

Sano, T., Inutsuka, S., Turner, N. J., & Stone, J. M. 2004, Progress of Theoretical Physics Supplement, 155, 409

Sano, T., Inutsuka, S.-I., & Miyama, S. M. 1998, ApJL, 506, L57

Sano, T., Miyama, S. M., Umebayashi, T., & Nakano, T. 2000, ApJ, 543, 486

Santos, N. C., Israelian, G., & Mayor, M. 2004, A&A, 415, 1153

Schäfer, C., Speith, R., & Kley, W. 2007, A&A, 470, 733

Schmitt, W., Henning, T., & Mucha, R. 1997, A&A, 325, 569

Schräpler, R. & Henning, T. 2004, ApJ, 614, 960

Sekiya, M. 1998, Icarus, 133, 298

Setiawan, J., Henning, T., Launhardt, R., et al. 2008, Nature, 451, 38

Shakura, N. I. & Sunyaev, R. A. 1973, A&A, 24, 337

Sicilia-Aguilar, A., Hartmann, L. W., Watson, D., et al. 2007, ApJ, 659, 1637

Smoluchowski, M. V. 1916, Zeitschrift fur Physik, 17, 557

Stone, J. M. & Pringle, J. E. 2001, MNRAS, 322, 461

Suttner, G. & Yorke, H. W. 2001, ApJ, 551, 461

Takeuchi, T., Clarke, C. J., & Lin, D. N. C. 2005, ApJ, 627, 286

Takeuchi, T. & Krauss, O. 2008, ApJ, 677, 1309

Takeuchi, T. & Lin, D. N. C. 2002, ApJ, 581, 1344

Takeuchi, T. & Lin, D. N. C. 2005, ApJ, 623, 482

Tanaka, H., Himeno, Y., & Ida, S. 2005, ApJ, 625, 414

Tanaka, H., Inaba, S., & Nakazawa, K. 1996, Icarus, 123, 450

Terebey, S., Shu, F. H., & Cassen, P. 1984, ApJ, 286, 529

Testi, L., Natta, A., Shepherd, D. S., & Wilner, D. J. 2003, A&A, 403, 323

Trieloff, M. & Palme, H. 2006, The origin of solids in the early Solar System (Planet Formation), 64

Tsiganis, K., Gomes, R., Morbidelli, A., & Levison, H. F. 2005, Nature, 435, 459

Turner, N. J., Sano, T., & Dziourkevitch, N. 2007, ApJ, 659, 729

Twomey, S. 1966, Journal of Atmospheric Sciences, 23, 405

van Boekel, R., Waters, L. B. F. M., Dominik, C., et al. 2003, A&A, 400, L21

Völk, H. J., Morfill, G. E., Roeser, S., & Jones, F. C. 1980, A&A, 85, 316

Warshaw, M. 1967, Journal of Atmospheric Sciences, 24, 278

Watson, A. M., Stapelfeldt, K. R., Wood, K., & Ménard, F. 2007, in Protostars and Planets V, ed. B. Reipurth, D. Jewitt, & K. Keil, 523–538

Weidenschilling, S. J. 1977a, MNRAS, 180, 57

Weidenschilling, S. J. 1977b, APSS, 51, 153

Weidenschilling, S. J. 1979, Bulletin of the American Astronomical Society, 11, 552

Weidenschilling, S. J. 1980, Icarus, 44, 172

Weidenschilling, S. J. 1984, Icarus, 60, 553

Weidenschilling, S. J. 1988, Formation processes and time scales for meteorite parent bodies in Meteorites and the Early Solar System (Univ. Arizona Press), 348–371

Weidenschilling, S. J. 2003, Icarus, 165, 438

Weidenschilling, S. J. 2006, Icarus, 181, 572

Weidenschilling, S. J. & Cuzzi, J. N. 1993, in Protostars and Planets III, ed. E. H. Levy & J. I. Lunine, 1031–1060

Weizsäcker, C. F. 1944, Über die Entstehung des Planetensystems, Vol. 22 (Z. Astrophys.)

Whipple, F. L. 1972, in From Plasma to Planet (New York: Wiley Interscience Division), 211.

Wilde, S. A., Valley, J. W., Peck, W. H., & Graham, C. M. 2001, Nature, 409, 175

Wilkinson, M., Mehlig, B., & Uski, V. 2007, ArXiv e-prints, 706

Williams, D. R. & Wetherill, G. W. 1994, Icarus, 107, 117

Williams, J. P., Blitz, L., & McKee, C. F. 2000, Protostars and Planets IV, 97

Wilner, D. J., D'Alessio, P., Calvet, N., Claussen, M. J., & Hartmann, L. 2005, ApJL, 626, L109

Wolf, S., Padgett, D. L., & Stapelfeldt, K. R. 2003, ApJ, 588, 373

Wurm, G., Paraskov, G., & Krauss, O. 2005, Icarus, 178, 253

Youdin, A. N. 2004, in ASP Conf. Ser. 323: Star Formation in the Interstellar Medium: In Honor of D. Hollenbach, C. McKee, and F. Shu (Francisco: Astronomical Society of the Pacific), 319–326

Youdin, A. N. & Chiang, E. I. 2004, ApJ, 601, 1109

Youdin, A. N. & Goodman, J. 2005, ApJ, 620, 459

Youdin, A. N. & Johansen, A. 2007, ArXiv e-prints

Youdin, A. N. & Shu, F. H. 2002, ApJ, 580, 494

Zsom, A. & Dullemond, C. P. 2008, A&A, 489, 931